AGING MECHANISMS OF LITHIUM-ION BATTERIES IN ELECTRIC VEHICLE APPLICATIONS

Guo, Jia

DOI (link to publication from Publisher):
10.54337/aau645693918

Publication date:
2023

Document Version
Publisher's PDF, also known as Version of record

Citation for published version (APA):
Guo, J. (2023). *AGING MECHANISMS OF LITHIUM-ION BATTERIES IN ELECTRIC VEHICLE APPLICATIONS*. Aalborg Universitetsforlag. https://doi.org/10.54337/aau645693918

AGING MECHANISMS OF LITHIUM-ION BATTERIES IN ELECTRIC VEHICLE APPLICATIONS

BY
JIA GUO

DISSERTATION SUBMITTED 2023

AALBORG UNIVERSITY
DENMARK

AGING MECHANISMS OF LITHIUM-ION BATTERIES IN ELECTRIC VEHICLE APPLICATIONS

by

Jia Guo

AALBORG UNIVERSITY
DENMARK

Dissertation submitted: October 2023

Dissertation submitted:	6. October, 2023
PhD supervisor::	Associate Professor Daniel-Ioan Stroe Aalborg University
Assistant PhD supervisor:	Prof. Kjeld Pedersen Aalborg University
PhD committee:	Professor Francesco Iannuzzo (chair) Aalborg University, Denmark Professor Dorthe Ravnsbæk Aarhus University, Denmark Associate Professor Jonas Mindemark Uppsala University, Sweden
PhD Series:	Faculty of Engineering and Science, Aalborg University
Department:	AAU Energy

ISSN (online): 2446-1636
ISBN (online): 978-87-7573-614-0

Published by:
Aalborg University Press
Kroghstræde 3
DK – 9220 Aalborg Ø
Phone: +45 99407140
aauf@forlag.aau.dk
forlag.aau.dk

Printed in Denmark by Stibo Complete, 2023

CV

Jia Guo was born in Shangluo, Shaanxi Province, China in 1994. He completed his master's degree at the School of Metallurgy and Environment, Central South University, Changsha, China, in 2020. He is currently a Ph.D. student at AAU Energy, Aalborg University, Aalborg, Denmark. His research interests are electrochemical test, mechanisms analysis, diagnosis, and materials synthesis. He also is the ECS and ISE student member.

Abstract

In electric vehicle applications, the aging of lithium-ion batteries is an inevitable process that has notable repercussions on the battery's lifespan, driving range, and safety aspects. The degradation rate of the battery is influenced by several factors, including charging protocols (such as constant current and pulse current charging), ambient temperature variations (including climate and seasonal changes), driving conditions (such as road conditions), and individual usage habits (including range and frequency). To enhance the battery's service life, it is crucial to study the underlying mechanisms of these external factors and identify the primary causes for battery aging. Here, the research objectives were simplified into battery aging in the charging process and driving process specific to electric vehicle scenarios, it becomes more manageable to study the factors and mechanisms that contribute to battery aging in these distinct environments. Therefore, in this thesis, battery state of health monitoring, electrochemical analysis, combined with in-situ testing and post-mortem analysis, were conducted to explore the aging mechanisms, and influencing factors of the battery during both charging and driving phases.

First, the battery voltage, current, and temperature parameters were monitored throughout the battery's aging process under constant current cycling. Regular reference performance tests are conducted to track the detailed degradation process using electrochemical analysis. Besides, innovative quantitative methods for post-mortem analysis of electrodes and materials were proposed, shedding light on the aging mechanisms. Those findings highlight the significant role of the solid electrolyte interface (SEI) film formation and gradual loss of active materials in battery aging. To address this, the pulse current charging protocols was employed to extend battery lifetime. In exploring the internal reaction mechanism during pulse current charging, in-situ Raman and in-situ synchrotron radiation testing were performed on fresh and aged electrodes. It reveals that pulse current charging mitigates structural changes in the electrode materials and suppresses alterations in the interface film.

To accurately study the battery's behavior during the driving process, discharging the battery under dynamic operating conditions was used to simulate real-world driving scenarios. Specifically, the Worldwide harmonized Light vehicles Test Cycle (WLTC) working conditions was used, which provide a comprehensive representation of road conditions and driving habits observed worldwide. By subjecting the battery to these dynamic load profiles, the battery performance and aging characteristics can be evaluated in a manner that closely mimics actual driving conditions experienced by electric vehicles. This approach enables to obtain valuable insights into the battery's degradation mechanisms under realistic driving scenarios. Building upon this framework, the effects of temperature and depth of discharge during the driving process is considered.

Therefore, throughout the entire thesis, a comprehensive analysis of the aging behavior of the battery during the charging and discharging processes was conducted, covering the entire battery system from the cell to the electrode and then to the materials levels. This provides important references for the design of battery management systems and next-generation batteries.

Resume

I elektriske køretøjsanvendelser er aldring af lithium-ion-batterier en uundgåelig proces, der har bemærkelsesværdige konsekvenser for batteriets levetid, kørselsrækkevidde og sikkerhedsaspekter. Batteriets nedbrydningshastighed påvirkes af flere faktorer, herunder opladningsprotokoller (såsom konstant strøm og pulsbaseret opladning), omgivelsestemperaturvariationer (herunder klima og sæsonmæssige ændringer), kørselsforhold (såsom vejforhold) og individuelle brugsvaner (herunder rækkevidde og hyppighed). For at forlænge batteriets levetid er det afgørende at undersøge de underliggende mekanismer for disse eksterne faktorer og identificere de primære årsager til batterialdring. Her blev forskningsmålene forenklet til batterialdring i opladningsprocessen og kørselsprocessen, specifikke for elektriske køretøjsscenarier, hvilket gør det mere håndterbart at studere de faktorer og mekanismer, der bidrager til batterialdring i disse distinkte miljøer. Derfor blev der i denne afhandling udført overvågning af batteriets sundhedstilstand, elektrokemisk analyse samt in-situ-test og post-mortem-analyse for at udforske aldringsmekanismer og påvirkende faktorer for batteriet under både opladnings- og kørselsfaser.

Først blev batterispænding, strøm og temperaturparametre overvåget i hele batteriets aldringsproces under konstant strømcyklus. Regelmæssige referencepræstationstests udføres for at følge den detaljerede nedbrydningsproces ved hjælp af elektrokemisk analyse. Derudover blev innovative kvantitative metoder til post-mortem-analyse af elektroder og materialer foreslået, hvilket kaster lys over aldringsmekanismerne. Disse fund fremhæver den betydningsfulde rolle, som dannelse af fast elektrolytgrænsefladefilm (SEI) og gradvis tab af aktive materialer spiller i batterialdring. For at imødegå dette blev pulsbaserede opladningsprotokoller anvendt for at forlænge batteriets levetid. Ved at udforske den interne reaktionsmekanisme under pulsbaseret opladning blev der udført in-situ Raman- og in-situ synkrotronstrålingstests på friske og aldrende elektroder. Det viser, at pulsbaseret opladning mindsker strukturelle ændringer i elektrodematerialerne og undertrykker ændringer i grænsefladefilmen.

For at studere batteriets adfærd nøjagtigt under kørselsprocessen blev batteriet afladet under dynamiske driftsbetingelser for at simulere virkelige kørescenarier. Specifikt blev Worldwide harmonized Light vehicles Test Cycle (WLTC) arbejdsbetingelser anvendt, hvilket giver en omfattende repræsentation af vejforhold og kørevaner, som observeres globalt. Ved at udsætte batteriet for disse dynamiske belastningsprofiler kan batteriets præstation og aldringsegenskaber evalueres på en måde, der tæt efterligner de faktiske kørselsbetingelser, som elektriske køretøjer oplever. Denne tilgang muliggør indhentning af værdifulde indsigter i batteriets nedbrydningsmekanismer under realistiske kørescenarier. Med udgangspunkt i denne ramme overvejes virkningerne af temperatur og dybde af afladning under kørselsprocessen.

Derfor blev der i hele afhandlingen gennemført en omfattende analyse af batterialdringsadfærd under opladnings- og afladningsprocesserne, der dækkede hele batterisystemet fra cellen til elektroden og derefter til materialeniveauerne. Dette giver vigtige referencepunkter for design af batteristyringssystemer og næste generation af batterier.

Acknowledgements

This thesis presents a summary of the research conducted for the Ph.D. dissertation titled “Mechanisms of Lithium-ion Battery Aging in Electric Vehicle Applications”. The Ph.D. project received support from both Aalborg University and the China Scholarship Council. Additionally, I extend my gratitude to the Otto Mønsteds Fund for their generous assistance in covering my accommodation and flights expenses during my study abroad period and my travel costs for conferences.

The Ph.D. project was successfully completed under the guidance of Associate Professors Daniel Stroe and Leonid Gurevich, as well as Professor Kjeld Pedersen. I am grateful for their patient and excellent guidance and the great learning environment they provided. Besides, I would like to extend my gratitude to Prof. Philipp Adelhelm and Dr. Yaolin Xu from Humboldt-Universität zu Berlin for providing me a valuable opportunity for half year visiting experience, access to experimental facilities, and their excellent guidance. Furthermore, I would also like to express my gratitude for the assistance and guidance provided by Peter Kjær Kristensen, Deyong Wang, Lars Rosgaard Jensen, and Kim Houtved Jensen from the Department of Materials Production, Donghong Yu and Xinxin Xiao from the Department of Chemistry and Bioscience, Aalborg University, Prof. Miran Gaberscek from National Institute of Chemistry.

Also, I want to say thanks to my colleagues. Because of you all, doing a Ph.D. isn’t dull anymore. I appreciate your trust, accompany, and encouragement. It keeps me feeling energized. Thanks for the help in life and study from Yaqi Li, Siyu Jin, Alejandro Gismero, Xin Sui, Xinrong Huang, Yunhong Che, Xingjun Li, Wendi Guo, Yusheng Zheng, and Wentao Liu. I am also grateful to my friends who have brought me help and happiness from Ziheng Wang, Pengwei Li, Xuejiao Li, Yichi Zhang, Zhihao Lin, Jiahong Liu, Hongyi Wang, Lingzhou Yu, Zhe Yang, Changjiang Bai, Yongchun Li, Yanchen Liu and Chen Liu. Finally, I’d like to express my gratitude to my warm roommate, Bo Yao, who has shared apartment with me for nearly three years.

Lastly, I’m profoundly grateful to my family, especially my parents, who made significant efforts to offer me a nurturing learning environment and opportunities. I also want to thank my siblings for sharing the family responsibilities.

Jia Guo

Aalborg University, October 3, 2023

Contents

Abstract V

Resume Vii

Acknowledgements ix

Report 1

Chapter 1. Introduction...3

1.1 Background 3

1.1.1 Diagnostic Methods 5

1.1.2 Constant Current Cycling... 6

1.1.3 Pulse Current Charging 6

1.1.4 Real Life Driving 7

1.2 State-of-art 7

1.3 Research Motivation 9

1.3.1 Research Objective.. 9

1.3.2 Project Limitations 10

1.4 Thesis Outline 10

1.5 List of Publications 12

Chapter 2. Battery Aging and Diagnosis Methods..15

2.1 Introduction.. 15

2.2 Battery and Battery Test.. 16

2.2.1 Full Cell Parameters 16

2.2.2 Battery Cell Test Station 17

2.2.3 Battery Test Protocols 18

2.3 Electrochemical Diagnosis Method 21

2.3.1 Incremental Capacity and Differential Voltage (IC-DV)........................ 21

2.3.2 Electrochemical Impedance Spectroscopy (EIS) 25

2.3.3 Coin Cells for Performance Evaluation... 27

2.3.4 Considerations and Advancements Related to the EIS Method 27

2.4 Materials Test Methods... 29

2.5 Summary 31

Chapter 3. Aging Mechanism for Battery in Constant Current Cycling 33
3.1 Aging of Full Cell 33
3.1.1 Cycling Performance.. 33
3.1.2 Impedance Analysis 35
3.2 Post-mortem Analysis 36
3.2.1 Loss of Li-ions 37
3.2.2 Degradation of Positive Electrode.. 39
3.2.3 Degradation of Negative Electrode 41
3.2.4 Degradation of Interface 42
3.3 Summary and Prospective.. 44
3.4 Summary 45
Chapter 4. Aging Mechanism for Battery in Pulse Current Charging 47
4.1 Introduction.. 47
4.2 Electrochemical Performance of Full Cell 48
4.3 Mechanisms at Electrodes Level... 52
4.3.1. Graphite Anode 52
4.3.2. NMC Cathode 56
4.3.3. Interface Degradation... 59
4.4 Summary 64
Chapter 5. Aging Mechanisms for Battery in Real Life Driving 65
5.1 Introduction.. 65
5.2 Aging of the Full Cell 66
5.2.1 Influence of Depth of Discharge 66
5.2.2 Influence of Temperature 67
5.3 Mechanisms of Battery Aging 68
5.3.1 Electrochemical Analysis.. 68
5.3.2 Post-mortem Analysis 74
5.4 Mechanism for Capacity Increase During Early Cycling.............................. 77
5.4.1 Capacity Increase Behavior.. 77
5.4.2 Electrochemical Analysis.. 78
5.4.3 Post-mortem for Coin Cell 80

5.5 Summary 82

Chapter 6. Conclusions and Future Work 83

6.1 Summary 83

6.2 Main Contributions 84

6.3 Research Perspectives 86

Literature list 89

Selected Publication 99

Lithium-Ion Battery Operation, Degradation, and Aging Mechanism in Electric Vehicles: An Overview [J1] 101

Understanding the Mechanism of Capacity Increase During Early Cycling of Commercial NMC/graphite Li-ion Batteries [J2] 125

Battery Impedance Spectrum Prediction From Partial Charging Voltage Curve by Machine Learning [J3] 139

Unravelling and Quantifying the Aging Processes of Commercial Li($Ni_{0.5}Co_{0.2}Mn_{0.3}$)O_2/graphite Li-ion Batteries under Constant Current Cycling [J4] 153

Unravelling the Mechanism of Pulse Current Charging for Enhancing the Stability of Commercial $LiNi_{0.5}Mn_{0.3}Co_{0.2}O_2$/graphite Lithium-ion Batteries [J5] 167

Can Electrochemical Impedance Spectroscopy be Replaced by Direct Current Techniques in Battery Diagnosis? [J6] 187

Machine Learning to Predict Electrochemical Impedance Spectra (EIS): Can EIS be Replaced by Constant Current Techniques [C1] 195

Unravelling and Quantifying the Aging Processes of Commercial Li($Ni_{0.5}Co_{0.2}Mn_{0.3}$)O_2/graphite Li-ions Batteries under Constant Current Cycling [C2] 199

LIST OF ACRONYMS

Li-ion	Lithium ion
SOH	State of health
SOC	State of charge
ICA	Incremental capacity analysis
DVA	Differential voltage analysis
IC-DV	Incremental capacity-differential voltage
OCV	Open circuit voltage
EIS	Electrochemical impedance spectroscopy
EFCs	Equivalent full cycles
SEI	Solid electrolyte interface
CEI	Cathode electrolyte interface
XRD	X-ray diffraction analysis
XAS	X-ray absorption spectroscopy
SEM	Scanning electron microscope
XPS	X-ray photoelectron spectroscopy
XAS	X-ray absorption spectroscopy
EXAFS	Extended X-Ray absorption fine structure
WLTP	Worldwide harmonized light vehicles test procedure
CC	Constant current
PC	Pulse current

LIST OF FIGURES

Figure 1-1 The arrangement from left to right consists of three types of EVs: Battery Electric Vehicles (BEV), Hybrid Electric Vehicles (HEV), and Plug-In Hybrid Electric Vehicles (PHEV), from left to right, and the battery operation modes in EV applications. Source [J1]…..……………………………………………………………………………...…4
Figure 1-2 Voltage and current curves for the battery in constant current - constant voltage (CC – CV) (top) and constant current (CC) (bottom) charging mode.………………………………6
Figure 1-3 Voltage and current curves for a battery in pulsed current charging mode.……..…7
Figure 1-4 Driving profile of (a) UDDS, (b) NEDC, (c) WLTC. Source [J1]…………………7
Figure 1-5 Thesis structure with related outcomes.……………………………………………11
Figure 2-1 Equipment and platform for full cell aging.………………………………………..17
Figure 2-2 Constant current cycling protocols for the battery aging with battery batch A.…...18
Figure 2-3 Pulse current charging protocols for the battery aging with battery batch A...........19
Figure 2-4 The WLTP driving cycle profile for a class 3 vehicle. Source: [J1]…….………..20
Figure 2-5 Battery batch A undergoes discharge according to the WLTP profile and cycling at various depths of discharge……………………………………………………….……….......21
Figure 2-6 Typically IC-DV curves for Graphite/Li, NMC/Li, and NMC/Graphite batteries. Source [J3]…………………………………………………………..……..….…….……22
Figure 2-7 Electrochemical curves from coin cell test. (a) The charging and discharging curves for all three different kinds of coin cells; (b) the DV curves that represent the charging process in a full cell; (c) IC curves of the graphite; and (d) the IC curves. Source: [J2]…………..….23
Figure 2-8 (a) EIS and corresponded equivalent circuit; (b) the relationship between Z' and $\omega^{\wedge(-1/2)}$. Source [J2]………………………………………………………………….……..26
Figure 2-9 EIS and DC impedance measurements, *e.g.* constant current techniques both can be used to quantify the battery impedance for $R_{\text{ohm+sei}}$, R_{ct}, and R_{mt}. Source: [J6].………………29
Figure 2-10 The EIS spectrum can be predicted by the battery constant current charging curve by machine learning method. Source: [J3]…………………………….…………………...30
Figure 3-1 (a) Charge and discharge curves; (b) IC curves; (c) evolution of SOH and the right shift of the b peak in (b); (d) Charging and discharging *cte*-OCV curves. Source: [J4][14].....34
Figure 3-2 EIS spectrum for (a) fresh battery and (b) aged battery. Source: [J4]……………....35
Figure 3-3 The EIS Nyquist plot is fit by (a) an equivalent circuit, and the fitted results for (b) R_{sei}; (c) R_{ct}. Source [J4]……………………………………...……………………...36
Figure 3-4 The temperature of battery outer surface. Source: [J4].…………………...……37
Figure 3-5 The negative and positive electrodes. Source: [J4]…………………………..…37
Figure 3-6 Negative electrode for (a) fresh battery, (b) aged battery and washed with DEC, and (c) aged negative electrode washed by DEC and by water. (d) The mechanism diagram of lithium compounds dissolved in water; (e) the quantified result of LiOH content; the Li 1s XPS results for (f) fresh battery and (g) aged battery. Source: [J4]……………………….……..38
Figure 3-7 SEM results of cross-section for (a) fresh positive electrode and (b) aged positive electrode, respectively; (c) XRD results. The SEM images for (d) fresh and (e) aged NMC particles, respectively; (f) Raman spectra; (g) EDS for aged positive electrode (h) XPS spectrum for aged positive electrode; (i) charge and discharge curve. Source: [J4]……….…………..40

Figure 3-8 (a) fresh negative electrode and (b) aged negative electrode cross-section images; top surface of (c) the fresh negative electrode and (d) aged negative electrode; SEM image of (e) fresh graphite particles, (f) aged graphite particles; (g) Raman spectra, (h) XRD patterns, and (i) charge and discharge voltage curves. Source: [J4]………………………..………..42
Figure 3-9 EIS result of (a) positive electrodes and (b) negative electrodes, (c) fitted results; XPS results of (d) positive electrodes, (e) negative; and (f) quantified results. Source: [J4]…45
Figure 3-10 A description of how battery capacity loss occurs, along with suggestions for extending the battery’s cycle life. Source: [J4]……………………………………..…...…47
Figure 4-1 The stability of batteries was evaluated over 1000 cycles using three different currents: constant current, 100 Hz current, and 2000 Hz current. Source: [J5]……………...48
Figure 4-2 The aging condition, dis/charge curves, and IC curves for batteries aging with (a1-a3) CC, (b1-b3) 100 Hz, and (c1-c3) 2000 Hz aging conditions. Source: [J5]……………….49
Figure 4-3 The electrochemical impedance (EIS) for the battery aged after 1000 cycles CC, 100 Hz, and 2000 Hz pulse charging current, from left to right. Source: [J5]…………………….50
Figure 4-4 The EIS analysis was conducted on the batteries after undergoing 1000 aging cycles. (a) illustrates the impedance mechanism along with the equivalent circuit diagram, (b) presents the fitted results of R_{sei} (electrolyte resistance) and R_{ct} (charge transfer resistance) at various state-of-charge (SOC) levels, specifically 10%, 30%, 50%, 70%, and 90%, (c) displays the DRT profiles for the CC-aged sample, while (d) shows the DRT profiles for the pulse-2000-aged sample. Source: [J5]……………………………………………………………...…………..52
Figure 4-5 (a) synchrotron Ex-XRD for fresh and aged graphite anode; (b) half-peak width for fresh and aged graphite; FE-SEM cross-section for (c) constane current aged graphite negative and (d) pulse current aged graphite negative. Source: [J5]…………………………….….53
Figure 4-6 In situ Raman spectrun of graphite in (a) constant current and (b) 250 Hz pulse current lithiation processes, and the structure of lithiated graphite under (c) constant current and (d) 250 Hz pulse current. Source: [J5]……………………………………………………..55
Figure 4-7 *Operando* dilatometry was employed to measure the increment of negative electrode thickness in constant current charging (a) and in pulse current charging (c); and the corresponded electrode potential were shown in (b) and (d), respectively. Source: [J5].……………………………………………………………………………...…………56
Figure 4-8 Post-mortem analysis of fresh and aged NMC cathodes. *Ex situ* synchrotron XRD results (a), and Ni K-edge *ex situ* XANES (b), *R* distance (c). Source: [J5]………………..…..57
Figure 4-9 Operando synchrotron X-ray Absorption Spectroscopy (XAS) were employed to reveal oxidation states and local atomic structure around Ni atoms during both constant current charging and pulse charging protocols. (a) the energy of Ni-edge evolves under the battery charging with constant current and pulse current; (b) Operdando test voltage profile and the corresponded half-peak energy ($E_{0.5}$) position; (c) the *R* distance under the constant current and pulse current charging; (d) Synchrotron XRD results of fresh, and aged cathode. Source: [J5]….…………………………………………………………………………………...59
Figure 4-10 the mechanisms for NMC cathode changed under pulsed current charging. Source: [J5].…………………………………………………………………………………..….60
Figure 4-11 Raman spectrums with 532 nm laser were performed for (a) CC and 2000 Hz aged negative electrodes surface, and (b) hanging off the top surface for the CC and 2000 Hz aged negative electrodes; FE-SEM images for the aged negative electrode by CC charging for (c1)

cross-section, and (c2) enlarged edge; FE-SEM images of pulse-2000 Hz aging graphite for (d1) cross-section, and (d2) enlarged edge. FE-SEM for enalrged graphite edge in constant currrent aging, and the EDS maping of O and C. Source: [J5]………………..…………..….61
Figure 4-12 The SEI quantified result for (a) fresh negative electrode, and for aged negative electrodes with (b) 1000 cycles of constant current aging, and (c) with 1000 cycles of 2000 Hz pulse current aging; (d) the etch-XPS spectrums for the battery electrodes with different etch time. Source: [J5]…………………………………………...………………….……….…..63
Figure 4-13 The mechanisms for SEI evolution under constant current charging and pulse current charging. Source: [J5]………………………………………………...…………....64
Figure 4-14 Pulse charging for commercial NMC/graphite batteries operates through several primary mechanisms to optimize their performance. Source: [J5].…………………………...65
Figure 5-1 the SOH for a battery aging at 25 °C and 100% DOD…………………………..…68
Figure 5-2 Battery aged by various depth of discharge (DOD), including 100% DOD, 75% DOD, and 45% DOD, at both of 35 °C (a) and 45 °C conditions (b).………………..….……69
Figure 5-3 The SOH curve of the battery under the aging conditions of 45% DOD at 35 °C and 45°C (a), and 75% DOD at 5 °C, 35 °C and 45 °C (b), respectively…………………….…….69
Figure 5-4 The charge-discharge curves from the battery reference performance test (RPT) after each 100EFCs in 35 °C aging condition (a-c); the incremental capacity analysis (ICA) is displayed in (d-f), and the differential voltage curve (DV) curves are illustrated in (g-i).….….71
Figure 5-5 The electrochemical impedance spectroscopy of battery in 35 °C aging condition with 100%, 75%, and 45% depth of discharge. The battery EIS results were tested at 90% SOC in the 25 °C oven…………………………………………………………………….……….....72
Figure 5-6 The charge-discharge curves from the battery reference performance test (RPT) after each 100EFCs in 45 °C aging condition (a-c); the incremental capacity analysis (ICA) is displayed in (d-f), and the differential voltage curve (DV) curves are illustrated in (g-i).….…73
Figure 5-7 The electrochemical impedance spectroscopy of battery in 45 °C aging condition with 100%, 75%, and 45% depth of discharge. The battery EIS results were tested at 90% SOC in the 25 °C oven.……………………………………………….………………….…..…......74
Figure 5-8 The charge-discharge curves from the battery reference performance test (RPT) after each 100EFCs in 75% DOD aging condition with 45 °C, 35 °C, and 5 °C (a-c); the incremental capacity analysis (ICA) is displayed in (d-f), and the differential voltage (DV) curves are illustrated in (g-i).……………………………………………………..……………..…..75
Figure 5-9 (a) coulombic efficiency comes from RPT test for battery with a 1 C current; the EIS of the battery is tested at 75% DOD aging condition with 45 °C, 35 °C, and 5 °C. The battery EIS results were tested at 90% SOC in the 25 °C oven.….…………………………...76
Figure 5-10 Synchrotron radiation ex-situ XRD was employed to analyze the structural characteristics of both the fresh positive electrode and those subjected to various aging conditions, specifically at 35 °C with 100% DOD, 35 °C with 45% DOD, 45 °C with 75% DOD, and 45 °C with 100% DOD……………………………………………….……………77
Figure 5-11 synchrotron radiation ex-situ XRD was employed to analyze the structural characteristics of both the fresh negative electrode and those subjected to various aging conditions, specifically at 35 °C with 100% DOD, 35 °C with 45% DOD, 45 °C with 75% DOD, and 45 °C with 100% DOD…………………………………………………….…...78
Figure 5-12 SEM image of negative electrode for battery aged at 5 °C and 75% DOD….……78

Figure 5-13 XPS results for positive electrode negative electrode after aging at various aging conditions, specifically at 35 °C with 100% DOD, 35 °C with 45% DOD, 45 °C with 75% DOD, and 45 °C with 100% DOD. A summary for positive electrode interface (a), and for negative electrode interface (b); the specific are shown in (c) and (d)……………..………....79
Figure 5-14 The batteries capacity fade during cycle aging under different conditions: (a) 45% DOD and 100% DOD at 35 °C, and (b) 75% DOD and 100% DOD at 45 °C. Source [J2]…….80
Figure 5-15 ICA and DV curves for battery aging at case 1 (a, e); case 2 (b, f); case 3 (c, g), and case 4 (d, h). Source: [J2] ……………………………………………………….………82
Figure 5-16 (a) The images show cross-sections and surface details, along with distribution maps obtained through EDS analysis; Images of a negative electrode that has undergone cycling in two different voltage ranges: 0.001 - 0.2 V (b-c) and 0.001 - 1.0 V (d-e). Source: [J2]…...…83

Part I

Report

Chapter 1. Introduction

1.1 Background

In past decades, the rapid growth of various industries has led to excessive greenhouse gas emissions, resulting in climate and environmental issues, such as global warming. As a response to these challenges, governments have felt compelled to set phased-out goals for using fossil fuels. For instance, the EU has committed to reducing greenhouse gas emissions by at least 55% below the 1990 levels by 2050 [1]. Battery energy storage has attracted much attention because it can solve the intermittent and unpredictable problems of clean energy, such as wind energy, tidal energy, and solar energy, which are being used to replace traditional fossil fuel energy. Batteries can supply stored energy during periods when there is no wind, tide, or sunlight available or when the renewable energy generation is lower than the demand. Furthermore, the adoption of electric vehicles (EVs) is anticipated to play a crucial role in addressing greenhouse gas emissions from transportation, which currently accounts for 22% of total emissions [2]. Some large-scale, long-term European research programs, such as BATTERY 2030+[3], [4] have been proposed with the vision of developing the sustainable batteries of the future..

Even though characterized by superior characteristics in comparison to all other battery technologies, the utilization of Lithium-ion (Li-ion) batteries in EVs is plagued by inevitable degradation issues, including capacity fade and increased internal resistance, which pose significant challenges for users and manufacturers alike [5]. Consequently, it is crucial to urgently develop a comprehensive understanding of battery aging in EVs. This understanding will enable us to (i) optimize battery materials, (ii) improve battery design, and (iii) provide valuable insights for the development of automotive battery systems.

Currently, researchers from various disciplines have approached the study of Li-ion battery aging from different perspectives. Certain scientists have focused on examining the effects of environmental and operational factors on battery degradation [6], whereas others have conducted post-mortem analyses of the internal components of battery cells to investigate the aging mechanism [7]. However, a comprehensive understanding of the direct relationship between battery operation, degradation in EV applications, and the corresponding aging mechanism is yet to be established.

At present, EVs can be classified into three main types based on their primary source of energy: Battery Electric Vehicles (BEV), Hybrid Electric Vehicles (HEV), and Plug-In Hybrid Electric Vehicles (PHEV). Figure 1-1 illustrates the energy flow within these three types of EVs [8]. Battery aging in EV applications is a complex and diverse process, influenced by various factors. While driving habits play a role, environmental conditions, such as temperature fluctuations in different seasons and regions also impact battery performance. Moreover, individual drivers experience differences in vehicle load, driving frequency, mileage, charging habits, and road conditions, leading to unique battery usage patterns. Consequently, standardizing battery operation in EV applications presents significant challenges, further complicating the study of aging mechanisms. However, factors such as driving habits, road conditions, and vehicle load predominantly impact battery aging while driving. Standardizing the protocol for electric vehicle charging can be achieved through a unified charging pile. Moreover, by considering the battery's working state, the battery usage can be divided into three distinct and separate processes: charging, driving, and standby. The primary focus of the battery management system design is often centered around the charging and discharging processes of the battery.

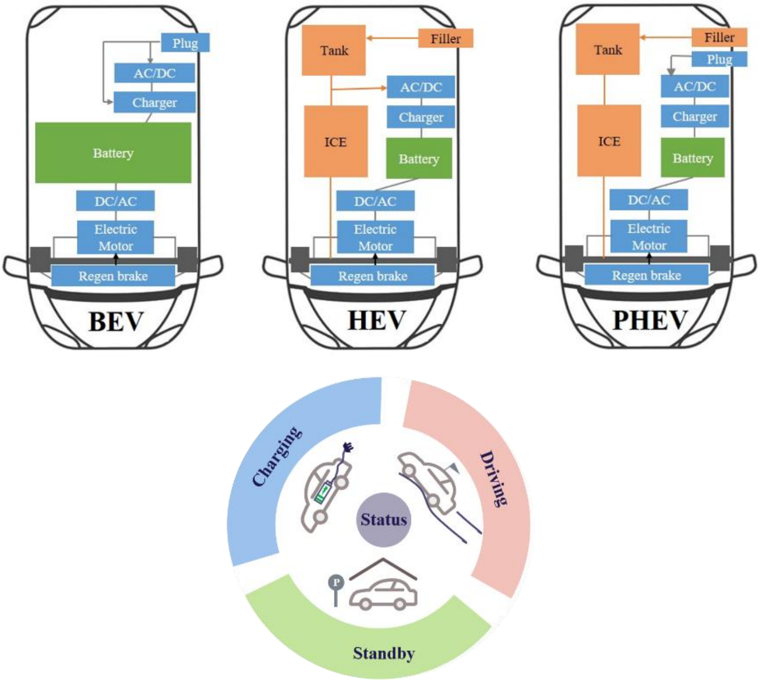

Figure 1-1 The arrangement from left to right consists of three types of EVs: Battery Electric Vehicles (BEV), Hybrid Electric Vehicles (HEV), and Plug-In Hybrid Electric Vehicles (PHEV), from left to right, and the battery operation modes in EV applications. Source [J1][8].

In order to meet the demanding requirements of EVs in terms of energy density and safety, Li-ion batteries have continuously improved and new chemistries have been proposed. Currently, Nickel Manganese Cobalt (NMC)-based Li-ion batteries have become the main choice for most EV manufacturers due to their superior performance (such as high gravimetric and volumetric energy density, low cost, and environmental friendliness [9]) in comparison to other chemistries. However, due to their structural instability during cycling, thermal instability and poor storage properties, especially for high-nickel ternary materials, NMC-based batteries are degrading fast, when used in EVs. Usually, the battery performance, such as available capacity, energy, and power, will usually degrade with the long-term battery operation. The aging performance has significant consequences on reliability and safety of a Li-ion battery system, as shown in Figure . 1[10]. Generally, the estimation of the battery health influenced by the history is also called as state of health (SOH) estimation. Based on the SOH result, the battery could be used properly without abuse and safety accidents[11]. The influence of the electrical, mechanical and/or thermal factors on the SOH needs to be analyzed based on the aging mechanism and degradation models. Then to guarantee the battery system's life, the design of the battery system could be optimized. An in-depth understanding of aging mechanisms is helpful to improve the lifespan of Li-ion batteries and subsequently increase the economic viability of these energy storage devices.

In analyzing battery mechanisms, a comprehensive understanding of battery aging often requires integrating electrochemical analysis and material detection techniques. It is crucial to identify reliable indicators that effectively capture battery aging, which can include monitoring changes in electrochemical performance and material structure throughout the aging process. The battery aging mechanisms are closely intertwined with the specific application scenario, with constant current charging and discharging conditions being the most prevalent. Besides, there is an urgent need to investigate mechanisms that optimize charging protocols to extend battery lifespan and gain insights into battery aging within real-world driving scenarios.

1.1.1 Diagnostic Methods

The battery diagnostic method includes electrochemical methods and physical methods. Typically, electrochemical methods such as battery charging-discharging curves, incremental capacity - differential voltage (IC-DV) curves, and electrochemical impedance spectroscopy (EIS) impedance spectrum, all can be used to diagnose the battery degradation level. The peak intensity in the IC-DV curves is connected to the amount of electrode materials, and the shift of peaks is related to the battery polarization. Besides, the increased impedance is shown in the evolution of the impedance spectrum obtained from EIS measurements. Those changes will be chose as diagnostic indictors. However, when using those method to diagnose the battery degradation, the indictors are challenging to select. Because different battery chemistries will have different evolution of the indictors during aging. Therefore, it is necessary to select the most meaningful indictors for selected batteries for electrochemical diagnostic.

Furthermore, the electrochemical methods are always dependent on the a priori knowledge of the user, and their accuracy is limited for aging mechanism studies, especially for the case of complex battery aging conditions. Post-mortem analysis and materials test are necessary to confirm and enrich the aging mechanisms identification.

1.1.2 Constant Current Cycling

In practical scenarios, the CV mode is often excluded because it consumes a significant amount of time due to the gradual reduction of the charging current, despite resulting in a relatively decreased charged capacity [12]. The typical constant current - constant voltage (CC-CV) [13] and constant current (CC) [14] charging profile are shown in Figure 1-2. After omitting the CV stage, the battery's aging mode will deviate from that observed in the CC-CV scenario. Throughout the aging process, it becomes essential to provide more information concerning the battery's heightened temperature, increased impedance, reduced capacity, fluctuations in voltage plateau, and the evolution of battery internal degradation.

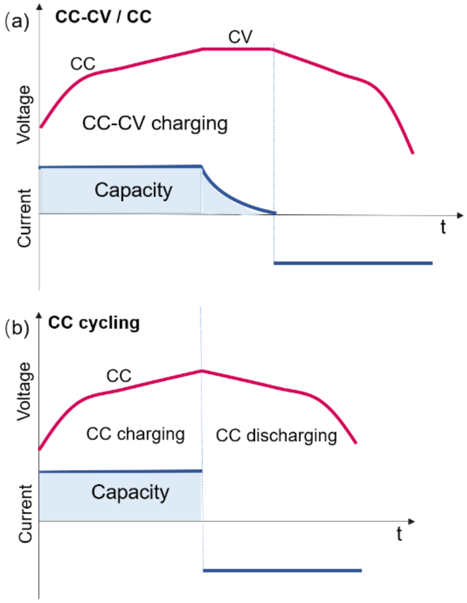

Figure 1-2 Voltage and current curves for the battery in constant current - constant voltage (CC – CV) (top) and constant current (CC) (bottom) charging mode.

1.1.3 Pulse Current Charging

Pulsed current charging has been proven to be one of the most promising battery charging protocols as shown in Figure 1-3, due to it is potential of extending the battery lifetime. As illustrated by Huang et al.[15], especially for the pulsed current with a high frequency (e.g., 2000 Hz and 100 Hz) the battery lifetime can be doubled. However, the aging mechanisms behind this behavior are unclear at present.

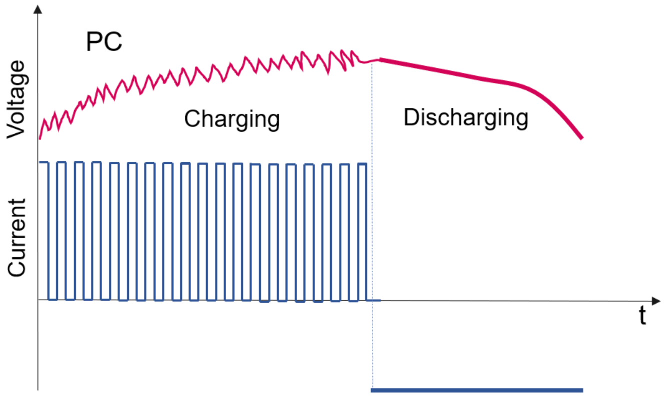

Figure 1-3 Voltage and current curves for a battery in pulsed current charging mode.

1.1.4 Real Life Driving

Unlike most of batteries aging in laboratory, which is performed with constant current, in real-life the batteries are discharged with an unregular current, which is influenced by vehicles, road conditions, climate and driving habits. To clarify the battery aging mechanisms during real life driving, batteries need to be discharged by some simulated dynamic working conditions, such as Urban Dynamometer Driving Schedule (UDDS) [16], New European Driving Cycle (NEDC) [17], and Worldwide Harmonized Light Vehicles Test Cycle (WLTC) driving cycles [18], as shown in Figure 1-4 [J1].

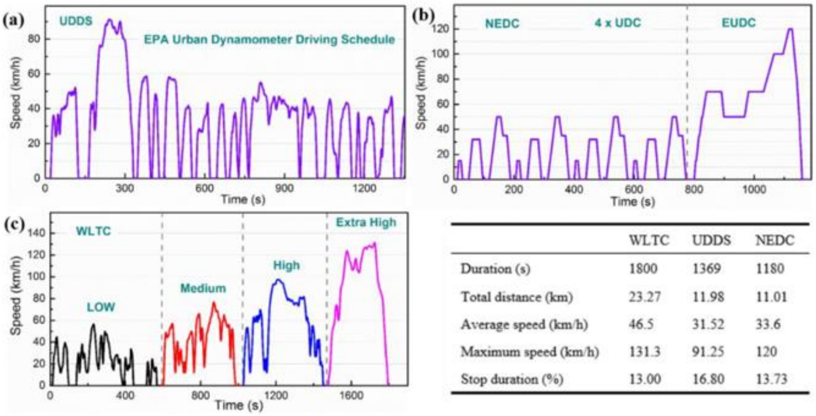

	WLTC	UDDS	NEDC
Duration (s)	1800	1369	1180
Total distance (km)	23.27	11.98	11.01
Average speed (km/h)	46.5	31.52	33.6
Maximum speed (km/h)	131.3	91.25	120
Stop duration (%)	13.00	16.80	13.73

Figure 1-4 Driving profile of (a) UDDS, (b) NEDC, (c) WLTC. Source [J1][8].

1.2 State-of-art

Li-ions batteries are rapidly advancing and show promise. Innovations in battery technology are crucial. Understanding battery degradation and mechanisms is vital for improving battery performance and lifespan through optimized operational profile, battery cells design and materials synthesis. Therefore, it’s crucial to choose precise electrochemical and material testing methods for diagnosing the battery’s degradation. This is particularly significant for analyzing commonly used CC charging and the potentially valuable mechanism of PC charging. Additionally, investigating the mechanisms of battery in driving process should closely resemble actual automotive operating conditions.

Electrochemical analysis and material testing technologies for diagnosing battery degradation have reached a relatively mature stage. During the analysis of the full battery aging, the most commonly used techniques include IC-DV curve and EIS [19]. When the IC-DV curve is used to diagnose battery degradation, the characteristic representing battery degradation typically deviates based on materials chemistries, battery cell parameters, and the magnitude of applied current [20]. It is necessary to identify the curve features that can represent specific battery aging before use. Furthermore, post-analysis and material testing have become increasingly diverse. In addition to common analyses such as X-ray Powder Diffraction (XRD), Scanning electron microscope (SEM), Raman, and X-ray photoelectron spectroscopy (XPS), *operando* testing and high-energy synchrotron radiation are also being gradually employed for the study of commercial battery mechanisms[21]. This, to some extent, supplements the qualitative/semi-quantitative of electrochemical research methods.

There are numerous studies on battery testing under constant current cycling; however, there are very few papers that delve into the underlying mechanisms in depth. Zhu et al. [22] conducted a comparison of battery aging under constant current (CC) and constant current-constant voltage (CC-CV) charging modes. They discovered that the battery’s lifespan is significantly extended under CC charging conditions, attributing this effect to lesser lithium loss and reduced degradation of active materials. However, the relative quantities of lithium loss and active electrode material degradation remain unclear. The process of aging and its underlying causes are even harder to discuss.

Pulse charging is considered a promising method for electric vehicle charging, as it can significantly prolong the battery lifespan of commercial batteries[22]–[25]. In addition, pulse current charging can effectively extend the lifespan of lithium metal batteries[26], [27]. Its mechanism is explained by the fact that pulse current effectively balances the issue of uneven distribution of Li-ionss[28]. The molecular dynamics mechanism behind how pulse current charging improves stability in commercial batteries is still unclear, and the effect of pulse current on electrode materials is not yet well understood.

In real-life application scenarios, battery aging will be even more complex. Stroe et al.[29], discharge the battery with a WLTP driving profile to simulate the driving conditions of the battery in real-life applications. However, the aging mechanisms of commercial battery in real-life applications is still unclear, especially in the influence of temperature and depth of discharge.

1.3 Research Motivation

A clear understanding of the battery’s aging mechanisms during actual operation, including both the aging processes during charging and during driving, is especially important for extending the battery lifespan. The application of electrochemical methods requires a precise understanding of the physical significance of the electrochemical curves (e.g., IC-DV and EIS), necessitating the identification of the most significant aging characteristics. Besides, the battery aging mechanisms in constant current charging and pulse current charging remains unclear, which hinders the development of battery charging techniques. Furthermore, battery aging under real-world driving conditions is a complex process, and there are limited available references. The impact of temperature and discharge depth remains largely unknown, highlighting the need for in-depth research.

1.3.1 Research Objective

The objective of this Ph.D. thesis is to select accurate electrochemical analysis methods and material testing techniques to analyze battery aging mechanisms towards real life battery operation driving. Firstly, it is necessary to uncover the intrinsic mechanisms of battery aging under CC charging conditions, including the aging pathways of the full battery and the physical degradation of electrodes and materials. Additionally, revealing the mechanisms by which pulsed current charging methods mitigate this degradation is necessary. Furthermore, the aging mechanisms of batteries in realistic EV operation and the influence of temperature and depth of discharge need to clarify. Thus, the technical objectives of this thesis can be summarized as follows:

O1: Finding effective methods for diagnosing the battery degradation.

O2: Unraveling the Li-ion battery aging mechanism during constant current cycling.

O3: Unraveling the Li-ion battery aging mechanisms during aging with pulsed current charging.

O4: Assessing the influence of the environmental and operating conditions on the degradation behavior of Li-ion battery.

O5: Understanding the Li-ion batteries aging mechanisms during real-life battery operation in EVs.

1.3.2 Project Limitations

Despite extensive efforts invested in mechanistic analysis, certain limitations persist in this Ph.D. thesis. These limitations can be summarized as follows:

L1: In this work, the most used NMC532/Graphite battery on the market was selected to reveal its aging mechanism under different working conditions. Due to the different electrode systems, these mechanisms may not be applicable in other high-nickel batteries.

L2: The mechanisms corresponding to the pulsed current charging to improve battery life were revealed, but the specific optimal charging frequency was not identified. Thus, its industrial potential needs to be further explored.

L3: To simplify the research objectives, the temperature used for aging the batteries is constant for each test case, which is inconsistent with the actual situation of battery operation in EVs. Therefore, the generated data might not be directly used for battery SOH estimation in practical use.

1.4 Thesis Outline

This Ph.D. thesis presents the findings and outcomes achieved during the Ph.D. period. It is structured into two primary sections: a research report and a collection of publications. The research report comprises six chapters, with the content aligning with the journal and conference outputs as illustrated in Figure 1-5.

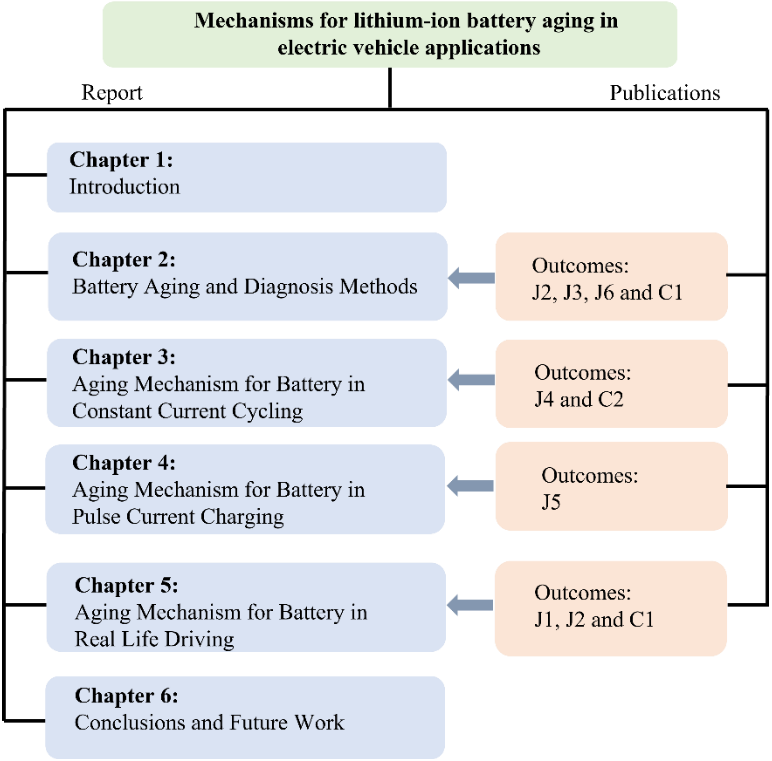

Figure 1-5 Thesis structure with related outcomes.

Chapter 1 – Introduction

An overview of Li-ion batteries employed in electric vehicles is introduced in this chapter. It describes the existing challenges and issues within this field, highlights the research objectives, and acknowledges the limitations of this research. Additionally, this chapter outlines the framework and lists the publications associated with this Ph.D. thesis.

Chapter 2 – Battery aging and diagnosis methods

This chapter provides the battery parameters utilized, the battery aging conditions, and the test platform employed. Additionally, various electrochemical methods are analyzed for battery health diagnosis, along with post-mortem analysis methods. Material testing methods, particularly battery impedance testing methods, are also described.

Chapter 3 – Aging mechanisms of battery during constant current cycling

In this chapter, the aging mechanism of batteries under constant current cycling was revealed. The electrochemical analysis and post-mortem study demonstrate that the capacity fading of commercial Li-ions batteries during constant current cycling conditions can be primarily attributed to the increase in interfacial film resistance and the loss of active materials.

Chapter 4 – Aging mechanism of battery during aging with pulsed current charging

In this chapter, the mechanism through which pulse charging enhances the lifespan of commercial batteries is explained. Pulse charging is essential for enhancing the mechanical stability of graphite during the Li-ions intercalation process, facilitating the kinetic process of Li-ions diffusion, and minimizing graphite cracking. Furthermore, pulse charging effectively suppresses the occurrence of interfacial side reactions.

Chapter 5 – Aging mechanism of battery during real life EV operation/driving

In this chapter, dynamic condition is employed to discharge the battery, aiming to unveil the aging mechanism of the battery in real-life driving scenarios. the effects of depth of discharge and temperature on the battery's health were explored and the underlying mechanisms behind these impacts were thoroughly analyzed.

Chapter 6 – Conclusions and future work

In this chapter, the main findings and conclusions of the thesis are summarized, and an outlook for future work is given based on the current research results.

1.5 List of Publications

Journal Papers

J1. **J. Guo**, Y. Li, K. Pedersen, and D. I. Stroe, "Li-ion battery operation, degradation, and aging mechanism in electric vehicles: An overview," *Energies*, vol. 14, no. 17. pp. 1–22, 2021

J2 **J. Guo**, Y. Li, J. Meng, K. Pedersen, L. Gurevich, and D. I. Stroe, "Understanding the mechanism of capacity increase during early cycling of commercial NMC/graphite Li-ions batteries," *Journal of Energy Chemistry*, vol. 74, pp. 34–44, 2022

J3 **J. Guo**, Y. Che, K. Pedersen, and D. Stroe, "Battery impedance spectrum prediction from partial charging voltage curve by machine learning," *Journal of Energy Chemistry*, vol. 79, pp. 211–221, 2023

J4 **J. Guo**, S. Jin, X. Huang, Y. Xu, Y. Li, P. Kristensen, D. Wang, K. Pedersen, L. Gurevich, and D. I. Stroe, "Unravelling and quantifying the aging processes of commercial $Li(Ni_{0.5}Co_{0.2}Mn_{0.3})O_2$/graphite Li-ions batteries under constant current cycling," *Journal of Materials Chemistry A*, vol. 11, pp. 41–52, 2023

J5 **J. Guo**, Y. Xu, P. Adelhlem, M. Exner, X. Huang, P. Kristensen, D. Wang, K. Pedersen, L. Gurevich, and D. I. Stroe, "Unravelling the mechanism of pulse current charging for enhancing the stability of commercial Li-ion battery". Submitted to *Energy & environment Science*

J6 **J. Guo**, Y. Xu, P. Li, K. Pedersen, and D. I. Stroe, "Can electrochemical impedance spectrum be replaced by constant current techniques for battery test?" Submitted to *Chemelectrochem*

Conference papers

C1 **J. Guo**, Y. Che, S. Jin, K. Pedersen, D. I. Stroe, "Machine learning to predict electrochemical impedance spectra (EIS): Can EIS be replaced by constant current techniques?" EIS 2023 12th International Symposium on EIS (EIS 2023), Beijing, China, 2023

C2 **J. Guo**, Y. Li, K. Pedersen, L. Gurevich, and D.-I. Stroe, "Unravelling the aging process of commercial $Li(Ni_{0.5}Co_{0.2}Mn_{0.3})O_2$/graphite Li-ions batteries under constant current cycling" International Society of Electrochemistry (ISE), Lyon, France, 2023

Other Publications which are not included in the thesis:

C3 **J. Guo**, Y. Li, K. Pedersen, L. Gurevich, and D.-I. Stroe, "Quantification of the lithium loss for commercial Li-ion batteries" ECS Meeting Abstracts, Gothenburg, Sweden, 2023

C4 **J. Guo**, Y. Li, K. Pedersen, L. Gurevich, and D.-I. Stroe, "The Influence and Degradation Mechanism of the Depth of Discharge on the Performance of NMC-Based Cathodes for Li-Ion Batteries," ECS Meeting Abstracts, vol. MA2022-01, no. 2, p. 252, Jul. 2022

J7. Y. Li, **J. Guo**, K. Pedersen, L. Gurevich, and D.-I. Stroe. Investigation of multi-step fast charging protocol and aging mechanism for commercial NMC/graphite Li-ions batteries. *Journal of Energy Chemistry*, 2023, 80: 237-246.

J8. Y. Che, X. Hu, X. Lin, **J. Guo**, R. Teodorescu. Health prognostics for Li-ions batteries: mechanisms, methods, and prospects. *Energy & Environmental Science*, 2023.

J9. Y. Li, **J. Guo**, K. Pedersen, L. Gurevich, and D.-I. Stroe. Recent Health Diagnosis Methods for Li-ions Batteries. Batteries, 2022, 8(7): 72.

J10 P. Li, X. Xia, **Guo J**. A review of the life cycle carbon footprint of electric vehicle batteries. *Separation and Purification Technology*, 2022, 296: 121389.

J11 **J. Guo**, W. Li. Synthesis of Single-Crystal $LiNi_{0.7}Co_{0.15}Mn_{0.15}O_2$ Materials for Li-Ion Batteries by a Sol–Gel Method. *ACS Applied Energy Materials*, 2021, 5(1): 397-406.

Chapter 2. Battery Aging and Diagnosis Methods

In this chapter, a detailed listing of selected battery parameters, aging conditions, and degradation diagnostics methods is provided. Furthermore, the understanding of various electrochemical diagnostic methods is summarized. The related scientific outcome is listed as follows:

J2 **J. Guo**, Y. Li, J. Meng, K. Pedersen, L. Gurevich, and D. I. Stroe, “Understanding the mechanism of capacity increase during early cycling of commercial NMC/graphite lithium-ion batteries,” *Journal of Energy Chemistry*, vol. 74, pp. 34–44, 2022

J3 **J. Guo**, Y. Che, K. Pedersen, and D. Stroe, “Battery impedance spectrum prediction from partial charging voltage curve by machine learning,” *Journal of Energy Chemistry*, vol. 79, pp. 211–221, 2023

J6 **J. Guo**, Y. Xu, P. Li, K. Pedersen, and D. I. Stroe, “Can electrochemical impedance spectrum be replaced by constant current techniques for battery test?” Submitted to *Chemelectrochem*

C1 **J. Guo**, Y. Che, S. Jin, K. Pedersen, D. I. Stroe, “Machine learning to predict electrochemical impedance spectra (EIS): Can EIS be replaced by constant current techniques?” EIS 2023 12th International Symposium on EIS (EIS 2023), Beijing, China, 2023

2.1 Introduction

During the operation of commercial Li-ions batteries, it is inevitable that they will undergo capacity degradation, voltage platform reduction, and resistance/impedance increase, which will lead to a decrease in the EV mileage or range. To comprehend the aging mechanism of Li-ions batteries, it becomes crucial to conduct accelerated aging studies specifically on the widely employed NMC532/graphite batteries found in the market[30]. These studies aim to analyze the aging process and elucidate the underlying mechanisms involved in these batteries.

To ensure relevance to the practical application of electric vehicles, researchers advocate for adopting the Worldwide Harmonized Light Vehicles Test Procedure (WLTP) working condition when studying battery discharging [31]. In terms of charging, constant current charging and constant current constant voltage charging are the prevailing methods commonly employed in recent research [32]. The aging process of batteries primarily revolves around the charging and WLTP discharging processes, as these conditions closely resemble real-world scenarios encountered in electric vehicle usage. By focusing on these aspects, researchers can gain valuable insights into the battery's aging behavior and performance in practical applications.

Battery state of health (SOH) analysis requires parameters like capacity, voltage, impedance, and information from charge and discharge curves. DC impedance measurements and electrochemical impedance spectroscopy (EIS) are important techniques for battery health diagnosis. During battery usage, the charging curve, specifically the increment capacity (IC) or differential voltage (DV) curve[20], is commonly used for degradation analysis, enabling the examination of the electrochemical process and voltage relationship. EIS is a non-invasive technique that examines changes in individual electrochemical processes over time. It helps diagnose battery health comprehensively. Material testing methods can be combined with electrochemical analysis to understand internal mechanisms better and enhance accuracy.

This section will introduce the batteries used for the analysis and the considered aging protocols. To assess the battery degradation, electrochemical methods such as IC-DV curve analysis and EIS testing was employed. These techniques allowed to analyze the changes in capacity and voltage relationships, as well as the electrochemical processes occurring within the battery. In addition to electrochemical methods, materials tests were also conducted to further examine the electrodes and materials degradation. By integrating these material testing techniques with electrochemical analysis, a comprehensive understanding of the battery aging and the underlying mechanisms involved was obtained.

2.2 Battery and Battery Test

2.2.1 Full Cell Parameters

This thesis investigates the aging of NMC 532/Graphite batteries, which are widely used in various daily-life applications, most notably EVs. Two batches of batteries were acquired from different companies for conducting aging tests and detailed analysis. Batch A was obtained from Shandong Golden cell Electronics Technology Co., Ltd., while Batch B was sourced from HAIDI company. The specific parameters of these battery batches are provided below Table 2-1:

These parameters were obtained by consulting the manufacturers and further validated through disassembling fresh battery cells for electrochemical and materials testing. The capacity of the electrodes was measured by assembling coin cells, and the physical parameters of the materials were obtained through microscopic measurements.

Table 2-1 Battery model and specific parameters for batch A and batch B

Item	**Batch A**	**Batch B**
Models	HTCNR 18650-2200mAh-	HDCNR 18650-2200-
Normal capacity	2200 mAh@0.5C	2200 mAh@0.5C
Standard Voltage	3.6 V	3.7 V
Cut-off voltage	4.2 ± 0.05 V	4.2 ± 0.05 V
Max. continuous Discharge current	6600 mA	6600 mA
Max. charge current	2200 mA	6600 mA
Electrodes materials	NMC532/Graphite	NMC532/Graphite
Electrolyte	-	$LiPF_6$ 12-20% (wt.) in
Positive electrode areal density (two sides)	29 mg/cm^2	29 mg/cm^2
Negative electrode areal density (two sides)	19.6 mg/cm^2	19.6 mg/cm^2
N/P	-	~1.1
Thickness of Al current collector	15 ± 2 μm	15 ± 2 μm
Thickness of Cu current collector	9 ± 2 μm	9 ± 2 μm

2.2.2 Battery Cell Test Station

The battery cells' aging, and reference performance tests were conducted using a Digatron test station (Digatron industrie-Elektronik GmbH, 52068 Aachen, Germany), as illustrated in Figure 2-1. The Electrochemical Impedance Spectroscopy (EIS) tester used in the experiments worked in a frequency range from 10 mHz to 6.5 kHz. During testing, the batteries were placed in ovens and climatic chambers to guarantee a reliable and uniform temperature.

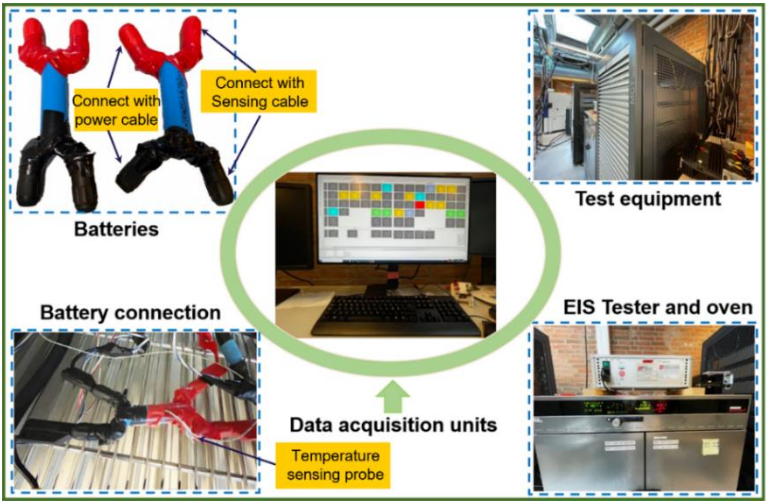

Figure 2-1 Equipment and platform for full cell aging.

2.2.3 Battery Test Protocols

In this study, the primary focus was to study the aging and mechanism for batteries under typical constant current cycling conditions. The effectiveness of pulse current charging in extending battery life was explored, and tests were conducted to evaluate battery degradation during discharging using realistic electric vehicle (EV) profiles. The study was divided into three categories, namely:

Constant Current Cycling: This involved subjecting the batteries (Batch A) to continuous cycling under constant current conditions. By repetitively charging and discharging the batteries at a constant current, the aim is to simulate common battery testing scenarios and observe the effects of aging over time. The battery batch A was employed to study the degradation mechanisms. The battery aging process was conducted in a climatic chamber maintained at a temperature of 35 °C. During the aging process, the battery underwent charging at a current of 2.2 A (equivalent to a 1 C-rate) from 2.5 V to 4.2 V, followed by discharging at a rate of 4.4 A (equivalent to a 2 C-rate) until reaching 2.5 V. Between the charge and discharge cycles, neither a constant voltage stage nor a rest period was included (Figure 2-2).

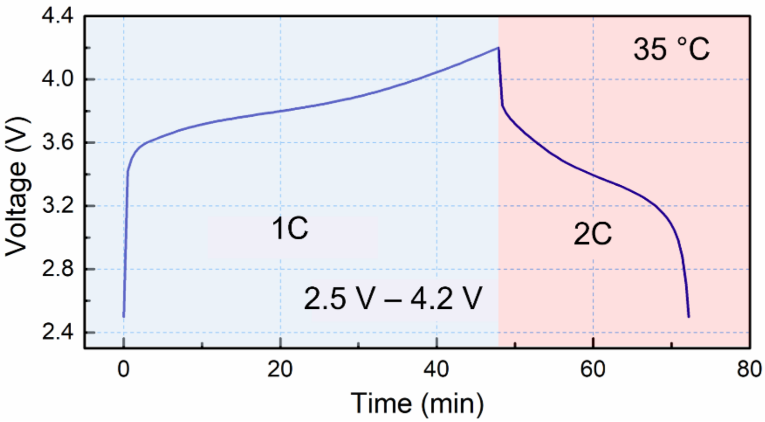

Figure 2-2 Constant current cycling protocols for the battery aging with battery batch A.

Pulsed current charging: In addition to constant current cycling, the influence of pulsed charging on battery aging was studied. Pulse charging involved delivering short bursts of high-current pulses during the charging process. The objective was to analyze how pulse charging influenced battery performance and degradation, with the aim of identifying strategies to enhance battery lifespan.

Pulse charging is implemented based on the constant current cycling condition by introducing equal interval relaxation periods to the charging process. The battery batch A is employed. During pulse charging, the charging current is intermittently paused at regular intervals, while maintaining the average charging current unchanged. This charging strategy is depicted in Figure 2-3. The discharge process, which involves discharging the battery at a rate of 2 C, remains constant throughout the pulse charging experiments. However, the frequency of the charging current pulses is varied, ranging from 100Hz to 2000Hz. This adjustment in the pulse frequency allows for the investigation of different charging strategies and their mechanisms for battery performance improving. The duty cycle of pulse charging is 50% for all cases.

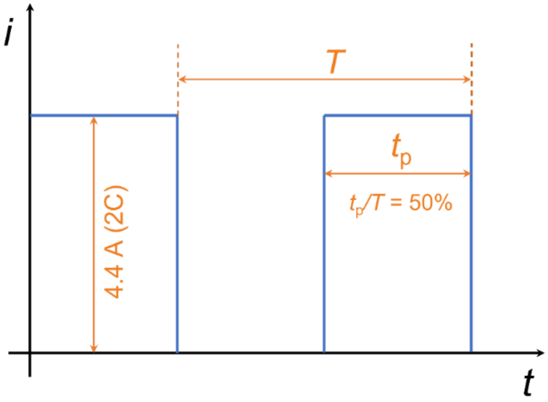

Figure 2-3 Pulse current charging protocols for the battery aging with battery batch A[33].

Battery Driving Simulation: WLTP discharge profile that emulated battery discharge during driving scenarios was performed at various temperature (5 °C, 25 °C, 35 °C, and 45 °C) and discharge of depths (45%, 75%, and 100%). By monitoring battery performance under simulated driving conditions, the aim is to optimize battery charging protocols to meet the demands of practical applications.

To better replicate the battery's aging process during real-world driving, the Worldwide Harmonized Light Vehicles Test Procedure (WLTP) condition is transformed into a current curve using (2-1) [29], enabling the battery to discharge accordingly. WLTC was developed with the aim of establishing a universally accepted standard for evaluating pollutant levels, energy consumption, and electric range in light-duty vehicles. This comprehensive standard was established based on extensive data collected from diverse regions, including the EU, USA, India, Korea, and Japan, encompassing approximately 765,000 kilometers of driving data. The dataset comprises various road types such as urban, rural, and motorway, as well as different driving conditions such as peak, off-peak, and weekend scenarios. It covers a wide range of vehicle categories, engines, and manufacturers, mirroring the real-world driving experience. The driving data specifically includes four categories of speed: low (L/60 km/h), medium (M/80 km/h), high (H/110 km/h), and extra-high (Ex-H/>110 km/h), which correspond to urban, rural, and motorway classifications (Figure 2-4) [34] [J1].

$$I = \frac{\frac{1}{2} \cdot \rho \cdot S \cdot C_x \cdot v^3 + C_r \cdot m_t \cdot g \cdot v + m_t \cdot a \cdot v}{\eta \cdot V} \tag{2-1}$$

Where, ρ is the air density, S is the vehicle frontal area, C_x is the drag coefficient, v is the speed of the vehicle, C_r is the rolling coefficient, m_t represents the mass of the vehicle, g is the gravity constant, η represents the overall efficiency of the vehicle[J1][8].

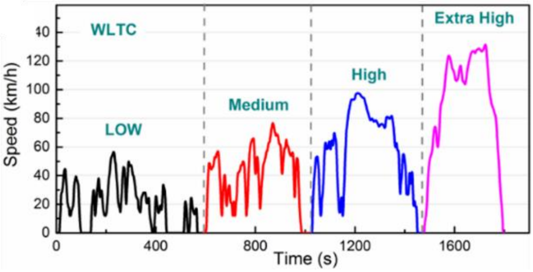

Figure 2-4 The WLTP driving cycle profile for a class 3 vehicle. Source: [J1][8].

Based on Eq. 2-1, the speed-time profile undergoes a conversion process, resulting in the generation of a corresponding current profile, which can be used to discharge the battery. The number of WLTP cycles is adjusted to accommodate variations in the depth of discharge (DOD), thereby ensuring that the cycles reflect aging patterns across different DOD levels, as shown in Figure 2-5. Besides, the batteries from batch B were aged at different temperatures, and the details are shown in Table 2-1.

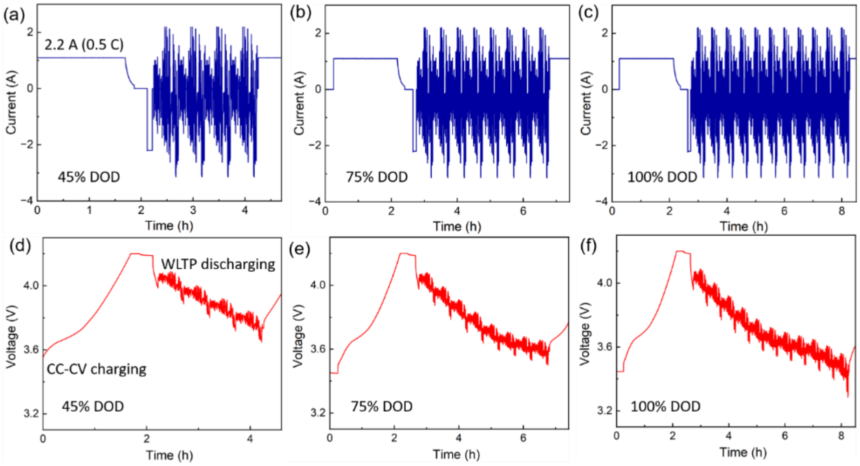

Figure 2-5 Battery batch A undergoes discharge according to the WLTP profile and cycling at various depths of discharge.

Table 2-1 The battery aging at different temperature with WLTP discharge profiles.

Items	45% DOD	75% DOD	100% DOD
45 °C	2 cells	2 cells	2 cells
35 °C	2 cells	2 cells	2 cells
25 °C			1 cell
5 °C		1 cell	

By the exploration of these different aging conditions, comprehensive insights into battery aging mechanisms were aimed to be gained, and strategies for improving battery performance and lifetime were sought to be identified.

2.3 Electrochemical Diagnosis Method

2.3.1 Incremental Capacity and Differential Voltage (IC-DV)

An IC curve is created by using Eq. (2-2) to distinguish the battery capacity with respect to the voltage change, where Q_t and V_t refer to the capacity and voltage at time t [35], [36]. The resulting IC diagram demonstrates the capacity contribution from various voltage plateaus of batteries and can be classified by peak height, position, and area. The process in which IC-DV evolves from the charging curve during a typical charging process is shown as Figure 2-6, including Graphite/Li, NMC/Li and NMC/Graphite batteries. More details can be found from [J3].

$$IC = \frac{dQ}{dV} = \frac{\Delta Q}{\Delta V} = \frac{Q_{t+1} - Q_t}{V_{t+1} - V_t} \tag{2-2}$$

Using Eq. (2-3), a DV curve is defined as the voltage derivative in relation to the discharge or charge capacity, reflecting an increase in voltage with the capacity decrease [37]:

$$DV = \frac{dV}{dQ} = \frac{\Delta V}{\Delta Q} = \frac{V_{t+1} - V_t}{Q_{t+1} - Q_t} \tag{2-3}$$

However, depending on the type of electrode materials and electrode configurations in a full cell, the correlation between the indicators (such as changes and shifts in peaks) in IC and DV curves and the degradation behavior differs. Understanding the connection between the IC-DV indications and the related performance of the battery's electrodes is essential. Deriving electrochemical curves is frequently used to look at degradation indicators. However, obtaining comprehensive information of nearly one hundred factors for battery is a challenging work [39]. Even a minor parameter error can lead to an inaccurate result, even misinterpretation the degradation indicators. In this study, the disparities in IC and DV curves were compared by using coin cell batteries. Following that, the deterioration indicators will be carefully examined at the levels of the electrode.

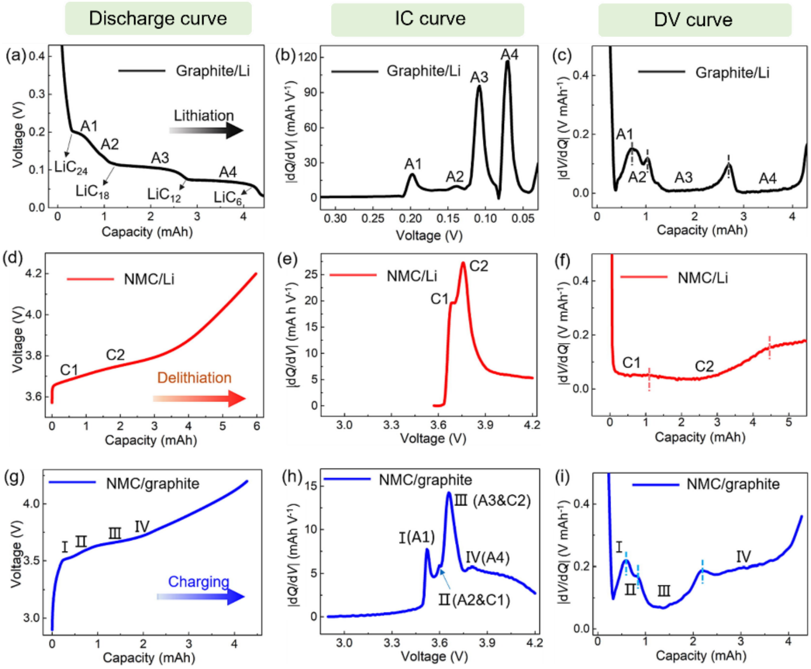

Figure 2-6 Typically IC-DV curves for Graphite/Li, NMC/Li, and NMC/Graphite batteries. Source: [J3][38].

The charging-discharging (*Q*-*V*) curves for coin cells made of NMC/Li, NMC/Graphite, and Graphite/Li are plotted in Figure 2-7 (a). Similar shapes can be seen in the NMC/Li and NMC/Graphite curves, which both show a clear high voltage plateau of the NMC positive electrode. However, there are notable differences between the two curves, primarily attributed to the voltage of the graphite electrode, which transitions between pure graphite and LiC_6. This variation accounts for the discrepancy in voltage plateau magnitude between NMC/Li and NMC/Graphite, as well as the rapid voltage increase during the early stages of the charging curve for NMC/Graphite. Figure 2-7 (b) depicts the corresponding discharge-voltage (DV) curves based on the *Q*-*V* curves in Figure 2-7 (a). The transitions between the neighboring voltage plateaus seen in Figure 2-7 (a) correlate to the peaks seen in the DV curves. Since the length of time of the voltage plateaus is related to the amount of active material in the electrodes, a change in the positions of these peaks denotes a change in that quantity. A decrease in the amount of Li-intercalated active material in the specific electrode is shown by a leftward shift of the DV peaks. On the contrary, a move to the right of the DV peaks denotes an increase in the amount of Li-intercalated active substance. Three distinct peaks identified as “a”, “b”, and “c” can be seen in the DV curves for the NMC/Graphite cell, and these peaks match those in the DV curve for the Graphite/Li cell. On the contrary, the DV curve for NMC/Li does not exhibit any prominent peaks, indicating a smooth variation in the positive electrode potential during charging. Therefore, the peaks labeled as a, b, and c in Figure 2-7 (b) are solely attributed to the graphite anode transitioning from a state of pure carbon C to LiC_6. Additionally, the capacity of the battery during the constant current period when charging at a low current is typically related to the remaining lithium stock [20], [40]. As a result, LLI is often quantified using the endpoint of the DV curve (max$(Q)_1$)), as shown in Eq. (2-4) [J2].

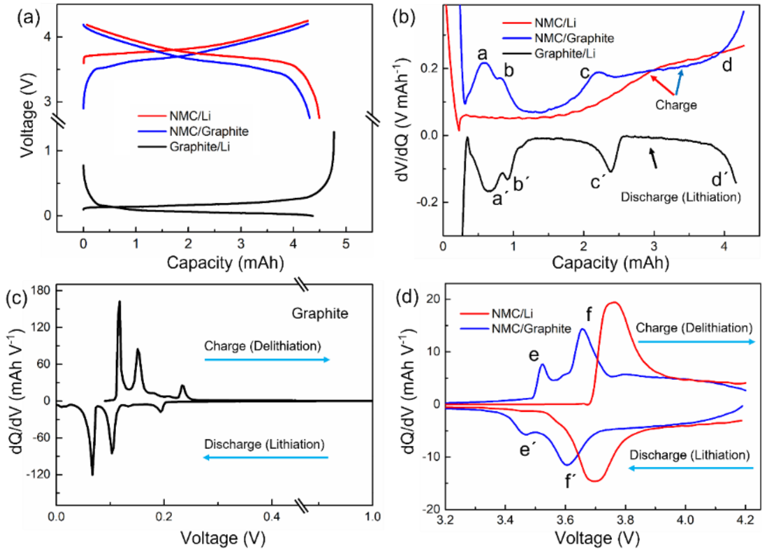

Figure 2-7 Electrochemical curves from coin cell test. Different electrode material combinations, including NMC/Li, NMC/Graphite, and Graphite/Li were used in the tests. (a) The charging and discharging curves for all three different kinds of coin cells; (b) the DV curves that represent the charging process in a full cell; (c) IC curves of the graphite; and (d) the IC curves of the NMC/Li and NMC/Graphite electrodes. Source: [J2][41].

Peaks in the IC curves indicating the phase transitions that take place during electrochemical reactions; these transitions are accompanied by plateaus in the voltage profiles and valleys in the DV curves.

Instead of depending exclusively on capacity degradation curves to determine the state of the battery, IC curves offer a more meaningful reference for measuring battery degradation as a function of voltage than DV curves do [42]. Three sets of oxidation/reduction peaks are present in the graphite, as shown in Figure 2-7 (c), which accounts for the difference in the IC curves for NMC/Li and NMC/Graphite, as shown in Figure 2-7 (d). Specifically, in the NMC/Li cell, the IC curve demonstrates a single pair of primary oxidation/reduction peaks, aligning well with the lone DV valley observed in Figure 2-7 (b). The graphite anode is responsible for an additional pair of peaks in the NMC/Graphite cell that are designated as e and e'. As a result, the strength of the e peak represents the graphite anode's capability within a given voltage plateau, providing information about the amount of available graphite. To estimate the degradation mode of LAM batteries based on Eq. (2–5), Dubarry et al. [20], [40], [42] used simulation techniques. In this equation, the subscript “1” denotes the battery in its initial state, while “i” represents the cycle number corresponding to its aging process.

$$\mathrm{LLI}_i = \frac{\max(Q)_1 - \max(Q)_i}{\max(Q)_1} \cdot 100 \tag{2-4}$$

$$\mathrm{LAM}_i = \frac{\max\left(\frac{\Delta Q}{\Delta V}\right)_1 - \max\left(\frac{\Delta Q}{\Delta V}\right)_i}{\max\left(\frac{\Delta Q}{\Delta V}\right)_1} \cdot 100 \tag{2-5}$$

Based on Eqs. (2) and (3), LAM can be assessed by looking at the lower peak (III) in the IC curve, which relates to the shortness of the major plateau (III) in the charging curve and the shallower main valley (III) in the DV curve. By expressing the charge capacity provided by the constant current charging stage in the charge curve, the endpoint of the DV curve acts as an indicator of LLI. LLI can also be measured using the region between the IC curve and the X-axis. For a comprehensive understanding of the IC and DV curves, their relationship to the electrodes, and the associated aging mechanisms, please refer to Table 2-2. More details can be seen in [J3].

Table 2-2 The primary degradation modes for graphite/Li, NMC/Li, and NMC/graphite connection with charge, IC, and DV curves [J3][38]

Change in charge curve	Change in IC curve	Change in DV curve	Most pertinent DMs
Full cell: smaller charging capacity, and upward trend. Anode: smaller lithiation capacity, and upward trend. Cathode: smaller delithiation capacity, and upward trend.	Full cell: shift toward lower or higher voltage, decrease of the height of the peaks. Anode: shift toward higher or lower voltage. Cathode: shift toward lower or higher voltage.	Full cell: shift toward lower capacity. Anode: shift toward lower capacity. Cathode: shift toward lower capacity.	LLI Quantified by Eq. (4)
Full cell: shorten of main plateau (III) Anode: shorten of A3 plateau. Cathode: shorten of C2 plateau.	Full cell: decrease of the highest peak (III). Anode: decrease of the A3 peak Cathode: decrease of the C2 peak	Full cell: decrease the depth of the main valley (III). Anode: decrease of the depth of the A3 valley. Cathode: decrease of the depth of the A3 valley.	LAM Quantified by Eq. (3)

2.3.2 Electrochemical Impedance Spectroscopy (EIS)

A schematic based on actual studies performed on a full 18650 cell is shown in Figure 2-8. The bulk resistance, which is correlated with the electrical conductivity of the electrolyte, separator, connector, and connection wires, can be represented by the R_{ohm} parameter [43]. The solid-state interface layer that forms on the electrode surfaces causes resistance, which is represented by the R_{sei}. Its value can be determined by fitting the EIS results [J2].

The frequency range from 50 to 0.2 Hz is referred to as the charge-transfer resistance, or R_{ct}. Finally, the straight line seen in the low-frequency region mostly relates to the concentration-polarized Li-ion diffusion resistance [44]. The obtained impedance data can be effectively fitted using an equivalent circuit, such as the one shown in the inserted section of Figure 2-8 (a), by employing ZsimDemo 3.30 software[45].

The calculation of the Li^+ diffusion coefficient ($D_{\mathrm{Li+}}$) in the electrode materials involves utilizing Eq. (2-6), while determining the Warburg factor (σ) requires applying Eqs. (2-7) and (2-9) [46], [47].

$$D_{Li^+} = \frac{R^2T^2}{2A^2n^2F^2C^2\sigma^2} \qquad (2-6)$$

$$Z_{re} = R_{ohm} + R_{ct} + \sigma\omega^{-1/2} \qquad (2-7)$$

$$\omega = 2\pi f \qquad (2-8)$$

$$Y_0 = \frac{1}{\sigma\sqrt{2}} \qquad (2-9)$$

Where, R represents the gas constant (8.314 J $mol^{-1}K^{-1}$), T represents the absolute temperature (298 K), A represents the surface area of the electrode, n denotes the quantity of electrons exchanged per molecule, F represents the Faraday constant (96485 C/mol), C represents the concentration of Li^+, and ω represents the angular frequency.

Since R, A, n, F, C, and T remain constant in this study, it is possible to calculate the relative change in Li-ion diffusion rate ($D_{\mathrm{Li+}}$ / initial $D_{\mathrm{Li+}}$). This can be done using the following equation: $D_1 : D_2 : D_3 : D_4 = 1/\sigma_1^2 : 1/\sigma_2^2 : 1/\sigma_3^2 : 1/\sigma_4^2$, where the Warburg factor (σ) corresponds to the slope of the fitted line depicted in Figure 2-8 (b). With this method, it is possible to calculate impedance values and determine the change trend of the Li-ion diffusion rate. More details can be seen in [J2].

R_{sei} and R_{ct} are linked to LLI. Additionally, the tail seen in the low-frequency area of the impedance spectrum, which corresponds to Y_0, is linked to LAM. The degradation contribution from each aging mode has been quantified using Eqs. (2-10) and (2-11) based on these relationships [J2].

$$\mathrm{LLI} = 100\,\frac{(R_{sei,i}+R_{ct,i})-(R_{sei,1}+R_{ct,1})}{R_{sei,1}+R_{ct,1}} \qquad (2-10)$$

$$\mathrm{LAM} = 100\,\frac{(Y_{0,1}-Y_{0,i})}{Y_{0,1}} \qquad (2-11)$$

Likewise, in Eqs. (2-10) and (2-11), the subscript “1” denotes the battery in its initial state, while *i* represents the cycle number corresponding to its aging process. The relationship between the aging modes and the variations in impedance spectrum characteristics can be described using these equations, as summarized in Table 2-6.

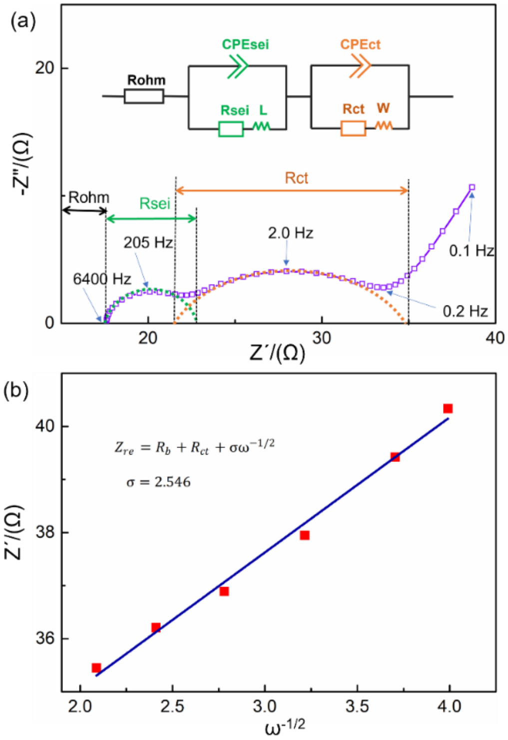

Figure 2-8 (a) EIS and corresponded equivalent circuit; (b) the relationship between *Z'* and $\omega^{\wedge(-1/2)}$. Source [J2][41].

Table 2-6 Relationship between the most important degradation modes and the impedance spectrum. Source [J2][41].

AR-ECM component	Most pertinent DMs
Increase in R_{sei} and R_{ct}	LLI Quantified by Eq. (2-10)
Increase in Y_0	LAM Quantified by Eq. (2-11)

2.3.3 Coin Cells for Performance Evaluation

To assess the performance of the aged electrodes, coin cells consisting of a Li metal anode and aged electrodes were assembled. These coin cells were then compared to coin cells assembled with fresh electrodes. By conducting this comparison, the electrode aging can be evaluated and analyzed. Haidi Company supplied pristine NMC positive electrodes and graphite negative electrodes that come from the same batch as the electrodes used in 18650 cells. If purchasing fresh electrodes directly from the manufacturer is not possible, another option is to remove the electrodes from fresh 18650 full cells. This approach can provide a viable solution for researchers or individuals who are unable to obtain fresh electrodes.

In order to create counter electrodes, discs of lithium metal with a diameter of 15 mm were combined with discs of both the positive electrode material and the negative electrode material that were both cut into 14 mm diameter discs. These electrode pairs were subsequently assembled into 2016-coin cell cases. The electrolyte used was 1 M LiF_6 in a mixture of dimethyl carbonate (DMC) and diethyl carbonate (DEC) with a 1:1 ratio. Each coin cell contained 5 drops of electrolyte, dispensed using a 1 ML pipette. The separator is polyethylene (PE).

2.3.4 Considerations and Advancements Related to the EIS Method

As the understanding of EIS continues to evolve, some constant current techniques now offer impedance information that was traditionally obtainable only through EIS. Furthermore, with the advancements in machine learning, it is now possible to predict the complete EIS spectrum using constant current charging curves.

2.3.4.1 EIS and DC impedance show similar results in impedance test

Both EIS and DC impedance measurements can be used to identify different battery electrochemical processes, such as the R_{sei}, R_{ct}, and R_{mt}[48], [49] (Figure 2-9). The EIS results are obtained based on the changing of the current frequency. With the frequency ($1/T$) changing, the transfer (electron conductive and Li-ions diffusion) process can be identified from the EIS spectrum. Similarly, DC constant current also can be used to measure the battery impedance. According to the duration of current applied, the battery impedance corresponding to different electrochemical processes can be calculated. This means that both EIS and DC constant current techniques can obtain battery impedance results, which are dependents on the rate of the chemical reaction process. Stolz et al[48]. summarized the mechanisms of EIS impedance and DC impedance, respectively. They stressed the advantages of constant current measurement techniques. Consistent with Stroe's study, the advantage of the DC pulse technique is that you can extract the impedance/resistance directly from the battery's real-life operation[50].

Considering that the same measure object, the battery system, both AC and DC measurement principles rely on discerning the reaction rates of diverse electrochemical processes to achieve process separation. Therefore, it is anticipated that DC technology may eventually replace EIS identification in impedance testing. However, how to distinguish the time period for R_{mt}, R_{ct} and R_{sei} in constant current tests is still a challenge. This is expected to be solved with the help of developments in computing science, such as employ advanced data fitting or prediction methods to ascertain the duration required for each individual reaction process.

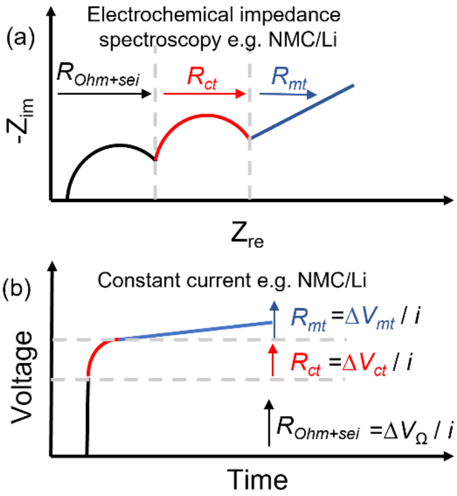

Figure 2-9 EIS and DC impedance measurements, *e.g.* constant current techniques both can be used to quantify the battery impedance for $R_{ohm+sei}$, R_{ct}, and R_{mt}[48]. Source: [J6].

2.3.4.3 EIS spectrum can be predicted from constant current charging curve

With the development of machine learning, it was found that the constant current charging curve can be used to predict the EIS spectrum with a very low error[51], [52]. The prediction process is shown in Figure 2-10. The model was trained using an extensive dataset of early measurement data. Obsoletely, EIS measurement can be replaced by constant current techniques with the support of machine learning. Moreover, this implies that a connection exists between EIS spectra and battery constant current charging curves. Thus, it can be concluded that the constant-current charging process also exhibits characteristics associated with Li-ion diffusion. However, the underlying mechanism remains to be clarified [C1].

Here, the implementation of DC measurement method demonstrates the potential to serve as a substitute for EIS in application. The development of machine learning can help DC charging curve replace the function of EIS to study and diagnose the battery electrochemical behavior.

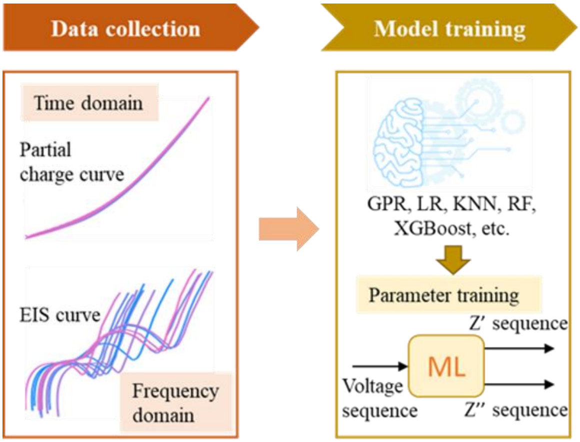

Figure 2-10 The EIS spectrum can be predicted by the battery constant current charging curve by machine learning method, and the training process is based on a huge dataset collected in early stage. Source: [J3][51].

Simplified DC impedance measurement instead of EIS measurement or the use of machine learning algorithms to estimate the battery impedance from extensive battery charging datasets have the potential to achieve realistic automotive battery impedance identification and further battery diagnosis and health estimation. Moreover, prediction methods such as machine learning can also realize the prediction from DC test curve to EIS by capturing the correlation between DC test curve and EIS results. This undoubtedly reflects the consistency between the DC impedance test and the AC impedance test.

2.4 Materials Test Methods

Post-mortem analysis

The 18650 cells were disassembled inside a glove box under an argon atmosphere using a sharp knife. The positive electrode and negative electrode were individually washed with DEC (diethyl carbonate). Subsequently, the washed electrodes were dried inside the glove box for several hours and then sealed in bags for testing purposes.

Scanning Electron Microscopy (SEM)

A Zeiss 1540 XB model of a Field Emission Scanning Electron Microscope (FESEM) was used to examine the morphology of the materials. The operation voltage is 20 KeV for imaging and analysis purposes. This instrument provides high-resolution imaging capabilities, allowing for detailed examination of the electrodes and particles morphology.

Raman test

Raman measurements were conducted using a Renishaw QONTOR instrument with a 532 nm laser. In-situ Raman tests were performed for fresh electrode in the support of the in-situ cell and biology Potentiostat SP 150.

X-ray diffraction analysis (XRD)

In section 4 and 5 ex-situ tests were conducted at the synchrotron P02.1 beamline at PETRA III (DESY, Hamburg) using a high-energy monochromatic X-ray beam (97.6 keV) in a transmission geometry. The purpose of the test was to evaluate the degradation of the electrode structure.

X-ray photoelectron spectroscopy (XPS)

A Specs XR50 apparatus fitted with a non-monochromated Al K (1487 eV) X-ray source and a Phobos 150 1D-DLD electron detector was employed to perform X-ray photoelectron spectroscopy (XPS) studies. By measuring the kinetic energy of the photoelectrons released, this arrangement enables the investigation of the samples' elemental composition and chemical states. The XPS technique provides valuable information about the surface chemistry and electronic structure of the aged electrode materials.

X-ray absorption spectroscopy (XAS)

During the first two cycles, NMC samples at various levels of charge were subjected to both in situ and ex situ X-ray Absorption Spectroscopy (XAS) measurements. The measurements were carried out at Berlin, Germany’s BESSY-II synchrotron light source KMC-2 beamline. At the KMC-2 beamline, XAS measurements were carried out at the Ni, Co, and Mn K-edges, allowing for the investigation of the electronic and structural properties of these elements in the NMC samples. The measurements provided valuable information about the oxidation states and local coordination environments of Ni, Co, and Mn during different stages of the charge-discharge process and the aged state.

For accurate energy calibration, pure metal foil samples were measured simultaneously with each NMC sample. This calibration ensured precise determination of the XAS spectra and allowed for accurate interpretation of the energy-dependent features. The ex-situ XAS samples were measured in the transmission mode, where the X-ray beam passes through the sample. This measurement configuration enabled the characterization of the samples' absorption spectra and provided insights into the electronic structure and chemical bonding of the NMC materials under investigation. The acquired spectra from the XAS measurements underwent data processing using the Athena Software package, including background correction, normalization, k^2-weighting, and Fourier transformation [53], [54].

2.5 Summary

The battery parameters, aging conditions, and diagnosis methods were presented in this chapter. The most widely used NMC 532 type commercial battery was chose for aging. The battery working conditions such as constant current cycling, pulse current charging, and real-life driving condition, using the standardized WLTC driving cycle, were performed. For mechanisms study, electrochemical methods, post-mortem analysis, and materials test were employed. Especially for electrochemical methods, the indictors in IC-DV curves for selected battery were explored and selected. Besides, in-situ tests such as in-situ Raman, in-situ XAS and operando EIS were performed.

Chapter 3. Aging Mechanism for Battery in Constant Current Cycling

In this chapter, the constant current cycling-induced aging of widely utilized commercial Li-ions batteries was studied. The operando EIS of both fresh and aged batteries, electrochemical cycling, and real-time temperature monitoring were recorded at full cell level. It's revealed that the capacity fade observed during battery operation is primarily caused by polarization. The formation of the solid-electrolyte interphase (SEI) and cathode-electrolyte interphase (CEI) are the main reasons for battery polarization as find out through post-mortem analysis results. Moreover, the irreversible loss of Li resulting from Li plating and SEI formation were quantified, which accounts for 16.8% of the total Li inside battery. These findings deepen the comprehension of the mechanisms of commercial LIBs degradation, and offer direction for the rational development of charging and discharging protocols with the goal of enhancing cycling stability and prolonging cycle life. The related scientific outcome is listed as follows:

J4 **J. Guo**, S. Jin, X. Huang, Y. Xu, Y. Li, P. Kristensen, D. Wang, K. Pedersen, L. Gurevich, and D. I. Stroe, "Unravelling and quantifying the aging processes of commercial $Li(Ni_{0.5}Co_{0.2}Mn_{0.3})O_2$/graphite lithium-ion batteries under constant current cycling," *Journal of Materials Chemistry A*, vol. 11, pp. 41–52, 2023

C2 **J. Guo**, Y. Li, K. Pedersen, L. Gurevich, and D.-I. Stroe, "Unravelling the aging process of commercial $Li(Ni_{0.5}Co_{0.2}Mn_{0.3})O_2$/graphite lithium-ion batteries under constant current cycling" ISE Meeting Abstracts, Lyon, France, 2023

3.1 Aging of Full Cell

3.1.1 Cycling Performance

Battery degradation mechanisms were initially assessed using ICA and cte-OCV techniques. Figure 3-1 (a) displays the charging and discharging voltage profiles obtained from 11 RPTs. With battery aging, the charge plateau gradually increases while the discharge plateau diminishes. The disparity between the charging and discharging curves corresponds to battery impedance and progressively widens over time. Simultaneously, the voltage plateau considerably shortens, leading to a reduced capacity. To delve deeper insights into the voltage plateau evolution, the charging-discharging curves in Figure 3-1 (a) were subjected to ICA analysis, yielding the results presented in Figure 3-1 (b) [J4].

The "a" peak in the IC curves arises from redox reactions occurring in both the graphite anode and cathode materials. The "b" peak in the IC curves primarily originates from the oxidation-reduction potential of the anode side. As the battery ages, both “a” and “b” peaks in the IC curves exhibit significant intensity reductions. Furthermore, all peaks noticeably shift to the right, with the “b” peak displaying the most pronounced change. Typically, the decrease in the peak intensity is correlated with the loss of active material within the battery. On the other hand, the shift of the peak is associated with the internal polarization of the battery, reflecting the changes in electrochemical processes and impedance within the battery. Battery aging is predominantly attributed to electrode material loss and the emergence of internal polarization [J4].

Furthermore, those findings revealed a consistent correlation between the movement of the “b” peak and the capacity fade of the battery (Figure 3-1 c). As the “b” peak shifted upright, it corresponded to a decline in the overall condition and performance of the battery. This further shows that battery aging is related to the internal impedance of the battery [C2].

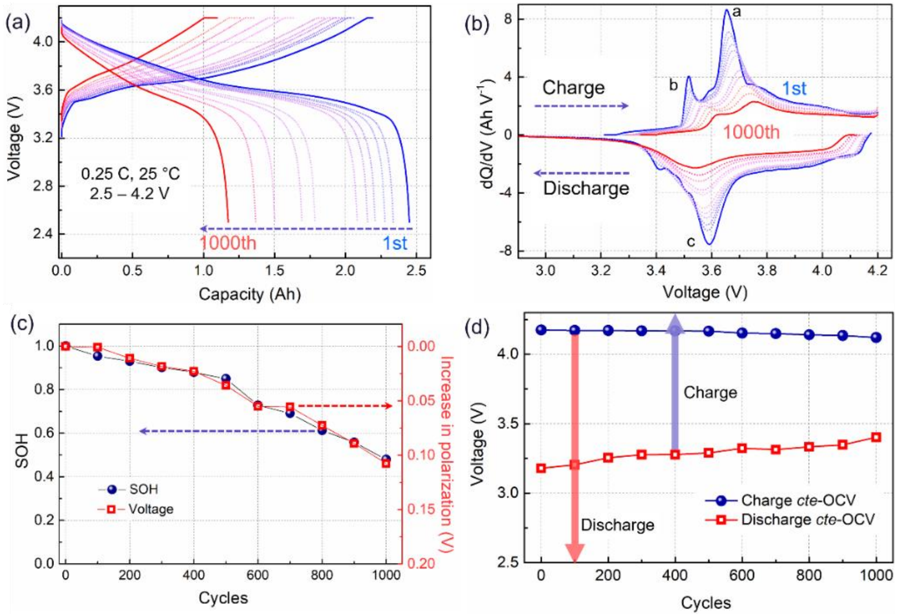

Figure 3-1 (a) Charge and discharge curves; (b) IC curves; (c) evolution of SOH and the right shift of the b peak in (b); (d) Charging and discharging *cte*-OCV curves. Source: [J4][14].

To analyze the evolution of the behavior of the open-circuit voltage (OCV) with battery aging, a close-to-equilibrium *cte*-OCV test was conducted[55], as depicted in Figure 3-1 (d). The discharging *cte*-OCV exhibits a gradual increase, primarily attributed to the rising polarization within the battery. As anticipated, there is no comparable rise in the charging *cte*-OCV; instead, a little decline is seen. As a result, the battery’s overall capacity for discharging and charging decreases, as well as the charging and discharging OCV range.

3.1.2 Impedance Analysis

To assess the polarization, operando electrochemical impedance spectroscopy (EIS) tests were conducted in the interval 6500 – 0.01 Hz. Figure 3-2 (a) and (b) present the Nyquist plots obtained from these measurements. After 1000 cycles, the EIS spectrums obviously increase in both real and imaginary parts, which means the battery impedance increases. In this case, the R_{ohm} component is not included in the equivalent circuit model because of the unstable ohmic impedance that is brought on by the unstable connector of the electrochemical workstation [J4].

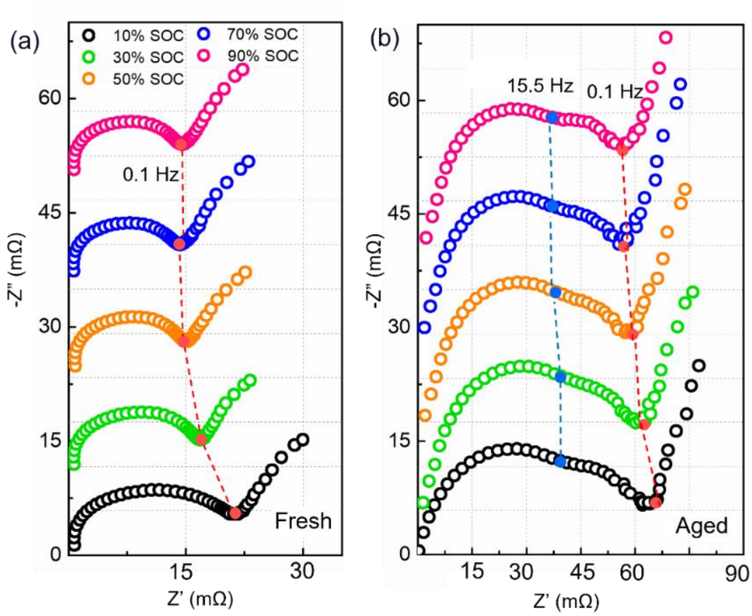

Figure 3-2 Electrochemical impedance spectroscopy (EIS) spectrum at various states of charge (SOC) for both a fresh cell (a) and an aged cell (b). Source: [J4][14].

The EIS spectrum exhibits four distinct regions at different frequency ranges, each representing different aspects of the battery's behavior, as shown in Figure 3-3 (a). In the extra high-frequency range (> 2000 Hz), the spectrum reflects the bulk resistance (R_{ohm}). The high-frequency (2000 – 10 Hz) range is related to the solid electrolyte interface resistance (R_{sei}), while the middle frequency range (10 – 0.1 Hz) denotes the charge transfer resistance (R_{ct}). Finally, in the low-frequency range (< 0.1 Hz), the spectrum provides information about the lithium diffusion process within the battery. The Nyquist plots shown in Figure 3-3 (a) were fitted using an equivalent circuit model, and the fitted result are shown in Figure 3-3 (b,c). Following 1000 cycles, the R_{sei} experienced a substantial four-fold increase from below 8 mΩ to approximately 30 mΩ, as illustrated in Figure 3-3 (b). Additionally, the R_{ct} exhibited an increase to over 20 mΩ, as depicted in Figure 3-3 (c). These findings indicate a notable degradation in the electrode interface and charge transfer processes within the battery. According to the findings reported in reference [55], the SEI film experiences partial rupture at high state of charge (SOC) due to the increased volume of the lithiated graphite. However, during the subsequent discharge process, the SEI film recovers and reforms. As a result, the R_{sei} tends to decrease during battery charging (i.e., when the SOC increases). Additionally, a higher SOC also indicates the active stage of the chemical process as well as a higher voltage. Consequently, a lower R_{ct} is observed at higher SOC conditions [J4].

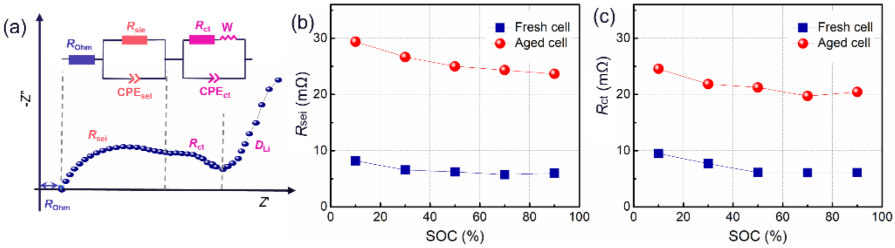

Figure 3-3 The EIS Nyquist plot is fit by (a) an equivalent circuit, and the fitted results for (b) R_{sei}; (c) R_{ct}. Source: [J4][14].

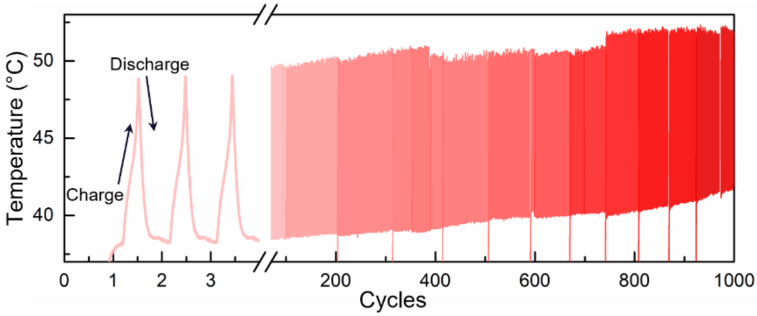

Figure 3-4 The temperature of battery outer surface. Source: [J4][14].

Furthermore, the temperature during the aging process is monitored using temperature sensors placed on the surface of the battery, as depicted in Figure 3-4. Throughout one dis/charge process, the temperature exhibits a similar trend to the state of charge (SOC) variations. As the battery state of charge (SOC) increases, the temperature gradually rises accordingly. Over the course of 1000 cycles, the battery temperature exhibits a consistent upward trend. This can be attributed to the heightened battery impedance, which generates additional Joule heat, resulting in further side reactions side reactions.

3.2 Post-mortem Analysis

After disassembling both the 1000 EFCs aged battery and a fresh battery, a post-mortem analysis was conducted for electrodes and materials. After washed by DEC, the electrodes are illustrated in Figure 3-5. The surface of the aged electrode is gritty, while the fresh electrodes are smooth. Notably, the aged positive electrode exhibits evident peeling off from cathode particles, while the negative electrode showcases uneven lithium plating on its surface. more details can be seen in [J4].

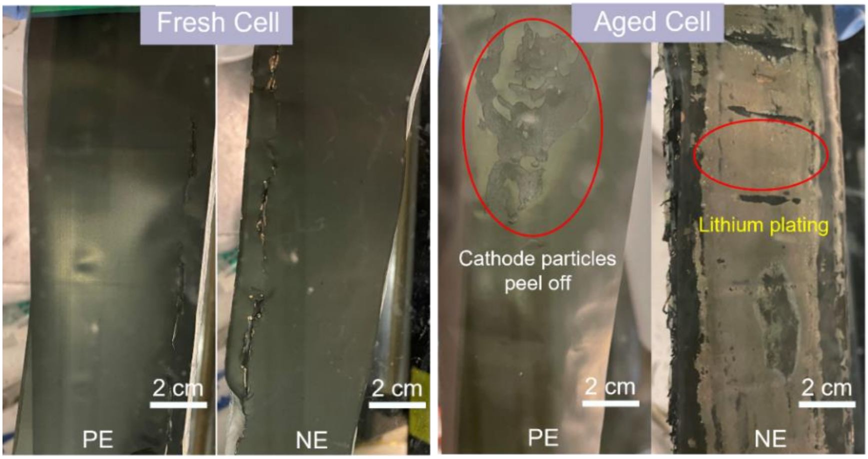

Figure 3-5 The negative and positive electrodes. Source: [J4][14].

3.2.1 Loss of Li-ions

Li-ion loss, leading to capacity reduction, primarily takes place on the negative electrode either as Li plating or surface film deposition. Smooth and well-rounded graphite particles can be seen on the new negative electrode in the scanning electron microscope (SEM) image shown in Figure 3-6. The aged graphite, on the contrary, shows a collapsed structure surrounded by a rough surface layer and numerous microscopic particles (Figure 3-6 (a, b)). The rough surface layer is identified as the SEI film, while the small particles are believed to be Li dendrites [56].

A portion of the disassembled negative electrode was washed with DEC and then submerged in water to produce a strong reaction and many bubbles were observed, proving the presence of irreversibly bound Li on the surface of the aged negative electrode. Upon reacting with water, the negative electrode undergoes a transformation, revealing a clean surface, as illustrated in Figure 3-6 (c) [J4].

Most of the particles and the rough surface layer vanish, revealing a collapsed graphitic structure. Water reacts with Li or Li compounds to produce this change. Table 3-2 [57] summarizes these Li compounds' possible reactions and solubility. Alkaline soluble LiOH is the reaction's main byproduct. In the manufacturing of nickel-rich materials, pH measurements have been widely used to quantify residual lithium [58]. The irreversible lithium in this study, which can react with water and dissolve as Li^+ and OH- ions, is quantified using the pH value. Figure 3-6 (d) shows this procedure, which is followed by an assessment of the total lithium loss on the graphite anode using XPS [C3].

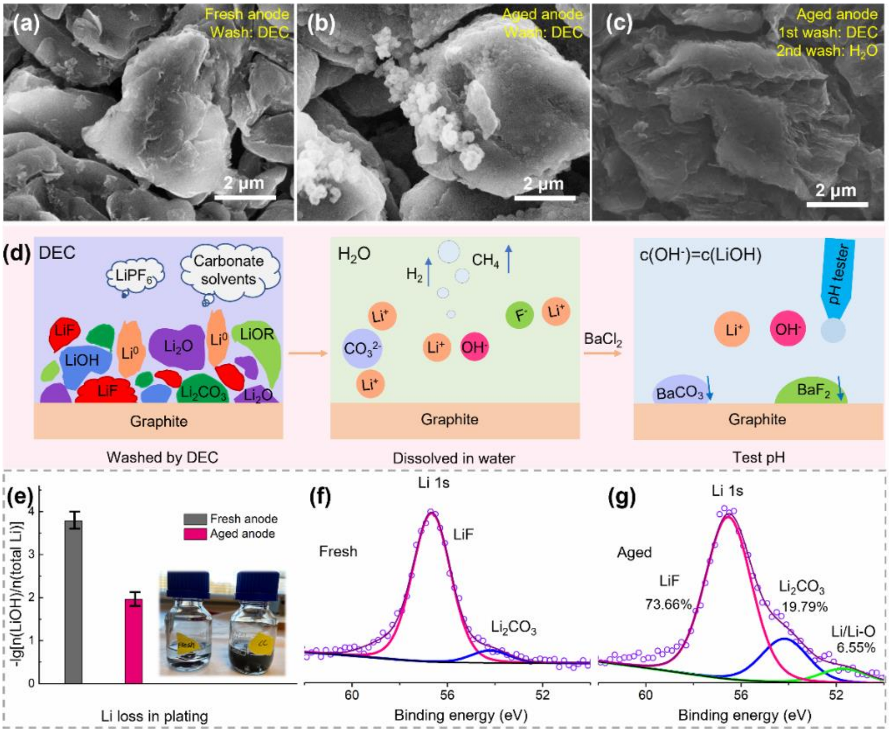

Figure 3-6 Negative electrode SEM images from (a) fresh battery, (b) aged battery and washed with DEC, and (c) aged negative electrode washed by DEC and by water. (d) The mechanism diagram of lithium compounds dissolved in water; (e) the quantified result of LiOH content; the Li 1s XPS results for (f) fresh battery and (g) aged battery. Source: [J4][14].

The pH values of the aged and fresh negative electrodes are measured as 10.64 and 8.81, respectively, as depicted in Figure 3-6 (e). Additionally, XPS analysis of the Li 1s peak was performed on the electrodes from Figure 3-6 (a) and Figure 3-6 (b), and the results are shown in Figure 3-6 (f) and Figure 3-6 (g), respectively. The aged negative electrode exhibits three fitted peaks corresponding to LiF, Li_2CO_3, and Li/Li-O compounds, representing 73.66%, 19.79%, and 6.55% of the total lithium, respectively. The Li/Li-O compounds align with the pH-quantified portion (1.10%). As a result, the aged negative electrode's quantifiable lithium loss is 16.82%. It is significant to note that during voltage recovery from a totally low SOC, some active Li is introduced into the graphite. As a result, the findings of the pH test and XPS show that the lithium loss is substantially less than the capacity loss (over 50%). More details are shown in [J4][14].

Table 3-2 The anode’s dissolved species of lithium or lithium compounds, or their interactions with water. Source: [J4][14].

Components	**Reactions with water**	**Species in**
Li	$2Li + 2H_2O = 2LiOH + H_2\uparrow$	Li^+, OH^-
Li_2O	$Li_2O + H_2O = 2LiOH$	
CH_3Li	$CH_3Li + H_2O = LiOH + CH_4\uparrow$	
ROLi	$ROLi + 2H_2O = 2LiOH + H_2\uparrow$	
LiOH	N.A.	
LiF	N.A.	Li^+, F^-
Li_2CO_3	N.A.	Li^+, CO_3^{2-}

3.2.2 Degradation of Positive Electrode

SEM cross-section pictures of the fresh and old positive electrodes are shown in Figure 3-7 (a) and (b), respectively. According to Figure 3-7 (a), the fresh positive electrode is 137 μm. After 1000 aging cycles, the average thickness experiences an increase to 153 μm, corresponding to a 11.7% increment, as shown in Figure 3-7 (b). Additionally, the presence of cracks is evident, extending towards the inner part of the electrode. This phenomenon leads to particle disintegration and the formation of intra-electrode voids, contributing to the overall increase in electrode thickness. Then, this further leads to the impedance increase [J4].

The leftward shift of the X-ray diffraction (XRD) pattern in Figure 3-7 (i) indicates that the cathode grains have expanded, which is another cause for the increased electrode thickness. Longer routes for charge transfer and Li diffusion as well as a higher internal resistance are the results of this expansion. In addition, a decrease in the splitting peaks (006/012) represents a decrease in crystallinity and an increase in the ratio of I(003)/I(104) point to increased Li/Ni cation mixing in the aged positive electrode [59] [J3].

Moreover, the particle shape clearly shows the degradation of the electrode material. The fresh cathode particles have a smooth surface (Figure 3-7 (d)). After aging, pulverization and cracking occurs (Figure 3-7 (e)). The presence of residual powders on the cathode particles surface is interface compositions, which will be examined using X-ray photoelectron spectroscopy (XPS) later. These cracks are also visible in the Raman spectrum (Figure 3-7 (f)), where the layered $LiNiO_2$ and $LiCoO_2$ in NMC (nickel-manganese-cobalt) cathode contribute to the Raman-active modes, particularly the A1g mode at 609 cm^{-1} and the E_g mode at 503 cm^{-1}, representing out-of-plane M-O stretching and in-plane O-M-O band, respectively [60]. $LiMnO_2$ is causes the emergence of additional weak bands. Indicating a higher abundance of the in-plane O-M-O band after aging, the increased E_g mode intensity is consistent with the development of cracks and the exposing of inner surfaces in Figure 3-7 (e).

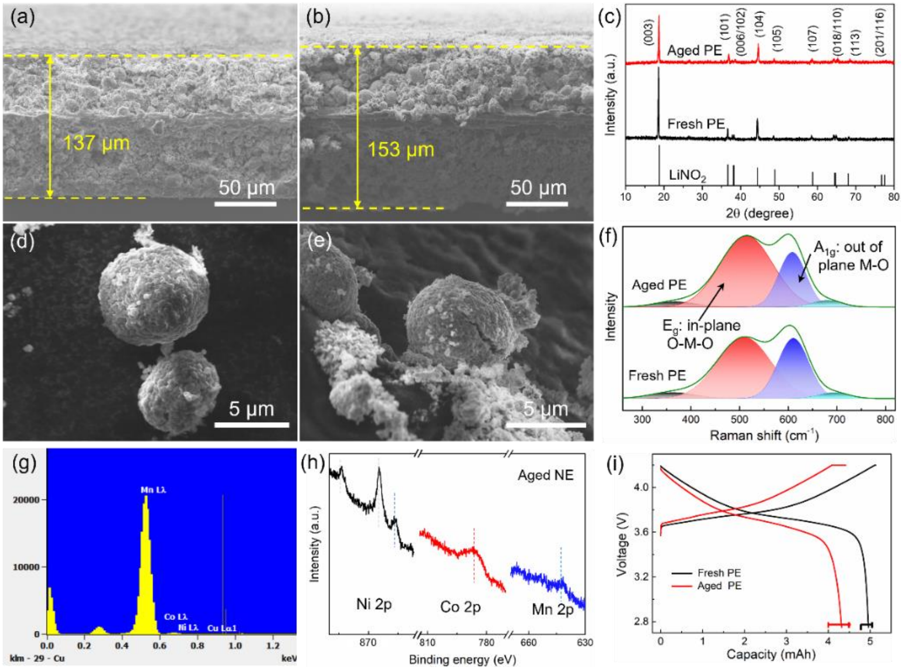

Figure 3-7 SEM results of cross-section for (a) fresh positive electrode and (b) aged positive electrode, respectively; (c) XRD results. The SEM images for (d) fresh and (e) aged NMC particles, respectively; (f) Raman spectra; (g) EDS for aged positive electrode (h) XPS spectrum for aged positive electrode; (i) charge and discharge curve. Source: [J4][14].

According to reports[61], when the electrolyte is damaged, hydrofluoric acid (HF) may be released. This acid may insert into the cathode particles and cause undesired side reactions, such as the dissolving of transition metals and their deposition on the negative electrode's surface. The presence of the transition metal elements Ni, Co, and Mn was verified by energy-dispersive X-ray spectroscopy (EDS) point scans, as shown in Figure 3-7 (g). Additionally, the XPS examination of the worn-out negative electrode surface (Figure 3-7 (h)) demonstrates the presence of Ni, Co, and Mn elements. According to earlier reports [62], [63], the deposition of Co on the graphite surface can hasten graphite exfoliation and seriously impair the performance of the entire battery.

From coin cell testing, it is possible to determine electrode degradation. The aged positive electrode has a larger charge plateau and a lower discharge plateau in Figure 3-7 (i), which suggests that polarization has occurred. Due to the increased internal resistance, the voltage reaches upper voltage quickly, causing an extended constant-voltage charging period and a reduction in battery capacity. But the battery keeps over 86% of its initial capacity [J4].

3.2.3 Degradation of Negative Electrode

After aging, the negative electrode undergoes a significant increase in thickness. Initially, the fresh negative electrode has a thickness of 200 μm (Figure 3-8 (a)), which subsequently expands to 271 μm (i.e., a 30.5% increase) (Figure 3-8 (b)). The aged negative electrode exhibits a large number of cracks and exfoliated particles, resulting in electrode thickening. Additionally, material detachment from the current collector results in an augmented charge R_{ct}, as shown in Figure 3-8 (e).

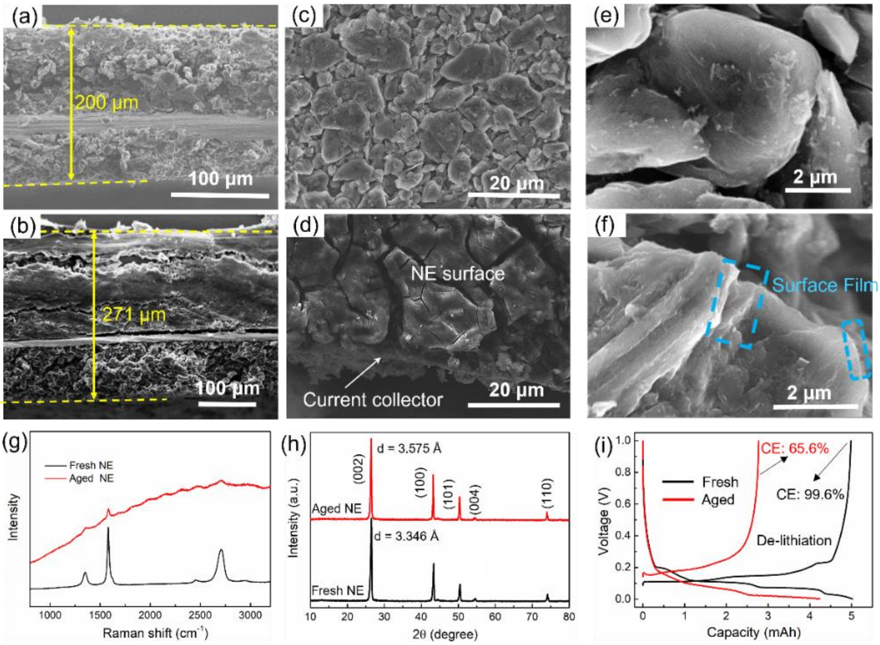

Figure 3-8 (a) fresh negative electrode and (b) aged negative electrode cross-section images; top surface of (c) the fresh negative electrode and (d) aged negative electrode; SEM image of (e) fresh graphite particles, (f) aged graphite particles; (g) Raman spectra, (h) XRD patterns, and (i) charge and discharge voltage curves. Source: [J4][14].

A top-view examination reveals a thick and cracked surface film atop the aged negative electrode (Figure 3-8 (d)). Furthermore, the SEM image (Figure 3-8 (f)) shows that the edges of the graphite particles are surrounded by a surface coating. This film is primarily responsible for the surface impedance experienced in batteries. Moreover, as the graphite degrades, the particles are deformed and take uneven forms.

Using Raman measurements with a laser wavelength of 532 nm, the interface structure of both the new and used negative electrodes was assessed (Figure 3-8 (g)). However, the Raman spectrum solely detects a faint graphitic phase at the interface of the aged negative electrode, suggesting that the interfacial precipitates have a thickness close to 500 nm. To evaluate structural changes, XRD patterns were used (Figure 3-8 (h)). These patterns showed that during aging, the graphite particles size changed, leading to volume expansion. The expansion serves as an additional factor contributing to the electrode's thickening as well as the increased battery impedance.

Figure 3-8 (i) provides an illustration on the negative electrode's capacity for fresh and aged negative electrodes by lithiation and delithiation the graphite in the range of 1.0 - 0.001 V. Less than 15% of the lithium-intercalated graphite was lost throughout the lithiation process, as noticed by the capacity fade that was seen. The initial charging voltage, mostly brought on by internal impedance, does, however, significantly influence the de-lithiation process. This results in a 44.4% capacity loss in the de-lithiation process compared to the fresh negative electrode since the aged negative electrode only has a 65.6% coulombic efficiency [J4].

3.2.4 Degradation of Interface

A SEI layer is created on the negative electrode surface through plating of Li compounds and other solvents. Similar terminology is used to describe the top layer of the positive electrode, which is known as the CEI". The SEI and CEI layers are often combined and referred to as the "electrode electrolyte interphase (EEI)"[64]. A thermodynamics potential gap between the electrodes and the electrolyte is created by the creation of the EEI layer, leading to a drop in battery potential during cycling [64]. This phenomenon is a major contributing factor to the overall performance degradation of the battery.

Impedance increase is identified as the primary cause of battery capacity degradation. Figure 3-9 (a) and (b) provide a comparison of the impedance evolution during cycling for both positive and negative electrodes; the fitted results are depicted in Figure 3-9 (c). The aged positive electrode exhibits a high R_{cei} value of 574.5 Ω compared to the fresh electrode (42.47 Ω); a second semicircle can be seen in the impedance spectra of the deteriorated positive electrode (Figure 3-9 (a)), showing a reduced electronic conductivity that is a result of cathode cracks and pulverization. Similarly, the impedance spectra of the negative electrode are presented in Figure 3-9 (b), with the aged negative electrode displaying an R_{sei} value of 1052 Ω, significantly higher than the R_{sei} value of 183 Ω for the fresh electrode. Therefore, the electrode impedance is primarily influenced by the interfacial film [J4].

XPS analysis was used on the fresh and aged batteries to investigate the compositional details of the EEI. The CEI composition was identified through XPS, and the tested F 1s, O 1s, C 1s, and Li 1s are displayed in Figure 3-9 (d). Notably, the percentage of lattice oxygen significantly increases in the O 1s spectrum for the aged positive electrode, which correlates with crack formation and the exposure of fresh surfaces within secondary particles[65], consistent with the SEM analysis in Figure 3-8 (f).

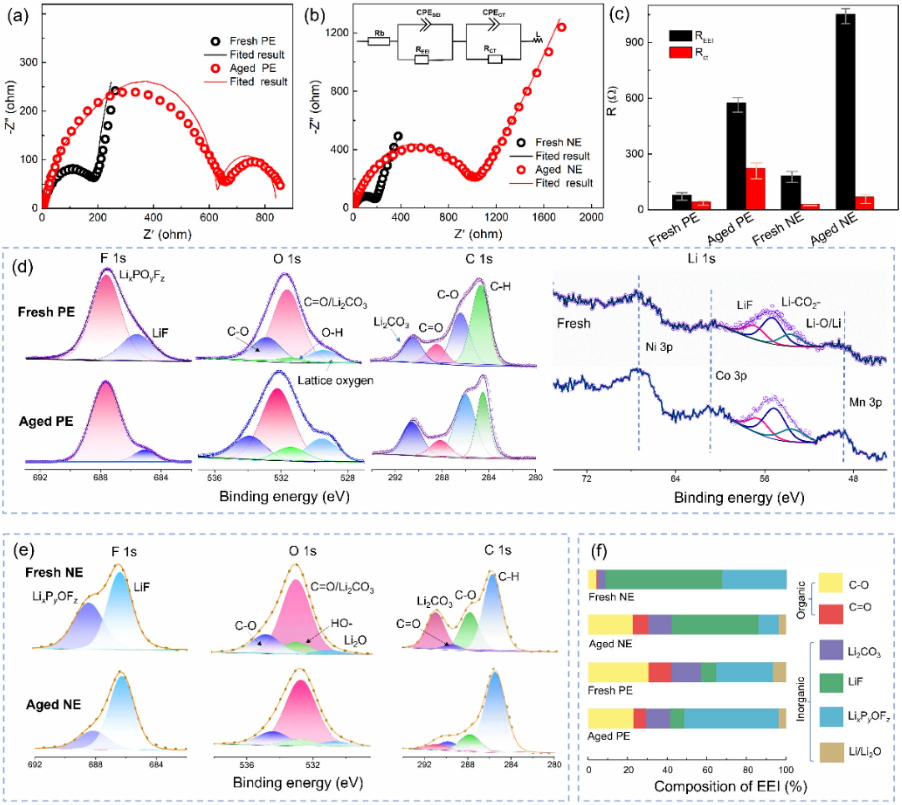

Figure 3-9 EIS result of (a) positive electrodes and (b) negative electrodes, (c) fitted results; XPS results of (d) positive electrodes, and (e) negative; and (f) quantified results. Source: [J4][14].

Regarding the SEI film, the formation of $Li_xP_yOF_z$ is attributed to reactions between trace amounts of H_2O and $LiPF_6$ in the electrolyte [66], representing the primary precipitated solid that can decompose to form Li_3PO_4 and LiF [67], [68]. In the Li 1s spectrum, Li_2CO_3 primarily arises from electrolyte decomposition [67]. Additionally, Li_2O (peak at 52.4 eV) can be ascribed to Li reducing CO_2 originating from the decomposition of Li_2CO_3 at high voltages (approximately 4.2 V) [69].

It is worth noting that the proportion of Li-O observed in this study is relatively lower compared to other related reports [70]. This is explained by the use of a lower upper cut-off voltage in this study (4.2 V) and the lack of a constant voltage charging step. Additionally, the reduction of the electrolyte solvent, such as Diethyl carbonate (DEC), is where the C-O and C=O compounds are produced.

To further analyze the XPS data quantitatively, Figure 3-9 (f) illustrates that inorganic compositions serve as the predominant components of the electrode electrolyte interphase (EEI), which are essential for generating the EEI's electronic insulation [64]. The decomposition of ethylene carbonate (EC), which is linked to electrolyte deterioration, is responsible for a higher concentration of organic compounds (such as C-O and C=O) on the aged negative electrode for the SEI film [66]. Moreover, Li^+ diffusion is primarily mediated by Li_2CO_3 and LiF as ionic carriers. The decreased percentage of LiF in the aged anode impedes the diffusion of Li-ions and contributes to the increased R_{sei} observed in Figure 3-3 (b) and Figure 3-9 (b). In contrast to the SEI film, the CEI film predominantly consists of $Li_xP_yOF_z$ and organic components, primarily resulting from $LiPF_6$ decomposition at high voltages on the positive electrode side [66]. Furthermore, the percentage of inorganic compounds ($Li_xP_yOF_z$, Li_2CO_3, LiF, Li_2O, and LiOH) increases after aging, indicating further CEI reformation. As a result, both the negative and positive electrodes experience changes in surface composition throughout cycling [J4].

3.3 Summary and Prospective

In conclusion, as illustrated in Figure 3-10, the battery capacity drops by 52% during CC cycling due to active material loss, Li ions loss, and increased interfacial impedance. Active material loss is below 15% on each electrode, while Li ions loss accounts for 16.8% of the capacity fading. The main factor impacting capacity retention is the increased resistance, which results in a 44% loss for the negative electrode and a 14% loss for the positive electrode. To enhance battery life, measures can be taken at the full-cell, electrode fabrication, and material levels. Implementing reasonable charging/discharging protocols like dynamic pulse current [71] and adjusting depth of discharge can stabilize the SEI film [72] and extend battery lifetime. Managing temperature through heat dissipation or cooling systems prevents side reactions and metal dissolution. Using durable binders, optimizing electrode thickness (N/P ratio), and employing single-crystal cathode materials can reduce active material loss and impedance increase. Constructing artificial SEI films inhibits particle pulverization and volume expansion, improving cycling stability[73].

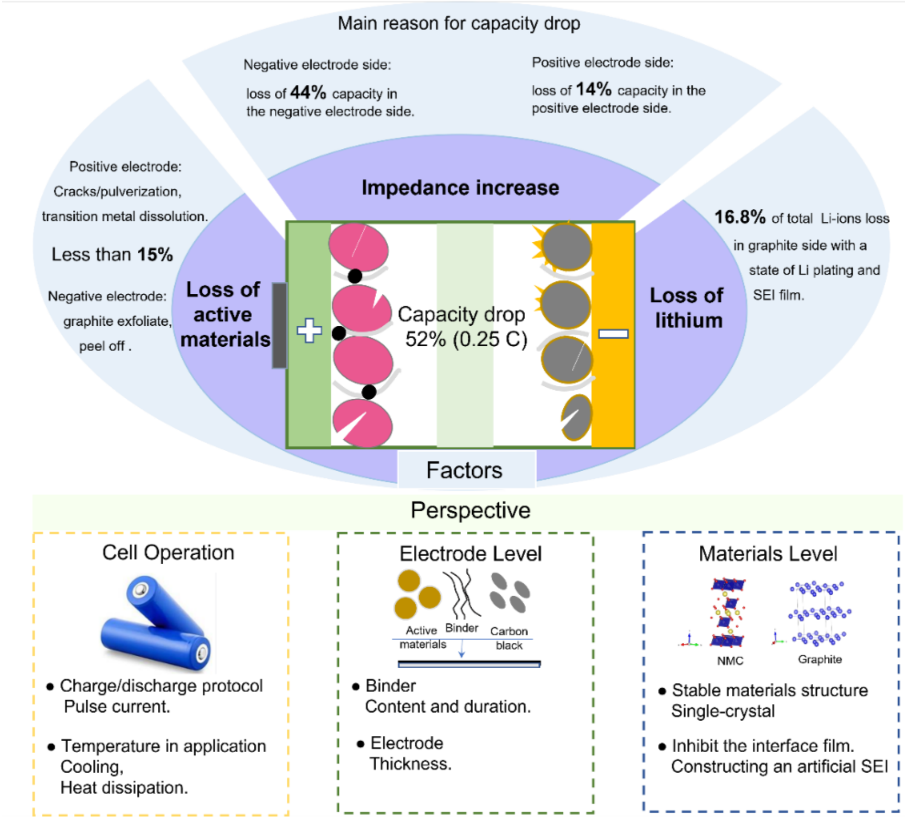

Figure 3-10 A description of how battery capacity loss occurs, along with suggestions for extending the battery’s cycle life. Source: [J4][14].

3.4 Summary

In this section, the aging of commercial $Li(Ni_{0.5}Co_{0.2}Mn_{0.3})O_2$/graphite batteries is investigated when subjected to CC cycling. After 1000 cycles, the capacity drops by 52% due to increased internal impedance. Both electrodes show significant impedance increase, mainly at both negative and positive electrode interface between electrode and electrolyte due to the EEI film formation. This leads to faster voltage collapse and reduced capacity. Higher impedance also increases heat generation, accelerating battery degradation. NCM particle cracking, transition metal dissolution, and increased interfacial impedance degrade the positive and negative electrodes. Li-plating and SEI films contribute to a 16.8% loss of active Li ions. These findings guide the development of cycling protocols for enhanced battery stability.

Chapter 4. Aging Mechanism for Battery in Pulse Current Charging

In this chapter, electrochemical diagnosis, post-mortem analysis, and in-situ testing methods were employed to investigate the mechanism underlying the lifetime improvement of commercial batteries by pulsed current charging. The application of pulsed current charging effectively mitigates the rise of battery impedance and minimizes the loss of electrode materials. Besides, the in-situ electrochemical test and post-mortem analysis further confirm that pulse current charge can reduce the degradation in both positive and negative electrodes, and inhibits the thicking of interface film. Therefore, through pulsed current charging, specifically at a frequency of 2000 Hz, the battery’s lifespan is significantly extended, resulting in a remarkable increase that exceeds twice its original service time. The related scientific outcome is listed as follows:

J5 **J. Guo**, Y. Xu, P. Adelhlem, M. Exner, X. Huang, P. Kristensen, D. Wang, K. Pedersen, L. Gurevich, and D. I. Stroe, “Unravelling the mechanism of pulse current charging for enhancing the stability of commercial Li-ion battery”. Submitted to *Advance Energy Materials*

4.1 Introduction

Batteries are gradually degraded over time, leading to a decrease in capacity, resistance/impedance increase, and safety issues. This limitation has posed challenges for both consumers and manufacturers, particularly in the case of the widely used NMC 532 battery chemistry[74]. Although several pulse charging protocols have been proposed to enhance battery performance and lifespan [75]–[77], the underlying mechanisms responsible for these improvements remain unclear [J5].

Pulse current has been employed for some types of batteries such as LFePO$_4$/Li [78] NMC/Graphite[79]–[81], LfePO$_4$/Carbon-based[82], [83], LCO/Graphite [84], and battery formats from coin cell to commercial battery. These studies have yielded encouraging outcomes, suggesting that pulsed current has the potential to significantly enhance battery stability, with improvements ranging from 0.5% to 34%. Li et al. [28] clearly clarify the mechanisms behind the stability improvement of Li-metal batteries, which is due to a loose association between cations and anions facilitates the transport of Li$^+$ ions and ultimately stabilizes the process of lithium electrodeposition. However, in commercial NMC/Graphite battery cells, the Li metal anode is not present, so the main mechanisms will be different.

Basically, the polarization, loss of Li-ions, and loss of active materials are the main reasons for battery degradation [85]. Previous work has demonstrated that the degradation of the battery is primarily attributed to two key factors: the formation of an interface film and the loss of active materials [14]. The formation of the interfacial film not only consumes Li-ions but also increases the internal impedance of the battery, resulting in a smaller OCV voltage range. The degradation of cathode and anode materials involves both structural deterioration and particle fragmentation. Therefore, the battery capacity drops.

Pulsed current charging is a promising technique to prolong the battery lifetime. The hysteresis of Li-ion diffusion creates concentration gradients near the electrodes during constant current charging. Pulsed current is expected to be used to alleviate the internal polarization of the battery. Furthermore, the relaxation time of the pulse current can facilitate the partial recovery of electrode materials' structural integrity.

Here, the batteries were aged with constant current and pulse current charging, respectively. The electrochemical analysis, in-situ test, and post-mortem analysis were performed to reveal the mechanism of pulse charging for improving battery stability.

4.2 Electrochemical Performance of Full Cell

Batteries show different cycling performance with constant current (CC), 100 Hz pulse current, and 2000 Hz pulse current. In the case of constant current (CC) aging, the battery exhibits a lifetime of only 500 cycles, before it reached 20% capacity fade. However, in the 2000 Hz aging case, the battery's lifetime extends beyond 1000 cycles, as shown in Figure 4-1. Undoubtedly, the implementation of pulsed current charging method effectively enhances the battery’s cycle performance [J5].

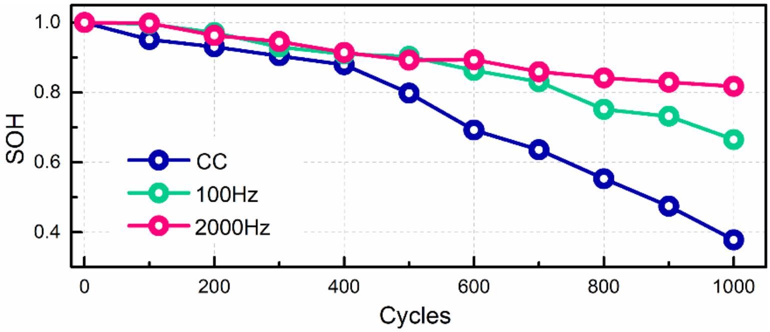

Figure 4-1 The stability of batteries was evaluated over 1000 cycles using three different currents: constant current, 100 Hz current, and 2000 Hz current. Source: [J5].

When comparing the charging and discharging curves during the initial cycle, it is observed that in all three cases (Figure 4-2 (a1-c2)), there is a clear upward trend in the charging plateaus and a corresponding downward trend in the discharging plateaus for the batteries after 1000 cycles. This effect is particularly pronounced in the case of the CC-aged battery and is attributed to the internal polarization occurring within the battery. As the pulse frequency increases, the range of plateaus shifts decreases, implying a lower polarization of the battery. Dubarry et al[86]. employed the shift of the II peak in the incremental capacity (IC) curve to quantify the increase in polarization. Here, the II peak in the IC curve shifts 0.166 V, 0.086 V, and 0.078 V for CC, 100Hz, and 2000Hz aging cases, respectively. Obviously, pulsed current charging demonstrates a mitigating effect on the internal polarization of the battery when compared to constant current (CC) charging. Peak I in the charging curve serves as an indicator for the loss of active materials in both the positive and negative electrodes[41].

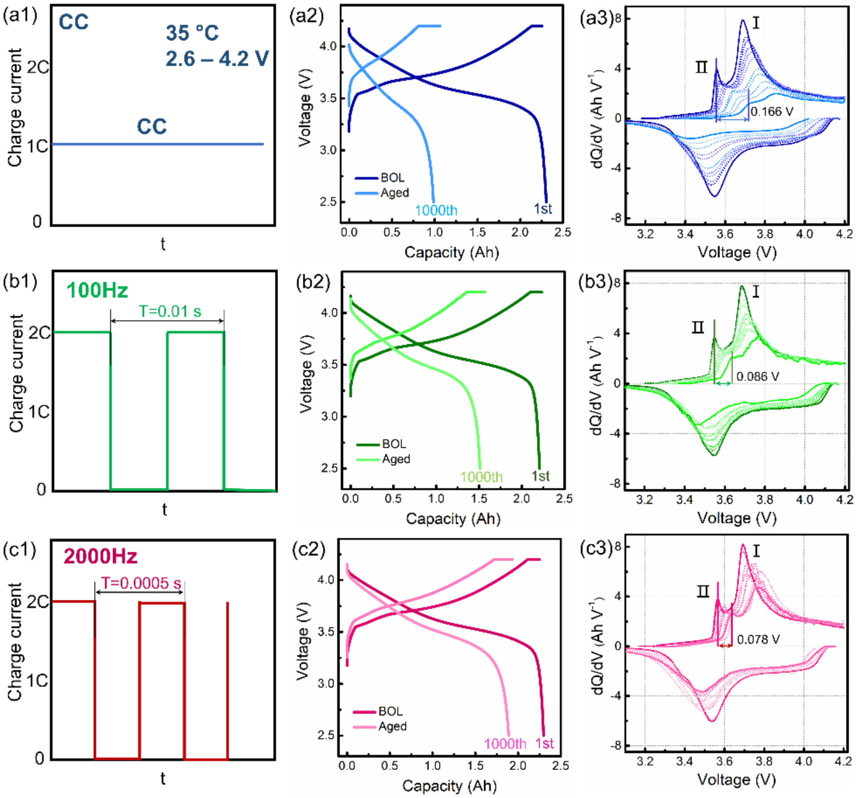

Figure 4-2 The aging condition, dis/charge curves, and incremental capacity (IC) curves for batteries aging with (a1-a3) CC, (b1-b3) 100 Hz, and (c1-c3) 2000 Hz aging conditions. Source: [J5].

Under CC charging, the intensity of peak I gradually diminishes and can nearly disappear after approximately 1000 cycles, indicating a substantial loss of active materials from both positive and negative electrodes. However, in the case of 2000 Hz pulse charging, peak I remains prominent even after 1000 cycles. This observation suggests that compared to CC charging, pulse charging significantly reduces the loss of active material. Preliminary diagnosis using electrochemical methods has revealed that the application of pulsed charging current helps alleviates the material loss and reduces the polarization inside the battery.

The impedance spectra obtained through Electrochemical Impedance Spectroscopy (EIS) for the batteries aged under CC charging, 100Hz, and 2000 Hz pulsed current are shown in Figure 4-3. The EIS test was performed at 90%, 70%, 50%, 30%, and 10% SOC. Since the ohmic impedance is greatly affected by the connector, the ohmic impedance will not be considered here, and the impedance will be moved to the coordinate origin. The impedance spectrum curve clearly shows that the impedance of the battery after aged under 2000 Hz pulsed current charging is significantly lower than that of the battery aged under after constant current CC charging. This indicates that the pulse current charging method effectively suppresses the internal polarization of the battery.

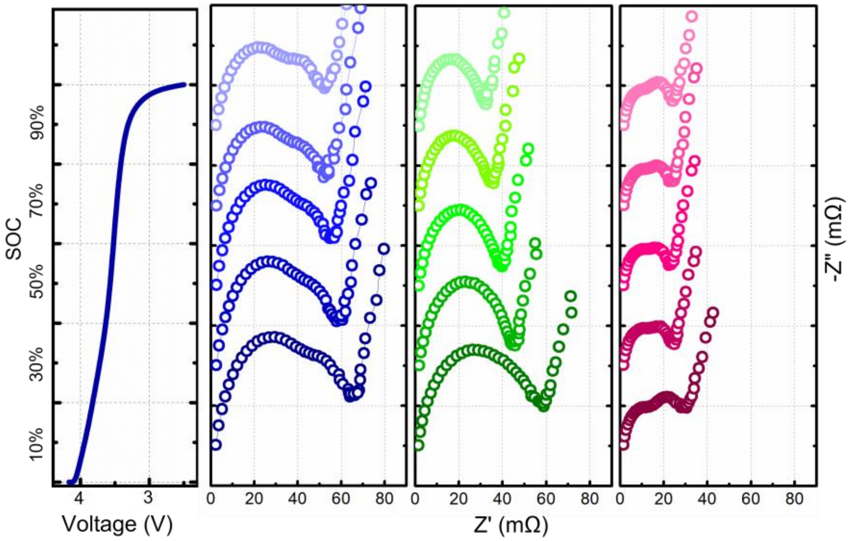

Figure 4-3 The electrochemical impedance (EIS) for the battery aged after 1000 cycles CC, 100 Hz, and 2000 Hz pulse charging current, from left to right. Source: [J5].

EIS has been proven to be an effective method for analyzing and quantifying the polarization phenomena occurring within batteries. This is since the electrochemical processes, represented by semicircles, display overlapping patterns in the Nyquist plots. Such overlap enables a comprehensive understanding of the impedance behavior of the battery, as depicted in Figure 4-4 (a)[87]. After subjecting the batteries to 1000 cycles, the values of R_{sei} and R_{ct} for both the CC and pulsed current aged batteries were determined and depicted in Figure 4-4 (b). Across all the curves, the R_{sei} and R_{ct} values exhibit a decreasing trend as the SOC increases. This trend indicates a strong correlation between the battery impedance and its SOC. Notably, the battery aged with a 2000 Hz pulsed current demonstrates higher sensitivity to SOC, along with lower R_{sei} and R_{ct} impedances compared to the CC charging case. This can be attributed to the significant capacity degradation observed during aging in the CC charging case. Consequently, the discharge process becomes limited to a narrower capacity and voltage range, resulting in higher impedance and a reduced range of impedance variations. The distribution of relaxation times (DRT) analysis is utilized to separate the intertwined electrochemical processes in the EIS data at different state-of-charge (SOC) levels. In the design of the equivalent circuit algorithm for DRT calculations, the time constant (τ) values between 10^{-2} and 10^{-1} represent the charge transfer process, while the crossing of Li-ions through the solid electrolyte interface (SEI) occurs between $10^{-3.5}$ and 10^{-2}.

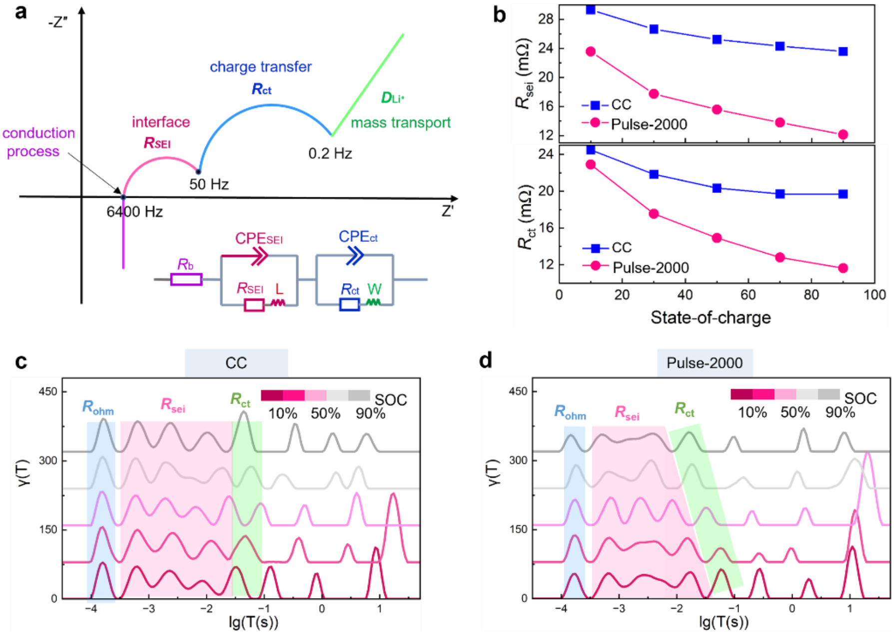

Figure 4-4 The EIS analysis was conducted on the batteries after undergoing 1000 aging cycles. (a) illustrates the impedance mechanism along with the equivalent circuit diagram, (b) presents the fitted results of R_{sei} (electrolyte resistance) and R_{ct} (charge transfer resistance) at various state-of-charge (SOC) levels, specifically 10%, 30%, 50%, 70%, and 90%, (c) displays the DRT profiles for the CC-aged sample, while (d) shows the DRT profiles for the pulse-2000-aged sample. Source: [J5].

The DRT analysis reveals that the battery aged using CC exhibits a higher impedance compared to the battery aged using the 2000 Hz pulsed charging. Particularly, the impedance attributed to the SEI, which is the limiting factor for the CC aged battery, is significantly reduced in the case of the 2000 Hz pulsed charging aged battery.

Additionally, the 2000 Hz pulsed charging aged battery demonstrate a decreasing trend in the T(s) from 10^{-1} s to 10^{-2} s as the SOC increases from 10% to 90%. Conversely, the T(s) values of the CC aged battery are less influenced by SOC. This indicates that the SEI film of the 2000 Hz pulsed charging aged battery possesses a lower impedance and a relatively stable electrochemical process.

Based on preliminary electrochemical diagnosis, these findings were attributed to the effective mitigation of SEI impedance and charge transfer impedance achieved by pulse charging. Additionally, pulse charging helps alleviate the loss of positive and negative electrode materials, which ultimately results in an extended lifespan for the battery.

4.3 Mechanisms at Electrodes Level

4.3.1. Graphite Anode

The impact of pulsed current on the aging of the graphite electrode was assessed through synchrotron radiation XRD analysis for fresh and aged graphite negative electrodes. The analysis revealed that the positions of the graphite peaks, including the (003) peaks, remained unchanged after battery aging, as depicted in Figure 4-5 (a). This indicates that the layer spacing of graphite remains consistent throughout the aging process. However, as the battery ages, the half-peak width of the (003) peak significantly increases, indicating pulverization of graphite particles and the collapse of the graphite structure, as shown in Fig 4-5 (b). In the case of the aged graphite electrode, as the frequency of the pulse current increases, the half-peak width gradually decreases. This suggests that the use of pulse current with appropriate relaxation time helps reduce the loss the graphite electrode.

The collapse and cracks of graphite particles have a profound effect on the deformation of the entire graphite electrode, resulting in swelling of the aged electrodes compared to the fresh ones[14]. However, the volume expansion of graphite after aging with pulsed current charging is significantly mitigated compared to the aging with constant current, as illustrated in Figure 4-5 (c). The negative electrode thickness increase rate decreases from 35% to 15% when subjected to a 2000Hz pulse, compared to CC.

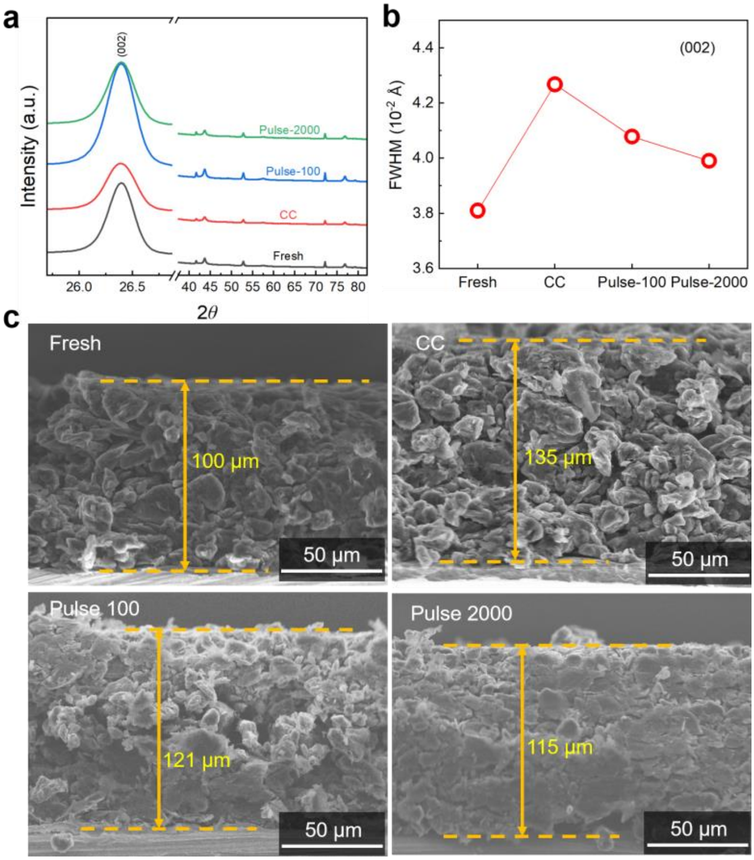

Figure 4-5 (a) synchrotron Ex-XRD for fresh and aged graphite anode; (b) half-peak width for fresh and aged graphite; FE-SEM cross-section for (c) constane current aged graphite negative and (d) pulse current aged graphite negative. Source: [J5].

To investigate the differentiation between pulsed current charging and CC charging processes in relation to the graphite structure, in-situ Raman spectroscopy was employed. This technique enabled us to directly observe and analyze real-time changes in the graphite structure throughout both charging protocols. Graphite commonly undergoes phase transitions, resulting in various interlayer states such as LiC_{48}, LiC_{24}, LiC_{18}, LiC_{12}, and LiC_6[51], [88]. The arrangement of Li-ions within graphite naturally seeks a lower energy state, maximizing the interaction between the embedded Li-ions and the graphite material[89]. Consequently, the arrangement of Li-ions in graphite is typically determined by the lowest energy state to ensure structural stability. In-situ Raman spectroscopy allows for the detection of slight structural changes during graphite lithiation, covering the voltage range from 1.0 V to 0.003 V. In Figure 4-6 (a), the Raman spectrum of graphite during constant current lithiation reveals four distinct stages of structural features. In stage I, graphite in the

C to LiC_{48} state is characterized by a single intense G band in the Raman curve. Transitioning to stage II, the intensity of the single G band peak decreases, and it transforms into a doublet band, indicating the conversion from LiC_{48} to LiC_{24} then to LiC_{18} compounds. Moving to stage III, the intensity of the doublet peak continues to decrease, with one of the doublet peaks becoming weaker during the LiC_{18} to LiC_{12} transition. In stage IV, the doublet band strengthens once again during the transition from LiC_{12} to LiC_6. This observation aligns with previous reports indicating that the doublet band in the Raman spectrum of graphite is associated with the uneven distribution of Li-ions within the graphite material during the intercalation process[90]. However, the application of pulsed current can alleviate this uneven distribution.

The in-situ Raman spectrum of graphite during pulsed current lithiation, as shown in Figure 4-6 (b), exhibits notable differences compared to constant current lithiation. Notably, there are no significant variations observed in stages I and II between pulse current lithiation and constant current lithiation. However, during stage III of graphite lithiation, the doublet peak undergoes a steady decrease in intensity, and one of the two peaks (left) disappears. By stage IV, only low-intensity single peaks are visible. These changes imply that the distribution of Li-ions in graphite becomes more even during lithiation, particularly in the stage where the Li-ions are deeply embedded. The application of pulsed current facilitates the recovery of graphite-embedded lithium towards a stable, low-energy state.

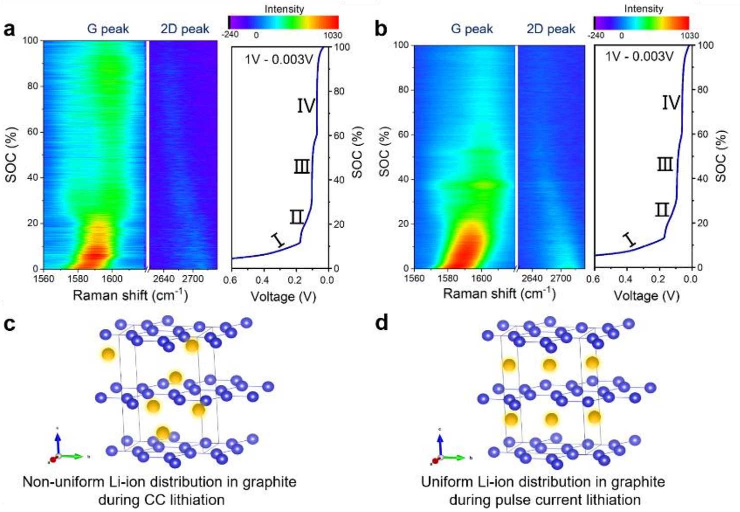

Figure 4-6 In situ Raman spectrun of graphite in (a) constant current and (b) 250 Hz pulse current lithiation processes, and the structure of lithiated graphite under (c) constant current and (d) 250 Hz pulse current. Source: [J5].

Graphite negative electrode thickness variations were monitored during the lithiation and delithiation processes using operando electrochemical dilatometry. As depicted in Figure 4-7, the graphite negative electrode displays substantial fluctuations in thickness during the CC cycling, indicating its instability process. In contrast, during pulsed current charging, the thickness variation notably diminishes. This discrepancy underscores the distinct lithium insertion behavior of graphite in these two scenarios. Under pulse current charging, lithium integration within the graphite becomes more uniform, resulting in reduced volume fluctuations and mitigated mechanical stress that might otherwise lead to graphite fracture, which is consistent with the in-situ Raman and SEM results.

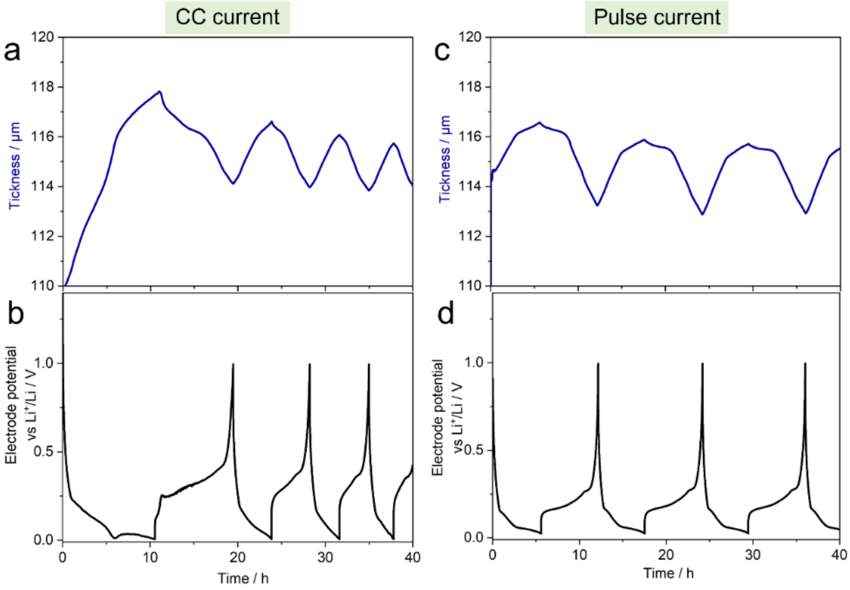

Figure 4-7 *Operando* dilatometry was employed to measure the increment of negative electrode thickness in constant current charging (a) and in pulse current charging (c); and the corresponded electrode potential were shown in (b) and (d), respectively. Source: [J5].

In summary, pulse charging plays a crucial role in controlling the structural changes of the graphite anode during the lithiation process, promoting more uniform Li-ions insertion. The application of pulsed current with appropriate relaxation time effectively mitigates the fragmentation and shrinkage of graphite particles. This effect is clearly observed in the significantly smaller volume change of the negative electrode after aging with pulsed current, compared to aging with constant current. Overall, pulsed charging demonstrates its potential in enhancing the stability and longevity of the graphite electrode for Li-ions batteries.

4.3.2. NMC Cathode

Ex situ synchrotron XRD and ex situ X-ray absorption near-edge structure (XANES) analyses were performed to examine the fresh and aged NMC532 cathodes, aiming to understand the degradation of the NMC cathode. The ex situ synchrotron XRD data offered detailed structural insights. In Figure 4-8a, the leftward shift of the (003) peak in the CC-aged electrode indicates an expansion of the crystal volume or layer spacing within NMC materials[91]. Additionally, the (018)/(110) double split peak's lower intensity under CC charging, compared to pulsed current charging, suggests decreased crystallinity[92]. In Figure 4-8b, the higher energy state of the Ni K-edge XANES spectrum after aging indicates partial nickel reduction in the aged electrodes. This reduction results in a significant contraction of the Ni-O bond length (*R*-distance) in the aged positive electrode, as shown in Figure 4-8c. The contraction is due to the smaller atomic radius of high-valent Ni (Ni^{3+} and Ni^{4+}) compared to Ni^{2+}[93], leading to a shortened *R*-distance. Furthermore, the peak intensity of the *R*-distance positively correlates with the coordination number[94], [95]. After aging, Ni exhibits a higher coordination number with oxygen atoms, particularly in electrodes aged under CC charging, showing a higher coordination number than those aged under pulse current charging. Consequently, pulse current charging during aging leads to fewer high-valent nickel oxides compared to CC charging, with these oxides potentially involving deteriorated lithium vacancies[96]. These findings emphasize the benefits of pulsed current charging in preserving the crystallinity and layered structure of NMC cathode materials.

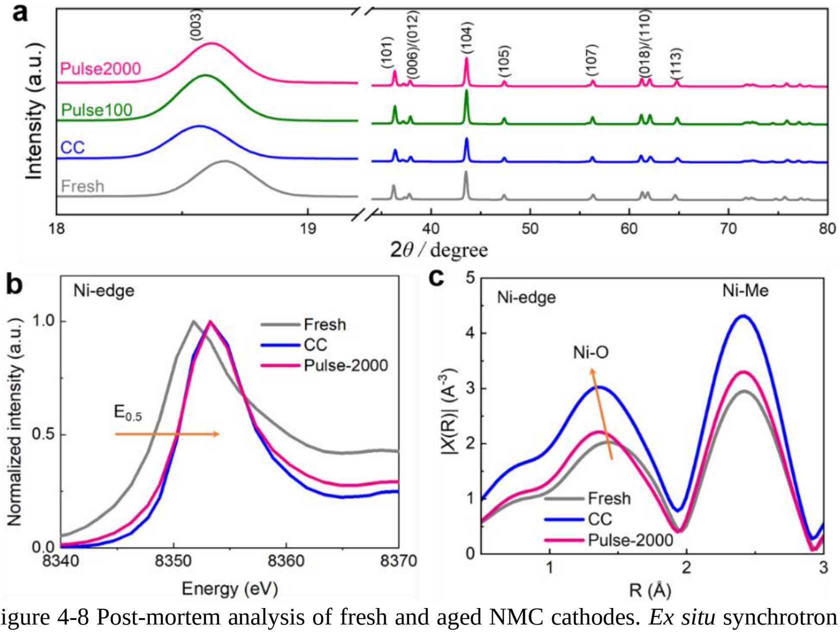

Figure 4-8 Post-mortem analysis of fresh and aged NMC cathodes. *Ex situ* synchrotron XRD results (a), and Ni K-edge *ex situ* XANES (b), *R* distance (c). Source: [J5].

The XRD findings reveal that the degradation of cathode materials primarily involves an expansion of cathode crystal volume and a reduction in the crystallinity of NMC cathode materials. Furthermore, XAS analysis highlights the strong connection between these deteriorations and the formation of a Li vacancy phase characterized by high-valence Ni-O bonding.

Operando X-ray absorption spectroscopy (XAS) has been employed to investigate the local chemical environment surrounding Ni atoms and the charge compensation mechanisms of NMC 532 electrode material. In Figure 4-9 (a), the Ni K-edge XANES (X-ray Absorption Near-Edge Structure) reveals a rightward shift during the initial charging of the battery, followed by a leftward shift to a lower energy position during discharging. This shift is associated with charge compensation achieved through the redox process between Ni^{2+} and Ni^{4+} ions.

Comparing the pulsed current cases with the CC case, the shift of the Ni edge in the pulsed current cases is more pronounced. This indicates that the energy state and valence state of the Ni element undergo more significant changes under pulsed current conditions. The quantified results, as shown in Figure 4-9 (b), demonstrate that under pulsed current charging, the Ni element tends to achieve a higher energy state and valence compared to the CC case.

In addition to Ni K-edge XANES, EXAFS (Extended X-ray Absorption Fine Structure) analysis was employed to investigate the correlation between the charge state and changes in the intensity of the Ni-O and Ni-transition metal (Ni-TM) bands Figure 4-9 (c). During the charging process, the intensity of the Ni-O peak exhibited a continuous increase, indicating an increase in oxygen coordination as the Ni valence state increased during NMC delithiation. Conversely, the intensity of the Ni-TM peak showed a decreasing trend, suggesting a decrease in coordination with the transition metals. Moreover, in the subsequent charging and discharging processes, the peak intensities of Ni-O and Ni-TM exhibited greater changes in the pulsed current case compared to the CC case. This observation aligns with the energy changes observed in the Ni edge, indicating a more pronounced degree of coordination number change in NCM materials under pulse current charging. Consequently, the Ni valence state tends to reach a higher level in pulse charging, as evidenced by the greater coordination number changes between Ni and transition metals.

Alongside these structural observations, the material structure undergoes a gradual deterioration. For the analysis of aged negative electrodes and a fresh positive electrode from 18650 full batteries, synchrotron XRD was utilized in the post-mortem examination. Figure 4-9 (d) illustrates the leftward shift of the (003) peak in the CC aged electrode, indicating an expansion of the layer spacing in NMC materials. Furthermore, the (018)/(110) double split peak in the CC case noticeably weakens, suggesting a reduction in crystallinity. These observations highlight the benefits of pulse charging in preserving the high crystallinity and inherent layered structure of NMC materials.

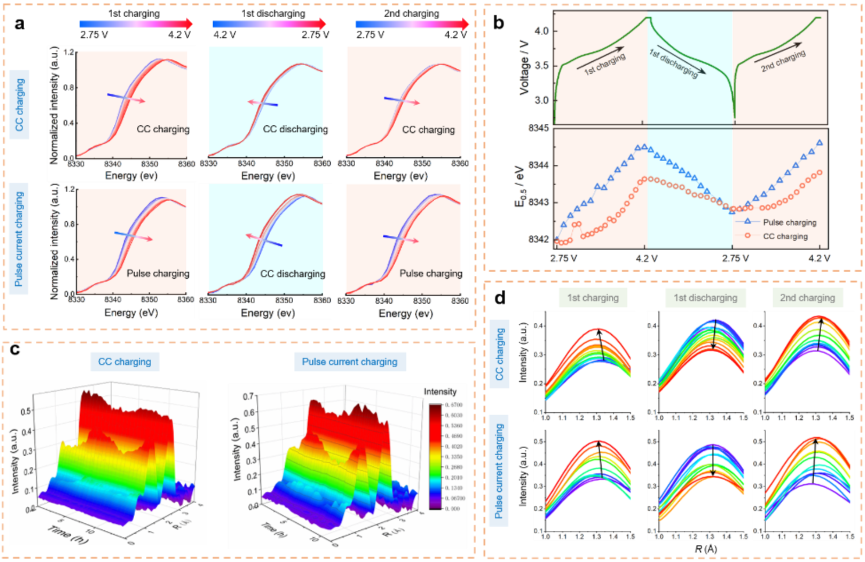

Figure 4-9 Operando synchrotron X-ray Absorption Spectroscopy (XAS) were employed to reveal oxidation states and local atomic structure around Ni atoms during both constant current charging and pulse charging protocols. (a) the energy of Ni-edge evolves under the battery charging with constant current and pulse current; (b) Operdando test voltage profile and the corresponded half-peak energy ($E_{0.5}$) position; (c) the *R* distance under the constant current and pulse current charging; (d) Synchrotron XRD results of fresh, and aged cathode. Source: [J5].

In summary, the degradation of NMC532 cathode material is intimately linked to structural changes within its crystal lattice. These alterations disrupt the layered structure of NMC materials. As depicted in Figure 4-10, pulse charging serves to mitigate this process. Moreover, operando XAS analysis unravel the valence state, energy, and coordination of Ni atoms within NMC under CC and pulse current charging conditions. Pulse charging promotes the advancement of the Ni element's valence state, while also reducing the fluctuation in bond length between Ni and O during battery charging. The relatively modest alterations in structure and Ni-O bond length induced by pulse current charging can account for the overall improvement in electrode structural stability.

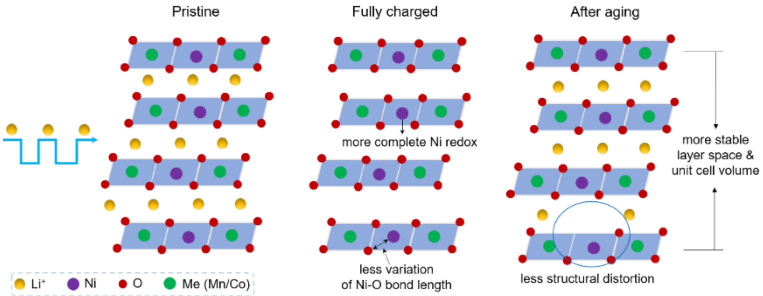

Figure 4-10 the mechanisms for NMC cathode changed under pulsed current charging. Source: [J5].

4.3.3. Interface Degradation

Pulsed current, as demonstrated in the electrochemical analysis, effectively reduces the increase in interfacial impedance by influencing the thickness, composition, and structure of the SEI. Figure 4-11 (a) displays the Raman spectra of all negative electrodes, exhibiting insignificant graphite D, G, D', and G' peaks. Heterogeneous peaks in the $1800 - 2500$ cm^{-1} range, originating from $Li_xP_yF_z$ compounds[97], are also observed. The weak D and G peaks can be attributed to graphite surfaces covered by the SEI. Comparing it to the CC aged battery, the 2000 Hz pulsed charging aged battery displays sharper graphite peaks, suggesting a higher light transmission through the SEI film. This indicates that the SEI film on the 2000 Hz pulsed charging aged battery may be thinner and/or composed of different materials compared to the CC aged battery. Subsequently, the top surface of the graphite electrode was scraped off using a flat blade, and clear Raman spectra were obtained for both the CC and 2000 Hz pulsed charging aged battery, as depicted in Figure 4-11b. Notably, the $Li_xP_yF_z$ peaks representing the SEI film disappear, confirming the presence of a film that covers the original graphite particle surface and affects the reflection of the 532 nm laser.

Observing the morphology of the SEI film presents a challenge due to its thin adherence to the graphite particle surface. To overcome this, cross sections of graphite particles were cut for SEI observation. In Figure 4-11 (c1), the CC case displays ruptured interfacial films distributed among the graphite particles. These film ruptures are caused by mechanical stresses arising from lithium ion diffusion during charging and discharging. Generally, the graphite particles under CC aging are surrounded by unstable surface films. The magnified edges in Figure 4-11 (c2) reveal non-uniformly distributed passivation film with a thickness of $100 - 200$ nm. In contrast, the garphite under 2000 Hz pulsed charging aged battery exhibits no visible membranes between graphite particles, as shown in Figure 4-11 (d1). This is attributed to the stability and thinness of the SEI film. The magnified edge area in Figure 4-11 (d2) shows a thin and tightly adhering film on the graphite surface. Notably, the passivation film's rupture at the interface of pulse-charged aged graphite during charging, discharging, and sample cutting is insignificant, while the resulting SEI film is thin. This suggests that pulse charging hinders SEI film growth and thickening, ensuring the stability of the produced passivation film.

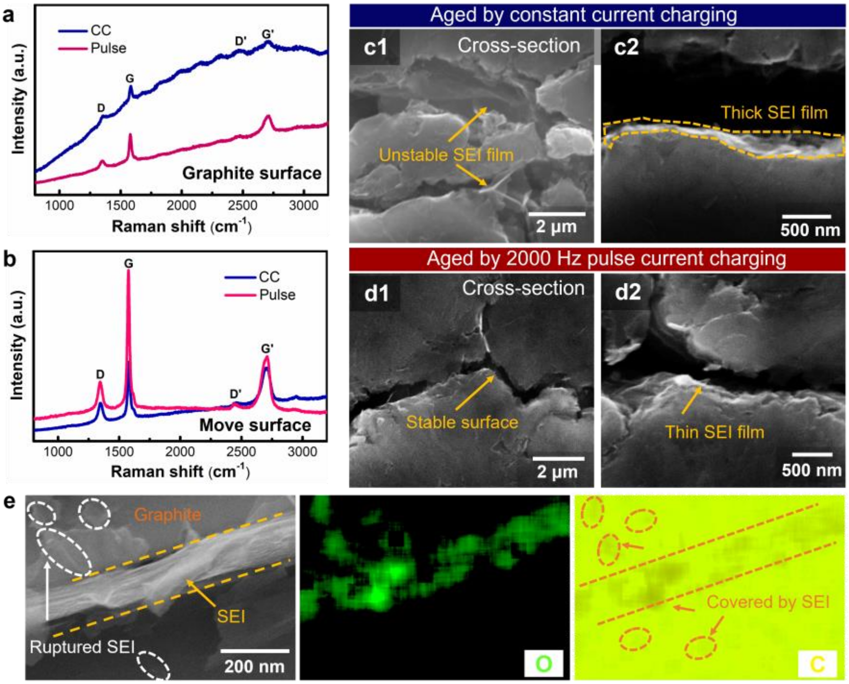

Figure 4-11 Raman spectrums with 532 nm laser were performed for (a) CC and 2000 Hz aged negative electrodes surface, and (b) hanging off the top surface for the CC and 2000 Hz aged negative electrodes; FE-SEM images for the aged negative electrode by CC charging for (c1) cross-section, and (c2) enlarged edge; FE-SEM images of pulse-2000 Hz aging graphite for (d1) cross-section, and (d2) enlarged edge. FE-SEM for enalrged graphite edge in constant currrent aging, and the EDS maping of O and C. Source: [J5].

Further analysis was conducted on the SEI film region shown in Figure 4-11 (c2) using EDS mapping analysis for O and C elements, as illustrated in Figure 4-11 (e). Unevenly thick SEI films are distributed around the graphite edges, with exfoliated nanoflakes present. The SEI film region corresponds to the distribution of O elements and appears as blurred spots in the C element mapping. This confirms that the observed interfacial film is indeed the SEI film. Some exfoliated nanosheets also appear in the O element mapping, while in the C element mapping, they are represented by missing dots, indicating that these regions represent ruptured SEI film. In contrast, the larger nanosheets correspond to graphite and are distributed along the outer edge of the graphite particles, sometimes even wrapped in the SEI film. These isolated graphites, separated by the passivation film, not only lead to active material loss but also contribute to an increase in the SEI film's thickness.

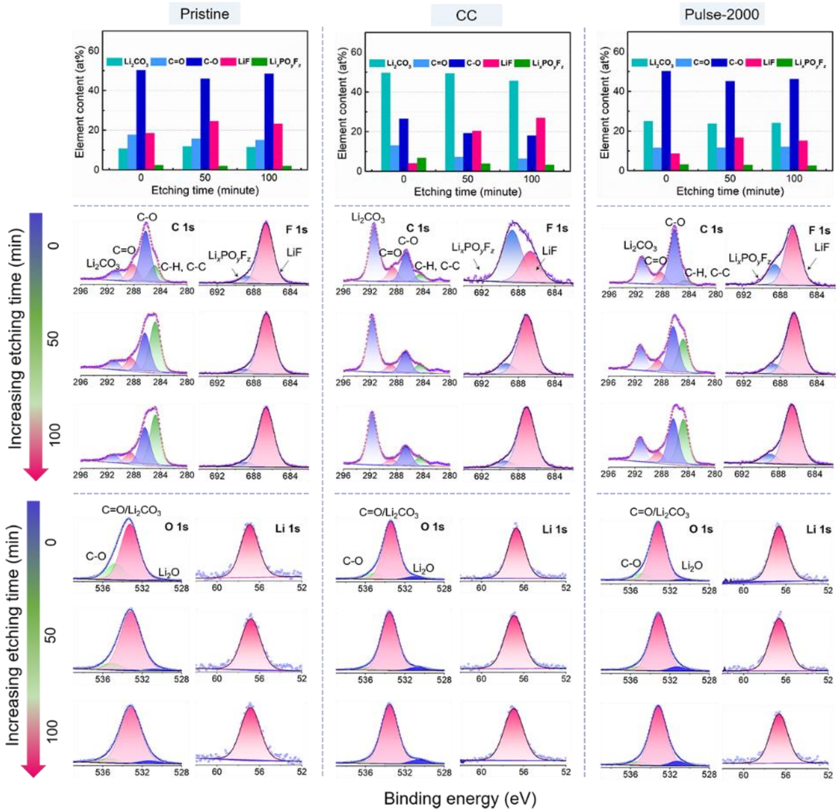

Figure 4-12 The SEI chemical composition obtained by quantitative the etch-XPS characterization result for (a) fresh negative electrode, and for aged negative electrodes with (b) 1000 cycles of constant current aging, and (c) with 1000 cycles of 2000 Hz pulse current aging; (d) the etch-XPS spectrums for C 1s, F 1s, O 1s, and Li 1s for the battery electrodes with different etch time. Source: [J5].

To investigate the formation of SEI films, etch-XPS was performed on fresh, CC aged, and 2000 Hz pulsed current aged graphite electrodes with different etch times (0, 50 min, and 100 min). The quantified results for F 1s, O 1s, C 1s, and Li 1s compounds are illustrated in Figure 4-12. The SEI film primarily consists of Li_2CO_3, C=O ($R\text{-}CH_2OCO_2Li$ and $-(CH_2CH\text{-}(OC(O)CF_3))n\text{-}$), C-O ($R\text{-}CH_2OLi$ and $\text{-}(CH_2CH_2O)n\text{-}$), LiF, and $Li_xPO_yF_z$[98]. Comparing the SEI film on the fresh negative electrode surface, the negative electrode of the CC aged battery exhibits a higher percentage of Li_2CO_3 at each etch depth. Li_2CO_3 is formed as a reaction product of semicarbonates with HF, water, or CO_2[99], while LiF, as a salt reduction product, originates from the reaction of HF with semicarbonates [100]. During aging, inorganic components such as Li_2CO_3 and LiF accumulate and increase on the graphite surface. Generally, SEI films on graphite surfaces are highly brittle due to their high inorganic salt content. This leads to a continuous rupture and reformation of the SEI film as the graphite volume shrinks during cycling aging. The debris from SEI rupture accumulates on the graphite surface, resulting in a loosely thickened SEI film.

However, the surface of the negative electrode of the 2000 Hz pulsed charging battery has fewer inorganic salts compared to both the fresh and CC aged negative electrodes. This is attributed to the ordered Li^+ insertion reaction during pulsed charging, which reduces electrolyte production and generates fewer by-products during SEI film re-formation. Consequently, a low content of inorganic salts implies a higher content of organic salts. The C-O compound content is significantly higher on the graphite of 2000 Hz pulsed charging aged battery surface than on the fresh and CC charging aged negative electrode surfaces. This increased C-O content enhances the flexibility of the SEI film, reducing its susceptibility to fracture during graphite volume expansion. As a result, the negative electrode interface aged by Pulse-2000 has a thinner SEI film.
Furthermore, the negative electrode interface of the 2000 Hz pulsed current aging battery demonstrates minimal variations in the ratio of different components as the etching depth increases from approximately 0 minutes to around 100 minutes. This indicates that the thin SEI film formed under pulsed charging is more uniform. The pulsed charging helps inhibit the increase in SEI impedance at the battery negative interface, and the mechanisms is depicted in Figure 4-13.

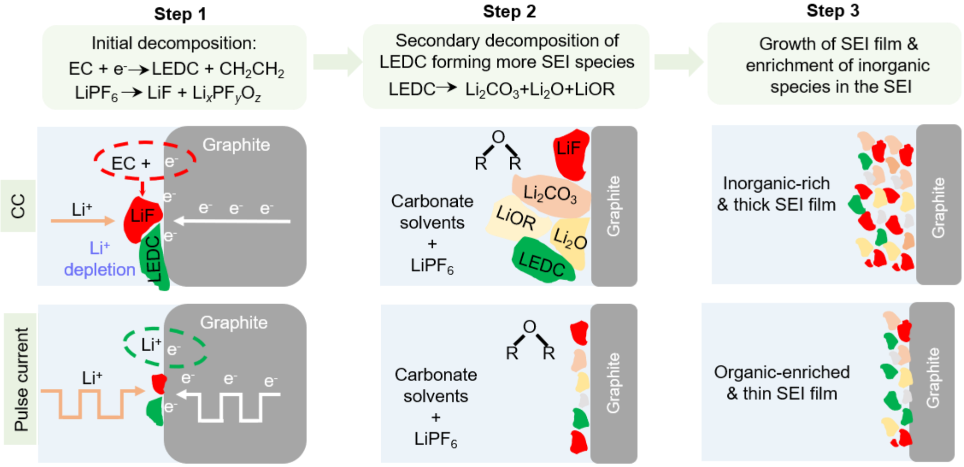

Figure 4-13 The mechanisms for SEI evolution under constant current charging and pulse current charging. Source: [J5].

The implementation of pulsed charging, particularly at a frequency of 2000 Hz, significantly extends the lifespan of the battery. After undergoing 1000 cycles, the battery exhibits a 41% increase in capacity retention rate compared to the constant current charging method. The underlying mechanisms are summarized in Figure 4-14.

Pulsed charging has been proven effective in reducing the impedance of the SEI film. This charging method helps suppress the formation of SEI film components and restricts the thickening process. One possible reason is that under pulsed current charging, the concentration gradient of Li-ions in the electrolyte weakens, thereby reducing the enrichment of solvent anions on the graphite surface. As a result, fewer side reactions occur between solvents and electrons, leading to the production of fewer SEI film components. Furthermore, the relaxation time associated with pulsed current promotes a more uniform distribution of Li-ions within the graphite material. This uniform distribution helps mitigate the mechanical damage and particle breakage of graphite particles. Similarly, the relaxation provided by the pulsed current enhances the changes in energy state and coordination number of the Ni atoms during battery charging. Consequently, the NMC cathode material maintains a favorable layer spacing and degree of crystallization under the conditions of pulse current charging.

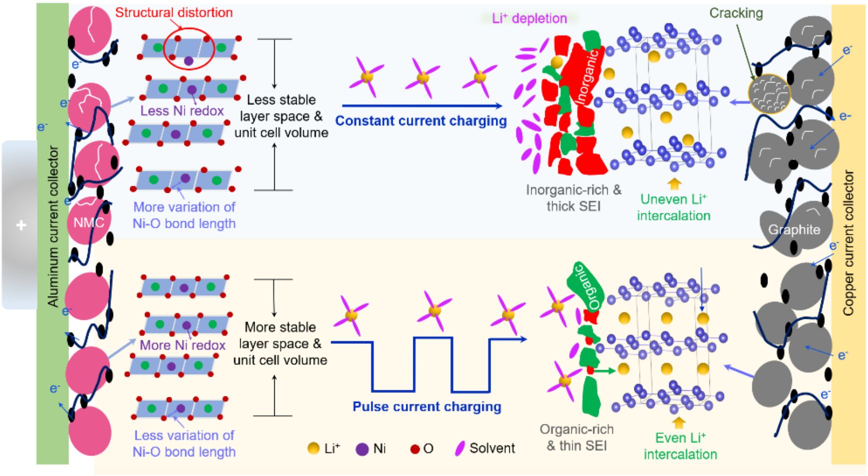

Figure 4-14 Pulse charging for commercial NMC/graphite batteries operates through several primary mechanisms to optimize their performance. Source: [J5].

Pulsed current charging protocols have the potential to extend battery life in various Li-ion battery applications. Those findings suggest that high-frequency square-wave current pulses at frequencies such as 100 Hz and 2000 Hz can be directly implemented for charging commercial batteries. However, optimizing the charging process may require considering additional factors. Firstly, it is important to investigate whether increasing the frequency beyond 2000 Hz can further enhance battery life. This requires evaluating the relationship between the diffusion rate of Li-ions and the duration of pulse current. Secondly, when optimizing the pulse current charging protocol for commercial batteries, it is crucial to address the impact of changing the duty cycle on the concentration gradient of the electrolyte and the stability of the electrode material. In-depth in situ testing, computational simulations, and extensive experimental verification are needed to fully understand these effects. Furthermore, evaluating the existing infrastructure and support for high-frequency pulse charging is essential. This ensures that the necessary equipment and facilities are available for implementing these charging protocols on a larger scale.

Moreover, the mechanisms and performance improvements observed in pulse current charging protocols can be applicable to other types of batteries, including $LiMn_2O$/graphite, $LiCoO_2$/graphite, $LiFePO_4$/graphite, and other NMC/graphite batteries. These batteries face similar challenges related to SEI film formation and graphite anode degradation. By gaining a comprehensive understanding of the structural changes and internal reactions occurring under different charging protocols, researchers and engineers can develop more promising and effective charging strategies. This deeper understanding will enable the optimization of charging protocols and the design of battery systems with improved performance, longevity, and safety.

4.4 Summary

By utilizing electrochemical methods for preliminary battery health diagnosis, it was observed that pulsed current charging effectively mitigates the increase in interfacial film impedance and prevents the loss of positive and negative electrode materials. In-situ synchrotron XAS results revealed significant improvements in the energy state and coordination number of Ni atoms during pulsed current charging, in contrast to constant current charging. This enhanced Ni redox activity contributes to the structural stability of the NMC cathode material. Furthermore, compared to constant current charging, pulsed current charging led to smaller changes in layer spacing and crystallization degree.

In-situ Raman tests demonstrated that Li-ions exhibit a more uniform intercalation pattern within graphite during pulsed current charging compared to constant current charging. Consequently, the pulverization of graphite particles, which occurs under constant current charging after 1000 cycles, was significantly reduced. As a result, there was a reduction in the loss of graphite from the negative electrode and a decrease in interfacial film resistance. Moreover, pulsed charging effectively suppressed the formation and thickening of the SEI film on the graphite surface, leading to a lower presence of inorganic components.

Overall, the utilization of pulsed current charging demonstrates significant advantages in maintaining the stability of electrode materials and interfaces. These findings provide valuable insights for the design of commercial batteries and the development of charging protocols.

Chapter 5. Aging Mechanisms for Battery in Real Life Driving

In this chapter, the battery aging mechanisms using realistic EV driving scenarios was studied, based on the WLTP standardized driving cycle. The influence of temperature and depth of discharge on the battery aging were assessed. High temperature (45 °C) accelerates the battery degradation due to the sever side reactions. Besides, low temperature (5 °C) also shortens the battery's lifetime to only 600-700 cycles due to the Li-ions deposition on the graphite side. Furthermore, battery degradation is also influenced by the DOD. When the battery is cycled at 45% DOD, the electrolyte decomposes and forms a surface film, which leads to a high battery impedance as well as a low discharge capacity. In contrast, when the battery is cycled at a large DOD (e.g., 100%), the degradation is faster compared with 75% DOD, which is due to more materials loss in a larger DOD. The related scientific outcome is listed as follows:

J1. **J. Guo**, Y. Li, K. Pedersen, and D. I. Stroe, "Lithium-ions battery operation, degradation, and aging mechanism in electric vehicles: An overview," *Energies*, vol. 14, no. 17. pp. 1–22, 2021

J2 **J. Guo**, Y. Li, J. Meng, K. Pedersen, L. Gurevich, and D. I. Stroe, "Understanding the mechanism of capacity increase during early cycling of commercial NMC/graphite Lithium-ions batteries," *Journal of Energy Chemistry*, vol. 74, pp. 34–44, 2022

5.1 Introduction

Battery degradation inventible occurs for electronic vehicle in real-life driving. Unlike in laboratory tests, the battery discharging in real life is influenced by work conditions (e.g., road conditions, driver habits, and climates). So, the battery degradation patterns will also differ from the ones during constant current cycling. Clarify the battery degradation mechanisms are crucial for accurate battery health management and lifetime prediction.

Battery degradation also is influenced by depth of discharge, temperature, and current. Usually, the battery degradation in laboratory testing is more and more severe with the increase of the DOD, which is due to more electrode materials' loss in larger DOD ranges. Besides, the temperature also affects the battery lifespan. In high temperatures, the side reactions are more active. In low temperature, the Li-ions will deposit on the graphite side resulting in a low battery capacity. More detailed information can be seen from the [J1][8].

Here, the in-situ test, electrochemical analysis, and post-mortem analysis will be employed to study the aging mechanisms for batteries in real-life driving.

5.2 Aging of the Full Cell

Initially, a battery was subjected to aging at 25 °C and 100% DOD. After undergoing 500 cycles, its SOH remained impressively high at 99.8%, as shown in Figure 5-1. This took close to 5 months. Therefore, to minimize aging time, the forthcoming battery aging experiments will be at temperatures of 35 °C and 45 °C.

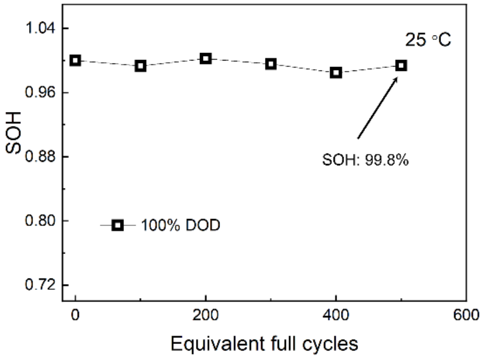

Figure 5-1 the SOH for a battery aging at 25 °C and 100% DOD.

5.2.1 Influence of Depth of Discharge

To explore the effects of DOD on battery aging, various discharge depths were examined, including 100% DOD, 75% DOD, and 45% DOD, under both 35 °C and 45 °C conditions, respectively. As depicted in Figure 5-2 (a, b), in contrast to the findings in the existing literatures, it is evident that the rate of battery aging decelerates with larger DOD[101], [102]. The battery cycling at a 45% DOD exhibits a more rapidly decline in capacity compared with 75% DOD and 100% DOD cases in both of 35 °C and 45 °C conditions. Under the aging condition of 35 °C, the battery subjected to a 75% DOD fully maintains its initial capacity even after 900 EFCs, as shown in Figure 5-2 (a). In contrast, the batteries aged under 45% DOD and 100% DOD conditions exhibit a gradual decline in battery capacity. Particularly, after 1300 cycles of aging, the battery aged under the 45% DOD condition experiences a significant capacity degradation; it decreases from 88% SOH to below 70% SOH, over only 200 EFCs, from 1300 EFCs to 1500 EFCs.

In 45 °C case, the battery SOH shows a similar trend with the 35 °C aging condition, as shown in Figure 5-2 (b). When the battery undergoes aging at 45% DOD, it exhibits the most rapid capacity drop, reaching only 40% SOH after 900 EFCs, which is even quicker than the aging condition at 35 °C. Furthermore, the battery aging under the relatively stable 75% DOD condition also shows a gradual decline in battery SOH, but it maintains over 90% SOH even after 1900 EFCs.

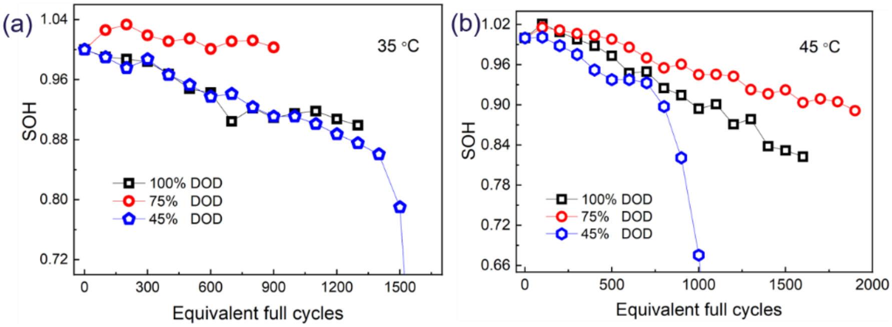

Figure 5-2 Battery aged by various depth of discharge (DOD), including 100% DOD, 75% DOD, and 45% DOD, at both of 35 °C (a) and 45 °C conditions (b).

5.2.2 Influence of Temperature

To study the influence of environment temperature on the battery degradation, the batteries were subjected to the aging condition with100% DOD and 75% DOD at different temperatures (35 °C, and 45 °C for 45% DOD; 5 °C, 35 °C, and 45 °C for 75% DOD), respectively. In Figure 5-3 (a), the batteries aging with 45% DOD are at 35 °C and 45 °C, respectively. At 45 °C, the battery SOH drops significantly faster than at 35 °C. High temperatures will aggravate the aging of the battery. At 100% DOD, the battery aging is most pronounced at 5 °C, as it experiences a significant degradation in capacity, as shown in Figure 5-3 (b); after only 700 EFCs, the battery's capacity reaches 91% of its initial value. At 45 °C, the battery shows an impressive ability to remain at 89% of its initial capacity even after undergoing 1900 EFCs. Similarly, at 35 °C, the battery demonstrates its ability to maintain its initial capacity even after 1000 EFCs.

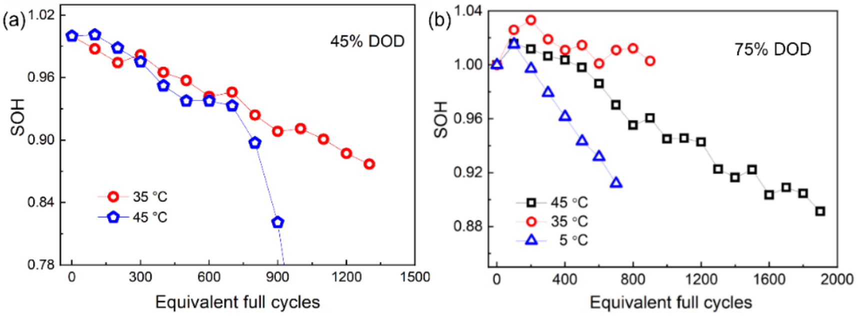

Figure 5-3 The SOH curve of the battery under the aging conditions of 45% DOD at 35 °C and 45°C (a), and 75% DOD at 5 °C, 35 °C and 45 °C (b), respectively.

In summary, the battery's SOH stability is higher under the 75% DOD aging condition compared to both the 100% DOD and 45% DOD conditions. It is worth noting that both high temperature (45 °C) and low temperature (5 °C) can accelerate the battery aging more, compared with 35 °C.

5.3 Mechanisms of Battery Aging

5.3.1 Electrochemical Analysis

At 35 °C, the charging and discharging curves of the battery under 100% DOD, 75% DOD, and 45% DOD are illustrated in Figure 5-4 (a-c). As the battery ages, the charging curve plateau exhibits an upward trend, while the discharging curve shows a downward trend. These trends are related to the increased impedance that occurs during battery aging. It is worth noting that during the 900th cycle at 100% DOD in the RPT, a notable separation is observed between the charge and discharge curves, indicating a significant increase in impedance. Surprisingly, despite this higher impedance, the charge and discharge capacity of the battery are relatively less affected. This impedance can be attributed to lose of connection, which causes changes in voltage plateaus. Therefore, the impedance from the external circuit has little effect on the battery capacity.

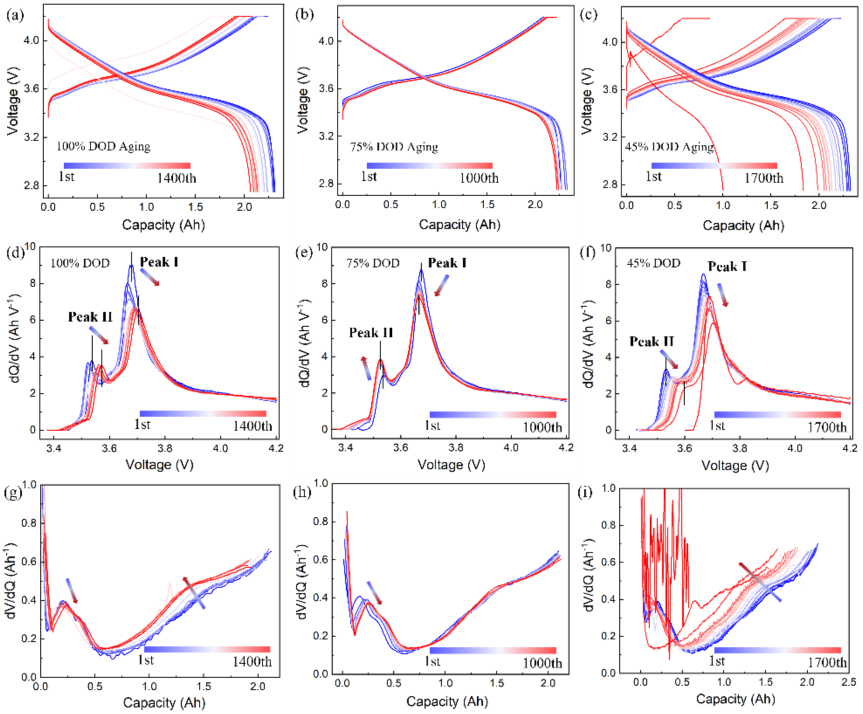

Figure 5-4 The charge-discharge curves from the battery reference performance test (RPT) after each 100EFCs in 35 °C aging condition (a-c); the incremental capacity analysis (ICA) is displayed in (d-f), and the differential voltage curve (DV) curves are illustrated in (g-i).

The incremental capacity analysis (ICA) curves corresponding to the battery charge curves are shown in Figure 5-4 (d-f). The right shift of peak II means that the internal polarization resistance of the battery increases, especially in the case of 100% DOD and 45% DOD. Notably, in the case of 75% DOD, the peak II shifts to the left. This shift is associated with the battery capacity increasing in the initial stage, which will be discussed in more detail later. The decreased I peak represents the loss of active materials from both the positive electrode and the negative electrode. In addition, the DV curve is employed to analyze the distribution of voltage changes in relation to battery capacity, shown in Figure 5-4 (g-i). All DV curves show a trend of shifting to the upper left, where shifting to the left implies loss of active lithium and shifting upward implies loss of active material. At 45% DOD, the left shift of the DV curve is most obvious, meaning the most severe lithium loss.

EIS plays a crucial role in further elucidating the aging process occurring within the battery. Figure 5-5 (a-c) illustrates the impedance spectra of the battery obtained under 100% DOD, 75% DOD, and 45% DOD cycle conditions. The fitted results for the SEI and charge transfer resistance are shown in Figure 5-3e and Figure 5-3f, respectively. Under a 45% DOD cycling condition, the battery exhibited a notable rise in interfacial film resistance, which is related to the side reactions inside battery[103]. Upon being subjected to 100% DOD cycling conditions, the battery demonstrated a pronounced charge transfer resistance, typically associated with material structural changes[104]. On the contrary, at 75% DOD, the battery displayed smaller interfacial film resistance and charge transfer resistance.

Furthermore, the frequency of some points (e.g., f_1, f_2, and f_3) associated with the speed of chemical reaction was chosen on the impedance spectrum to serve as indicators of the battery's aging condition (Figure 5-5 (d)). Point f_1 on the impedance spectrum corresponds to the electron conduction process (R_{ohm}) occurring within the battery, along with a portion of the Li-ionscrossing the SEI film process (R_{sei}). The frequency f_2 is influenced by the interaction between Li-ionsand the SEI film, as well as the partial charge transfer process. The frequency f_3 represents the point at which Li-ionsinitiate diffusion in the solid phase, and its limiting factor is primarily attributed to the charge transfer process. There is minimal variation observed in f_1, indicating that the electronic conductivity and the passage of Li-ionsthrough the SEI film in the initial stage of the battery occur at higher frequencies (greater than 200 Hz) without significant changes for all three cases. As the battery ages, the frequency corresponding to the f_2 point experiences a significant decrease, especially for the 45% DOD and 100% DOD cases. This means that in battery aging, as the resistance of the SEI film increases, it takes longer for Li-ionsto pass through the SEI film. Furthermore, as the battery ages, the frequency associated with the charge transfer process decreases. This effect is particularly pronounced in the case of 100% DOD, where the reduction in frequency is most noticeable. This frequency shift indicates a slowdown in the kinetics of the charge transfer reactions within the battery, which can be attributed to the electrode degradation.

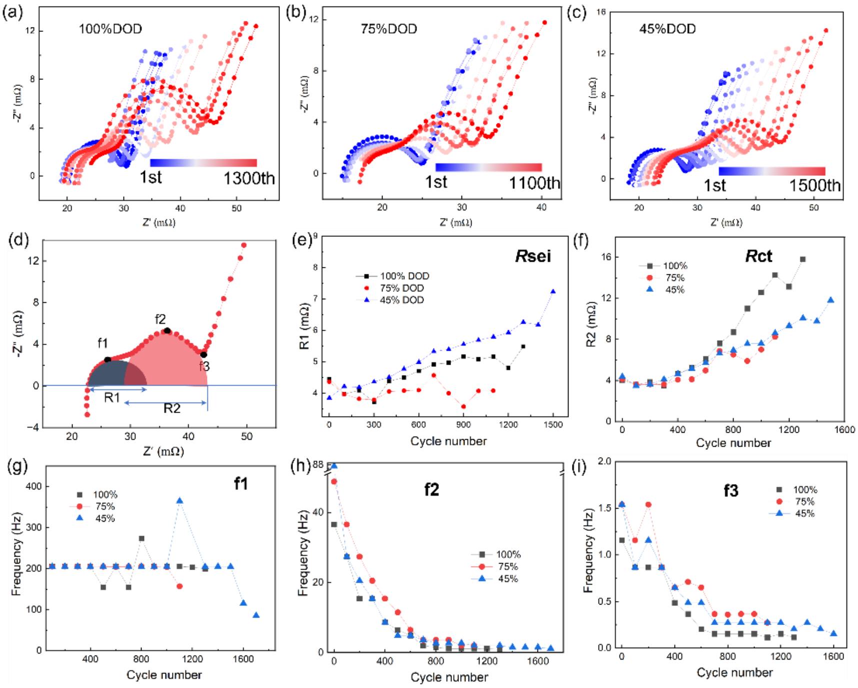

Figure 5-5 The electrochemical impedance spectroscopy of battery in 35 °C aging condition with 100%, 75%, and 45% depth of discharge. The battery EIS results were tested at 90% SOC in the 25 °C oven.

At 45 °C, the aging behavior of the battery under the influence of DODs is similar to what is observed at 35°C. Battery aging at 100% DOD and 45% DOD shows a more quickly drop in capacity. The battery charging-discharging curves are shown in Figure 5-6 (a-c). The battery aging is most obvious under 45% DOD, where the voltage decays more rapidly. This faster voltage decay indicates a significant increase in the battery's internal impedance [105]. Additionally, at 45% DOD, the IC curve exhibits a more pronounced rightward shift, indicating a more significant battery polarization. This polarization effect is also evident in Figure 5-6 (i), where the DV curve demonstrates a noticeable leftward shift.

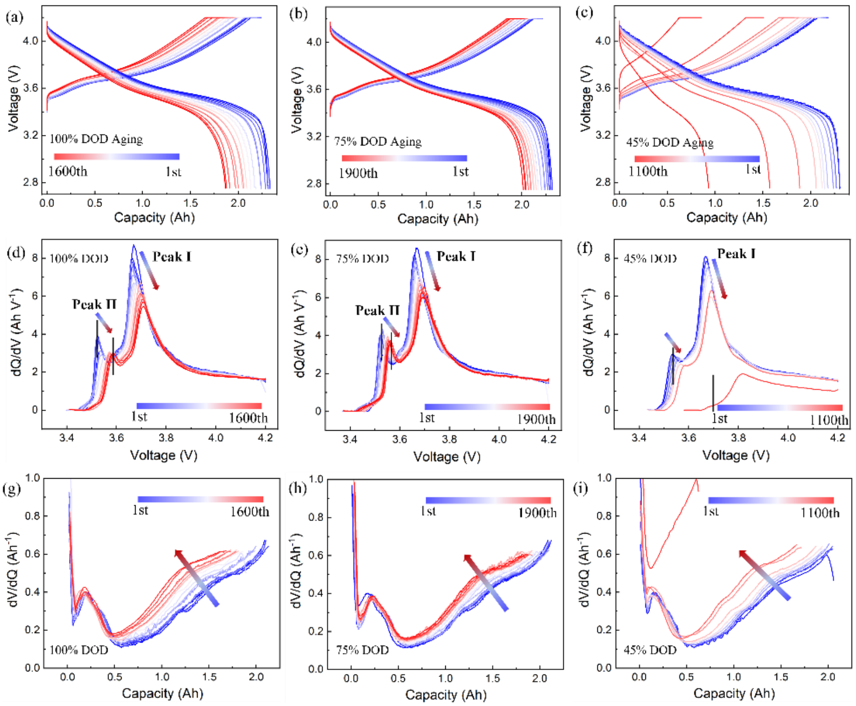

Figure 5-6 The charge-discharge curves from the battery reference performance test (RPT) after each 100EFCs in 45 °C aging condition (a-c); the incremental capacity analysis (ICA) is displayed in (d-f), and the differential voltage curve (DV) curves are illustrated in (g-i).

The corresponding EIS results are shown in Figure 5-7. The battery subjected to aging with 45% DOD exhibits a higher interface film impedance than other conditions. This higher impedance suggests that the aging process at 45% DOD produces a more significant interfacial film and side reactions. In contrast, battery aging at 100% DOD showed a more pronounced increase in the charge transfer impedance, which can be related to the degradation of electrode materials.

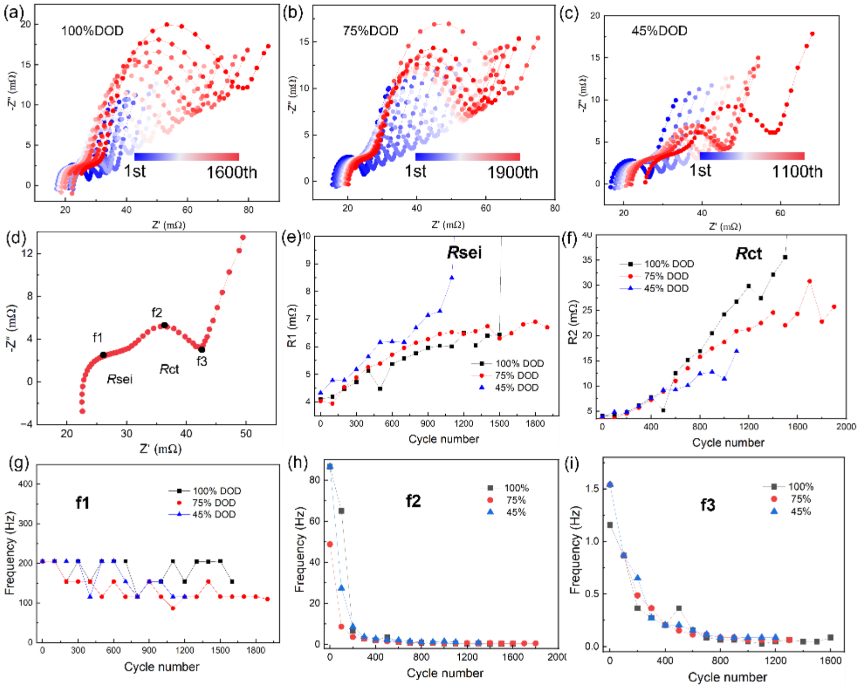

Figure 5-7 The electrochemical impedance spectroscopy of battery in 45 °C aging condition with 100%, 75%, and 45% depth of discharge. The battery EIS results were tested at 90% SOC in the 25 °C oven.

In conclusion, the battery aged at 75% DOD is more stable in SOH performance than the cases of 100% DOD and 45% DOD. At 100% DOD aging, the increased charge transfer impedance that is related to active materials loss is more obvious. In contrast, the increasing of the interfacial film resistance associated with the surface film is especially evident at 45%DOD.

5.3.1.2 Influence of the temperature

To study why the battery degradation is more serious at 45 °C and 5 °C than at 35°C, the battery charging-discharging curves and IC-DV curves are shown in Figure 5-8. From the charging-discharging curves presented in Figure 5-8 (a-c), one can notice that the battery capacity drops more quickly at 45 °C and 5 °C, than at 35°C. Besides, the II peaks of the IC curves shifted to varying direction, as shown in Figure 5-8 (d-f). At 45 °C and 5 °C, the II peak of the IC curve shift to the right, implying an increase in battery polarization. At 35 °C, the II peak shift to the left, representing a highly active reaction inside the battery. Furthermore, after only 700 cycles, the battery in the 5 °C aging condition shows an obvious decrease in I peak intensity, which means the loss of active materials. Furthermore, the DV curves of 45 °C and 5 °C cases show a left shift, representing the loss of Li-ions, as shown in Figure 5-8 (g-i).

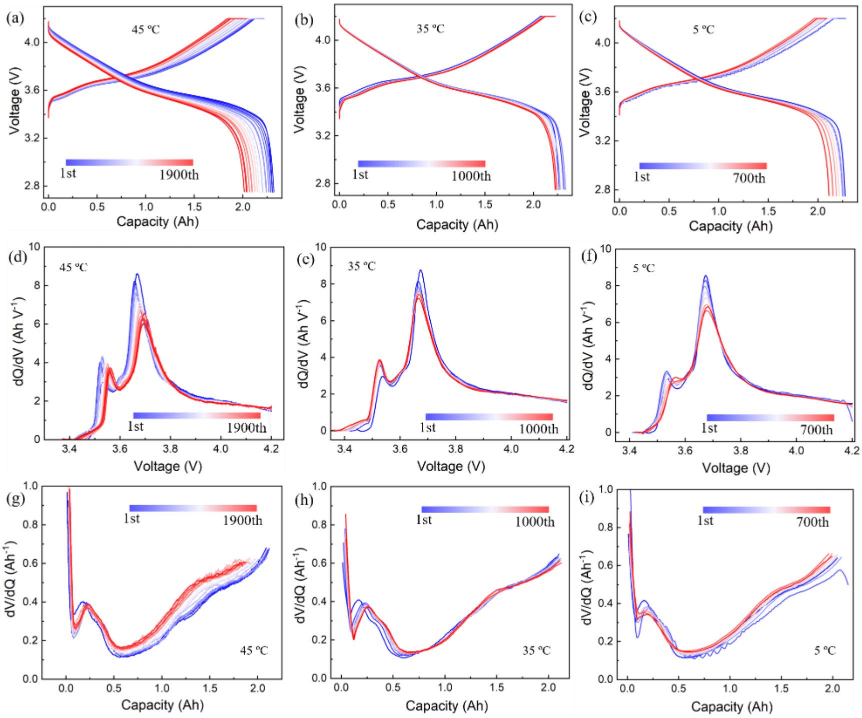

Figure 5-8 The charge-discharge curves from the battery reference performance test (RPT) after each 100EFCs in 75% DOD aging condition with 45 °C, 35 °C, and 5 °C (a-c); the incremental capacity analysis (ICA) is displayed in (d-f), and the differential voltage (DV) curves are illustrated in (g-i).

In the RPT test, the coulombic efficiency of the battery is related to the battery aging temperature. After aging at 5 °C, the battery shows a low coulombic efficiency, as shown in Figure 5-9 (a). With temperature increasing, the coulombic efficiency also shows an increasing trend. This observation indicates that in low-temperature environments aging, Li-ion activity is diminished, and Li-ions are more susceptible to loss during cycling. From the EIS results Figure 5-9 (b-d), the battery aging at higher temperature show more increased impedance.

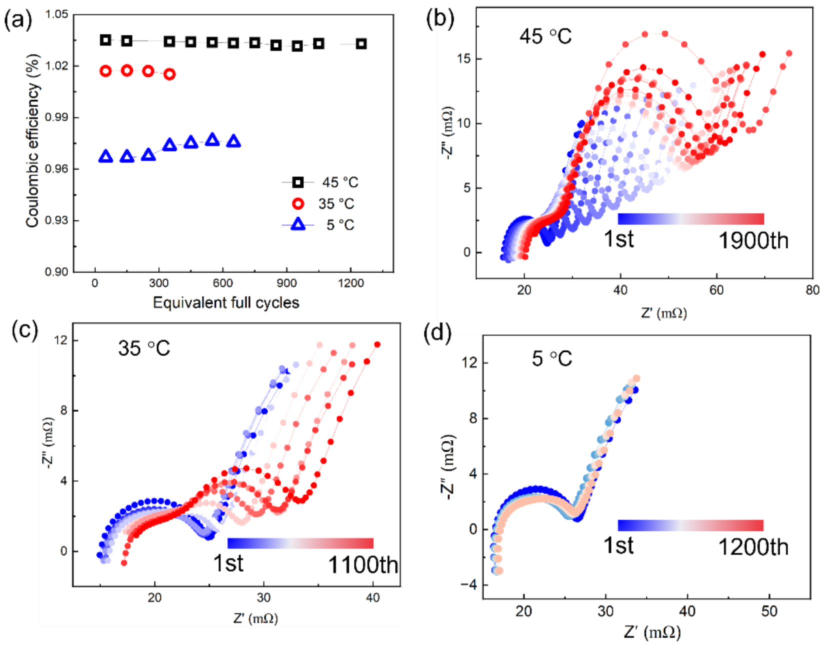

Figure 5-9 (a) coulombic efficiency comes from RPT test for battery with a 1 C charge/discharge process; the EIS of the battery is tested at 75% DOD aging condition with 45 °C, 35 °C, and 5 °C. The battery EIS results were tested at 90% SOC in the 25 °C oven.

5.3.2 Post-mortem Analysis

5.3.2.1 Structure Analysis

To further study the battery aging at electrodes and materials levels, the batteries were disassembled, after ageing to 80% SOH at five aging conditions (5 °C with 75% DOD, 35 °C with 100% DOD, 35 °C with 45% DOD, 45 °C with 75% DOD, and 45 °C with 100% DOD). The synchrotron radiation ex-situ XRD results from the fresh positive electrode, 35 °C with 100% DOD (35-100% DOD), 35 °C with 45% DOD (35-45% DOD), 45 °C with 75% DOD (45-75% DOD), and 45 °C with 100% DOD (45-100% DOD) are shown in Figure 5-10. After aging, the (003) peak left shifts, which means positive electrode materials obviously changed in crystal structure. Especially for the battery aged at 35-100% DOD and 45-100% DOD cases, it means larger DOD (100% DOD) accelerates the positive electrode degradation compared with 75% DOD and 45% DOD.

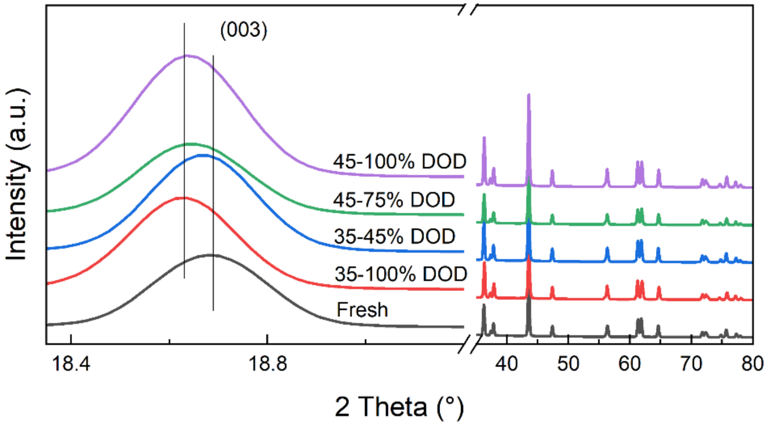

Figure 5-10 Synchrotron radiation ex-situ XRD was employed to analyze the structural characteristics of both the fresh positive electrode and those subjected to various aging conditions, specifically at 35 °C with 100% DOD, 35 °C with 45% DOD, 45 °C with 75% DOD, and 45 °C with 100% DOD.

At the same time, synchrotron radiation ex-situ XRD also was employed to measure the structure of negative electrode. the results are shown in Figure 5-11. The (002) peak is not shift after battery aging in all aging cases, which means the graphite layer space and graphite crystal structure is not changed in this aging condition. However, the half-peak width broadens as the battery ages, which means the graphite crystallization area decreases. This is related to the crushing of graphite particles. After battery aging, the graphite particles become more and more smaller, especially for battery aging at 35-100% DOD and 45-100% DOD cases, which further prove that graphite particles degradation more at 100% DOD.

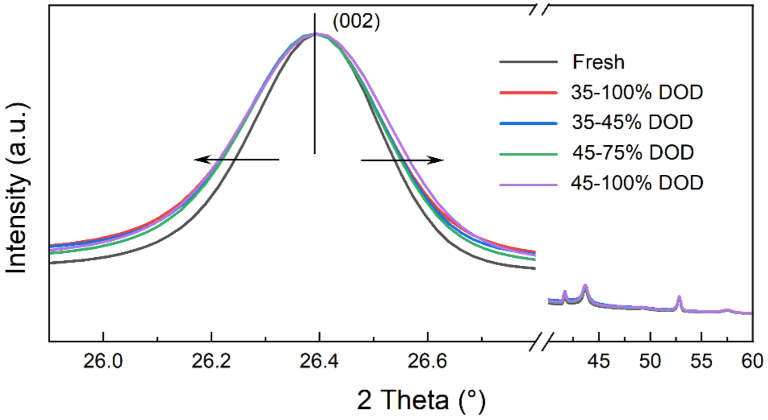

Figure 5-11 synchrotron radiation ex-situ XRD was employed to analyze the structural characteristics of both the fresh negative electrode and those subjected to various aging conditions, specifically at 35 °C with 100% DOD, 35 °C with 45% DOD, 45 °C with 75% DOD, and 45 °C with 100% DOD.

The synchrotron radiation *ex*-situ XRD results consistent well with the EIS analysis, that battery electrodes materials degradation more in 100% DOD, resulting in a higher R_{ct} as well as a serious SOH drop.

5.3.2.2 Morphology Analysis

The short circuit occurs for the battery aged at 5 °C and 75% DOD, only after 700 EFCs. The SEM images is shown in Figure 5-12. Lithium dendrites are very visible and puncture the separator causing a short circuit. The deposition of lithium occurs at low temperatures, which is the main reason for the low coulombic efficiency of batteries and serious capacity fading.

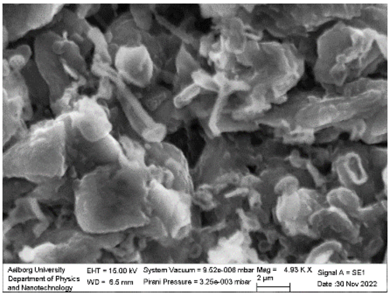

Figure 5-12 SEM image of negative electrode for battery aged at 5 °C and 75% DOD.

5.3.2.3 Interface Analysis

The XPS is employed to measure the chemical compositions for aged positive electrode, and aged negative electrode, as shown in Figure 5-13. For positive electrode aged at the higher DOD (35-45% DOD), more LiF appears on the positive electrode surface, which is the main component of the CEI film, as shown in Figure 5-13 (a). Besides, at negative electrode side, the Li_2CO_3 forms more for 45-75% DOD and 45-100% DOD cases. This demonstrates that the formation of interface films is more likely to take place within high DOD ranges (45% DOD) and under higher temperature conditions (45 °C). This is consistent with the EIS analysis results that R_{sei} increase more for higher DOD range and high temperature.

In conclusion, batteries tend to produce interface films at higher temperatures (e.g., 45 °C) and higher voltage ranges (e.g., 45% DOD), which increase the internal impedance of the battery and lead to SOH drop. In low temperature (e.g., 5 °C), the lithium plating occurs, which leads to lithium loss as well as a low coulomb efficiency. Then, lithium dendrite forms and lead to battery short circuit occurs. Furthermore, active materials from positive and negative are prone degradation more at larger DOD range (100% DOD), which can lead to active materials loss and R_{ct} increase.

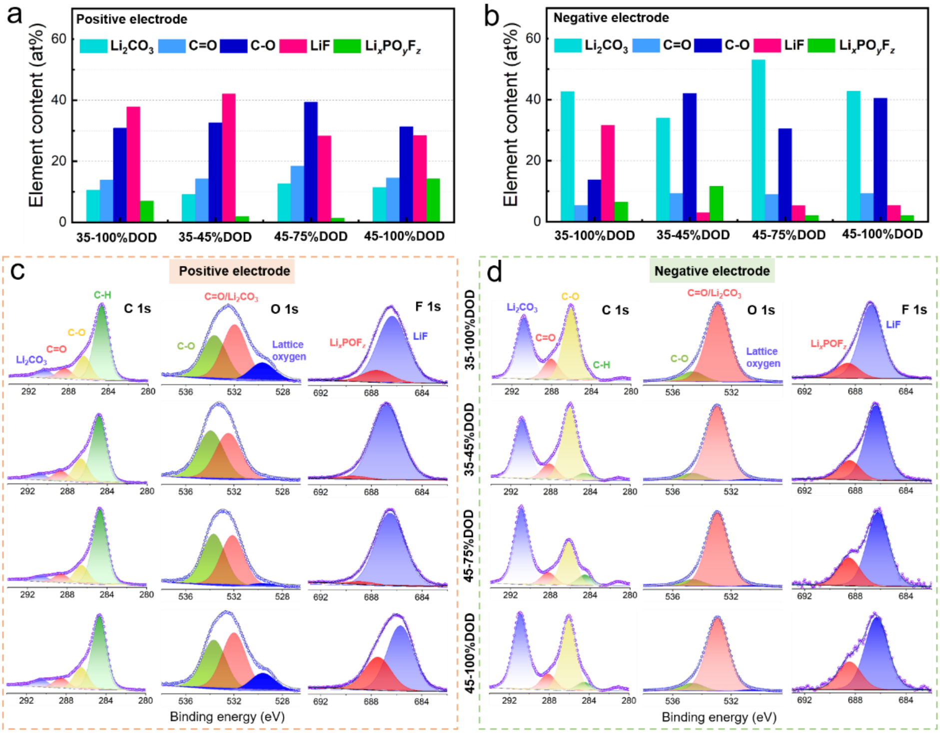

Figure 5-13 XPS results for positive electrode negative electrode after aging at various aging conditions, specifically at 35 °C with 100% DOD, 35 °C with 45% DOD, 45 °C with 75% DOD, and 45 °C with 100% DOD. A summary for positive electrode interface (a), and for negative electrode interface (b); the specific are shown in (c) and (d).

5.4 Mechanism for Capacity Increase During Early Cycling

5.4.1 Capacity Increase Behavior

As previously stated, caused by the combined effects of DOD and temperature, some batteries displayed an obvious capacity rise during the first 200–300 EFCs. The SOH evolution of the cells over the first 400 EFCs is shown in Figure 5-14. The capacity trend of cells cycled at 45% DOD and 100% DOD, at 35 °C, is shown in Figure 5-14 (a). In the first 100 EFCs of the aging test, the cells aged at 100% DOD showed a minor capacity increase, which was followed by an overall reduce in capacity. In the first 200 EFCs, cells aged at 45% DOD showed a decreasing capacity trend. The batteries aged at 45 °C show a similar initial capacity growth trend in Figure 5-14 (b). Compared to batteries aging at 75% DOD, batteries aged at 100% DOD showed a 1%

capacity increase in the first 200 EFCs, followed by a quicker capacity decrease. Regarding the temperature influence on batteries aged at 100% DOD, a more significant increase (i.e., 1%) was observed at 45 °C compared to the increase at 35 °C (i.e., 0.3%). More details can be seen from [J2].

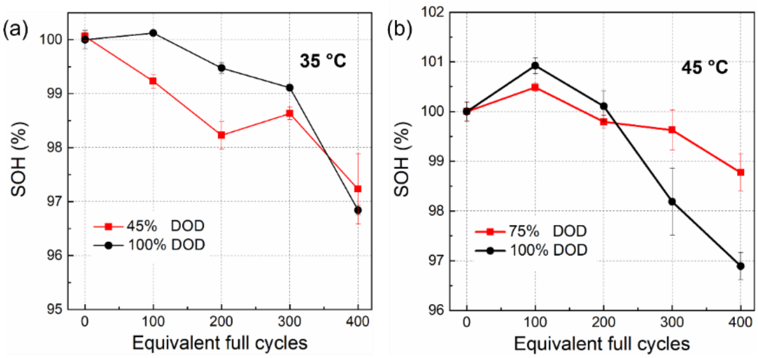

Figure 5-14 The batteries capacity fade during cycle aging under different conditions: (a) 45% DOD and 100% DOD at 35 °C, and (b) 75% DOD and 100% DOD at 45 °C. Source: [J2] [41].

5.4.2 Electrochemical Analysis

Using the DVA and ICA techniques, the electrochemical behavior of the 18650 full batteries was investigated. Figure 5-15 (a-d) display the IC curves for batteries aged at different scenarios. For convenience in descripting the 4 battery aging scenarios, unique names have been assigned to each scenario (Table 5-1) [J2][41].

Table 5-1 The test matrix for 18650 full cell aging[41]

	45% DOD	75% DOD	100% DOD
35 °C	Case 1	-	Case 2
45 °C	-	Case 3	Case 4

In every case, an increase in EFCs causes a drop in the main peak’s intensity at 3.7 V. This decline suggests a loss of active materials in either the positive or negative electrode. In case 1, there is a loss of intensity and a movement to the right for the peak at 3.53 V. Due to the decreased activity of graphite, the decreasing intensity reflects a lesser contribution of graphite capacity during this phase transition process. The rise in the internal resistance of the fully charged battery, which causes a smaller electrochemical window and decreased capacity, is thought to be the cause of the peaks shift toward the right.

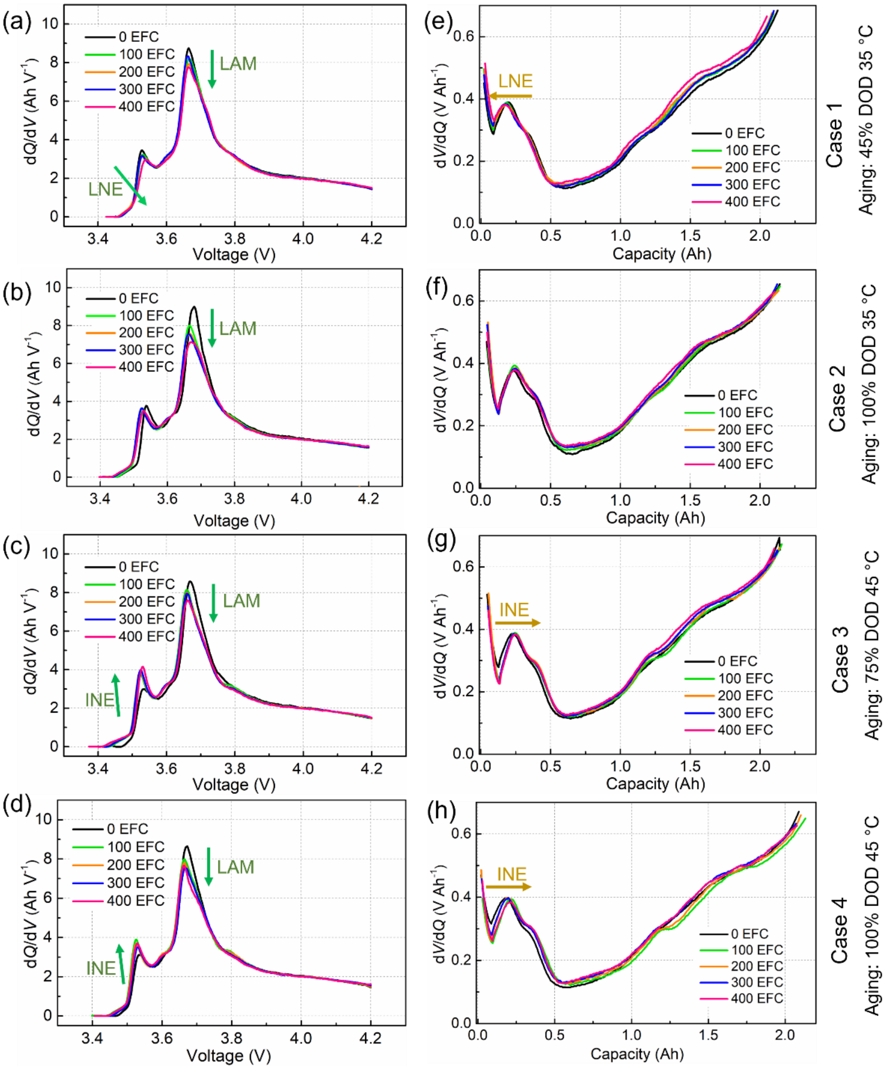

Figure 5-15 ICA and DV curves for battery aging at case 1 (a, e); case 2 (b, f); case 3 (c, g), and case 4 (d, h). Source: [J2] [41].

In Case 3, a decreasing trend is observed in the main peak of the IC curve, while there are no changes in the secondary peak of the IC curve and DV curve. This consistency indicates stable cycling performance. The strength of the peak at 3.53 V, increases in Case 3 and 4, indicating that the graphite anode has a greater capacity than is currently available. Finally, the expansion of the electrochemical window and an increase in the capacity in the whole cell are associated to the shift of the peak in Case 2 and Case 4 towards a lower voltage direction. The DV curves for the four situations under discussion are shown in Figure 5-15 (e-h). These curves clearly show the space between two successive phase transitions. In Case 1, the main peak in the DV curves shifts to the left as the cycling progresses, indicating that the graphite is unable to effectively accommodate the Li-ions. Surprisingly, in both case 3 and case 4, the main peak in the DV curves shifts towards the high-capacity direction during cycling. This shift signifies an extended graphite lithiation plateau and an increased availability of graphite in the anode. EIS result also confirms that battery impedance is reduced for those batteries, and the details are shown in [J2] [41].

5.4.3 Post-mortem for Coin Cell

Two groups of coin cells underwent cycling within voltage ranges of 0.001 – 0.2 V and 0.001 – 1.0 V, corresponding to 45% and 100% DOD in a full cell, respectively. After completing 25 EFCs (where 1 EFC equals 4 mAh), the two-coin cells were charged to a fully delithiated state at 1.5 V. Subsequently, the cells were disassembled to conduct post-mortem analysis. More details see [J2]. For the coin cell cycled between 0.001 and 0.2 V, the FESEM pictures of the cross-section and the EDS analysis of the carbon (C) and oxygen (O) elements are displayed in Figure 5-16 (a). On the copper current collector, the graphite particles, which range in size from 10 to 20 m, are evenly spaced out. The surface of the SEI layer and inorganic salt compounds are the main sources of oxygen in the system. This shows that the SEI coating is dispersed across the cycled electrode’s surface.

Figure 5-16 (b) displays intact graphite particles with smooth surfaces that are well bonded to the copper current collector. This smooth surface, referred to as the basal plane as described in [106], poses a challenge for Li-ions to traverse. The tight covalent bonds between internal carbon atoms make the basal plane chemically resistant, resulting in a low Li-ions diffusion coefficient. The concentration of Li-ions at the anode-electrolyte interface caused by the slow diffusion rate results in the development of “dead lithium” and lithium dendrites [107].

Figure 5-16 (c) illustrates the growth of small-sized lithium dendrites, as well as the presence of the SEI film, on the surface of the negative electrode. The formation of lithium dendrites and the SEI film are the main factors contributing to the loss of lithium inventory and the damage to the graphite, leading to a decrease in capacity. These findings explain the obvious capacity decline seen in the first cycles of full cells that have experienced a 45% DOD.

The FESEM picture of the electrode cross-section is shown in Figure 5-16 (d) for the coin cell that was cycled between 0.001 and 1.0 V. It reveals a soft texture resulting from layer separation within the graphite particles. On the surface of the graphite, the basal plane is no longer visible, and instead, clusters of graphite nanosheets are formed. The increase in graphite spacing inevitably reduces electronic conductivity, resulting in an elevated charge transfer resistance. This phenomenon can be attributed to the larger variation in the interlayer spacing of graphite during charge and discharge at a larger depth of discharge (DOD). Consequently, the graphite layers are exfoliated into nanosheets, as illustrated in Figure 5-16 (e), exposing a greater graphite surface area to the electrolyte, thereby facilitating Li-ions transport. As a result, graphite nanosheets expedite the lithiation and delithiation processes, enabling Li-ions to be inserted into graphite with lower ionic resistance. As a result, the battery's capacity increases, and the initial charge voltage decreases. These findings provide a clear explanation for the observed capacity increase in the early cycling stage of the battery [j2].

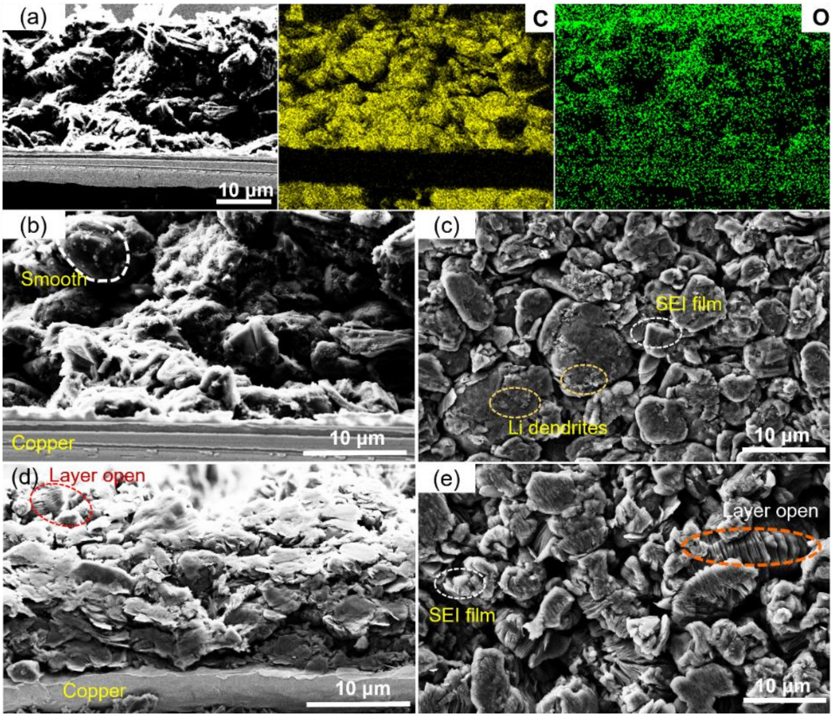

Figure 5-16 (a) The images show cross-sections and surface details, along with distribution maps obtained through EDS analysis; Images of a negative electrode that has undergone cycling in two different voltage ranges: 0.001 - 0.2 V (b-c) and 0.001 - 1.0 V (d-e). Source: [J2] [41].

In summary, it can be concluded that there is an increased capacity during the early aging stage, particularly for larger DOD values such as 100% DOD and 75% DOD. The initial capacity increase of 1% seen in one of the examples under 100% DOD cycling, and high temperature exacerbates this process. The evolution of *d*-spacing throughout cycling showed that it does not entirely recover when graphite is in the delithiated condition. This expanded d-spacing contributes to a low insertion resistance, leading to an increased battery capacity [J2].

5.5 Summary

The battery aging mechanisms in realistic EV driving scenarios were described in this chapter. Battery degradation is accelerated by high temperature (45 °C) or low temperature (5 °C), compared with 35 °C and 25 °C, because the side reactions are severe in high temperature, and the lithium plating and dendrite formation are severe at low temperature. Besides, the batteries degrades more when they are cycled in a higher DOD (45%) or a larger DOD (100%), compared with the middle DOD (75%). This behavior is caused by the electrolyte that decomposes easy at a higher voltage range, and by the active materials that are easy to damage in larger DOD cycling. Furthermore, the battery capacity increase during early cycling, which is related to the separates of the graphite layer in large DOD and high temperature work conditions.

Chapter 6. Conclusions and Future Work

In this chapter, the conclusions and contributions of this Ph.D. project are summarized, while topics for prospective and future work are also listed.

6.1 Summary

This Ph.D. thesis focus on unrevealing and studying the degradation mechanisms of commercial Li-ion batteries. First, the battery aging indictors are selected from electrochemical curves including IC-DV curves, EIS impedance spectra, and battery charging curves. Second, the battery degradation mechanisms during battery aging with constant current were identified by electrochemical diagnosis and post-mortem analysis. Then, the battery degradation during pulse current charging and realistic EV driving aging were studied by in-situ tests as well as electrochemical diagnosis, and post-mortem analysis.

In chapter 2, the battery parameters, aging conditions, and diagnosis methods were introduced; in this Ph.D. thesis, the diagnostics methods, which have been used were electrochemical methods, post-mortem analysis, and materials tests. The indictors in the IC-DV curves for selected battery were explored and selected; the shift of the secondary peak in the IC curves represents the increase of the battery polarization. The decrease of the main peak in the IC curves means the loss of positive and negative electrodes materials. Furthermore, some ex-situ and in-situ test were introduced to perform tests at material-level.

In chapter 3, the aging mechanisms of commercial $Li(Ni_{0.5}Co_{0.2}Mn_{0.3})O_2$/graphite batteries, which were aged under constant current cycling were investigated. After 1000 cycles, the battery capacity drops by 52% due to an increased internal impedance. Both the positive and negative electrodes show significant impedance increase, mainly at the interface with the electrolyte, due to EEI film formation. This leads to a faster voltage collapse and reduced capacity. A higher impedance also increases the heat generation, accelerating battery degradation. NCM particles' cracking, transition metal dissolution, and increased interfacial impedance degrade the positive and negative electrodes. Li-plating and SEI films contribute to a 16.8% loss of active Li-ions. These findings can guide the development of cycling protocols for enhanced stability.

In chapter 4, various techniques, including electrochemical analysis, post-mortem analysis, and in-situ testing, were employed to investigate the underlying mechanism responsible for the extended cycle life of batteries when continuously aged with pulsed current charging. Remarkably, utilizing a pulse current with a frequency of 2000 Hz was found to double the battery's original lifespan. By utilizing electrochemical methods for preliminary battery health diagnosis, it was observed that pulsed current charging effectively mitigates the increase of the interfacial film impedance and prevents the loss of positive and negative electrode materials. In-situ XAS results revealed significant improvements in the energy state and coordination number of Ni atoms during pulsed current charging, in contrast to constant current charging. This enhanced Ni redox activity contributes to the structural stability of the NMC cathode material. Furthermore, compared to the constant current charging, pulsed current charging led to smaller changes in the layer spacing and crystallization degree. Regarding the graphite, in-situ Raman tests demonstrated that Li-ions exhibit a more uniform intercalation pattern within graphite during pulsed current charging compared to constant current charging. Consequently, the pulverization of graphite particles, which occurs under constant current charging after 1000 cycles, was significantly reduced. This reduction in pulverization resulted in a thinner graphite negative electrode and slow-down the formation of the SEI film on the graphite surface. As a result, there was a reduction in the loss of graphite from the negative electrode and a decrease in interfacial film resistance. Moreover, etch-XPS analysis at different depths confirmed that pulsed charging effectively suppressed the formation and thickening of the SEI film on the graphite surface, leading to a lower presence of inorganic components. Overall, the utilization of pulsed current charging demonstrates significant advantages in maintaining the stability of electrode materials and interfaces. These findings provide valuable insights for the design of commercial batteries and the development of charging protocols.

In chapter 5, the battery aging in realistic EV driving scenarios was studied. Battery degradations are quicker in high temperature (45 °C) and/or low temperature (5 °C), compared with the medium temperature of 35 °C and 25 °C. This behavior is because the side reactions are accelerated in high temperature, and the lithium plating occurs easier at low temperature. Besides, it was found out that the batteries' degradation is more quickly at a high DOD (45%) or a full DOD range (100% DOD), compared with the battery aging at a medium DOD (75% DOD), which is because the electrolyte is easier to decompose at a higher voltage range, and the active materials are easier to damage in full cycling. Besides, the mechanism of battery capacity increase in the initial hundreds of cycle aging is attributed to the graphite negative electrode; the graphite shows an open layer state and accelerates the lithium diffusion process, resulting in an increased battery capacity.

6.2 Main Contributions

The main findings within this Ph.D. dissertation can be summarized as follows:

- Identification of the aging indicators in the electrochemical diagnostics methods (i.e., EIS impedance spectra and IC-DV curves) of electrochemical method for impedance test and battery health diagnosis

Electrochemical diagnostic indicators differ based on the battery chemistry and electrode materials. Through the assembly of both coin half-cells and coin full-cells, as well as a comparative analysis of electrochemical curves between them, a comprehensive understanding of the peaks in the IC-DV curves for the NMC532/Graphite battery was provided. This approach revealed which indictors (i.e., peaks or valley in the IC-DV curves) are valuable for the assessment of graphite anode degradation and cathode material deterioration.

- Unraveling the behavior and aging mechanisms during battery aging with constant current cycling

During constant current cycling, as the battery undergoes aging, its internal resistance progressively rises, resulting in an increased heat generation. Consequently, this increased heat production and voltage effects lead to the decomposition of electrolyte and to side reactions, which material loss within the battery. This combination of factors, leading to the growth of the interface film and the impedance increase, contributes to the battery capacity drop.

- Proposing a novel method for quantifying the lithium loss in the graphite anode

A novel method to quantify the Li-ions loss from the graphite anodes is proposed. This method is based on measuring the LiOH pH which, combined with the XPS analysis, can calculate the Li-ions loss in the graphite negative electrode of the whole battery. This method offers significantly higher accuracy compared to electrochemical analysis and is more straightforward to apply than gas chromatography.

- Clarification of the mechanisms which are responsible for the extension of the battery lifespan during pulsed current charging.

A combination of electrochemical testing, post-mortem analysis and in-situ testing was used to reveal the mechanisms behind the battery aging with pulsed current charging. Pulsed current effectively balance the Li-ions diffusion and electron conduction processes, inhibiting the decomposition of electrolyte and the formation of the SEI film. Furthermore, the intermittent relaxation periods offer significant benefits in maintaining the stability of the electrode material structure.

- Identification of the degradation mechanisms during realistic EV driving scenarios

During realistic EV driving scenarios, the battery capacity fade is more serious at higher DOD (i.e., 45% DOD) and/or elevated temperatures (i.e., 35 °C and 45 °C). In addition, when the temperature is as low as 5 °C, the battery is prone to short circuit due to dendrite growth. In a larger DOD, the voltage and temperature of battery are also high, which accelerate the battery degradation. At high temperature, the side reactions are accelerated, which is the main reason for the battery degradation.

6.3 Research Perspectives

This Ph.D. thesis has investigated the battery aging mechanisms during constant current cycling, pulsed current charging, and realistic EV driving cases. However, some work still needs to be performed based on the finding of this report. Some of them are summarized below:

- The quantification of materials loss and lithium loss still needs a more accurate approach

  The post-mortem analysis process inevitably causes damage to the electrodes and materials, and the quantification method is based on an idealized modes (degradation is evenly distribution), thus producing inevitable quantification errors. Therefore, some more accurate methods need to be proposed to quantify the loss of Li-ions and loss of active materials.

- The parameters for pulse current charging need to further optimal in future work.

  The mechanisms of pulsed current charging were unrevealed, with a specific focus on the role of frequency of the pulsed current, while the investigation of the duty cycle’s impact still needs to be studied. Additionally, the effectiveness of higher frequencies remains an open question, requiring further simulation for a comprehensive understanding.

- In realistic EV driving scenarios, the most suitable DOD and operation temperature for reducing the battery degradation still needs to be optimized.

  Various battery degradation mechanisms were investigated across different DOD levels and temperatures. Nevertheless, additional research is required to pinpoint the ideal DOD and operating temperature for optimal battery performance and lifetime.

- The electrochemical diagnostic methods need to simplify, especially for the case of the EIS impedance test

  DC impedance and EIS testing each possess distinct advantages, yet their limitations are evident. EIS can identify and examine specific electrochemical processes, but the test conditions are very strict. On the other hand, the DC impedance testing is rapid but lacks deep electrochemical insight. Those findings indicate that the underlying mechanisms of DC impedance testing and EIS testing are the same, which based on the specific electrochemical process, suggest the need for the development of a simplified electrochemical impedance testing method.

LITERATURE LIST

[1] European Parliament, “BRIEFING Towards climate neutrality: Fit for 55 package,” *Eur. Parliam.*, no. 6, p. PE 733.513, 2022.

[2] Ricardo energy & Environment, “Determining the environmental impacts of conventional and alternatively fuelled vehicles through LCA,” *Eur. Comm. DG Clim. Action*, p. 456, 2020.

[3] Y. Scientists, “Batteries of the Future A Perspective from Young Scientists in Europe Sustainable Batteries: Full circle, Full cycle BATTERY 2030PLUS CSA.”

[4] World Economic Forum; Global Battery Alliance, “A Vision for a Sustainable Battery Value Chain in 2030,” no. September, pp. 10–11, 2019.

[5] L. Albertsen, J. L. Richter, P. Peck, C. Dalhammar, and A. Plepys, “Circular business models for electric vehicle lithium-ion batteries: An analysis of current practices of vehicle manufacturers and policies in the EU,” *Resour. Conserv. Recycl.*, vol. 172, no. 443, p. 105658, 2021, doi: 10.1016/j.resconrec.2021.105658.

[6] M. A. Pellow, H. Ambrose, D. Mulvaney, R. Betita, and S. Shaw, “Research gaps in environmental life cycle assessments of lithium ion batteries for grid-scale stationary energy storage systems: End-of-life options and other issues,” *Sustain. Mater. Technol.*, vol. 23, no. X, p. e00120, 2020, doi: 10.1016/j.susmat.2019.e00120.

[7] N. El Ghossein, A. Sari, P. Venet, S. Genies, and P. Azaïs, “Post-Mortem Analysis of Lithium-Ion Capacitors after Accelerated Aging Tests,” *J. Energy Storage*, vol. 33, no. November 2020, p. 102039, 2021, doi: 10.1016/j.est.2020.102039.

[8] J. Guo, Y. Li, K. Pedersen, and D. I. Stroe, “Lithium-ion battery operation, degradation, and aging mechanism in electric vehicles: An overview,” *Energies*, vol. 14, no. 17. pp. 1–22, 2021, doi: 10.3390/en14175220.

[9] V. Müller *et al.*, “Effects of Mechanical Compression on the Aging and the Expansion Behavior of Si / C-Composite | NMC811 in Different Lithium-Ion Battery Cell Formats,” vol. 166, no. 15, pp. 3796–3805, 2019, doi: 10.1149/2.1121915jes.

[10] X. Han *et al.*, “A review on the key issues of the lithium ion battery degradation among the whole life cycle,” *eTransportation*, vol. 1, p. 100005, 2019, doi: 10.1016/j.etran.2019.100005.

[11] X. Li, C. Yuan, and Z. Wang, “State of health estimation for Li-ion battery via partial incremental capacity analysis based on support vector regression,” *Energy*, vol. 203, p. 117852, 2020, doi: 10.1016/j.energy.2020.117852.

[12] C. Suarez and W. Martinez, “Fast and Ultra-Fast Charging for Battery Electric

Vehicles - A Review," *2019 IEEE Energy Convers. Congr. Expo. ECCE 2019*, pp. 569–575, 2019, doi: 10.1109/ECCE.2019.8912594.

[13] D. Rajagopalan Kannan and M. H. Weatherspoon, "The Effect of Pulse Charging on Commercial Lithium Cobalt Oxide (LCO) Battery Characteristics," *Int. J. Electrochem. Sci.*, vol. 16, no. September, pp. 1–14, 2021, doi: 10.20964/2021.04.30.

[14] J. Guo *et al.*, "Unravelling and quantifying the aging processes of commercial Li(Ni0.5Co0.2Mn0.3)O2/graphite lithium-ion batteries under constant current cycling," *J. Mater. Chem. A*, vol. 11, no. 1, pp. 41–52, 2022, doi: 10.1039/d2ta05960f.

[15] X. Huang, W. Liu, A. B. Acharya, J. Meng, R. Teodorescu, and D. I. Stroe, "Effect of Pulsed Current on Charging Performance of Lithium-Ion Batteries," *IEEE Trans. Ind. Electron.*, vol. 69, no. 10, pp. 10144–10153, 2022, doi: 10.1109/TIE.2021.3121726.

[16] A. Rousseau, N. Shidore, R. Carlson, and V. Freyermuth, "Research on PHEV battery requirements and evaluation of early prototypes," *7th Int. Adv. Automot. Batter. Ultracapacitor Conf. AABC*, 2007.

[17] B. Degraeuwe and M. Weiss, "Does the New European Driving Cycle (NEDC) really fail to capture the NOX emissions of diesel cars in Europe?," *Environ. Pollut.*, vol. 222, no. X, pp. 234–241, 2017, doi: 10.1016/j.envpol.2016.12.050.

[18] E. Massaguer, A. Massaguer, T. Pujol, M. Comamala, L. Montoro, and J. R. Gonzalez, "Fuel economy analysis under a WLTP cycle on a mid-size vehicle equipped with a thermoelectric energy recovery system," *Energy*, vol. 179, pp. 306–314, 2019, doi: 10.1016/j.energy.2019.05.004.

[19] K. Uddin, G. H. Chouchelamane, C. Pastor-fern, W. D. Widanage, and J. Marco, "A Comparison between Electrochemical Impedance Spectroscopy and Incremental Capacity-Differential Voltage as Li-ion Diagnostic Techniques to Identify and Quantify the Effects of Degradation Modes within Battery Management Systems," *J. Power Sources*, vol. 360, pp. 301–318, 2017, doi: 10.1016/j.jpowsour.2017.03.042.

[20] G. Seo *et al.*, "Rapid determination of lithium-ion battery degradation: High C-rate LAM and calculated limiting LLI," *J. Energy Chem.*, vol. 67, pp. 663–671, 2022, doi: 10.1016/j.jechem.2021.11.009.

[21] Y. Li, J. Guo, K. Pedersen, and L. Gurevich, "Recent Health Diagnosis Methods for Lithium-Ion Batteries," *batteries*, vol. 8, p. 72, 2022.

[22] J. Zhu *et al.*, "Investigation of lithium-ion battery degradation mechanisms by combining differential voltage analysis and alternating current impedance," *J. Power Sources*, vol. 448, no. November 2019, pp. 28–30, 2020, doi: 10.1016/j.jpowsour.2019.227575.

[23] D. R. Rajagopalan Kannan and M. H. Weatherspoon, "The effect of pulse

charging on commercial lithium nickel cobalt oxide (NMC) cathode lithium-ion batteries," *J. Power Sources*, vol. 479, no. October, p. 229085, 2020, doi: 10.1016/j.jpowsour.2020.229085.

[24] K. K. Duru, C. Karra, P. Venkatachalam, S. A. Betha, A. Anish Madhavan, and S. Kalluri, "Critical Insights into Fast Charging Techniques for Lithium-Ion Batteries in Electric Vehicles," *IEEE Trans. Device Mater. Reliab.*, vol. 21, no. 1, pp. 137–152, 2021, doi: 10.1109/TDMR.2021.3051840.

[25] D. Ji *et al.*, "Research on adaptability of charging strategy for electric vehicle power battery," *J. Power Sources*, vol. 437, no. July, pp. 1–9, 2019, doi: 10.1016/j.jpowsour.2019.226911.

[26] G. Qiu, L. Lu, Y. Lu, and C. Sun, "Effects of Pulse Charging by Triboelectric Nanogenerators on the Performance of Solid-State Lithium Metal Batteries," *ACS Appl. Mater. Interfaces*, vol. 12, no. 25, pp. 28345–28350, 2020, doi: 10.1021/acsami.0c08681.

[27] J. Zhang, Z. Zhou, Y. Wang, Q. Chen, G. Hou, and Y. Tang, "Pulsed Current Boosts the Stability of the Lithium Metal Anode and the Improvement of Lithium-Oxygen Battery Performance," *ACS Appl. Mater. Interfaces*, vol. 14, pp. 50414–50423, 2022, doi: 10.1021/acsami.2c15347.

[28] Q. Li, S. Tan, L. Li, Y. Lu, and Y. He, "Understanding the molecular mechanism of pulse current charging for stable lithium-metal batteries," *Sci. Adv.*, vol. 3, no. 7, pp. 1–10, 2017, doi: 10.1126/sciadv.1701246.

[29] D. I. Stroe, M. Swierczynski, S. K. Kær, E. M. Laserna, and E. S. Zabala, "Accelerated aging of lithium-ion batteries based on electric vehicle mission profile," in *2017 IEEE Energy Conversion Congress and Exposition, ECCE 2017*, 2017, vol. 2017-Janua, pp. 5631–5637, doi: 10.1109/ECCE.2017.8096937.

[30] G. Qian *et al.*, "Value-creating upcycling of retired electric vehicle battery cathodes," *Cell Reports Phys. Sci.*, vol. 3, no. 2, p. 100741, 2022, doi: 10.1016/j.xcrp.2022.100741.

[31] J. Klink *et al.*, "Thermal fault detection by changes in electrical behaviour in lithium-ion cells," *J. Power Sources*, vol. 490, 2021, doi: 10.1016/j.jpowsour.2021.229572.

[32] S. Hemavathi and A. Shinisha, "A study on trends and developments in electric vehicle charging technologies," *J. Energy Storage*, vol. 52, no. PC, p. 105013, 2022, doi: 10.1016/j.est.2022.105013.

[33] X. Huang *et al.*, "Lithium-Ion Battery Lifetime Extension With Positive Pulsed Current Charging," *IEEE Trans. Ind. Electron.*, vol. PP, pp. 1–8, 2023, doi: 10.1109/TIE.2023.3250850.

[34] B. Ciuffo *et al.*, "Development of the Worldwide Harmonized Test Procedure for Light-Duty Vehicles Pathway for Implementation in European Union Legislation," *Transp. Res. Rec.*, vol. 2503, no. 1, pp. 110–118, 2015, doi:

10.3141/2503-12.

[35] B. Ospina Agudelo, W. Zamboni, and E. Monmasson, "Application domain extension of incremental capacity-based battery SoH indicators," *Energy*, vol. 234, p. 121224, 2021, doi: 10.1016/j.energy.2021.121224.

[36] W. Pan, X. Luo, M. Zhu, J. Ye, L. Gong, and H. Qu, "A health indicator extraction and optimization for capacity estimation of Li-ion battery using incremental capacity curves," *J. Energy Storage*, vol. 42, no. November 2020, p. 103072, 2021, doi: 10.1016/j.est.2021.103072.

[37] H. Kato, Y. Kobayashi, and H. Miyashiro, "Differential voltage curve analysis of a lithium-ion battery during discharge," *J. Power Sources*, vol. 398, no. June, pp. 49–54, 2018, doi: 10.1016/j.jpowsour.2018.07.043.

[38] J. Guo, Y. Che, K. Pedersen, and D. I. Stroe, "Battery impedance spectrum prediction from partial charging voltage curve by machine learning," *J. Energy Chem.*, vol. 79, pp. 211–221, 2023, doi: 10.1016/j.jechem.2023.01.004.

[39] T. C. Pan, E. J. Liu, H. C. Ku, and C. W. Hong, "Parameter identification and sensitivity analysis of lithium-ion battery via whale optimization algorithm," *Electrochim. Acta*, p. 139574, 2021, doi: 10.1016/j.electacta.2021.139574.

[40] C. Pastor-Fernández, K. Uddin, G. H. Chouchelamane, W. D. Widanage, and J. Marco, "A Comparison between Electrochemical Impedance Spectroscopy and Incremental Capacity-Differential Voltage as Li-ion Diagnostic Techniques to Identify and Quantify the Effects of Degradation Modes within Battery Management Systems," *J. Power Sources*, vol. 360, pp. 301–318, 2017, doi: 10.1016/j.jpowsour.2017.03.042.

[41] J. Guo, Y. Li, J. Meng, K. Pedersen, L. Gurevich, and D. I. Stroe, "Understanding the mechanism of capacity increase during early cycling of commercial NMC/graphite lithium-ion batteries," *J. Energy Chem.*, vol. 74, pp. 34–44, 2022, doi: 10.1016/j.jechem.2022.07.005.

[42] M. Dubarry, C. Truchot, and B. Y. Liaw, "Synthesize battery degradation modes via a diagnostic and prognostic model," *J. Power Sources*, vol. 219, pp. 204–216, 2012, doi: 10.1016/j.jpowsour.2012.07.016.

[43] Y. He, F. Ning, Q. Yang, Q. Song, B. Li, and F. Su, "Structural and thermal stabilities of layered Li (Ni 1 / 3 Co 1 / 3 Mn 1 / 3) O 2 materials in 18650 high power batteries," *J. Power Sources*, vol. 196, no. 23, pp. 10322–10327, 2011, doi: 10.1016/j.jpowsour.2011.08.042.

[44] M. Gaberšček, "Understanding Li-based battery materials via electrochemical impedance spectroscopy," *Nature Communications*, vol. 12, no. 1. pp. 19–22, 2021, doi: 10.1038/s41467-021-26894-5.

[45] Q. Xie, Z. Hu, C. Zhao, S. Zhang, and K. Liu, "LaF3-coated Li[Li0.2Mn0.56Ni0.16Co0.08]O2 as cathode material with improved electrochemical performance for lithium ion batteries," *RSC Adv.*, vol. 5, no.

63, pp. 50859–50864, 2015, doi: 10.1039/c5ra06243h.

[46] Y. Wang, J. Zhang, J. Xue, X. Ke, and G. Liang, “LiFePO4/C composites with high compaction density as cathode materials for lithium-ion batteries with high volumetric energy density,” *Ionics (Kiel).*, vol. 27, no. 11, pp. 4687–4694, 2021, doi: 10.1007/s11581-021-04078-x.

[47] Y. Chen *et al.*, “High-voltage electrochemical performance of LiNi0.5Co0.2Mn0.3O2 cathode material via the synergetic modification of the Zr/Ti elements,” *Electrochim. Acta*, vol. 281, pp. 48–59, 2018, doi: 10.1016/j.electacta.2018.05.154.

[48] L. Stolz, M. Gaberšček, M. Winter, and J. Kasnatscheew, “Different Efforts but Similar Insights in Battery R&D: Electrochemical Impedance Spectroscopy vs Galvanostatic (Constant Current) Technique,” *Chem. Mater.*, vol. 34, no. 23, pp. 10272–10278, 2022, doi: 10.1021/acs.chemmater.2c02376.

[49] A. Waligo and P. Barendse, “A comparison of the different broadband impedance measurement techniques for lithium-ion batteries,” *ECCE 2016 - IEEE Energy Convers. Congr. Expo. Proc.*, pp. 1–7, 2016, doi: 10.1109/ECCE.2016.7854661.

[50] S. B. Vilsen, S. K. Kaer, and D. I. Stroe, “Log-Linear Model for Predicting the Lithium-ion Battery Age Based on Resistance Extraction from Dynamic Aging Profiles,” *IEEE Trans. Ind. Appl.*, vol. 56, no. 6, pp. 6937–6948, 2020, doi: 10.1109/TIA.2020.3020529.

[51] J. Guo, Y. Che, K. Pedersen, and D. Stroe, “Battery impedance spectrum prediction from partial charging voltage curve by machine learning,” *J. Energy Chem.*, vol. 79, pp. 211–221, 2023, doi: 10.1016/j.jechem.2023.01.004.

[52] Y. Duan, J. Tian, J. Lu, C. Wang, W. Shen, and R. Xiong, “Deep neural network battery impedance spectra prediction by only using constant-current curve,” *Energy Storage Mater.*, vol. 41, no. 5, pp. 24–31, 2021, doi: 10.1016/j.ensm.2021.05.047.

[53] B. Ravel and M. Newville, “ATHENA, ARTEMIS, HEPHAESTUS: Data analysis for X-ray absorption spectroscopy using IFEFFIT,” *J. Synchrotron Radiat.*, vol. 12, no. 4, pp. 537–541, 2005, doi: 10.1107/S0909049505012719.

[54] S. D. Kelly *et al.*, “X-ray absorption fine structure determination of pH-dependent U-bacterial cell wall interactions,” *Geochim. Cosmochim. Acta*, vol. 66, no. 22, pp. 3855–3871, 2002, doi: 10.1016/S0016-7037(02)00947-X.

[55] D. Anseán *et al.*, “Fast charging technique for high power LiFePO4 batteries: A mechanistic analysis of aging,” *J. Power Sources*, vol. 321, pp. 201–209, 2016, doi: 10.1016/j.jpowsour.2016.04.140.

[56] P. Zhang *et al.*, “Influence of Current Density on Graphite Anode Failure in Lithium-Ion Batteries,” *J. Electrochem. Soc.*, vol. 166, no. 3, pp. A5489–

A5495, 2019, doi: 10.1149/2.0701903jes.

[57] C. Fang *et al.*, “Quantifying inactive lithium in lithium metal batteries,” *Nature*, vol. 572, no. 7770, pp. 511–515, 2019, doi: 10.1038/s41586-019-1481-z.

[58] X. G. Yang, S. Ge, T. Liu, Y. Leng, and C. Y. Wang, “A look into the voltage plateau signal for detection and quantification of lithium plating in lithium-ion cells,” *J. Power Sources*, vol. 395, no. April, pp. 251–261, 2018, doi: 10.1016/j.jpowsour.2018.05.073.

[59] H. Wei *et al.*, “Lithium-rich manganese-based cathode materials with highly stable lattice and surface enabled by perovskite-type phase-compatible layer,” *Nano Energy*, vol. 88, no. June, p. 106288, 2021, doi: 10.1016/j.nanoen.2021.106288.

[60] R. E. Ruther, A. F. Callender, H. Zhou, S. K. Martha, and J. Nanda, “Raman Microscopy of Lithium-Manganese-Rich Transition Metal Oxide Cathodes,” *J. Electrochem. Soc.*, vol. 162, no. 1, pp. A98–A102, 2015, doi: 10.1149/2.0361501jes.

[61] D. Zhang *et al.*, “Lithium hexamethyldisilazide as electrolyte additive for efficient cycling of high-voltage non-aqueous lithium metal batteries,” *Nat. Commun.*, vol. 13, p. 6966, 2022, doi: 10.1038/s41467-022-34717-4.

[62] A. Ejigu *et al.*, “On the Role of Transition Metal Salts During Electrochemical Exfoliation of Graphite: Antioxidants or Metal Oxide Decorators for Energy Storage Applications,” *Adv. Funct. Mater.*, vol. 28, no. 48, 2018, doi: 10.1002/adfm.201804357.

[63] K. Wang, L. Xing, K. Xu, H. Zhou, and W. Li, “Understanding and Suppressing the Destructive Cobalt(II) Species in Graphite Interphase,” *ACS Appl. Mater. Interfaces*, vol. 11, no. 34, pp. 31490–31498, 2019, doi: 10.1021/acsami.9b08949.

[64] C. Yan *et al.*, “Toward Critical Electrode/Electrolyte Interfaces in Rechargeable Batteries,” *Adv. Funct. Mater.*, vol. 30, no. 23, pp. 1–21, 2020, doi: 10.1002/adfm.201909887.

[65] Y. Mao *et al.*, “High-Voltage Charging-Induced Strain, Heterogeneity, and Micro-Cracks in Secondary Particles of a Nickel-Rich Layered Cathode Material,” *Adv. Funct. Mater.*, vol. 29, no. 18, 2019, doi: 10.1002/adfm.201900247.

[66] M. Liu, J. Vatamanu, X. Chen, L. Xing, K. Xu, and W. Li, “Hydrolysis of LiPF6-Containing Electrolyte at High Voltage,” *ACS Energy Lett.*, vol. 6, no. 6, pp. 2096–2102, 2021, doi: 10.1021/acsenergylett.1c00707.

[67] W. Zhao *et al.*, “Toward a stable solid-electrolyte-interfaces on nickel-rich cathodes: LiPO2F2 salt-type additive and its working mechanism for LiNi0.5Mn0.25Co0.25O2 cathodes,” *J. Power Sources*, vol. 380, no. December 2017, pp. 149–157, 2018, doi: 10.1016/j.jpowsour.2018.01.041.

[68] W. Deng *et al.*, “Competitive Solvation-Induced Concurrent Protection on the Anode and Cathode toward a 400 Wh kg-1Lithium Metal Battery,” *ACS Energy Lett.*, vol. 6, no. 1, pp. 115–123, 2021, doi: 10.1021/acsenergylett.0c02351.

[69] J. N. Zhang, Q. Li, Y. Wang, J. Zheng, X. Yu, and H. Li, “Dynamic evolution of cathode electrolyte interphase (CEI) on high voltage LiCoO2 cathode and its interaction with Li anode,” *Energy Storage Mater.*, vol. 14, no. February, pp. 1–7, 2018, doi: 10.1016/j.ensm.2018.02.016.

[70] N. Mao, T. Zhang, Z. Wang, and Q. Cai, “A systematic investigation of internal physical and chemical changes of lithium-ion batteries during overcharge,” *J. Power Sources*, vol. 518, no. November 2021, p. 230767, 2022, doi: 10.1016/j.jpowsour.2021.230767.

[71] X. Huang, W. Liu, A. B. Acharya, J. Meng, R. Teodorescu, and D. I. Stroe, “Effect of Pulsed Current on Charging Performance of Lithium-ion Batteries,” *IEEE Trans. Ind. Electron.*, vol. 69, no. 10, pp. 10144–10153, 2021, doi: 10.1109/TIE.2021.3121726.

[72] S. Zhu, C. Hu, Y. Xu, Y. Jin, and J. Shui, “Performance improvement of lithium-ion battery by pulse current,” *Journal of Energy Chemistry*, vol. 46. pp. 208–214, 2020, doi: 10.1016/j.jechem.2019.11.007.

[73] W. H. Li *et al.*, “Highly Improved Cycling Stability of Anion De-/Intercalation in the Graphite Cathode for Dual-Ion Batteries,” *Adv. Mater.*, vol. 31, no. 4, 2019, doi: 10.1002/adma.201804766.

[74] G. Qian *et al.*, “Value-creating upcycling of retired electric vehicle battery cathodes,” *Cell Reports Phys. Sci.*, vol. 3, no. 2, p. 100741, 2022, doi: 10.1016/j.xcrp.2022.100741.

[75] P. A. K. Jun Li, Edward Murphy, Jack Winnick, “Li2001.Pdf,” *J. Power Sources*, vol. 102, no. 1–2, pp. 302–309, 2001, [Online]. Available: https://www.sciencedirect.com/science/article/pii/S0378775301008205.

[76] P. Keil and A. Jossen, “Charging protocols for lithium-ion batteries and their impact on cycle life-An experimental study with different 18650 high-power cells,” *J. Energy Storage*, vol. 6, pp. 125–141, 2016, doi: 10.1016/j.est.2016.02.005.

[77] N. Iqbal and S. Lee, “Stress-regulated pulse charging protocols via coupled electrochemical-mechanical model for the mechanical stability of electrode materials in lithium-ion batteries,” *J. Power Sources*, vol. 536, no. September 2021, p. 231376, 2022, doi: 10.1016/j.jpowsour.2022.231376.

[78] S. Li *et al.*, “Effects of pulse charging on the performances of lithium-ion batteries,” *Nano Energy*, vol. 56, no. 30, pp. 555–562, 2019, doi: 10.1016/j.nanoen.2018.11.070.

[79] X. Huang *et al.*, “Lifetime Extension of Lithium-Ion Batteries With Low-Frequency Pulsed Current Charging,” *IEEE J. Emerg. Sel. Top. Power*

Electron., vol. 11, no. 1, pp. 57–66, 2023, doi: 10.1109/JESTPE.2021.3130424.

[80] D. R. Rajagopalan Kannan and M. H. Weatherspoon, “The effect of pulse charging on commercial lithium nickel cobalt oxide (NMC) cathode lithium-ion batteries,” *J. Power Sources*, vol. 479, no. July, p. 229085, 2020, doi: 10.1016/j.jpowsour.2020.229085.

[81] L. R. Chen, S. L. Wu, D. T. Shieh, and T. R. Chen, “Sinusoidal-ripple-current charging strategy and optimal charging frequency study for Li-ion batteries,” *IEEE Trans. Ind. Electron.*, vol. 60, no. 1, pp. 88–97, 2013, doi: 10.1109/TIE.2012.2186106.

[82] M. Abdel Monem *et al.*, “Lithium-ion batteries: Evaluation study of different charging methodologies based on aging process,” *Appl. Energy*, vol. 152, pp. 143–155, 2015, doi: 10.1016/j.apenergy.2015.02.064.

[83] M. Abdel-Monem, K. Trad, N. Omar, O. Hegazy, P. Van den Bossche, and J. Van Mierlo, “Influence analysis of static and dynamic fast-charging current profiles on ageing performance of commercial lithium-ion batteries,” *Energy*, vol. 120, no. 2017, pp. 179–191, 2017, doi: 10.1016/j.energy.2016.12.110.

[84] D. Rajagopalan Kannan and M. H. Weatherspoon, “The Effect of Pulse Charging on Commercial Lithium Cobalt Oxide (LCO) Battery Characteristics,” *Int. J. Electrochem. Sci.*, vol. 16, pp. 1–14, 2021, doi: 10.20964/2021.04.30.

[85] Y. Che, X. Hu, X. Lin, J. Guo, and R. Teodorescu, “Health prognostics for lithium-ion batteries: mechanisms, methods, and prospects,” *Energy Environ. Sci.*, vol. 16, no. 2, pp. 338–371, 2023, doi: 10.1039/d2ee03019e.

[86] M. Dubarry, V. Svoboda, R. Hwu, and B. Y. Liaw, “Incremental capacity analysis and close-to-equilibrium OCV measurements to quantify capacity fade in commercial rechargeable lithium batteries,” *Electrochem. Solid-State Lett.*, vol. 9, p. 10, 2006, doi: 10.1149/1.2221767.

[87] W. Hu, Y. Peng, Y. Wei, and Y. Yang, “Application of Electrochemical Impedance Spectroscopy to Degradation and Aging Research of Lithium-Ion Batteries,” *J. Phys. Chem. C*, vol. 127, no. 9, pp. 4465–4495, 2023, doi: 10.1021/acs.jpcc.3c00033.

[88] Z. Chen *et al.*, “Sustainable Energy & Fuels,” vol. 4, no. 11, 2020, doi: 10.1039/d0se00175a.

[89] J. Asenbauer, T. Eisenmann, M. Kuenzel, A. Kazzazi, Z. Chen, and D. Bresser, “The success story of graphite as a lithium-ion anode material-fundamentals, remaining challenges, and recent developments including silicon (oxide) composites,” *Sustainable Energy and Fuels*, vol. 4, no. 11. Royal Society of Chemistry, pp. 5387–5416, 2020, doi: 10.1039/d0se00175a.

[90] L. J. Hardwick, H. Buqa, and P. Novák, “Graphite surface disorder detection using in situ Raman microscopy,” *Solid State Ionics*, vol. 177, no. 26-32

SPEC. ISS., pp. 2801–2806, 2006, doi: 10.1016/j.ssi.2006.03.032.

[91] M. N. Ates, Q. Jia, A. Shah, A. Busnaina, S. Mukerjee, and K. M. Abraham, “Mitigation of Layered to Spinel Conversion of a Li-Rich Layered Metal Oxide Cathode Material for Li-Ion Batteries,” *J. Electrochem. Soc.*, vol. 161, no. 3, pp. A290–A301, 2014, doi: 10.1149/2.040403jes.

[92] H. H. Ryu, B. Namkoong, J. H. Kim, I. Belharouak, C. S. Yoon, and Y. K. Sun, “Capacity Fading Mechanisms in Ni-Rich Single-Crystal NCM Cathodes,” *ACS Energy Lett.*, vol. 6, no. 8, pp. 2726–2734, 2021, doi: 10.1021/acsenergylett.1c01089.

[93] J. Yu *et al.*, “Formation of FeOOH Nanosheets Induces Substitutional Doping of CeO2−x with High-Valence Ni for Efficient Water Oxidation,” *Adv. Energy Mater.*, vol. 11, no. 4, pp. 1–7, 2021, doi: 10.1002/aenm.202002731.

[94] L. Zhu *et al.*, “Ruthenium-nickel-nickel hydroxide nanoparticles for room temperature catalytic hydrogenation,” *J. Mater. Chem. A*, vol. 5, no. 17, pp. 7869–7875, 2017, doi: 10.1039/c7ta01437f.

[95] H. Zhu *et al.*, “In Situ Probing Multiple-Scale Structures of Energy Materials for Li-Ion Batteries,” *Small Methods*, vol. 4, no. 6, pp. 1–30, 2020, doi: 10.1002/smtd.201900223.

[96] R. Ruess, M. A. Ulherr, E. Trevisanello, S. Schröder, A. Henss, and J. Janek, “ Transition Metal Oxides and Li 2 CO 3 as Precursors for the Synthesis of Ni-Rich Single-Crystalline NCM for Sustainable Lithium-Ion Battery Production ,” *J. Electrochem. Soc.*, vol. 169, no. 7, p. 070531, 2022, doi: 10.1149/1945-7111/ac8242.

[97] L. Cabo-Fernandez, A. R. Neale, F. Braga, I. V. Sazanovich, R. Kostecki, and L. J. Hardwick, “Kerr gated Raman spectroscopy of LiPF6 salt and LiPF6-based organic carbonate electrolyte for Li-ion batteries,” *Phys. Chem. Chem. Phys.*, vol. 21, no. 43, pp. 23833–23842, 2019, doi: 10.1039/c9cp02430a.

[98] H. Bryngelsson, M. Stjerndahl, T. Gustafsson, and K. Edström, “How dynamic is the SEI?,” *J. Power Sources*, vol. 174, no. 2, pp. 970–975, 2007, doi: 10.1016/j.jpowsour.2007.06.050.

[99] B. Han *et al.*, “Additive stabilization of SEI on graphite observed using cryo-electron microscopy,” *Energy Environ. Sci.*, vol. 14, no. 9, pp. 4882–4889, 2021, doi: 10.1039/d1ee01678d.

[100] D. Aurbach, Y. Ein-Ely, and A. Zaban, “The Surface Chemistry of Lithium Electrodes in Alkyl Carbonate Solutions,” *J. Electrochem. Soc.*, vol. 141, no. 1, pp. L1–L3, 1994, doi: 10.1149/1.2054718.

[101] A. Marongiu, M. Roscher, and D. U. Sauer, “Influence of the vehicle-to-grid strategy on the aging behavior of lithium battery electric vehicles,” *Appl. Energy*, vol. 137, pp. 899–912, 2015, doi: 10.1016/j.apenergy.2014.06.063.

[102] N. Wassiliadis *et al.*, “Quantifying the state of the art of electric powertrains

in battery electric vehicles: Range, efficiency, and lifetime from component to system level of the Volkswagen ID.3," *eTransportation*, vol. 12, p. 100167, 2022, doi: 10.1016/j.etran.2022.100167.

[103] S. S. Zhang, K. Xu, and T. R. Jow, "Electrochemical impedance study on the low temperature of Li-ion batteries," *Electrochim. Acta*, vol. 49, no. 7, pp. 1057–1061, 2004, doi: 10.1016/j.electacta.2003.10.016.

[104] Y. C. Chien, H. Liu, A. S. Menon, W. R. Brant, D. Brandell, and M. J. Lacey, "Rapid determination of solid-state diffusion coefficients in Li-based batteries via intermittent current interruption method," *Nat. Commun.*, vol. 14, no. 1, p. 2289, 2023, doi: 10.1038/s41467-023-37989-6.

[105] D. Andre, M. Meiler, K. Steiner, C. Wimmer, T. Soczka-Guth, and D. U. Sauer, "Characterization of high-power lithium-ion batteries by electrochemical impedance spectroscopy. I. Experimental investigation," *J. Power Sources*, vol. 196, no. 12, pp. 5334–5341, 2011, doi: 10.1016/j.jpowsour.2010.12.102.

[106] H. L. Andersen, L. Djuandhi, U. Mittal, and N. Sharma, "Strategies for the Analysis of Graphite Electrode Function," *Adv. Energy Mater.*, vol. 11, no. 48, pp. 1–21, 2021, doi: 10.1002/aenm.202102693.

[107] Y. Chen, X. Dou, K. Wang, and Y. Han, "Lithium Dendrites Inhibition via Diffusion Enhancement," *Adv. Energy Mater.*, vol. 9, no. 17, pp. 1–7, 2019, doi: 10.1002/aenm.201900019.

Part II

Selected Publication

Journal Publication 1

Lithium-Ion Battery Operation, Degradation, and Aging Mechanism in Electric Vehicles: An Overview [J1]

J. Guo, Y. Li, K. Pedersen, D. -I. Stroe

This paper is accepted by *Energies* 2021, 14(17).

energies

Review

Lithium-Ion Battery Operation, Degradation, and Aging Mechanism in Electric Vehicles: An Overview

Jia Guo [1,2], Yaqi Li [1,2], Kjeld Pedersen [2] and Daniel-Ioan Stroe [1,*]

[1] Department of Energy Technology, Aalborg University, 9220 Aalborg, Denmark; jgu@energy.aau.dk (J.G.); yaqili@mp.aau.dk (Y.L.)
[2] Department of Material Production, Aalborg University, 9220 Aalborg, Denmark; kp@mp.aau.dk
[*] Correspondence: dis@energy.aau.dk; Tel.: +45-99403327

Abstract: Understanding the aging mechanism for lithium-ion batteries (LiBs) is crucial for optimizing the battery operation in real-life applications. This article gives a systematic description of the LiBs aging in real-life electric vehicle (EV) applications. First, the characteristics of the common EVs and the lithium-ion chemistries used in these applications are described. The battery operation in EVs is then classified into three modes: charging, standby, and driving, which are subsequently described. Finally, the aging behavior of LiBs in the actual charging, standby, and driving modes are reviewed, and the influence of different working conditions are considered. The degradation mechanisms of cathode, electrolyte, and anode during those processes are also discussed. Thus, a systematic analysis of the aging mechanisms of LiBs in real-life EV applications is achieved, providing practical guidance, methods to prolong the battery life for users, battery designers, vehicle manufacturers, and material recovery companies.

Keywords: lithium-ion battery; electric vehicles; aging mechanism; battery degradation

Citation: Guo, J.; Li, Y.; Pedersen, K.; Stroe, D.-I. Lithium-Ion Battery Operation, Degradation, and Aging Mechanism in Electric Vehicles: An Overview. *Energies* **2021**, *14*, 5220. https://doi.org/10.3390/en14175220

Academic Editor: Tek Tjing Lie

Received: 28 July 2021
Accepted: 18 August 2021
Published: 24 August 2021

1. Introduction

Lithium-ion batteries (LiBs) with high energy density are receiving increasing attention because of their environmental friendliness and are widely used in electric vehicles (EVs) worldwide [1]. Battery degradation problems, such as capacity fading and internal resistance increasing, inevitably occur with time and use. These cause great trouble to users and manufacturers [2]. A clear understanding of how batteries age in EVs is urgently needed to: (i) optimize the battery materials, (ii) improve battery cell production, and (iii) guide the design of automotive battery systems.

At present, scientists from different fields have researched, from different perspectives, the aging of LiBs. Some scientists specifically discussed the impacts of environmental and operational factors on battery degradation [3], while others studied the battery aging mechanism through the post-mortem analysis of the internal components of the battery cell [4]. However, a close connection between the battery operation and degradation in EV applications and the corresponding aging mechanism has not yet been established. Thus, a review is necessary in order to systematically and comprehensively describe the aging of LiBs in EVs.

Many reviews on battery aging have been published presenting the battery degradation and aging mechanisms. The main contents of these reviews are summarized in Table 1. These reviews are mostly based on analyzing laboratory accelerated aging test results, which are mainly obtained using constant charging/discharging current and are significantly different from the battery operation in EVs. Besides, most of them lack the connection with the battery operation scenarios, and focus only on the degradation behavior of the battery itself; in reality, the influential factors on battery charging, discharging and standby are different, and aging should be described independently based on the operation status. Moreover, the battery chemistries reviewed in these works mainly involved stable

$LiCoO_2$ and $LiFePO_4$, which are more stable and mature and are not considered to be state-of-the-art technology for EVs. Therefore, the aging mechanisms of widely EV-used Ni-rich battery chemistries ($LiNi_{1-x}M_xO_2$, M = Co, Mn and Al. (NMC) and (NCA)) need further study. In order to address this gap, in this paper, we review the NMC and NCA battery operation, degradation, and the corresponding aging mechanisms in real-life-EV use.

Table 1. An overview of the published literature related to battery aging.

References	Topic			Chemistries
	Operation	Degradation	Aging Mechanism	
Han et al., 2019 [5]		√	√	LMO, LCO, LFP, NMC
Tian et al., 2020 [6]		√		LMO, LFP, NMC
Mocera et al., 2020 [7]			√	LFP
Woody et al., 2020 [8]		√	√	LCO, LMO, LFP, NCA, NMC
Vetter et al., 2005 [9]			√	LCO, LMO, NMC
Broussely et al., 2005 [10]			√	LCO, NMC
Barre et al., 2013 [11]	√		√	LCO
Birkl et al., 2017 [12]		√		LCO
Palacin et al., 2018 [13]			√	LMO, LCO, NMC, NCA
Xiong et al., 2020 [14]		√	√	LFP, NCA, NMC
Teichert et al., 2020 [15]		√		NMC
Alipour et al., 2020 [16]		√	√	LCO, LFP, NMC, NCA
Chen et al., 2021 [17]	√	√		LCO
Yang et al., 2021 [18]	√	√		NMC, NCA

In this article, we analyzed the applications of LiBs in current EVs, and divided the battery operation scenario into three modes: charging, standby, and driving. The influence on EV battery degradation from the corresponding factors for these modes is studied, respectively. Finally, the relationship between the battery operation mode and the aging mechanisms of battery cell components (i.e., anode, cathode, and electrolyte) is established in order to clearly describe LiBs aging in real EV use.

The remainder of this paper is structured as follows: in Section 2, we will introduce the LiBs chemistries used in EV applications. Section 3 will describe in detail the battery operation modes in EV application. Section 4 will present the LiBs degradation in EV applications. Section 5 will discuss the aging mechanisms of LiBs, which are caused by the EV operation, and Section 6 provides concluding remarks.

2. LiBs in EV Applications

2.1. Electric Vehicle Applications

Depending on the primary source of energy, EVs can be classified mainly into the following three types: Battery Electric Vehicles (BEV), Hybrid Electric Vehicles (HEV) and Plug-In Hybrid Electric Vehicles (PHEV). The energy flow in these three types of EVs is presented in Figure 1.

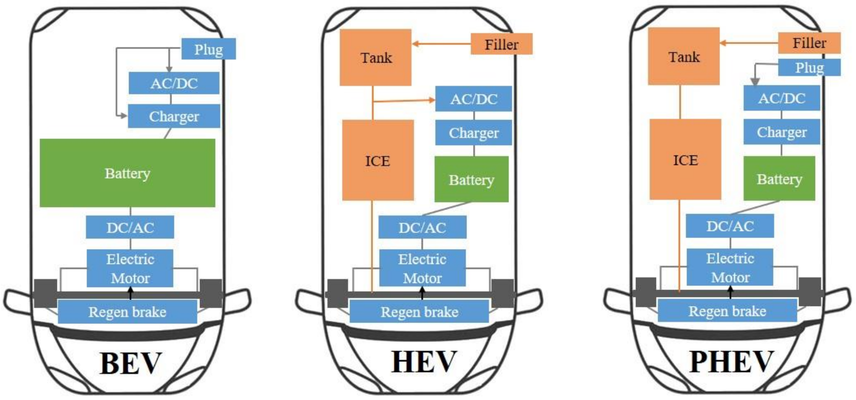

Figure 1. The schematic representation of the three types of EVs; from left to right: Battery Electric Vehicles (BEV), Hybrid Electric Vehicles (HEV), and Plug-In Hybrid Electric Vehicles (PHEV).

BEVs are completely powered by electrical energy from batteries. The external energy is supplied only by plugging the BEV into the electricity grid for charging, and there is no on-board electricity generation. Depending on the EV manufacture, batteries powering BEV usually have a capacity between 20 kWh and 80 kWh, which ensure a range of up to 663 km [19,20]. Because the energy is supplied only by batteries, the BEV requires a larger battery pack size and capacity than other EVs.

HEVs are the most commonly used EV technology, combining an internal combustion engine (ICE) and an electric motor. In their powertrain, fossil fuel is the only external energy powering the ICE, and the energy for charging the battery is obtained from the braking process. The electric motor is used to power the vehicle for a short distance or to support the main engine (e.g., at a stoplight) [21]. Thus, HEVs require the lowest battery capacity, which is between 1.3 kWh and 1.6 kWh [19]. No charging plug for connection to the electricity grid exists in HEVs, which is usually considered to be a fuel-efficiency measure. Therefore, the battery capacity and size requirements are relatively low.

The powertrain of PHEVs is similar to the one of HEVs, and consists of an ICE and an electric engine; however, the main difference is that the PHEV can be plugged into an external source (e.g., EV charger) for charging. Furthermore, the HEV battery can also be charged throughout the regenerative braking processes. PHEVs have batteries with a larger capacity than HEVs, and, thus, they can extend the driving mileage when using electricity alone. Traditionally, this type of vehicle is powered by 50% gasoline and 50% electricity. The size of the battery capacity for PHEV applications is usually between 4.5 kWh and 10 kWh [22].

There are many types of EVs in the market and each of them has individual specifics. The most popular EVs in the market, classified according to their type, are summarized in Table 2 [19,23,24]. Furthermore, the global market share of HEV, PHEV, and BEV in 2020 is shown in Figure 2 [25].

Table 2. The comparison of the main characteristics of EVs in the market.

Type	Manufacturer	Battery-Only Range (km)	Battery Capacity (kWh)
HEV	Toyota Prius IV BMW 225xe Audi A3 e-tron Toyota Prius III	/	1.3–1.6
PHEV	Chevy Volt	64	18.4
	Toyota Prius XW30	21	5.2
	Jaguar I-Pace	470	90.0
BEV	Tesla Model S	663	100.0
	BMW i3	246	42.2
	Nissan Leaf	364	62.0
	Renault Zoe	395	52

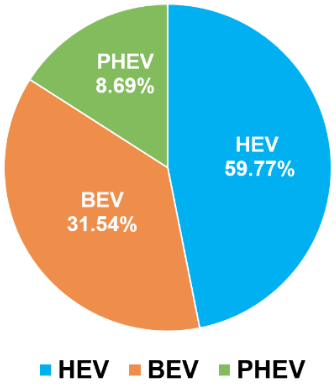

Figure 2. The global market share of HEV, PHEV, and BEV in 2020 (based on [25]).

2.2. Lithium-Ion Chemistries in EV Applications

There is a growing demand for commercial LiBs with a high energy density for powering EVs. The energy density is mainly determined by the operating voltage of the active battery materials and their specific capacity. There are many types of LiBs with wide application prospects, such as spinel LMO/LNMO cathode [26], olivine LFP cathode [27,28], and layered NMC/NCA [29]. Among them, the group of Ni-rich layered oxides ($LiNi_{1-x}M_xO_2$, M = Co, Mn, and Al) have both higher gravimetric and volumetric specific capacities than other intercalation-type cathode materials [30]. Moreover, the high working voltage of $LiNi_{1-x}M_xO_2$ meets the withstand voltage of the current electrolytes. Therefore, the NMC and NCA are widely used in current EV models [31]. More details of NMC and NCA-based batteries will be discussed in the following sections.

The performance of these Ni-rich cathode materials is greatly influenced by the properties of the used elements (i.e., Ni, Co, and Mn orAl). The capacity of the batteries is mainly provided by Ni; however, the use of Ni also leads to a poor cycle life and thermal stability. On the other hand, Mn and Al offer an improved cycle life and safety. Furthermore, Co contributes to the electronic conductivity, ensuring a lower resistance. The $LiNi_xCo_yMn_zO_2$ (x = 1/3, 0.5, 0.6, 0.7, and 0.8) materials with high energy density, long cycle life, and excellent thermal stability have attracted much attention [32]. With the increasing of Ni content, the specific discharge capacity and total residual lithium also increase, but the corresponding capacity retention and safety characteristics gradually decrease [32,33]. However, this does not hinder its large-scale application in real life, due to the high reversible capacity, discharge working voltage, and relatively low costs for Ni-rich materials [34]. Among them, researchers replace the Mn element of $LiNi_xCo_yMn_zO_2$ with certain amounts of Al element [35]. The prepared $LiNi_{0.8}Co_{0.15}Al_{0.05}O_2$ shows better thermal stability and cyclability than NMC cathodes [36].

The anode is used to store Li^+ in the charging process. The traditional anode raw material is graphite (LiC_6) with a capacity of 372 mAh/g. In addition, lithium titanate (LTO) with an operating voltage of around 1.55 V (vs. Li^+/Li) has been considered for various vehicle applications. It enables the LTO to avoid self-discharge when working as an anode and thus enhances its safety and stability [37]. A brief comparative analysis of these chemistries is presented in Table 3 [30].

Table 3. A brief comparative analysis of common chemistries.

Electrode		$V_{Average}$ (v)	V_{Max} (v)	Specific Capacity (mAh g^{-1}/mAh cm^{-3})	Gravimetric Energy (wh kg^{-1})
Cathode	$LiNi_{0.8}Co_{0.15}Al_{0.05}O_2$	3.7	4.6	220/979	758
	$LiNi_{1/3}Co_{1/3}Mn_{1/3}O_2$	3.6	4.7	160/712	576
	$LiNi_{0.5}Co_{0.2}Mn_{0.3}O_2$	3.6	4.7	170/757	612
	$LiNi_{0.6}Co_{0.2}Mn_{0.2}O_2$	3.6	4.7	180/810	648
	$LiNi_{0.7}Co_{0.15}Mn_{0.15}O_2$	3.6	4.7	190/855	684
	$LiNi_{0.8}Co_{0.1}Mn_{0.1}O_2$	3.6	4.7	200/930	720
Anode	graphite	0.6	3	372/735	190
	LTO	1.55	2.5	175/607	263.5

3. Battery Operation in EV Application

The battery in EV applications is complex and diverse, as well as in the influence of various factors. It not only depends on driving habits, but also will be affected by environmental factors, such as the temperature, which varies from season-to-season and region-to-region. The load of the vehicle, driving frequency and mileage, charging habits and road conditions are different for different drivers, which puts the battery in a different situation. Therefore, it is very difficult to standardize the battery operation in EV applications and even more difficult to estimate its state-of-health. However, the factors (e.g., driving habits, road conditions, load of the vehicles and so on) mainly affect battery aging during driving. As a result, according to the battery working state, we can divide the battery usage status into three independent processes (charging process, driving, and standby) and study them separately, as illustrated in Figure 3.

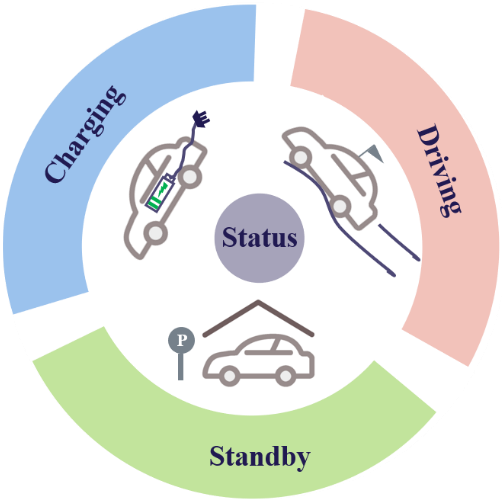

Figure 3. The battery operation modes in EV applications.

3.1. EV Battery Charging

The most used protocol for charging LiB is a constant current constant voltage (CC-CV), which consists of a constant current charging phase during which the battery voltage increases up to the cut-off value, followed by a constant voltage phase until the current falls to near-zero, as shown in Figure 4a. The battery charging protocol is closely related to the daily usage of the EV and to the battery's SOH, which will be reflected in the charging time. In order to reduce the charging time and negative effect on the battery from high currents, several alternative charging protocols are proposed in the literature, which are: Multistage Constant Current (MCC) charging, Pulse Charging (PC), Constant Power Constant Voltage (CP-CV), Variable Current Profile (VCP) and Constant Current Pulsed Charging (CC-PC) [38–41].

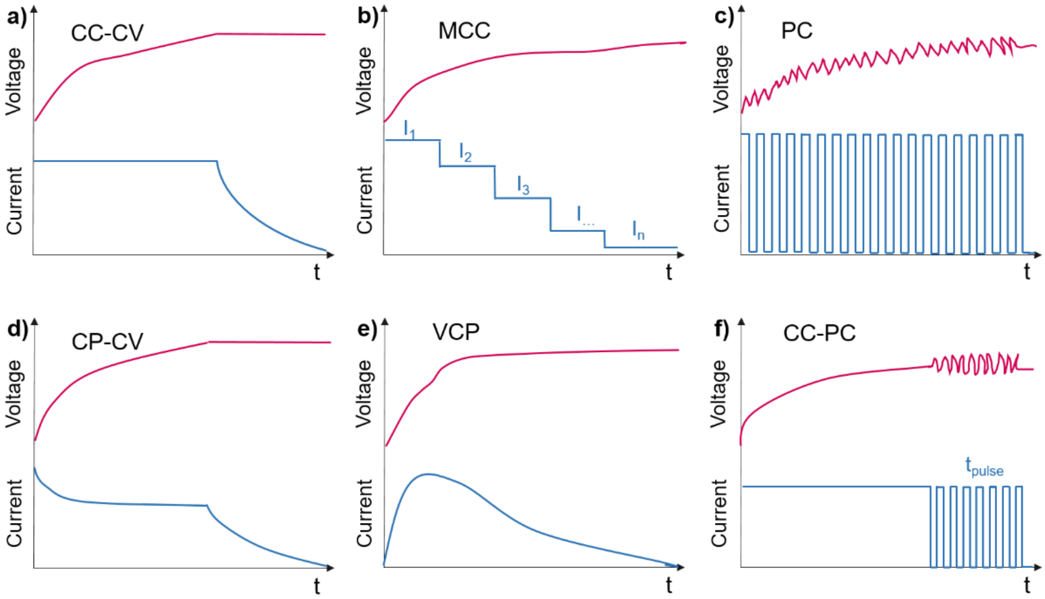

Figure 4. Schematic illustration of different charging protocols: (**a**) Constant Current Constant Voltage (CC-CV); (**b**) Multistage Constant Current (MCC); (**c**) Pulse Charging (PC); (**d**) Constant Power Constant Voltage (CP-CV); (**e**) Variable Current Profile (VCP); (**f**) Constant Current Pulsed Charging (CC-PC).

To achieve fast charging and slow down the battery's aging process, researchers proposed the Multistage Constant Current (MCC) protocol as one of the earliest charging types. This method sets different current levels during the charging process, as illustrated in Figure 4b, in order to minimize battery degradation. This is a very promising charging method, but the optimal value and duration of the current level need to be further researched [42]. To reduce the concentration polarization and mechanical stresses, charging is periodically interrupted by short rest periods (as presented in Figure 4c) or discharge pulses in the pulse charging protocols [41]. In [38], the authors found that the cycle life is similar to the battery when charged by CC-CV method; nevertheless, according to the results presented in [41], there is no overall agreement regarding the positive and/or negative effects on battery performance and lifetime of the pulsed charging methods. Besides, this charging method is complex, and also involves many factors to consider, such as pulsed current amplitude, its duty cycle, and pulse frequency, hindering its large-scale application [43]. The CP-CV protocol provides a low-current near the end of charging to alleviate metallic lithium plating at the anode (Figure 4d). However, as presented in [44], a fast capacity fading can be observed from a 0.5 C CP-CV charging, which is caused by high polarization in the initial CP-charging. Furthermore, some complex variable current profiles have been used for battery charging (Figure 4e). Sikha et al. designed, in [45], a varying current profile (VCP) protocol, which is less damaging than the pure CV charging in the early cycles. However, this profile, too, resulted in a significant capacity degradation compared to that of CC-CV with the same mean current. Another battery charging protocol is the CC-PC charging protocol which combines a constant current and pulsed charging (Figure 4f). The application cost of the charging protocol is relatively low, avoiding voltage control and variable charging currents [40]. But, it can deteriorate the cycle life due to pulses leading to an exceedance voltage in the high voltage period [38].

At present, the standardized CC-CV protocol is widely applied in real-life applications (e.g., EVs), while the other presented charging protocols, developed based on an array of physical motivations which include plenty of advantages in some certain conditions (such as fast-charging), are mainly applied at the research stage or even at a reduced-scale in real life. Currently, the EVs are mainly charged by the CC-CV protocol. In the aging analysis section (Sections 4 and 5), we mainly discuss the aging mechanisms which are caused by the CC-CV charging protocols.

3.2. EV Driving Operation

3.2.1. Real-Life Scenarios

The driving profiles of EVs in real life are diverse. They mainly depend on the vehicle design, the behavior of the driver, and the external environment, resulting in difference in service life and health status. Generally, the vehicle design considers multiple factors in order to meet the needs of different consumers, including the overall dimensions, passenger capacity, tire type and shape, specific front area, and body type [46]. This will make the EVs operate differently in different situations, and lead to different energy demands. In addition, the battery pack sizing and output power are also different. Driver behavior is also related to different traffic conditions. Furthermore, the external environment conditions (e.g., mainly ambient temperature, but also precipitation, wind, etc.) also have an important effect on the battery loading and, subsequently, on the range of the EV. All of these factors make EV driving very diverse. Therefore, it is difficult to study, analyze, and propose a unified set of aging mechanisms for batteries operated in EVs using real-life data. There is limited available literature regarding battery usage harvested from real-life operations. For example, Jafari et al. analyzed, in [47], the real-world daily driving undertaken by a fleet of connected vehicles. The data set contains the records of the connected vehicles volunteered by drivers using their vehicles in the US. The data from 50 driving cycles of 50 drivers were used to evaluate EV driving during an entire year.

In order to simulate the driving conditions of the EVs and evaluate the degradation behavior of the batteries, researchers developed a series of driving cycle profiles based on extensive real-life data, which fully considers various factors (e.g., driving habits, road conditions, load of the vehicles, vehicles type, weather, and so on). These standardized EV driving profiles are very convenient for laboratory battery testing and performance-degradation evaluation.

3.2.2. Driving Cycle Profiles

Many countries and organizations create their standard driving cycle based on their roads and environment, in order to assess the performance of EVs and their batteries [44]. The driving cycle consists of a series of repetitive sequences of vehicle operating modes that represent the driving models, as shown in Figure 5.

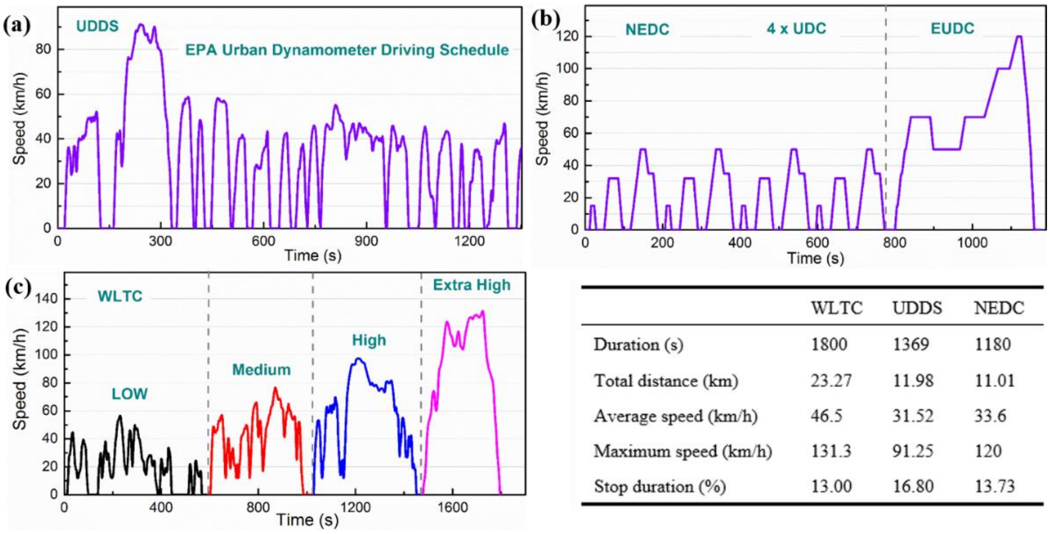

	WLTC	UDDS	NEDC
Duration (s)	1800	1369	1180
Total distance (km)	23.27	11.98	11.01
Average speed (km/h)	46.5	31.52	33.6
Maximum speed (km/h)	131.3	91.25	120
Stop duration (%)	13.00	16.80	13.73

Figure 5. The driving cycle profiles of (**a**) UDDS, (**b**) NEDC and (**c**) WLTC for a class 3 vehicle.

The EPA Urban Dynamometer Driving Schedule (UDDS), presented in Figure 5a, is commonly called the “LA4” or “the city test”; the UDDS represents city driving conditions and has been used as the standard driving cycle in United States since 1972 for light-duty vehicle testing. The New European Driving Cycle (NEDC) is also an early driving cycle that was introduced in 1996 and divided into two parts, as shown in Figure 5b. The first part simulates urban driving conditions which are repeated four times and the second part simulates extra-urban driving conditions with a high speed. With the regulation of EURO 6, which is the most recent emission standard for passenger cars imposed by the European Union Commission, the light-duty vehicles are tested with an updated standard driving cycle, the World Harmonized Light Vehicles Test Cycle (WLTC), which provides more dynamic driving behaviors [48]. WLTC was generated to define a globally harmonized standard for determining the levels of pollutants, energy consumption, and the electric range for light-duty driving, from approximately 765,000 km of data gathered in five different regions: EU, USA, India, Korea, and Japan. The “real world” driving data contains different road characteristics (urban, rural, and motorway) and driving conditions (peak, off-peak, weekend), covering a wide range of vehicle categories, various engines and manufacturers. This is similar to the different kinds of roads that are commonly travelled on, containing a low speed (L/ < 60 km/h), a medium (M/ < 80 km/h), a high speed (H/ < 110 km/h) and extra-high speed (Ex-H/ > 110 km/h), corresponding to the urban, rural and motorway classification, as shown in Figure 5c. Nowadays, more and more manufactures use WLTC to evaluate the performance of PHEV, HEV and BEV. In below table, a comparison of the aforementioned driving cycles is presented.

To prove the validity of the WLTC profile for EVs studies, Ben-Marzouk et al. [49] collected the real-life EV data for two years on ten EVs, and built synthetic profiles of the real application M1 and real application M2, as shown in Figure 6. These profiles are compared with the WLTC profile and they show great similarity in terms of aging, especially for the real application M1. These results validate the use of the WLTC profile in aging tests and aging studies of EV batteries.

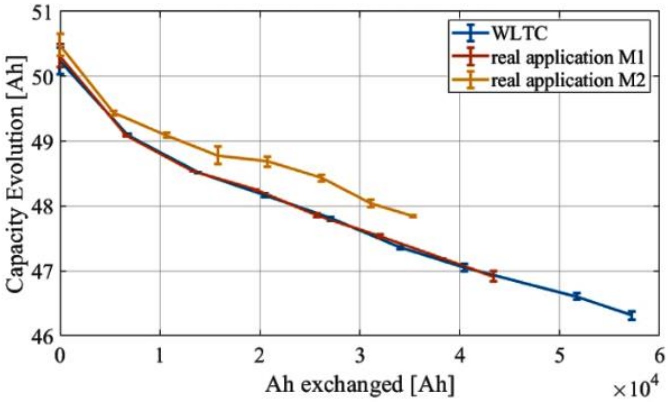

Figure 6. Evolution of the capacity of the batteries according to Ah exchanged for each aging profile [49].

3.3. *EV Standby Operation*

In EV applications, the standby state accounts for a large proportion of the entire battery service life. As presented in [50], the standby time can reach 90% of the total vehicle operation. This means that calendar aging cannot be ignored when assessing battery degradation and lifetime in such applications. In [51], Swierczynski et al. showed that more than 75% of capacity fade was caused by calendar aging during the EV operation. Thus, it is particularly important to study the calendar aging process and related factors, such as the state-of-charge (SOC) and temperature. In normal conditions, the calendar aging process is slow, and it takes several years or even tens of years for a battery to end its service life by calendaring only. In actual research, elevated temperature and/or high SOC levels are often used to accelerate battery aging.

4. Aging in EV Application

4.1. *Aging in Charging*

The LiBs aging in the charging process is related to many factors, such as the cut-off voltage, current rate, and temperature. Using a high cut-off voltage, more capacity can be charged and a high charging current can significantly shorten the charging period. However, in these cases, the degradation process of LiBs will be greatly accelerated. The most common factors affecting the charging process and their variations are shown in Figure 7.

4.1.1. Impact of Charging Voltage

Slight overcharging or reduction in the cut-off voltage have an obvious impact on the degradation of LiBs. In [52] the author accelerated the battery aging by 300 mV overcharging. The schematic diagram is shown in Figure 8a. They designed a cycle aging experiment for 18650-type batteries (i.e., 2 Ah, NMC/graphite) and charged one of them in the voltage range of 2.75–4.5 V, while another battery in was charged in the nominal range of 2.75–4.2 V. The battery charging/discharging profiles are shown in Figure 8b. As expected, the overcharged battery has an 18% higher capacity than the battery charged in the nominal conditions; however, for the overcharged batteries (three overcharged cells tested at the same condition) the capacity fade is pronounced, as shown in Figure 8c. The SOH drops to 80% after only approximately 40 cycles, which is much quickly than for the battery aged under normal voltage (which needed over 100 cycles to reach the same SOH). Thus, overcharging the battery highly accelerates the degradation process.

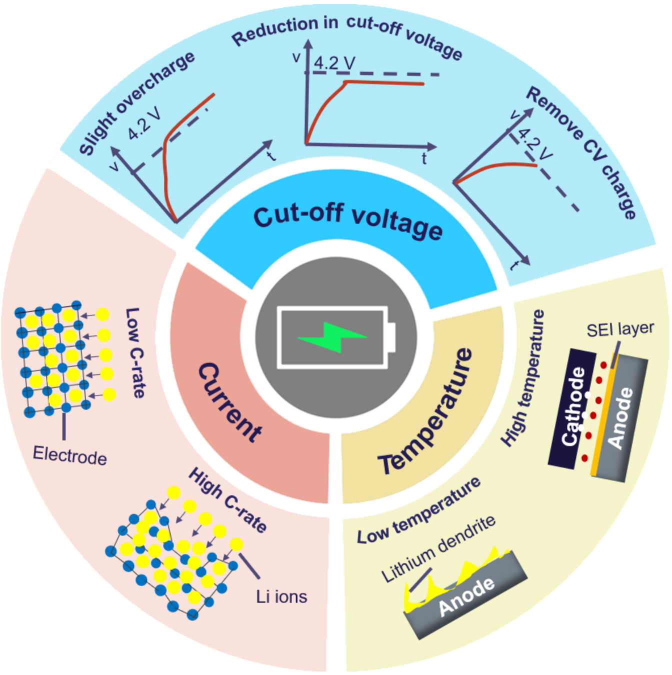

Figure 7. The influence on the battery aging from the factors of the charging process.

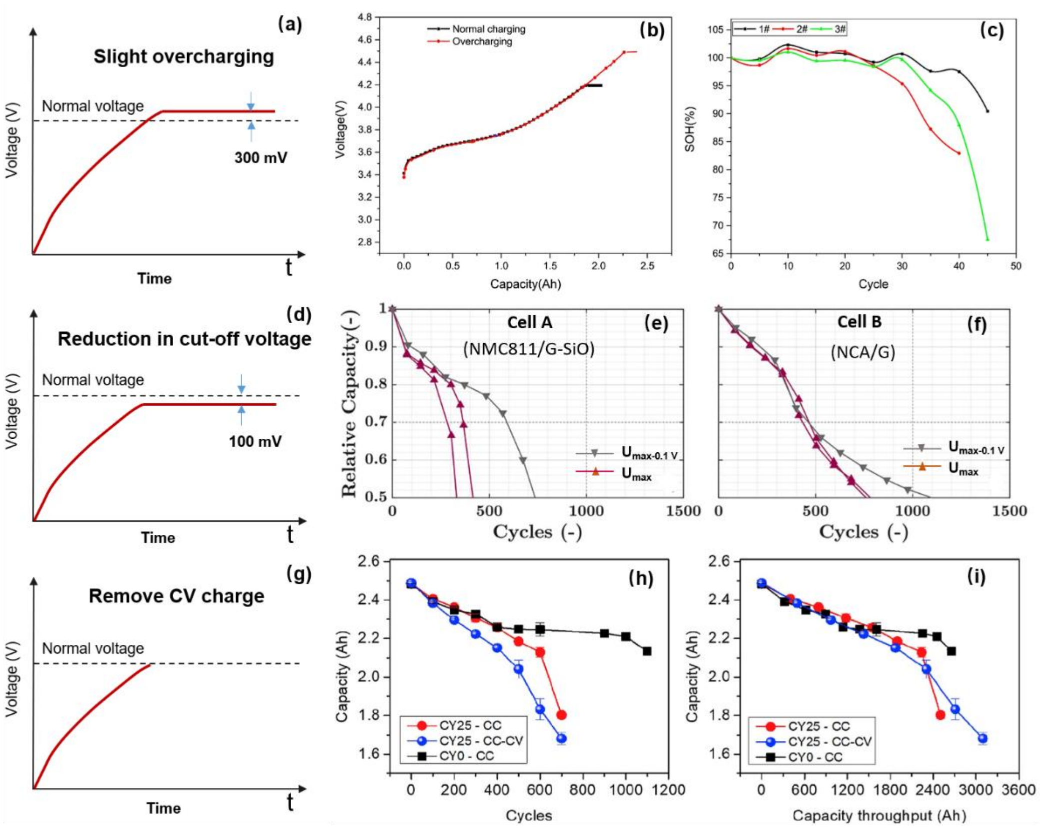

Figure 8. The effect of the charging voltage on the battery capacity fade. (**a**) the schematic diagram of slight overcharging; (**b**) charging/discharging profiles for standard and overcharge cells, (**c**) capacity fading of three LiBs under the same overcharging cycling condition (2.75–4.5 V) [52]. (**d**) the schematic diagram of reduction in cut-off voltage; (**e**) the capacity fade curves for cell A, (**f**) the capacity fade curves for cell B [53]. (**g**) the schematic diagram of CC charging protocol; (**h**) capacity degradation curves based on cycles; (**i**) capacity degradation curves based on throughput [54].

In contrast, in [53], Rathieu et al. charged two different types of batteries with a slight reduction of 100 mV in the cut-off voltage, as shown in Figure 8d. For battery A (i.e., 3.0 Ah, NMC 811/G-SiO), the reduction of the cut-off voltage led to both a lower charging time and a lower degradation (Figure 8e); however, this results in a reduction of the charged capacity (i.e., only 83%). For battery B (i.e., 2.5 Ah, NCA/G), there is no significant reduction in the charging time or in the degradation (Figure 8f), but a lower capacity is achieved (i.e., 89%).

Furthermore, in [54], the author analyzed the contribution of the constant voltage process to the battery charging, and charged 18650-type batteries (2.5 Ah, NMC/Graphite, and NCA/Graphite) by the CC (2.5 A to 4.2 V) (Figure 8g) and CC-CV protocols (2.5 A to 4.2 V and 0.1 A cut-off current) at room temperature, respectively. The battery charged with the CC-CV protocol lost 20% of its capacity after 500 cycles, while the battery charged only with the CC protocol reached the same degradation level after 600 cycles, as shown in Figure 8h. From Figure 8i, it can be seen that the batteries contribute a similar total capacity throughput charged by CC-CV and CC protocols. However, using the CC-CV protocol, more capacity (about 20%) can be charged in comparison to the CC protocol.

It can be concluded that slight overcharging will increase the capacity but will obviously accelerate the battery aging. For the reduction in cut-off voltage and the removing of the CV charging, there is no significant reduction in the charging time and in the degradation, but a lower capacity is achieved.

4.1.2. Impact of the Charging Current

In charging, the current I_{ch} is an important parameter for charging speed. Spingler et al. [55] charged batteries (i.e., NMC/graphite, 3.3 Ah) with a constant current between 1.0 C and 2.0 C. The capacity loss and both average and maximum local irreversible expansion per cycle are shown in Figure 9a. With the increase of the C-rate, the battery capacity fade becomes more and more obvious. Furthermore, the irreversible expansion and capacity loss are correlated with a bivariate correlation of 0.996. This means that a higher charging rate will lead to a larger irreversible expansion, corresponding to a growing tendency for capacity loss. Especially for the 2 C charging, the fade of capacity is about 30 mAh per cycle.

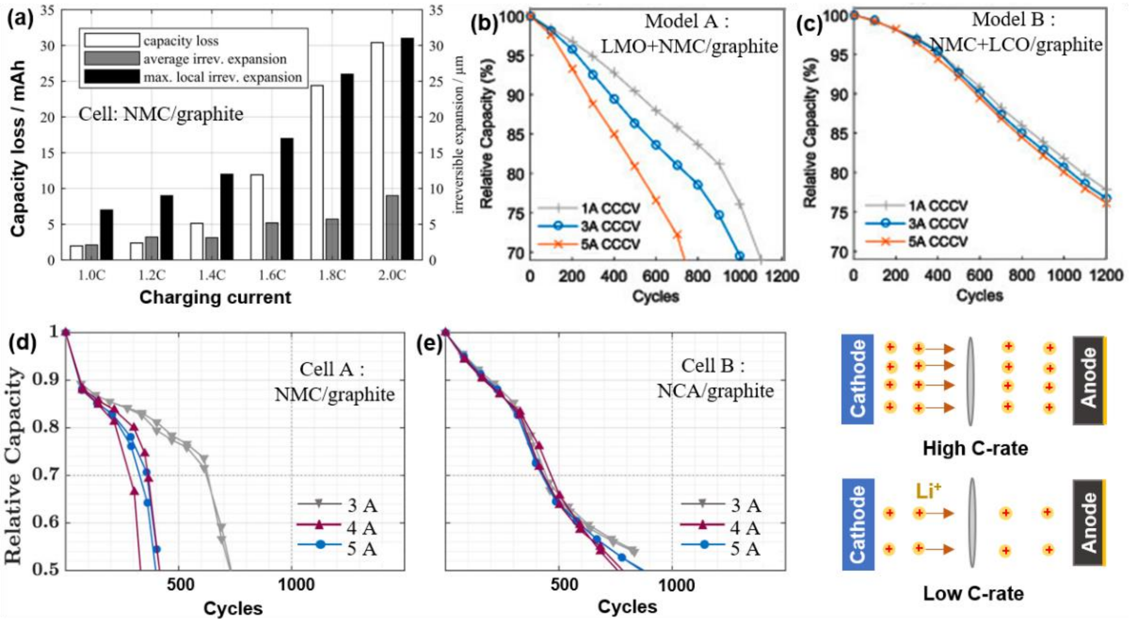

Figure 9. (**a**) Capacity loss and irreversible expansion per cycle as a function of C-rate in CC-CV charging [55]; (**b**,**c**) cycle life for different combinations of moderate (3 A) and high (5 A) charging current I_{ch} and discharging current I_{dis} [38]; (**d**,**e**) impact of charge current I_{ch} on cycle life at 25 °C for two types of batteries [53].

Keil et al. analyzed the impact of high charging currents on the cycle life of two different types of batteries: Model A (i.e., (LMO+NMC)/graphite) and Model B (i.e., (NMC+LCO)/graphite), as shown in Figure 9b,c, respectively [38]. For the Model A battery cell (Figure 9b), the increase in the charging C-rate (from 1 C to 5 C) increases the battery degradation (i.e., capacity fade). On the other hand, for the Model B battery cells, (Figure 9c) the battery degradation is not influenced by the charging C-rate, which may be related to the composition of the cathode.

Furthermore, in [53], the authors compared the influence of three different charging currents (i.e., 3 A, 4 A, and 5 A) on two LiBs, cell A (i.e., NMC/graphite) and cell B (i.e., NCA/graphite), considering two cells for each aging condition. The capacity degradation tendency, which is presented in Figure 9d (cell A) and Figure 9e (cell B), is similar for the two investigated chemistries; in the beginning, there is a high capacity loss, followed by a slower capacity fade in the middle of the life cycle, and ending with a sudden capacity degradation period. For cell A, the capacity fade behavior of the battery cells charged with 5 A and 4 A is similar, and a faster degradation is observed than for the cells charged with 3 A (especially after 20% capacity fade). On the other hand, it can be observed that the degradation paths are similar for cell B under all the currents from 3 A to 5 A (Figure 9e).

Based on the above studies, it can be concluded that, in most cases, higher charging current rates result in the faster degradation of LiBs; however, both the degradation trend and the influence of the charging rate change from chemistry-to-chemistry.

4.1.3. Impact of Charging Temperature

At low-temperatures, LiBs are characterized. In [56], the authors assessed the battery (i.e., NCA/graphite, 2.9 Ah) charging in different low temperatures (i.e., −5 °C, −10 °C, −15 °C and −20 °C). After charging to full state, they set a 3 h rest at room temperature for the batteries, and then discharged all the batteries at 25 °C. At low temperatures, not only is the charging efficiency lowered, but the energy that can be charged is correspondingly reduced. Moreover, the authors found that the capacity obviously declines, with the reduction in the ambient charging temperature. In the harsh conditions of −20 °C, the battery capacity drops to 72% after only eight cycles. In contrast, at higher temperatures (>+40 °C), the charging capacity increases and the internal resistance decreases further, compared with charging at room temperature [57].

To conclude, the aging of the battery during the charging process is affected by the cut-off voltage, current and temperature. High cut-off voltage, high current and extreme temperatures (both low and high temperatures) will accelerate the battery aging.

4.2. Aging in Driving

The battery degradation in EV driving is sensitive to a variety of factors from the behavior of the user to the environmental conditions. The mileage of the EV's daily use is related to the battery depth of discharge (DOD); driving speed and acceleration are related to the battery discharge current; and the main environmental factor that influences the battery aging is the temperature. These factors and the corresponding influences on the battery are summarized in Figure 10.

Performing laboratory accelerated aging test is an effective method to analyze degradation in EV batteries. In [58], Stroe et al. carried out a daily aging profile (e.g., WLTC), which consisted of 22 h cycling and 2 h stand-by, as presented in Figure 11a, and analyzing and assessing the aging of NMC-based battery cells. Furthermore, the temperature changed monthly in accordance with the climate of Seville, Spain. After eleven months of accelerated aging, the two tested cells lost approximately 10% of their initial capacity (Figure 11b). A slow down tendency of the capacity fade appeared as the aging of the battery evolved, and the authors attributed this to the irreversible capacity loss caused by the formation and growth of the solid electrolyte interface (SEI) layer in the initial stages. The relationship between the monthly capacity fade and the temperature is shown in Figure 11c. The highest capacity fade occurs in the first month, approximately 3%, corresponding to a cycling temperature of 36 °C. They also found that the degradation is minimal when the battery is cycled at 26 °C (approximately room temperature). In addition, the increase of internal resistance accelerates as the aging process evolves during the eleven months of testing (Figure 11d). In [59], the author obtained a similar conclusion that the capacity of pouch cell (e.g., NMC/graphite, 20 Ah) will fade more quickly in high-temperature driving. They show that after 2184 cycles, the battery lost 19.2% capacity when aged using the WLTC at 45 °C. On the contrary, when the battery was aged at a temperature of 10 °C, almost no capacity degradation was observed after 1428 cycles.

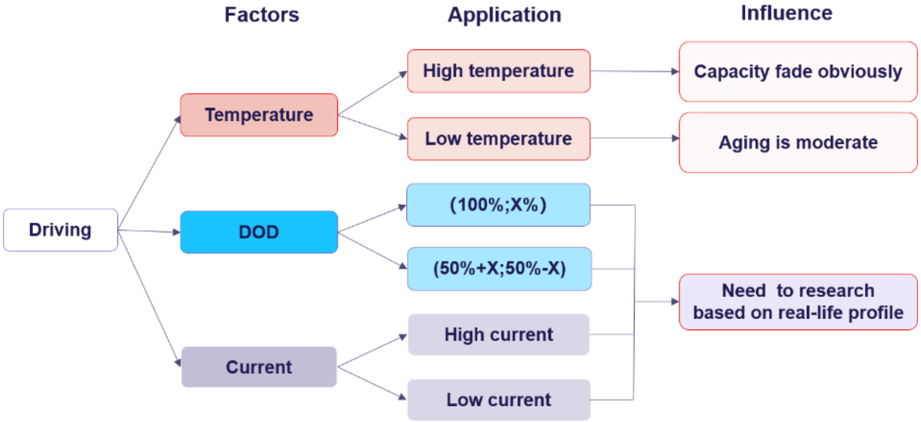

Figure 10. The influence in battery aging from common factors in driving (WLTC) test.

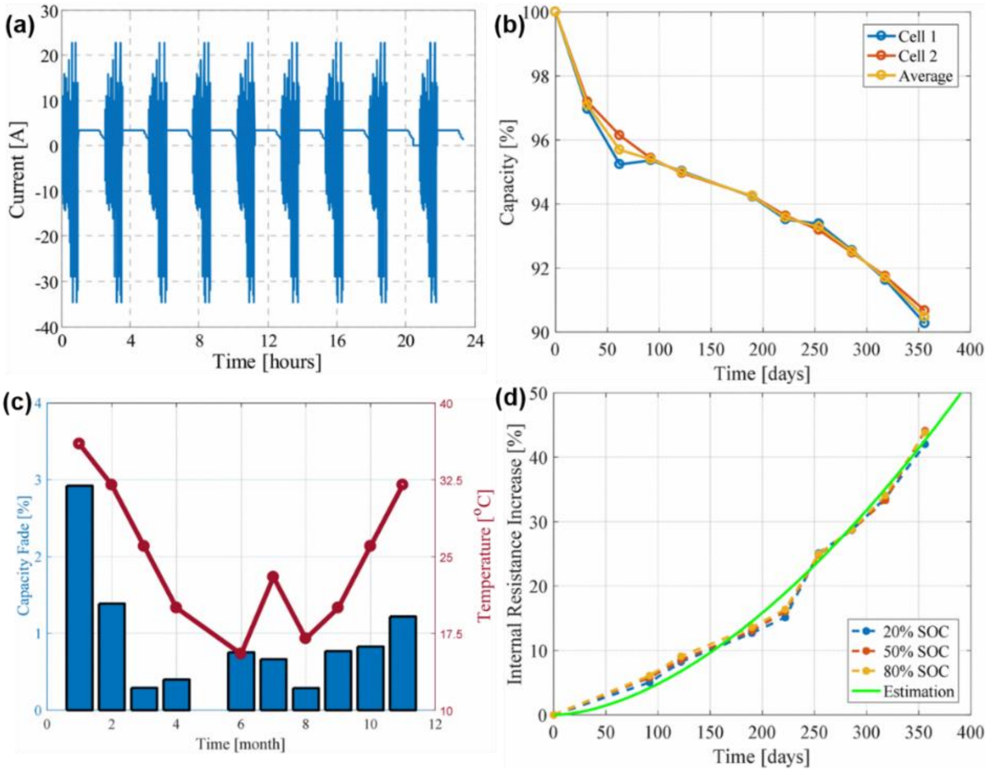

Figure 11. (**a**) One−day load current profile for accelerated aging based on WLTC driving cycle; (**b**) capacity fade of the tested NMC-based cells during eleven months of accelerated aging tests; (**c**) correlation between the monthly measured battery capacity fade and the considered temperature; (**d**) measured internal resistance increase at different SOC [58].

In [58], it was predicted that the battery will reach 20% capacity fade under the considered aging profile (based on the WLTC driving cycle) after approximately 5.8 years. To further accelerate battery aging, Simolka et al. selected the last part of the WLTC driving cycle (called "extra high"), corresponding to high currents, and named it as "AP1" [60]. Based on AP1, the authors then doubled the current load in order to create a new profile: "AP2". The capacity fade of the LFP/G cells was tested based on AP1 and AP2 profiles; at the same time, two DODs (i.e., 50% and 100%) were performed. These methods are very suitable for studying the real-life applications of batteries in EVs. However, there are few studies about NMC and NCA battery discharge based on these methods, currently.

Overdischarging also leads to the degradation of the battery. In [61], the author found that overdischarging deteriorates the electrode materials. On the one hand, as the discharging cut-off voltage decreases, the surface temperature of the battery increases significantly, leading to transition metal dissolution at cathode; on the other hand, overdischarging causes irreversible structural transformation of cathode and anode, resulting in a decrease in capacity. As presented by Lai et al. in [62], the critical over-discharging range for the DOD is from 115% to 120%. When over-discharging exceeds this range (i.e., more than 20% overdischarging), the rate of capacity degradation is greatly accelerated. If the open-circuit voltage of the battery does not recover to values higher than 2 V during the rest process, this may lead to an irreversible internal short circuit. Even worse, an explosion caused by overdischarge when the external temperature is high has been reported [63].

It can be concluded that high temperatures will accelerate battery degradation in real-life driving. Furthermore, overdischarging will also lead to battery degradation.

4.3. Aging in Standby

The standby state takes up a considerable amount of time in EVs' real-life operation, and the contribution to total aging is significant. The pace of the degradation process during standby, known as calendar aging, varies depending on the SOC and temperature.

The effect of the SOC and temperature on the capacity fade of NMC-based LiBs is exemplified in Figure 12a [64]. It is evident that the battery capacity fade is more notable at high temperatures than at a moderate temperature. In addition, high SOCs will also accelerate capacity fade due to the high voltage. As expected, the highest capacity degradation occurs in the toughest conditions, with a high storage SOC (80%), and the highest temperatures (45 °C) among these cases. The calendar aging situation is presented in Figure 12b. In [65], the authors varied the storage SOC from 5% to 95%, and obtained a similar conclusion that a higher SOC (i.e., over 70%) will accelerate the battery (e.g., LTO/NMC) aging significantly during 300 days of calendar aging. However, there is no evident capacity degradation in cells with a SOC below 70%, even at 60 °C. This behavior occurs because the LTO/NMC cells are more stable than other cells, even at high temperatures. However, as reported in [66], when the cells (i.e., LMO+NMC/graphite) were stored at a middle SOC (i.e., 50%), the degradation is faster than for the cells which were stored at extreme SOCs (i.e., 10% and 90%). This is different from what was presented in previous literature that showed an increase in degradation by increasing the SOC at 25 °C. However, it is obvious from most of the available literature that storage/idling the LiBs at low SOCs and in low temperatures will result in slower capacity fade and, subsequently, a long lifetime. Some of the recent work investigating the calendar aging of NMC- and NCA-based LiBs is summarized in Table 4.

Table 4. Comparison of calendar aging procedures and main conclusion from some work in current literature.

Battery Type	Chemistry	Temperature °C	SOC (%)	Main Conclusion	Sources
SIMCAL (2009–2012)	NMC	0, 25, 45 and 60	0, 30, 65, 80 and 100	Higher SOC leads to higher capacity loss; temperature over 30 °C begin to accelerate the aging	[67]
Panasonic NCR18650BD	LiC_6/NCA	10, 25 and 45	20, 50 and 90	Accelerate aging obviously occurs in 45 °C or 90% SOC case	[68]
Panasonic NCR18650PD	G/NCA	10, 25 and 40	30, 45, 60, 75 and 90	Higher temperature leads to higher capacity fade from 10 °C to 40 °C	[69]
Panasonic NCR18650PD	G/NCA	25, 40 and 50	5, 10, 20, 30, 40, 45, 50, 55, 60, 65, 70, 80, 90, 95 and 100	Accelerate aging with the increasing of SOC or storage temperature	[70]
SanyoUR18650E	G/NMC				
EIG NMC pouch cell	G/NMC	10, 25 and 45	10, 40 and 80	Higher SOC accelerates capacity fade, which is prominent at a higher temperature than at moderate temperature	[59]
Pouch cell	LTO/NMC	40, 60 and 80	5, 20, 55, 70, 90 and 95	There is no obvious relationship between temperature and capacity fade for LTO/NMC, while the internal resistance increased significantly.	[65]
EIG NMC pouch cell	G/NMC	25, 35 and 45	20, 35, 50, 65, 80 and 100	Accelerate aging with the increasing of SOC or storage temperature	[64]

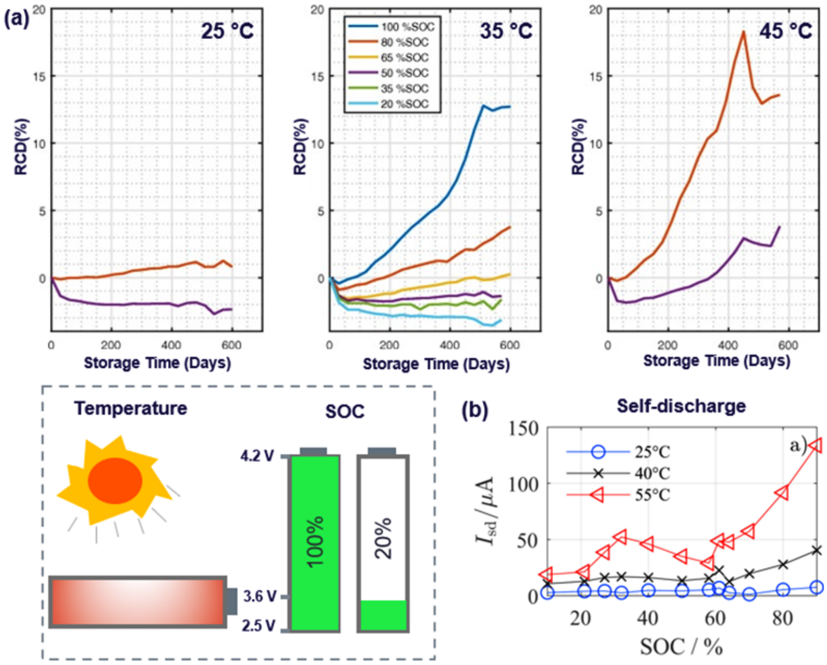

Figure 12. Battery performance-degradation during standby operation; (**a**) the influence of temperature and SOC on the battery capacity during calendar aging [64]; (**b**) self-discharge current for different temperature and SOCs [71].

Self-discharge is also an important process during calendar aging, which results in voltage decay and lower available energy. In [71], the authors analyzed the self-discharge dependence on the temperature and SOC in a commercial cell. As shown in Figure 12b, they found a self-discharge current from 2.0 µA to 4.5 µA at 25 °C, which is equivalent to 0.04–0.1% of the reversible capacity loss in one month; as the standby temperature increase from 25 °C to 55 °C, the self-discharge current increase to 135 µA at 90% SOC. Furthermore, the self-discharge current increases with the increase of SOC, and the growth trend is particularly obvious at a high temperature of 55 °C.

Based on the above analysis, during standby operation, high temperature and high SOC, the degradation of the battery will be accelerated and the self-discharge phenomenon will be more obvious.

4.4. Aging in Whole Application

Aging during standby operation is a very slow process, and it may take more than ten years at room temperature before a battery reaches its end-of-life (EOL); however, this operation takes up to 80% of the battery operation time in EV applications [72]. As such, the impacts of standby aging cannot be underestimated. Low temperatures (e.g., 0–25 °C) and a low SOC can effectively slow down the battery aging in standby [73].

Aging during the charging process is inevitable. Compared with driving aging, the charging aging process is easier to be controlled. Usually, various charging methods can be used to minimize the battery degradation and reduce the charging time.

Usually, the main aging of the battery is caused by driving [47]. Driving aging is the most complicated and uncontrollable. It is related to the driver's route and driving environment, and differs due to different driving conditions.

In short, suitable temperatures, low SOC states in the standby process, and optimized charging methods can minimize battery aging. For the complicated aging during driving operation, some external protection measures (e.g., thermal management, battery pack design, and so on) are necessary to prolong the life of battery.

5. Aging on Lithium-Ion Batteries

In Section 4, we separately analyzed the battery degradation in charging, driving and standby operation, and the corresponding stress factors (e.g., temperature, current, overdischarging etc.) were also summarized. The reason for battery degradation is that these factors lead to deterioration in the internal components of LiBs. In this section, we systematically review the main aging mechanisms at both the anode and cathode of LiBs, as well as in the electrolyte.

5.1. Aging at the Cathode

Changes in the cathode, such as phase transition, cracking in particles, transition metal dissolution (TMD), CEI film formation, binder decomposition, and loss contrast with collector have an evident influence on the aging of LiBs [5,8].

The loss of active materials on the cathode is a common aging process and is reflected in many aspects. The cathode structure is prone to changes during both standby, charging and driving aging [12]. Especially in high current rate operations, many Li^+ achieve intercalation or de-intercalation from the cathode in a short time, which influences the irreversible disorder phase transition in the cathode structure. Even worse, battery long-term cycling under high voltage or high current will lead to cracks in the cathode material. The generated fractures hinder the diffusion of Li^+ and lead to severe capacity fade [74]. Furthermore, the appearance of cracks will result in an unstable structure of the cathode, which by prolonged cycling, will further cause powdering and collapse of the cathode materials [75]. If the cracks are distributed inside the cathode, the diffusion of Li^+ is difficult to achieve due to the lack of contact with the electrolyte, this may result in some cathode materials being in an "isolated" state. Moreover, the battery operation at a high voltage (at high SOC level) or high environment temperature will accelerate the dissolution of the transition metal (TMD), especially for the Mn element, which dissolves in organic solvents, producing water and HF [76]. The produced HF continues to dissolve the transition metals and the Li^+ on the surface of the cathode, leading to significant capacity fade [77].

The loss of the Li^+ in the cathode is mainly attributed to the formation of the cathode-electrolyte interface (CEI) film. The CEI film, which is similar to SEI film, consists of lithium alkyl carbonates, lithium alkoxides (ROLi), Li_2CO_3, etc. [78]. These compounds result mainly from the side reaction between cathodes and electrolytes. Operation of the battery at a high voltage (SOC) will accelerate the decomposition of electrolytes and produce more

HF which erodes the cathode, resulting in more CEI ingredients [76]. Furthermore, when the battery is in charging and driving with high current rates, the side reactions will also be enhanced because large currents increase the temperature significantly. The electrolyte is easily decomposed at high temperatures, and this will accelerate CEI production [79]. Operation at high temperatures will also lead to binder decomposition and the current collector dissolution. The degradation of the binder will lead to the structure of the positive electrode being unstable, as a loss of contact in the electrodes results in an internal resistance rise in battery [80].

All these main degradation mechanisms, corresponding to the cathode, are presented in Figure 13.

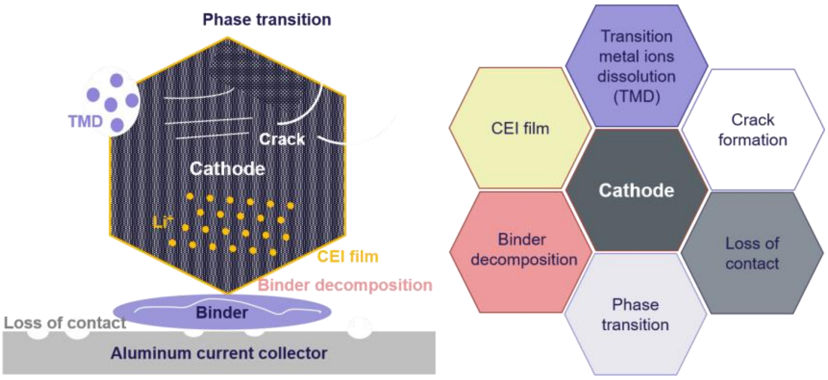

Figure 13. The main degradation mechanisms at the cathode of a lithium-ion battery.

5.2. Aging at the Electrolyte

The electrolyte transports Li^+ between the cathode and anode, and it is an important part of LiBs. The cycle stability, capacity, safety, and operating condition of LiBs are dependent on the electrolyte [81]. Conventional electrolytes usually consist of lithium hexafluorophosphate ($LiPF_6$) and other organic carbonates, such as ethyl methyl carbonate (EMC), dimethyl carbonate (DMC), and diethyl carbonate (DEC).

The $LiPF_6$ is not stable, and it can be easily decomposed into LiF and PF_5 [82]. The electrolyte aging starts with the reaction of organic carbonates and PF_5. From the electrochemical reaction at the charged anode, these products will then form a surface film on the anode, known as SEI film [83]. At the same time, a CEI film will form on the cathode surface. The stable and dense surface film can inhibit the electrode's surface exposure to electrolytes, effectively reducing the reaction between the electrolytes and electrode [84]. However, the continuous rupture and regeneration of the SEI and CEI films during the battery cycling will continue to consume Li^+. This will result in reduced battery capacity. At present, some electrolyte lithium additives have been added to the electrolyte to form a more stable SEI film [85–87].

Especially in the charged state or at high temperatures, the electrolyte decomposition is an inherent risk, leading to gas formation inside batteries; this may lead to severe developments, such as a rise in the inner pressure of the battery cell, fire, or even explosions. In [88], Gerelt-Od et al. investigated the overcharging of battery cells from 4.2 to 4.4 V in moderate temperatures of 35–45 °C, which are the normal operating conditions in real life. Four main gases (i.e., H_2, CH_4, CO_2, and CO) were detected when cells were exposed to the aforementioned electrical and thermal conditions. With the increase in battery voltage, more H_2 will be produced.

5.3. Aging at the Anode

The major aging mechanisms at the anode of LiBs are solid electrolyte interphase (SEI) formation, anode volume expansion, lithium metallization, loss of contact, and transition metal ions reduction.

The process of SEI film formation is complex and mainly happens during the first several charging and driving process. In those processes, firstly, the Li^+ from the cathode and the organic compounds from the electrolyte reacts with the graphite anode producing an SEI film with a thickness usually estimated between a few angstroms up to tens of nanometers [89]. The formation of SEI film consumes Li^+, resulting in the loss of the lithium inventory, and, subsequently, capacity fade. The SEI formation can consume up to 10% of the initial battery capacity [90]. A stable SEI film is beneficial to the anode, as it coats the anode surface and inhibits the direct contact between the electrolyte and the anode, reducing further side reactions. Furthermore, the SEI film also has high selective permeability for Li^+. However, the SEI growth is difficult to control, because it is highly dependent on the type of material and morphology of the anode, battery temperature, electrolyte composition, and electrochemical conditions [8]. Moreover, the SEI film is easy to corrode after the long-term operation of the battery. Subsequently, the cracked SEI film will expose the anode to the electrolyte, leading to additional SEI growth and capacity loss. Electrolyte decomposition and side reactions will produce gas and exacerbate this degradation process. Even worse, during charging and driving, the graphite volume expands by approximately 10% [9]. Cracking of the SEI film is accelerated by cycling at high DOD levels and/or idling the battery at elevated SOCs. All of these processes will consume Li^+ to generate the SEI film, resulting in capacity fade and resistance increase.

The formation of lithium metal is also a common aging mechanism at the anode side. When the LiBs operate at high SOC, the anode will be intercalated with a lot of Li^+, resulting in a low potential of the anode (i.e., the redox potential of Li/Li^+ close to 0 V) [91]. When the partial anode polarization potential is below this voltage, the Li^+ will deposit on the anode surface, forming metallic lithium. Especially during cycling at a high DOD or during long-term idling at a high SOC, lithium dendrites will grow on the anode [92]. The formation of lithium dendrites not only reduces the usable Li^+, but also destroys the anode structure and, possibly, pierces the separator leading to short circuits and thermal runaway [93]. Finally, charging the battery with high current rates, which are greater than the speed of Li^+ diffusion to the anode, will lead to lithium plating. Moreover, the operation of the LiBs at low temperatures will lead to a slow Li^+ diffusion, producing more lithium plating and dendrite on the anode [94].

A high SOC state results in a high $Q_{\mathrm{NMC/SiC,}}$ which is related to the side reactions at the anode, including the dissolution of the Cu current collector and oxidation of the electrolyte. At the same time, a high temperature will accelerate this process. When the battery is stored in a high SOC, the self-discharge occurs significantly. Driven by the potential difference between the cathode and anode, the dissolved transition metal ions move from the cathode to the anode and are reduced by the charged anode forming metals deposits [95]. As a result, the deposited metals in an inactive state (e.g., "dead lithium") appear in the anode or on the copper current collector surface. The deposited metals, as cathode, then combine with the anode to form a micro-battery, which greatly reduces the current efficiency and aggravates the available capacity fade of the LiBs [96].

All the aforementioned anode aging mechanisms are illustrated in Figure 14.

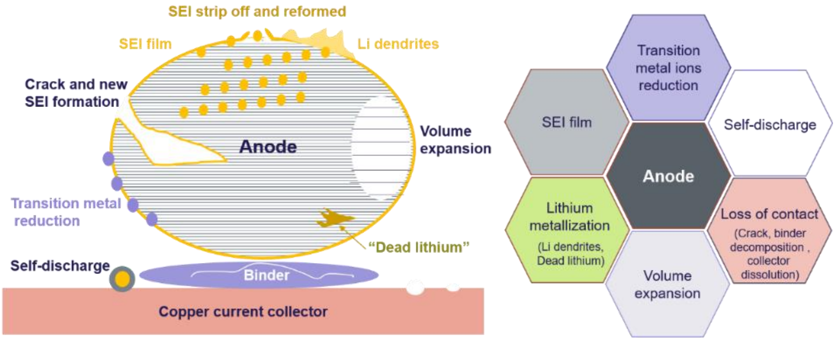

Figure 14. The main degradation mechanism at the anode side of a lithium-ion battery.

6. Conclusions

Because of their intrinsic properties, such as higher energy densities and low cost, Ni-based LiBs chemistries (i.e., NMC and NCA) are the preferred choices for powering EVs. As such, this work is mostly focused on reviewing the aging mechanisms and degradation behavior of these chemistries when used in various EV applications.

The long-term operation of LiBs in EVs involves many complex aging mechanisms. According to different application scenarios, this paper analyzes the battery aging behavior under EV charging, standby, and driving conditions, respectively. For all of the aforementioned conditions, we have individually linked the battery stress factors (e.g., temperature, cut-off voltage, etc.) to the battery performance and degradation behavior in EV applications. The effect of these stress factors (i.e., temperature, SOC, current, cut-off voltage, and DOD) on the degradation of the battery cathode, electrolyte, and anode is then fully analyzed. Therefore, this article provides a comprehensive review of the degradation of the battery performance parameters under EV operation, using driving cycles.

By minimizing exposure to the conditions that most accelerate battery aging, the life-span of the battery can be prolonged. High-temperature operation will cause side reactions in the battery, while lithium metalization on the anode is accelerated at low temperatures. Furthermore, a high charging current reduces the EV charging time but accelerate the battery aging to a significant extent. Finally, the high SOC operation (e.g., high cut-off voltage, idling at high SOC, and/or cycling at high DOD) also lead to accelerated degradation on the battery. All of these factors, which are specific to the EV battery operation, the triggered degradation mechanisms, and the effect on the battery performance parameters, are illustrated in Figure 15.

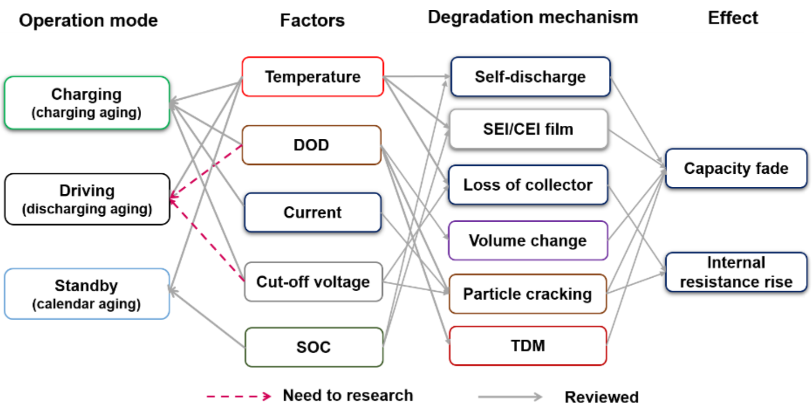

Figure 15. The main degradation mechanism of batteries in EV applications.

However, the battery degradation problem still needs further research, especially regarding EVs operation. At present, the literature regarding battery performance-degradation and subsequent aging mechanism identification is very limited and, frequently, is based on data that is obtained using standardized driving cycles, which do not always reflect the real-life battery operation in EVs.

Author Contributions: J.G. wrote the paper, J.G. and D.-I.S., designed the structures of the paper; Y.L. and K.P. reviewed the paper. All authors have read and agreed to the published version of the manuscript.

Funding: J.G. was supported by a grant from the China Scholarship Council (no. 202006370035); Y.L. was supported by a grant from the China Scholarship Council (no. 202006220024).

Institutional Review Board Statement: Not applicable.

Informed Consent Statement: Not applicable.

Data Availability Statement: Not applicable.

Conflicts of Interest: The authors declare no conflict of interest.

References

1. Deng, J.; Bae, C.; Denlinger, A.; Miller, T. Electric Vehicles Batteries: Requirements and Challenges. *Joule* **2020**, *4*, 511–515. [CrossRef]
2. Albertsen, L.; Richter, J.L.; Peck, P.; Dalhammar, C.; Plepys, A. Circular business models for electric vehicle lithium-ion batteries: An analysis of current practices of vehicle manufacturers and policies in the EU. *Resour. Conserv. Recycl.* **2021**, *172*, 105658. [CrossRef]
3. Pellow, M.A.; Ambrose, H.; Mulvaney, D.; Betita, R.; Shaw, S. Research gaps in environmental life cycle assessments of lithium ion batteries for grid-scale stationary energy storage systems: End-of-life options and other issues. *Sustain. Mater. Technol.* **2020**, *23*, e00120. [CrossRef]
4. El Ghossein, N.; Sari, A.; Venet, P.; Genies, S.; Azaïs, P. Post-Mortem Analysis of Lithium-Ion Capacitors after Accelerated Aging Tests. *J. Energy Storage* **2021**, *33*, 102039. [CrossRef]
5. Han, X.; Lu, L.; Zheng, Y.; Feng, X.; Li, Z.; Li, J.; Ouyang, M. A review on the key issues of the lithium ion battery degradation among the whole life cycle. *eTransportation* **2019**, *1*, 100005. [CrossRef]
6. Tian, H.; Qin, P.; Li, K.; Zhao, Z. A review of the state of health for lithium-ion batteries: Research status and suggestions. *J. Clean. Prod.* **2020**, *261*, 120813. [CrossRef]
7. Mocera, F.; Soma, A.; Clerici, D. Study of aging mechanisms in lithium-ion batteries for working vehicle applications. In Proceedings of the 2020 Fifteenth International Conference on Ecological Vehicles and Renewable Energies, Monte-Carlo, Monaco, 10–12 September 2020.
8. Woody, M.; Arbabzadeh, M.; Lewis, G.M.; Keoleian, G.A.; Stefanopoulou, A. Strategies to limit degradation and maximize Li-ion battery service lifetime-Critical review and guidance for stakeholders. *J. Energy Storage* **2020**, *28*, 101231. [CrossRef]
9. Balakrishnan, P.G.; Ramesh, R.; Prem Kumar, T. Safety mechanisms in lithium-ion batteries. *J. Power Sources* **2006**, *155*, 401–414. [CrossRef]
10. Broussely, M.; Biensan, P.; Bonhomme, F.; Blanchard, P.; Herreyre, S.; Nechev, K.; Staniewicz, R.J. Main aging mechanisms in Li ion batteries. *J. Power Sources* **2005**, *146*, 90–96. [CrossRef]
11. Barré, A.; Deguilhem, B.; Grolleau, S.; Gérard, M.; Suard, F.; Riu, D. A review on lithium-ion battery ageing mechanisms and estimations for automotive applications. *J. Power Sources* **2013**, *241*, 680–689. [CrossRef]
12. Birkl, C.R.; Roberts, M.R.; McTurk, E.; Bruce, P.G.; Howey, D.A. Degradation diagnostics for lithium ion cells. *J. Power Sources* **2017**, *341*, 373–386. [CrossRef]
13. Palacín, M.R. Understanding ageing in Li-ion batteries: A chemical issue. *Chem. Soc. Rev.* **2018**, *47*, 4924–4933. [CrossRef]
14. Xiong, R.; Pan, Y.; Shen, W.; Li, H.; Sun, F. Lithium-ion battery aging mechanisms and diagnosis method for automotive applications: Recent advances and perspectives. *Renew. Sustain. Energy Rev.* **2020**, *131*, 110048. [CrossRef]
15. Teichert, P.; Eshetu, G.G.; Jahnke, H.; Figgemeier, E. Degradation and aging routes of ni-rich cathode based li-ion batteries. *Batteries* **2020**, *6*, 8. [CrossRef]
16. Alipour, M.; Ziebert, C.; Conte, F.V.; Kizilel, R. A review on temperature-dependent electrochemical properties, aging, and performance of lithium-ion cells. *Batteries* **2020**, *6*, 35. [CrossRef]
17. Chen, Y.; Kang, Y.; Zhao, Y.; Wang, L.; Liu, J.; Li, Y.; Liang, Z.; He, X.; Li, X.; Tavajohi, N.; et al. A review of lithium-ion battery safety concerns: The issues, strategies, and testing standards. *J. Energy Chem.* **2021**, *59*, 83–99. [CrossRef]
18. Yang, S.; Zhang, C.; Jiang, J.; Zhang, W.; Zhang, L.; Wang, Y. Review on state-of-health of lithium-ion batteries: Characterizations, estimations and applications. *J. Clean. Prod.* **2021**, *314*, 128015. [CrossRef]
19. Balali, Y.; Stegen, S. Review of energy storage systems for vehicles based on technology, environmental impacts, and costs. *Renew. Sustain. Energy Rev.* **2021**, *135*, 110185. [CrossRef]
20. Tesla Other Europe. Powerwall. Available online: https://www.tesla.com/en_eu/powerwall (accessed on 18 July 2021).
21. Gerssen-Gondelach, S.J.; Faaij, A.P.C. Performance of batteries for electric vehicles on short and longer term. *J. Power Sources* **2012**, *212*, 111–129. [CrossRef]
22. Ajanovic, A.; Haas, R. Electric vehicles: Solution or new problem? *Environ. Dev. Sustain.* **2018**, *20*, 7–22. [CrossRef]
23. Ahmadian, A.; Mohammadi-Ivatloo, B.; Elkamel, A. A Review on Plug-in Electric Vehicles: Introduction, Current Status, and Load Modeling Techniques. *J. Mod. Power Syst. Clean Energy* **2020**, *8*, 412–425. [CrossRef]
24. EVD Compare Hybrid and Electric Vehicles-EV Database UK 2019. Available online: https://ev-database.uk/ (accessed on 18 July 2021).
25. Bureau of Transportation Statistics. Hybrid-Electric, Plug-in Hybrid-Electric and Electric Vehicle Sales. Available online: https://www.bts.gov/content/gasoline-hybrid-and-electric-vehicle-sales (accessed on 18 July 2021).
26. Li, Y.; Guo, J.; Chen, Y.; Deng, S.; Zhu, J.; Cao, G.; Lei, T.; Zhang, J. Phase transition regulation and Cd-O/Cd-F compounds multi-effect. *Ionics* **2020**, *26*, 1681–1693. [CrossRef]
27. Zhang, B.; Xu, Y.; Wang, J.; Lin, J.; Wang, C.; Chen, Y. Lanthanum and cerium Co-doped $LiFePO_4$: Morphology, electrochemical performance and kinetic study from −30–+50 °C. *Electrochim. Acta* **2019**, *322*, 134686. [CrossRef]
28. Sui, X.; Świerczyński, M.; Teodorescu, R.; Stroe, D.I. The degradation behavior of lifepo4/c batteries during long-term calendar aging. *Energies* **2021**, *14*, 1732. [CrossRef]

29. Zhu, J.; Cao, G.; Li, Y.; Wang, S.; Deng, S.; Guo, J.; Chen, Y.; Lei, T.; Zhang, J.; Chang, S. Nd_2O_3 encapsulation-assisted surface passivation of Ni-rich $LiNi_{0.8}Co_{0.1}Mn_{0.1}O_2$ active material and its electrochemical performance. *Electrochim. Acta* **2019**, *325*, 134889. [CrossRef]
30. Wu, F.; Maier, J.; Yu, Y. Guidelines and trends for next-generation rechargeable lithium and lithium-ion batteries. *Chem. Soc. Rev.* **2020**, *49*, 1569–1614. [CrossRef] [PubMed]
31. Li, W.; Lee, S.; Manthiram, A. High-Nickel NMA: A Cobalt-Free Alternative to NMC and NCA Cathodes for Lithium-Ion Batteries. *Adv. Mater.* **2020**, *32*, 2002718. [CrossRef]
32. Xu, L.; Zhou, F.; Liu, B.; Zhou, H.; Zhang, Q.; Kong, J.; Wang, Q. Cathode Material for High Energy Density Li-Ion Batteries. *Int. J. Electrochem.* **2018**, *2018*, 6930386. [CrossRef]
33. Noh, H.; Youn, S.; Seung, C.; Sun, Y. Comparison of the structural and electrochemical properties cathode material for lithium-ion batteries. *Power Sources* **2013**, *233*, 121–130. [CrossRef]
34. Zheng, J.; Yang, Z.; Dai, A.; Tang, L.; Wei, H.; Li, Y.; He, Z.; Lu, J. Boosting Cell Performance of $LiNi_{0.8}Co_{0.15}Al_{0.05}O_2$ via Surface Structure Design. *Small* **2019**, *15*, 1904854. [CrossRef] [PubMed]
35. Hu, G.; Liu, W.; Peng, Z.; Dua, K.; Cao, Y. Synthesis and electrochemical properties of $LiNi_{0.8}Co_{0.15}Al_{0.05}O_2$ prepared from the precursor $Ni_{0.8}Co_{0.15}Al_{0.05}OOH$. *J. Power Sources* **2012**, *198*, 258–263. [CrossRef]
36. Wang, S.; Li, Y.; Liu, S.; Deng, S.; Chen, Y.; Zhu, J.; Zhang, J.; Guo, J.; Chang, S. Superior Electrochemical and Kinetics Performance of $LiNi_{0.8}Co_{0.15}Al_{0.05}O_2$ Cathode by Neodymium Synergistic Modifying for Lithium Ion Batteries. *J. Electrochem. Soc.* **2020**, *167*, 090509. [CrossRef]
37. He, Y.F.; Chu, D.Y.; Zhuo, Z. Cycle Stability of Dual-Phase Lithium Titanate (LTO)/TiO_2 Nanowires as Lithium Battery Anode. *J. Multidiscip. Appl. Nat. Sci.* **2021**, *1*, 54–61. [CrossRef]
38. Keil, P.; Jossen, A. Charging protocols for lithium-ion batteries and their impact on cycle life-An experimental study with different 18650 high-power cells. *J. Energy Storage* **2016**, *6*, 125–141. [CrossRef]
39. Tomaszewska, A.; Chu, Z.; Feng, X.; O'Kane, S.; Liu, X.; Chen, J.; Ji, C.; Endler, E.; Li, R.; Liu, L.; et al. Lithium-ion battery fast charging: A review. *eTransportation* **2019**, *1*, 100011. [CrossRef]
40. Serhan, H.A.; Ahmed, E.M. Effect of the different charging techniques on battery life-time: Review. In Proceedings of the 2018 International Conference on Innovative Trends in Computer Engineering, ITCE, Aswan, Egypt, 19–21 February 2018; pp. 421–426. [CrossRef]
41. Huang, X.; Li, Y.; Acharya, A.B.; Sui, X.; Meng, J.; Teodorescu, R.; Stroe, D.I. A review of pulsed current technique for lithium-ion batteries. *Energies* **2020**, *13*, 2458. [CrossRef]
42. Attia, P.M.; Grover, A.; Jin, N.; Severson, K.A.; Markov, T.M.; Liao, Y.H.; Chen, M.H.; Cheong, B.; Perkins, N.; Yang, Z.; et al. Closed-loop optimization of fast-charging protocols for batteries with machine learning. *Nature* **2020**, *578*, 397–402. [CrossRef] [PubMed]
43. Huang, X.; Li, Y.; Meng, J.; Sui, X.; Teodorescu, R.; Stroe, D.I. The Effect of Pulsed Current on the Performance of Lithium-ion Batteries. In Proceedings of the ECCE 2020-IEEE Energy Conversion Congress and Exposition, Detroit, MI, USA, 11–15 October 2020; pp. 5633–5640. [CrossRef]
44. Paul, T.; Mesbahi, T.; Durand, S.; Flieller, D.; Uhring, W. Study and influence of standardized driving cycles on the sizing of li-ion battery / supercapacitor hybrid energy storage. In Proceedings of the 2019 IEEE Vehicle Power and Propulsion Conference, VPPC 2019-Proceedings, Hanoi, Vietnam, 14–17 October 2019. [CrossRef]
45. Sikha, G.; Ramadass, P.; Haran, B.S.; White, R.E.; Popov, B.N. Comparison of the capacity fade of Sony US 18650 cells charged with different protocols. *J. Power Sources* **2003**, *122*, 67–76. [CrossRef]
46. Varga, B.O.; Sagoian, A.; Mariasiu, F. Prediction of electric vehicle range: A comprehensive review of current issues and challenges. *Energies* **2019**, *12*, 946. [CrossRef]
47. Jafari, M.; Gauchia, A.; Zhao, S.; Zhang, K.; Gauchia, L. Electric Vehicle Battery Cycle Aging Evaluation in Real-World Daily Driving and Vehicle-to-Grid Services. *IEEE Trans. Transp. Electrif.* **2017**, *4*, 122–134. [CrossRef]
48. Patel, S.S.; Asakit, J. Real Driving Particulate Emissions from a Gasoline PHEV. Master's Thesis, Chalmers University of Technology, Goteborg, Sweden, 2020.
49. Ben-marzouk, M.; Pelissier, S.; Clerc, G.; Member, S.; Sari, A. Generation of a real-life battery usage pattern for electrical vehicle application and aging comparison with the WLTC profile. *IEEE Trans. Veh. Technol.* **2021**, *9545*, 5618–5627. [CrossRef]
50. Eddahech, A.; Briat, O.; Woirgard, E.; Vinassa, J.M. Remaining useful life prediction of lithium batteries in calendar ageing for automotive applications. *Microelectron. Reliab.* **2012**, *52*, 2438–2442. [CrossRef]
51. Swierczynski, M.; Stroe, D.I.; Stan, A.I.; Teodorescu, R.; Kær, S.K. Lifetime Estimation of the Nanophosphate LiFePO4/C Battery Chemistry Used in Fully Electric Vehicles. *IEEE Trans. Ind. Appl.* **2015**, *51*, 3453–3461. [CrossRef]
52. Liu, J.; Duan, Q.; Ma, M.; Zhao, C.; Sun, J.; Wang, Q. Aging mechanisms and thermal stability of aged commercial 18650 lithium ion battery induced by slight overcharging cycling. *J. Power Sources* **2020**, *445*, 227263. [CrossRef]
53. Mathieu, R.; Briat, O.; Gyan, P.; Vinassa, J.M. Comparison of the impact of fast charging on the cycle life of three lithium-ion cells under several parameters of charge protocol and temperatures. *Appl. Energy* **2021**, *283*, 116344. [CrossRef]
54. Zhu, J.; Dewi Darma, M.S.; Knapp, M.; Sørensen, D.R.; Heere, M.; Fang, Q.; Wang, X.; Dai, H.; Mereacre, L.; Senyshyn, A.; et al. Investigation of lithium-ion battery degradation mechanisms by combining differential voltage analysis and alternating current impedance. *J. Power Sources* **2020**, *448*, 28–30. [CrossRef]

55. Spingler, F.B.; Wittmann, W.; Sturm, J.; Rieger, B.; Jossen, A. Optimum fast charging of lithium-ion pouch cells based on local volume expansion criteria. *J. Power Sources* **2018**, *393*, 152–160. [CrossRef]
56. You, H.; Dai, H.; Li, L. *The Aging Law of Low Temperature Charging of Lithium-Ion Battery*; SAE Technical Papers; Tongji University: Shanghai, China, 2019.
57. Lindgren, J.; Lund, P.D. Effect of extreme temperatures on battery charging and performance of electric vehicles. *J. Power Sources* **2016**, *328*, 37–45. [CrossRef]
58. Stroe, D.I.; Swierczynski, M.; Kær, S.K.; Laserna, E.M.; Zabala, E.S. Accelerated aging of lithium-ion batteries based on electric vehicle mission profile. In Proceedings of the 2017 IEEE Energy Conversion Congress and Exposition, ECCE 2017, Cincinnati, OH, USA, 1–5 October 2017; pp. 5631–5637. [CrossRef]
59. Hosen, M.S.; Karimi, D.; Kalogiannis, T.; Pirooz, A.; Jaguemont, J.; Berecibar, M.; Van Mierlo, J. Electro-aging model development of nickel-manganese-cobalt lithium-ion technology validated with light and heavy-duty real-life profiles. *J. Energy Storage* **2020**, *28*, 101265. [CrossRef]
60. Simolka, M.; Heger, J.F.; Kaess, H.; Biswas, I.; Friedrich, K.A. Influence of cycling profile, depth of discharge and temperature on commercial LFP/C cell ageing: Post-mortem material analysis of structure, morphology and chemical composition. *J. Appl. Electrochem.* **2020**, *50*, 1101–1117. [CrossRef]
61. Ouyang, D.; Weng, J.; Chen, M.; Liu, J.; Wang, J. Experimental analysis on the degradation behavior of overdischarged lithium-ion battery combined with the effect of high-temperature environment. *Int. J. Energy Res.* **2020**, *44*, 229–241. [CrossRef]
62. Lai, X.; Zheng, Y.; Zhou, L.; Gao, W. Electrical behavior of overdischarge-induced internal short circuit in lithium-ion cells. *Electrochim. Acta* **2018**, *278*, 245–254. [CrossRef]
63. Ouyang, D.; Chen, M.; Liu, J.; Wei, R.; Weng, J.; Wang, J. Investigation of a commercial lithium-ion battery under overcharge/over-discharge failure conditions. *RSC Adv.* **2018**, *8*, 33414–33424. [CrossRef]
64. De Hoog, J.; Timmermans, J.M.; Ioan-Stroe, D.; Swierczynski, M.; Jaguemont, J.; Goutam, S.; Omar, N.; Van Mierlo, J.; Van Den Bossche, P. Combined cycling and calendar capacity fade modeling of a Nickel-Manganese-Cobalt Oxide Cell with real-life profile validation. *Appl. Energy* **2017**, *200*, 47–61. [CrossRef]
65. Bank, T.; Feldmann, J.; Klamor, S.; Bihn, S.; Sauer, D.U. Extensive aging analysis of high-power lithium titanate oxide batteries: Impact of the passive electrode effect. *J. Power Sources* **2020**, *473*, 228566. [CrossRef]
66. Stroe, D.I.; Schaltz, E. Lithium-Ion Battery State-of-Health Estimation Using the Incremental Capacity Analysis Technique. *IEEE Trans. Ind. Appl.* **2020**, *56*, 678–685. [CrossRef]
67. Ben-Marzouk, M.; Chaumond, A.; Redondo-Iglesias, E.; Montaru, M.; Pélissier, S. Experimental protocols and first results of calendar and/or cycling aging study of lithium-ion batteries-The MOBICUS project. *World Electr. Veh. J.* **2016**, *8*, 388–397. [CrossRef]
68. Liu, K.; Ashwin, T.R.; Hu, X.; Lucu, M.; Widanage, W.D. An evaluation study of different modelling techniques for calendar ageing prediction of lithium-ion batteries. *Renew. Sustain. Energy Rev.* **2020**, *131*, 110017. [CrossRef]
69. Keil, P.; Jossen, A. Impact of Dynamic Driving Loads and Regenerative Braking on the Aging of Lithium-Ion Batteries in Electric Vehicles. *J. Electrochem. Soc.* **2017**, *164*, A3081–A3092. [CrossRef]
70. Keil, P.; Schuster, S.F.; Wilhelm, J.; Travi, J.; Hauser, A.; Karl, R.C.; Jossen, A. Calendar Aging of Lithium-Ion Batteries. *J. Electrochem. Soc.* **2016**, *163*, A1872–A1880. [CrossRef]
71. Zilberman, I.; Sturm, J.; Jossen, A. Reversible self-discharge and calendar aging of 18650 nickel-rich, silicon-graphite lithium-ion cells. *J. Power Sources* **2019**, *425*, 217–226. [CrossRef]
72. Wang, D.; Coignard, J.; Zeng, T.; Zhang, C.; Saxena, S. Quantifying electric vehicle battery degradation from driving vs. vehicle-to-grid services. *J. Power Sources* **2016**, *332*, 193–203. [CrossRef]
73. Yang, S.; Deng, C.; Zhang, Y.; He, Y. State of charge estimation for lithium-ion battery with a temperature-compensated model. *Energies* **2017**, *10*, 1560. [CrossRef]
74. Han, Y.; Heng, S.; Wang, Y.; Qu, Q.; Zheng, H. Anchoring Interfacial Nickel Cations on Single-Crystal $LiNi_{0.8}Co_{0.1}Mn0.1O_2$ Cathode Surface via Controllable Electron Transfer. *ACS Energy Lett.* **2020**, *5*, 2421–2433. [CrossRef]
75. Guo, J.; Li, Y.; Chen, Y.; Deng, S.; Zhu, J.; Wang, S.; Zhang, J.; Chang, S.; Zhang, D.; Xi, X. Stable interface Co_3O_4 -coated $LiNi_{0.5}$ $Mn_{1.5}$ O_4 for lithium-ion batteries. *J. Alloys Compd.* **2019**, *811*, 152031. [CrossRef]
76. Zhou, R.; Huang, J.; Lai, S.; Li, J.; Wang, F.; Chen, Z.; Lin, W.; Li, C.; Wang, J.; Zhao, J. A bifunctional electrolyte additive for H_2O/HF scavenging and enhanced graphite/$LiNi_{0.5}Co_{0.2}Mn_{0.3}O_2$ cell performance at a high voltage. *Sustain. Energy Fuels* **2018**, *2*, 1481–1490. [CrossRef]
77. Hemmelmann, H.; Dinter, J.K.; Elm, M.T. Thin Film NCM Cathodes as Model Systems to Assess the Influence of Coating Layers on the Electrochemical Performance of Lithium Ion Batteries. *Adv. Mater. Interfaces* **2021**, *8*, 2002074. [CrossRef]
78. Jie, Y.; Ren, X.; Cao, R.; Cai, W.; Jiao, S. Advanced Liquid Electrolytes for Rechargeable Li Metal Batteries. *Adv. Funct. Mater.* **2020**, *30*, 1910777. [CrossRef]
79. Hekmatfar, M.; Hasa, I.; Eghbal, R.; Carvalho, D.V.; Moretti, A.; Passerini, S. Effect of Electrolyte Additives on the $LiNi_{0.5}Mn_{0.3}Co_{0.2}O_2$ Surface Film Formation with Lithium and Graphite Negative Electrodes. *Adv. Mater. Interfaces* **2020**, *7*, 1901500. [CrossRef]
80. Zhao, C.Z.; Zhao, Q.; Liu, X.; Zheng, J.; Stalin, S.; Zhang, Q.; Archer, L.A. Rechargeable Lithium Metal Batteries with an In-Built Solid-State Polymer Electrolyte and a High Voltage/Loading Ni-Rich Layered Cathode. *Adv. Mater.* **2020**, *32*, 1905629. [CrossRef]

81. Li, Y.; Wan, S.; Veith, G.M.; Unocic, R.R.; Paranthaman, M.P.; Dai, S.; Sun, X.G. A Novel Electrolyte Salt Additive for Lithium-Ion Batteries with Voltages Greater than 4.7 V. *Adv. Energy Mater.* **2017**, *7*, 1601397. [CrossRef]
82. Heiskanen, S.K.; Kim, J.; Lucht, B.L. Generation and Evolution of the Solid Electrolyte Interphase of Lithium-Ion Batteries. *Joule* **2019**, *3*, 2322–2333. [CrossRef]
83. Horsthemke, F.; Leißing, M.; Winkler, V.; Friesen, A.; Ibing, L.; Winter, M.; Nowak, S. Development of a lithium ion cell enabling in situ analyses of the electrolyte using gas chromatographic techniques. *Electrochim. Acta* **2020**, *338*, 135894. [CrossRef]
84. Wang, C.; Yu, L.; Fan, W.; Liu, J.; Ouyang, L.; Yang, L.; Zhu, M. Lithium Difluorophosphate As a Promising Electrolyte Lithium Additive for High-Voltage Lithium-Ion Batteries. *ACS Appl. Energy Mater.* **2018**, *1*, 2647–2656. [CrossRef]
85. Deng, K.; Zeng, Q.; Wang, D.; Liu, Z.; Wang, G.; Qiu, Z.; Zhang, Y.; Xiao, M.; Meng, Y. Nonflammable organic electrolytes for high-safety lithium-ion batteries. *Energy Storage Mater.* **2020**, *32*, 425–447. [CrossRef]
86. Schultz, C.; Vedder, S.; Streipert, B.; Winter, M.; Nowak, S. Quantitative investigation of the decomposition of organic lithium ion battery electrolytes with LC-MS/MS. *RSC Adv.* **2017**, *7*, 27853–27862. [CrossRef]
87. Rinkel, B.L.D.; Hall, D.S.; Temprano, I.; Grey, C.P. Electrolyte oxidation pathways in lithium-ion batteries. *J. Am. Chem. Soc.* **2020**, *142*, 15058–15074. [CrossRef]
88. Gerelt-Od, B.; Kim, J.; Shin, E.; Kang, H.; Kim, N.; Jo, C.; Son, H.; Yoon, S. In situ Raman investigation of resting thermal effects on gas emission in charged commercial 18650 lithium ion batteries. *J. Ind. Eng. Chem.* **2021**, *96*, 339–344. [CrossRef]
89. Fedorov, R.G.; Maletti, S.; Heubner, C.; Michaelis, A.; Ein-Eli, Y. Molecular Engineering Approaches to Fabricate Artificial Solid-Electrolyte Interphases on Anodes for Li-Ion Batteries: A Critical Review. *Adv. Energy Mater.* **2021**, *2101173*, 2101173. [CrossRef]
90. An, S.J.; Li, J.; Daniel, C.; Mohanty, D.; Nagpure, S.; Wood, D.L. The state of understanding of the lithium-ion-battery graphite solid electrolyte interphase (SEI) and its relationship to formation cycling. *Carbon* **2016**, *105*, 52–76. [CrossRef]
91. Agubra, V.; Fergus, J. Lithium ion battery anode aging mechanisms. *Materials* **2013**, *6*, 1310–1325. [CrossRef] [PubMed]
92. Yan, C.; Cheng, X.B.; Tian, Y.; Chen, X.; Zhang, X.Q.; Li, W.J.; Huang, J.Q.; Zhang, Q. Dual-Layered Film Protected Lithium Metal Anode to Enable Dendrite-Free Lithium Deposition. *Adv. Mater.* **2018**, *30*, 1707629. [CrossRef] [PubMed]
93. Xu, X.L.; Wang, S.J.; Wang, H.; Xu, B.; Hu, C.; Jin, Y.; Liu, J.B.; Yan, H. The suppression of lithium dendrite growth in lithium sulfur batteries: A review. *J. Energy Storage* **2017**, *13*, 387–400. [CrossRef]
94. Persson, K.; Sethuraman, V.A.; Hardwick, L.J.; Hinuma, Y.; Meng, Y.S.; Van Der Ven, A.; Srinivasan, V.; Kostecki, R.; Ceder, G. Lithium diffusion in graphitic carbon. *J. Phys. Chem. Lett.* **2010**, *1*, 1176–1180. [CrossRef]
95. Li, J.; Xing, L.; Zhang, L.; Yu, L.; Fan, W.; Xu, M.; Li, W. Insight into self-discharge of layered lithium-rich oxide cathode in carbonate-based electrolytes with and without additive. *J. Power Sources* **2016**, *324*, 17–25. [CrossRef]
96. Liao, X.; Huang, Q.; Mai, S.; Wang, X.; Xu, M.; Xing, L.; Liao, Y.; Li, W. Understanding self-discharge mechanism of layered nickel cobalt manganese oxide at high potential. *J. Power Sources* **2015**, *286*, 551–556. [CrossRef]

Journal Publication 2

Understanding the Mechanism of Capacity Increase During Early Cycling of Commercial NMC/graphite Li-ion Batteries [J2]

J. Guo, Y. Li, J. Meng, K. Pedersen, L. Gurevich, and D. I. Stroe

This paper is accepted by *Journal of Energy Chemistry* 2022, 34-44 (74).

Journal of Energy Chemistry 74 (2022) 34–44

Contents lists available at ScienceDirect

Journal of Energy Chemistry

journal homepage: www.elsevier.com/locate/jechem

http://www.journals.elsevier.com/journal-of-energy-chemistry/

Understanding the mechanism of capacity increase during early cycling of commercial NMC/graphite lithium-ion batteries

Jia Guo [a,b], Yaqi Li [a,b,*], Jinhao Meng [c], Kjeld Pedersen [b], Leonid Gurevich [b], Daniel-Ioan Stroe [a]

[a] AAU Energy, Aalborg University, Aalborg 9220, Denmark
[b] Department of Materials and Production, Aalborg University, Aalborg 9220, Denmark
[c] College of Electrical Engineering, Sichuan University, Chengdu 610065, Sichuan, China

ARTICLE INFO

Article history:
Received 23 May 2022
Revised 1 July 2022
Accepted 6 July 2022
Available online 12 July 2022

Keywords:
Capacity increasing
Lithium-ion battery
Full cell
Coin cell
Graphite anode

ABSTRACT

A capacity increase is often observed in the early stage of Li-ion battery cycling. This study explores the phenomena involved in the capacity increase from the full cell, electrodes, and materials perspective through a combination of non-destructive diagnostic methods in a full cell and post-mortem analysis in a coin cell. The results show an increase of 1% initial capacity for the battery aged at 100% depth of discharge (DOD) and 45 °C. Furthermore, large DODs or high temperatures accelerate the capacity increase. From the incremental capacity and differential voltage (IC-DV) analysis, we concluded that the increased capacity in a full cell originates from the graphite anode. Furthermore, graphite/Li coin cells show an increased capacity for larger DODs and a decreased capacity for lower DODs, thus in agreement with the full cell results. Post-mortem analysis results show that a larger DOD enlarges the graphite d-space and separates the graphite layer structure, facilitating the Li^+ diffusion, hence increasing the battery capacity.

1. Introduction

Lithium-ion (Li-ion) batteries have been widely used in electric vehicles (EVs) due to their high energy density, low self-discharge, and long lifetimes [1]. However, the inevitable degradation under charge/discharge cycle has significant consequences on safety and reliability of the battery system [2,3]. The aging behavior of batteries during the initial charge/discharge cycles is particularly critical for state-of-health analysis, lifetime prediction, and holds keys to the development of high-performance batteries [4]. A gradual capacity increase is one of the most anomalous behaviors in the early stages of battery cycling, which results in an increase in stored energy. This behavior may lead to unstable operation of a battery system or even cause accidents.

Some researchers used data-driving approaches to predict the battery cycling life and consider the capacity increases in their algorithms [5–8]. These approaches usually require extensive battery testing and large data sets. If the capacity increase can be understood from the perspective of underlying physical mechanisms perspective, the effect can be eliminated by improving cells' manufacturing process or by optimizing the charging and discharging profiles. Up to now, the mechanism responsible for the battery capacity increase or recovery during initial charge/discharge stages has been rarely studied.

Several previous studies, summarized in Table 1, have reported an increase in battery capacity during cycling aging; however, the understanding of the underlying mechanisms is limited. Gyenes et al. [9] proposed the so-called "overhang" mechanism to explain the increasing in capacity during aging. They have found that Li-ions are inserted into the overhang region of graphite anode during the high state of charge in initial cycles, followed by diffusion of Li-ions from the overhang regions in the subsequent cycling, hence causing a slight capacity excess. Nevertheless, it is still difficult to explain the continuous capacity increase over hundreds of cycles due to a limited amount of lithium ions deposited in overhangs. Lewerenz et al. [10] have extended this approach with the concept of the so-called "passive electrode", where the anode potential is affected by the potential difference between the active and the passive regions of the anode, which results in a low potential of the anode and a capacity rise of the full cell. However, these mechanisms cannot explain the variety of situations in which the capacity increased is observed. In [5], Severson et al. found a trend of capacity increase during the initial cycles for all the 124 aged cells. They explained this behavior by Dubarry's description, i.e., the loss of negative electrode material leads to a high potential difference in the cell [11]. Dubar-

---

[*] Corresponding author.
E-mail address: yaqili@mp.aau.dk (Y. Li).

https://doi.org/10.1016/j.jechem.2022.07.005
2095-4956/

Table 1
An overview of the publications related to capacity increasing of Li-ion battery in cycling.

References	Electrodes	Battery type	Relative capacity increase/cycles	Mechanism suggested
Gyenes et al. [9]	NMC/graphite	Pouch cell	1%	Diffusion of Li ions from the overhang region of graphite anode.
Lewerenz et al. [10]	LFP/graphite	18650	0.4%–1.7%/200	Diffusion of Li ions from passive electrode areas.
Severson et al. [5]	LFP/graphite	A123 18650	0.2%/100	Loss of negative material change the potentials.
Dubarry et al. [11]	LFP/graphite	Coin cell	1%	Loss of negative electrode.
Kobayashi et al. [12]	LFP/graphite	Large-scale cells 100 Wh	20%/recovery cycling	Non uniform Li-ion distribution is formed under shallow cycling and leads to capacity loss. It can be restored.

ry's experiment is performed by simulating the loss of the negative electrode material, resulting in a rise of the voltage plateau of the full cell, and subsequently an increased capacity. Kobayashi et al. [12] aged the battery with a shallow depth-of-discharge (DOD) (40%–60%) for 250 days, and then trained it at 100% DOD. Surprisingly, the capacity lost during the shallow cycling, could be, to a large extent gradually recovered during the full cycles. The authors attributed it to a non-uniform distribution of Li-ions created during shallow cycling.

Overall, the experimental evidence points to the fact that the capacity increase is related to the extent of DOD. However, the mechanisms related to this behavior has not been fully explained yet.

The analysis in the above studies has been mainly focused on non-destructive methods such as electrochemistry simulation, characteristics of charging-discharging curves, and in-situ pulse test (e.g., electrochemical impedance spectroscopy (EIS)). These powerful techniques have been widely used in previous studies and carried out at full-cell level; however, those techniques are less effective at the electrode and/or material level.

Ex-situ techniques such as X-ray diffraction (XRD) and field emission scanning electron microscope (FESEM) can often provide in-depth analysis of the material and electrode degradation, revealing the internal aging mechanisms of the battery. Nevertheless, for this purpose, the cells have to be disassembled.

The framework reported in the present study combines both in-situ and ex-situ approaches to analyze the capacity-increasing mechanism on the full-cell, electrode, and material levels, ensuring that the full-cells under test are not destructed. Specifically: (1) the 18650 full cells are aged at different DODs and temperature to study the effect of those factors on capacity increase; (2) fresh positive electrode/Li-metal (NMC/Li), fresh positive electrode/fresh negative electrode (NMC/graphite), and fresh negative electrode/Li-metal (graphite/Li) are assembled in coin cells to analyze the degradation indicators from the electrochemical characteristic curves (IC-DV); (3) according to the degradation indicators in (2), the IC-DV curves from full cells are studied, and the aging mechanism in full cell level is analyzed by EIS; (4) according to the inference results from (3), the influence in capacity increasing is further studied at the coin cell level. Using this framework, the mechanism of capacity increase is thoroughly explained and discussed.

The structure of the paper is as follows: Section 2 describes the full cell aging experiment and presents details about coin cells fabrication and testing. Section 3 analyzes the data from full cell aging and deduces the targeted aging mechanism. Section 4 presents an in-depth analysis of the aging mechanism at both electrode and materials levels. Section 5 is a summary of our main conclusion.

2. Experimental

2.1. Full cell testing

Full cell testing was carried out on commercially available 18650 full cells, manufactured by Haidi company, with a capacity of 2.2 Ah and a nominal voltage of 3.7 V; $LiNi_{0.5}Co_{0.2}Mn_{0.3}O_2$ and synthetic graphite were used as cathode and anode materials, respectively. Seven cells were tested using a Digatron battery test station in four cycling cases, as summarized in Table 2. Two cells were tested for every test case, except for case 1, where one battery was tested. Thus, data from seven battery cells were collected. The test program is shown in Fig. S1.

Aging test: The cycling aging tests were performed based on the following procedure. Initially, the cells were charged to 4.2 V using a constant current-constant voltage (CC-CV) profile with a 0.5 C constant current. The cells were considered fully charged when the current decreased to 0.11 A. In the next step, the cells were discharged to certain SOC values, as summarized in Table 2, using a synthetic current profile with an average current of 0.19 C. The same synthetic current profile was used for all the four cases.

Reference performance test (RPT): To analyze and quantify the effect from the operating DODs and temperatures, RPTs at 25 °C were performed, after every 100 equivalent full cycles (EFCs). To measure the capacity, the cells were charged to 4.2 V using a CC-CV profile with a 0.5 C current; the cells were considered fully charged when the cut-off current reached a value of 0.11 A. After a one hour pause, the cells were discharged to 2.75 V under 0.5 C constant current. In addition, the EIS spectra of the cells were measured, using a Digatron Firing Circuits EIS analyzer, in the frequency range of 6.5 kHz to 10 mHz, considering high, medium, and low frequency points; the obtained EIS spectra were fitted with an appropriate equivalent circuit model using the ZsimDemo software (Ametek company), as presented in Section 3.3.

2.2. Coin cell assembly and testing

NMC positive electrodes and graphite negative electrodes were also provided by Haidi company, which are from the same batch as the electrodes used in the 18650 full cells. It is also feasible to obtain the electrodes from disassembling fresh 18650 full cells,

Table 2
The test matrix for 18650 full cell aging.

	45% DOD	75% DOD	100% DOD
35 °C	Case 1	–	Case 2
45 °C	–	Case 3	Case 4

so readers can refer to it if fresh electrodes cannot be obtained from the manufacturer. Both positive electrodes and negative electrodes were cut into 14 mm-diameter-discs, which were paired with 15 mm-diameter-lithium metal discs and assembled into 2016-coin cell cases. The electrolyte was 1 M LiF_6 in dimethyl carbonate (DMC)/diethyl carbonate (DEC) mixed in 1:1 ration, and the amount is 5 drops with a 1 mL pipette in each coin cell.

Coin cell test for degradation indicators: NMC/Li, NMC/graphite and graphite/Li were assembled as coin cells as described in the previous section. NMC/Li and NMC/graphite coin cell were charged with 0.1 C-rate (1 C = 150 mAh g^{-1}) to 4.2 V, then charged under constant voltage of 4.2 V until the current reduced to 0.01 mA; then, the cells were discharged to 2.75 V by 0.1 C constant current. The graphite/Li coin cells were charged and discharged between 1.5 and 0.001 V by a constant current of 0.4 mA which corresponds to a 0.1 C current (i.e., 0.15 mA) in the test of the NMC/Li and NMC/graphite coin cells.

Coin cell test for evaluating the graphite electrode: Graphite/Li coin cell were repeatedly charged and discharged by a constant current of 0.8 mA which is the same as 0.2 C current in the test of NMC/Li and NMC/graphite cells. The voltage ranges were set to 1.0–0.001 and 0.2–0.001 V, which correspond well with the graphite available capacity in the full cell with 100% DOD and 45% DOD. XRD (Panalytical company) was performed to measure the graphite anode structure at 45 kV with a scanning speed of 2°/min. The FESEM (Zeiss 1540 XB) was used to observe the graphite morphology at 20 keV.

3. Capacity increase in full cell

3.1. Capacity increase

The initial RPT tests revealed an abnormal capacity increase in some cells during the first 200–300 EFCs under the combined influence of DOD and temperature. Fig. 1 shows the state of health (SOH) evolution for full cells during the first 400 EFCs. After initial 200–300 EFCs, all the cells eventually showed an expected decline in capacity. In Fig. 1(a), we present the capacity evolution of the cells cycled under 45% DOD and 100% DOD at 35 °C. The cells aged at 100% DOD showed a slight increase in capacity in the first 100 EFCs, then the capacity started to decrease in later stages of the aging test. The cells aged at 45% DOD exhibit a decrease trend in capacity in initial 200 EFCs. A similar capacity increase trend was also observed for the cells aged at 45 °C, as shown in Fig. 1(b). In the first 200 EFCs, both the cases of 75% DOD and 100% DOD show capacity increase. For the 100% DOD aged cells, a 1% capacity increase is observed in the first 200 EFCs, after which a faster (than for cells aged at 75% DOD) capacity fade occurs. Regarding the influence of temperature for the cells aged at 100% DOD, the capacity increase by 1% at 45 °C, which is more obvious comparing with the 0.3% increase at 35 °C.

To summarize, for the tested battery cells, an increase in capacity, which appears in early aging stages, is more obvious for larger DODs (such as 100% DOD and 75% DOD). Furthermore, the temperature exacerbates this effect for 100% DOD cycling.

3.2. Analysis of degradation indicators

To further study the capacity increase in 18650 cells at electrodes level, a number of advanced techniques have been used in literature to identify and quantify the electrochemical aging behavior in Li-ion batteries [13], such as incremental capacity and differential voltage (IC-DV) and EIS. These techniques use characteristic peaks or shape of the test curves as indicators to recognize battery aging.

3.2.1. Incremental capacity and differential voltage (IC-DV)

An IC curve is obtained by differentiating the battery capacity with respect to the voltage change, using Eq. (1), where Q_t and V_t correspond to the capacity and voltage at the time t [14,15]. The obtained IC plot shows the capacity contribution from certain voltage plateaus of batteries, and can be quantified by peak height, position, and area.

$$\mathrm{IC}=\frac{\mathrm{d}Q}{\mathrm{d}V}=\frac{\Delta Q}{\Delta V}=\frac{Q_{t+1}-Q_t}{V_{t+1}-V_t} \tag{1}$$

Similar to an IC curve, a DV curve is defined as the derivative of voltage with respect to the charge or discharge capacity, using Eq. (2), which reflects a change in voltage with the capacity evolution [16]

$$\mathrm{DV}=\frac{\mathrm{d}V}{\mathrm{d}Q}=\frac{\Delta V}{\Delta Q}=\frac{V_{t+1}-V_t}{Q_{t+1}-Q_t} \tag{2}$$

However, for IC and DV curves, the relationship between the indicators (change and shift in peaks) and the degradation behavior varies according to the type of electrode materials and the electrode parameters in a full cell. It is necessary to clarify the relation between the IC-DV indicators and the corresponding performance of the electrodes in a certain battery. Generally, electrochemical curve simulation is used to analyze the degradation indicators. However, it requires a detailed knowledge of over one hundred parameters in a full cell [17], which is difficult to collect. A slight

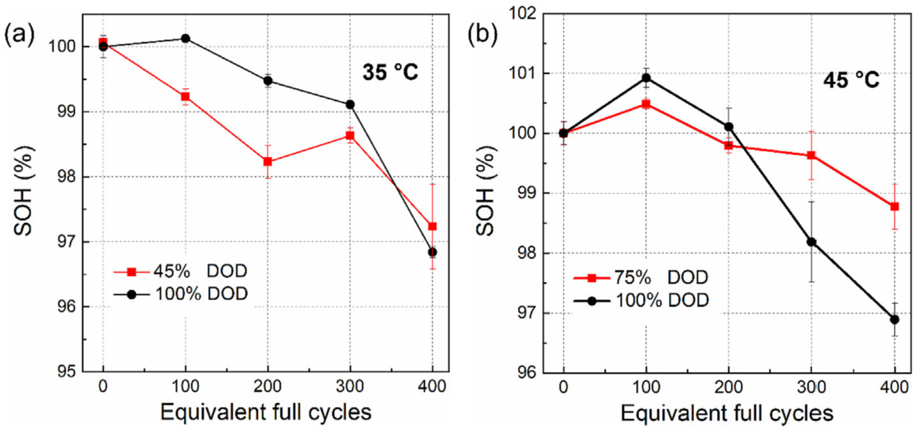

Fig. 1. Capacity fade in full cells during cycle aging at (a) 45% DOD and 100% DOD, at 35 °C, (b) 75% DOD and 100% DOD at 45 °C. The RPT test were carried out in the voltage range of 2.75–4.2 V with 0.5 C-rate (1.1 A) at 25 °C; error bars represent the standard deviation between two cells in each case.

error in parameters could lead to wrong simulation results and misunderstanding of the degradation indicators. Here, we propose to use coin cell batteries to compare the difference in IC and DV curves between half-cells (NMC/Li and Graphite/Li) and full coin cells (NMC/Graphite). Afterwards the degradation indicators will be clearly analyzed at electrode level.

Fig. 2(a) shows the charging-discharging (*Q*-*V*) curves of NMC/Li, NMC/Graphite and Graphite/Li coin cells, respectively. Overall, the shapes of NMC/Li and NMC/Graphite curves are similar and exhibit the typical high voltage plateau for NMC positive electrode. There are several distinctions between the two curves, where the graphite voltage governs the gap between the curves of NMC/Li and NMC/Graphite by transforming between pure graphite and LiC_6. That is reflected in a higher voltage plateau of NMC/Li and a rapid voltage rise in early stage of charging curve for NMC/Graphite. Based on the *Q*-*V* curves in Fig. 2(a), the corresponding DV curves were obtained and are shown in Fig. 2(b). Peaks in DV curves mark transitions between the two adjacent voltage plateaus in Fig. 2(a). Therefore, a shift in the peaks positions corresponds to a change in the duration time of voltage plateaus, which, in turn, is related to the amount of active material in the electrodes. Consequently, the left shift of DV peaks means that the amount of Li-intercalatable active materials in the respective electrode is reduced. Conversely, a shift of DV peaks to the right means an increase in the amount Li-intercalatable active materials. The NMC/Graphite DV curves show three evident peaks “I”, “II”, and “III”, corresponding well to the peaks in DV curve for the Graphite/Li cell. In contrast, there is no obvious peak in the DV curve for NMC/Li, which means that the potential on the positive electrode changes smoothly during charging. Hence, I, II, and III peaks visible in Fig. 2(b) are determined by the graphite anode changing the state from C to LiC_6.

The peaks in the IC curves represent phase transitions during electrochemical reactions, which related to the plateaus in voltage profiles and valleys in DV curves, respectively. The peaks represent the battery capacity increase in certain voltage intervals. Compared with DV curves, IC curves present cell degradation indicators as a function of voltage, which provides a better reference to the state of a battery as compared to the capacity dependence [11]. As shown in Fig. 2(c), the graphite anode has three pairs of oxidation/reduction peaks, which are the main reason for the gap between the IC curves corresponding to the NMC/Li and NMC/Graphite, as illustrated in Fig. 2(d). Regarding the NMC/Li cell, the IC curve shows only a pair of main oxidation/reduction peaks, which corresponds well with the only one DV valley in Fig. 2(b). The NMC/Graphite shows an extra pair of peaks V and V́, attributed to the graphite anode. Therefore, the intensity of the V peak represents the capacity of the graphite anode in a certain voltage plateau, which also indicates the amount of available graphite in the negative electrode.

3.2.2. Electrochemical impedance spectroscopy (EIS)

The impedance spectrum of a typical Li-ion cell is shown in Fig. 3. Although the figure is schematic, it was drawn based on the real 18650 full cell experiments. The impedance is composed of two partially overlapped semicircles from high frequency to middle frequency, and a straight slopping line at the low frequency end. The R_{ohm} represents the bulk resistance, which is related to the electric conductivity of electrolyte, separator, connector, and connection cable [18]. R_{sei} is the resistance caused by the solid-state interface film on the electrode surfaces. Its value corresponds to the diameter of the fitted semicircle at a relative high frequency region (about 6400–50 Hz). R_{ct} represents the charge-transfer resistance, corresponding to the diameter of the fitted semicircle at the medium frequency region (about 50–0.2 Hz), and the straight line in the low frequency region mainly corresponds to Li-ion diffusion resistance due to the concentration polarization [19]. The measured EIS data can be simulated by an equivalent circuit, like shown in the insert in Fig. 3(a), using ZsimDemo 3.30 software.

Furthermore, the Li^+ diffusion coefficient (D^+_{Li}) in the solid electrode can be calculated using Eq. (3), where the Warburg factor (σ) can be calculated by Eqs. (4) and (5) [20,21]

$$D_{\mathrm{Li}^+} = \frac{R^2T^2}{2A^2n^2F^2C^2\sigma^2} \tag{3}$$

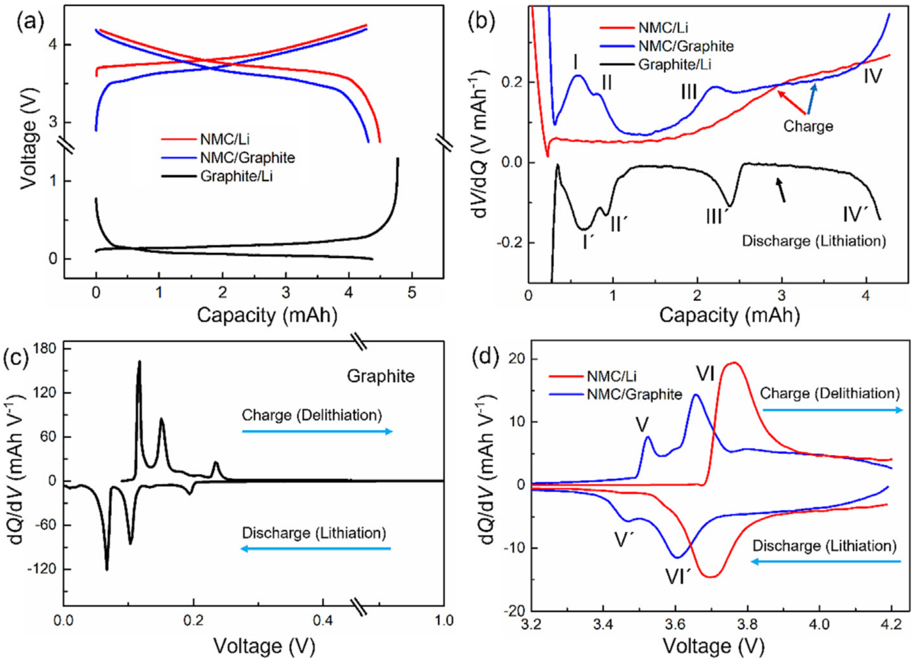

Fig. 2. The electrochemical behavior of electrodes in coin cell. The experiments were performed in coin cells with the combinations of NMC/Li (2.75–4.2 V, 0.1 C), NMC/Graphite (2.75–4.2 V, 0.1 C) and Graphite/Li (0.001–1.5 V, 0.1 C). (a) Charging and discharging curves for the three types of coin cells; (b) the DV curves corresponding to the charging process in a full cell; (c) IC curves of the graphite anode; (d) IC curves of the NMC/Li and NMC/Graphite.

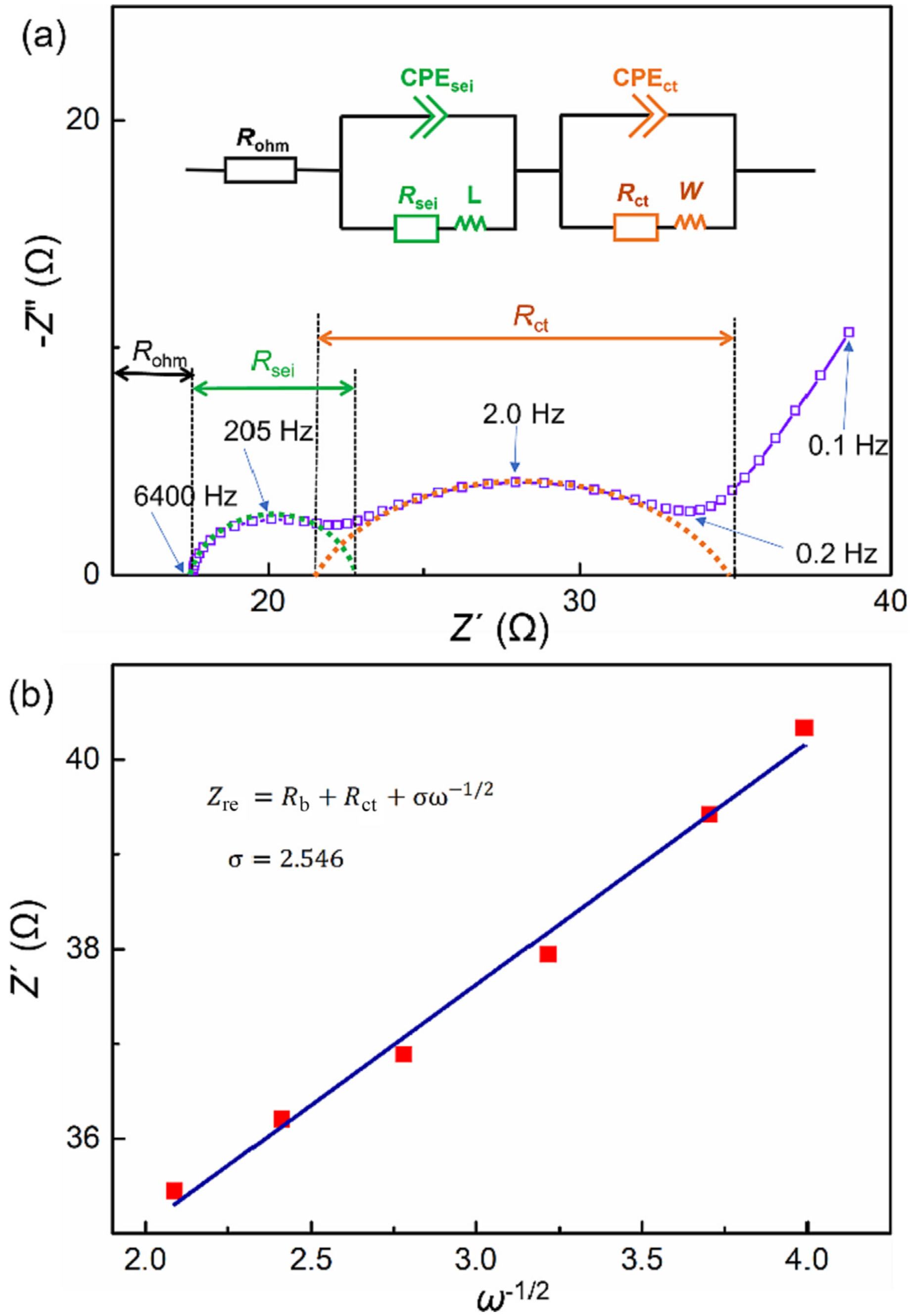

Fig. 3. (a) Typical EIS spectra of the Li-ion cell and the equivalent circuit used to fit the Nyquist curve; (b) the relationship between Z' and $\omega^{-1/2}$ based on (a).

$$Z_{re} = R_{ohm} + R_{ct} + \sigma\omega^{-1/2} \tag{4}$$

$$\omega = 2\pi f \tag{5}$$

where R is the gas constant (8.314 J mol^{-1}K^{-1}), T is the absolute temperature (298 K), A is the surface area of the electrode, n is the number of the transferred electrons per molecule, F is the Faraday constant (96,485 C/mol), C is the concentration of Li$^+$, R_{ohm} is the charge transfer resistance, and ω is the angular frequency.

R, A, n, F, C, and T are the same for the four types of full batteries used in this research. Therefore the relative change in Li-ion diffusion rate (D_{Li}^{+} / initial D_{Li}^{+}) can be calculated, such as D_1:D_2:D_3:D_4=$\frac{1}{\sigma_1{}^2}:\frac{1}{\sigma_2{}^2}:\frac{1}{\sigma_3{}^2}:\frac{1}{\sigma_4{}^2}$, where the Warburg factor (σ) is the slope of the fitted line, as shown in Fig. 3(b). In this way, the impedances and the trend of the relative change in the Li-ion diffusion rate can be calculated.

3.3. Mechanism identification

The voltage curves of the 18650 full cells in the four aging cases are shown in Fig. 4. All the curves show the plateau and the overall shape very similar to the charging/discharging curves of the NMC/-graphite coin cell, presented in Fig. 2(a). This indicates that it is feasible to study the degradation indicators by the coin cells in Section 3.2. In the charging curves shown in Fig. 4, a lower initial charging voltage corresponds to a higher final charging capacity as well as a higher discharging capacity in every case. Therefore, the increase of the capacity is related to the increase in the electrochemical window of charging in full cells. For this phenomenon,

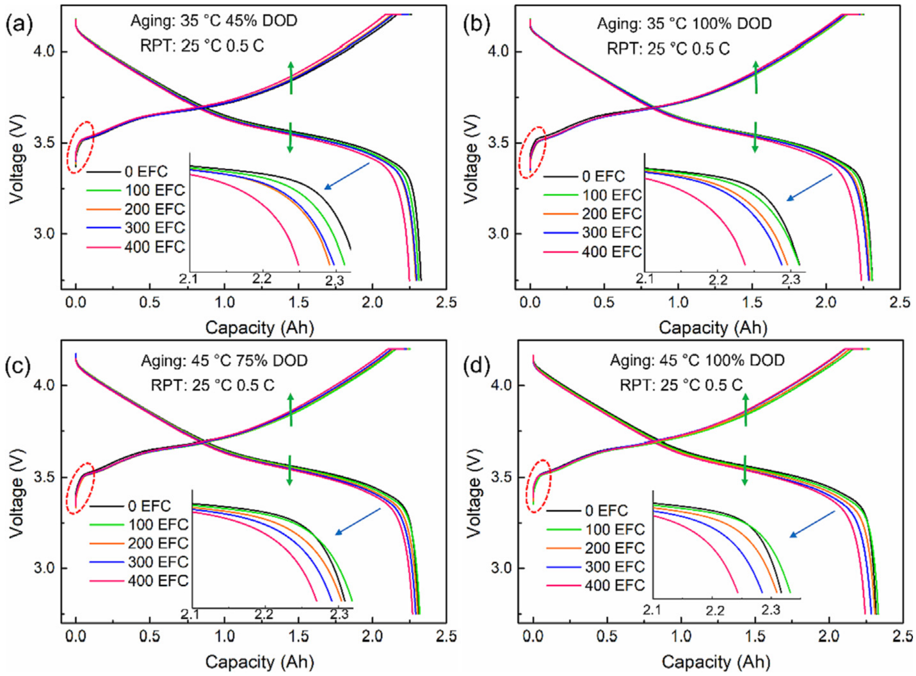

Fig. 4. Charging/discharging curves of the 18650-type cell aging in (a) case 1; (b) case 2; (c) case 3; and (d) case 4.

the most common explanations come from Dubarry's electrochemical modeling, where the simulation results show that the loss of anode graphite will lead to an increase in the main discharging voltage plateau (about 3.7 V), resulting in an increased capacity of the full cell [11]. Obviously, this simulation result cannot be used to explain the capacity increasing behavior in our experiment, because, in all the cases, the main discharging plateau shows a decreasing trend with the cycling evolution, as marked with the green arrow in Fig. 4.

The DVA and ICA techniques were used to study the electrochemical behavior of the 18650 full cells based on the capacity-voltage curves presented in Fig. 4. The IC curves corresponding to the cells aged in the four considered cases are shown in Fig. 5(a–d). The curves exhibit similar characteristic and shape to the NMC/Graphite coin cell in Fig. 2(b and d). This further proves that the mechanism analysis described in Section 3.2 is applicable to full cells.

Based on the indicators discussed in Section 3.1 (i.e., for an IC curve, the main peak intensity represents the amounts of active materials while the secondary peak is related to the available graphite in the anode), the intensity of the main peak around 3.7 V decreases with the number of EFCs for all cases; this behavior is related to the loss of active materials in the positive electrode or negative electrode. Regarding the peak around 3.53 V, it shows a decrease and a displacement towards right trend for cases 1. The decrease of peak intensity means that the graphite contributes less capacity in this phase transition process due to the reduced active graphite. The reason for the shift of the 3.53 V peak towards right is due to the increase in the internal resistance of full cell, corresponding to a reduced electrochemical window as well as a lower capacity. The case 3 only show a decrease trend in main peak of IC curve, and there is no change in secondary peak of IC curve and DV curve, which is consistent with the stable cycling performance in Fig. 1. On the contrary, the peak intensity at 3.53 V in case 3 and case 4 show an increasing trend, which means an increase in the available capacity of the graphite anode. Finally, the shift of the peak towards a lower voltage direction in case 2 and case 4 corresponds to a wider electrochemical window as well as an increased capacity in the full cell. This is consistent with the lower initial charging voltage illustrated in Fig. 4(c and d).

The DV curves, which can clearly show the gap between two adjacent phase transitions, for the four cases are shown in Fig. 5 (e–h). As expected, the main peak in the DV curves shifts to left with the cycle evolution for case 1 because the graphite fails to adequately accommodate the Li-ions. However, the main peak in DV curves of case 3 and case 4 unexpectedly shift to high-capacity direction with the cycling, which means an extended graphite lithiation plateau as well as more available graphite in anode. For further analysis, we have to employ electrochemical impedance spectroscopy (EIS) technique to measure the impedance in battery.

The evolution of the EIS spectra of the full cells during the first 400 EFCs, in each of the four aging cases is presented in Fig. 6; the EIS have been measured at 90% SOC and the curves were fitted using the circuit presented in Fig. 3(a). The evolution during aging of the elements of the circuit is presented in Fig. 6(b).

As shown in Fig. 6(b), there is a minor change in R_{ohm} for case 1. In the more severe aging conditions of case 2, case 3, and case 4, the R_{ohm} increases gradually. The increase of R_{ohm} is more obvious in case 4, as the higher temperature and the larger DOD range accelerate the degradation of electrolyte, separator, and current collector. The R_{sei} shows an increasing trend in all four cases, which is related to the continuous formation, shedding and precipitation of the SEI film, resulting in an increased interface impedance. The mechanism will be discussed in section 4, specifically. The R_{ct} trends to increase for all four cases, which can be attributed to crack formation or structural changes in the graphite and NMC during cycling, resulting in a poor electronic conductivity [13]. However, the R_{ct} shows the same gradually increasing trend, as observed for the capacity, from case 1 to case 4. Furthermore, the Li^{+} diffusion rate shows an increasing trend with cycling evolution in cases 2–4 (see Fig. 6b).

In conclusion, there is an increase in capacity of the first 100–300 cycles of the full cell, which is more obvious in a higher temperature and larger DOD aging cases. From the analysis of the Q-V, IC, and DV results, it can be concluded that the graphite anodes

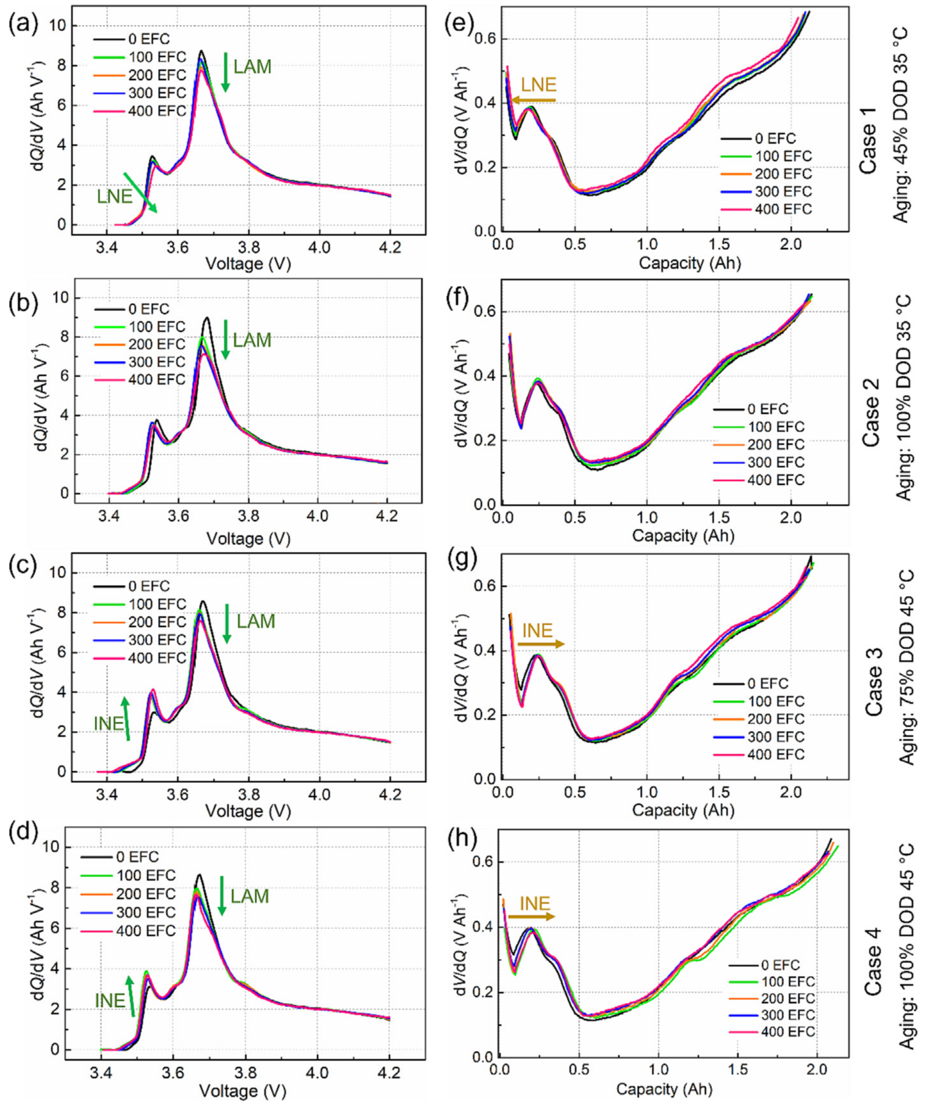

Fig. 5. IC and DV curves for full cell aging at (a, e) case 1; (b, f) case 2; (c, g) case 3, and (d, h) case 4. The curves are derived based on the capacity measurements performed at 25 °C and 0.5 C-rate. LAM represents the loss of active materials, such as positive electrode and negative electrode; LNE represents the loss of available negative electrode; INE represents the increase of available negative electrode in cycling.

cycled at 100% DOD exhibited enhanced graphite anode characteristics with the cycling. Furthermore, EIS further proves that the Li^+ diffusion coefficient in the graphite anode has improved with the cycling in the same conditions. These behaviors correspond well to the increase in the battery capacity, which is observed in the initial cycling stage. However, the charge-transfer resistance increases obviously, especially for cycle aging at elevated temperatures and larger DODs. The specific reasons are further analyzed from the electrodes and material levels.

4. Capacity increase in the graphite anode

Graphite/Li coin cells were assembled, in which the graphite negative electrode is the same as in the 18650 full cells provided by the same commercial company. Two group coin cells were cycled in the voltage ranges 0.001–0.2 and 0.001–1.0 V, which correspond to 45% DOD and 100% DOD in a full cell. The cycling performance is shown in Fig. 7(a). Due to the high potential of pure graphite (2.8 V, Li vs. Li^+), it contributes a high lithiation capacity when discharged to 0.001 V in the first point. In the large DOD (i.e., 0.001–1.0 V), the capacity shows an increase trend in the initial cycling stage. In contrast, the capacity shows a sharp decreasing trend and then increases in stages, when the coin cell is cycled between 0.001–0.2 V. This performance behavior is consistent with the performance of the 18650 cells, regarding the influence of DOD, as well as with the increasing trend of the secondary peak of the IC curves presented in Fig. 5. Furthermore, as reported in [22], the NMC material exhibits a continuously decreasing trend of the capacity in different DODs. Therefore, one can conclude that the initial capacity increase of the 18650 full cells is caused by the graphite negative electrode.

Ex-situ XRD was performed to study the structure change of the graphite in different state of charges. The IC curves corresponding to the graphite lithiation and delithiation process are shown in the left-hand side of Fig. 7(b). In the IC curve, the middle point is the lithium saturation state, and the lithium content gradually decreases to two sides, where the peaks in the lithiation process correspond to the following transitions $LiC_{30} \rightarrow LiC_{18}$, $LiC_{18} \rightarrow LiC_{12}$ and $LiC_{12} \rightarrow LiC_6$. LiC_6 is the full lithiation state of graphite [23]. The change in lithium content is not only reflected in the voltage of graphite, but also in the evolution of

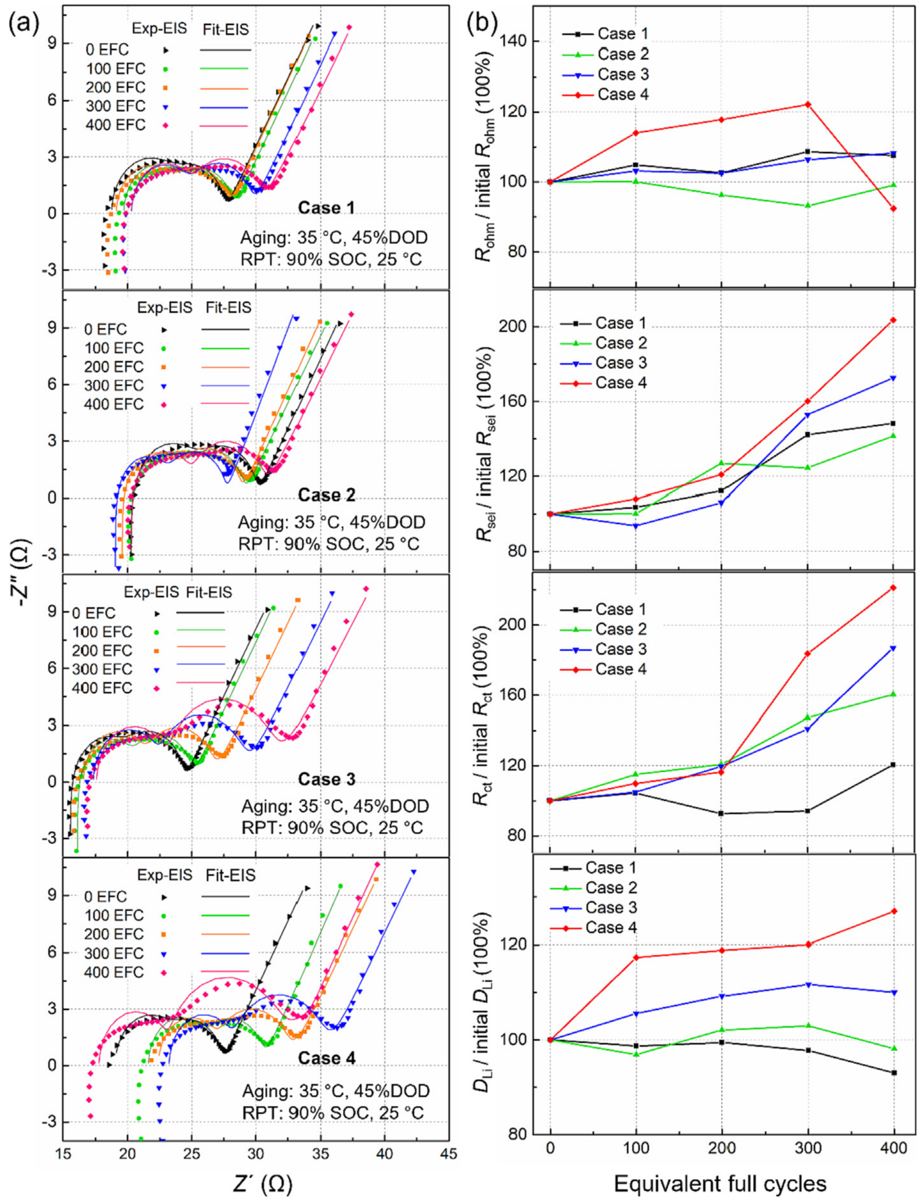

Fig. 6. The experimental and corresponding fitting result of EIS for 18650 cells (a) EIS spectrum of the four cases; (b) corresponds resistances result.

the structure. XRD results of graphite with different charging states are shown in the middle of Fig. 7(b). All XRD patterns exhibit evident graphite characteristic peaks at around 27°, which shifts with the voltage evolution. The corresponding *d*-spacing (C–C distance) values are calculated by HighScore Plus software and presented in the right-side of Fig. 7(b). With the voltage decreasing, the C–C distance show an increasing trend due to the increased lithium content. Cycling in a larger voltage range (i.e., 0.001–1.0 V) means a larger variation in the interlayer spacing. When the graphite lithiation occur from 0.27 to 0.001 V, the *d*-spacing (C–C distance) increases by 8.8%, then it gradually recovers. As the variation in *d*-spacing, the SEI film may break down, form again, and lithium salt precipitation, resulting in an increased R_{sei} as also illustrated in Fig. 6.

After 25 EFCs (where 1EFC = 4 mAh), the two-coin cells were charged to a fully de-lithiation state (i.e., 1.5 V), then they were disassembled to perform post-mortem analysis. The XRD patterns of the cycled graphite anodes are shown in Fig. 7(c). For fresh graphite, we have measured a 3.31 Å *d*-spacing. After cycling, the *d*-spacing has increased to 3.47 and 3.66 Å, when aging the cells between 0.001–0.2 and 0.001–1.0 V, respectively. As it can be observed, a larger voltage interval enlarges the graphite interlayer spacing, which is beneficial to the diffusion of Li^+ [24]. This behavior was further proved by EIS results, which are presented in Fig. S2. This is consistent with the increase in Li-ion diffusion coefficient (see Fig. 6), obtained from the EIS analysis, for the full cell aged at larger DOD.

The morphology of the cycled graphite electrodes between 0.001–0.2 and 0.001–1.0 V cases were characterized by FESEM and the images are shown in Fig. 8. For the coin cell cycled between 0.001 and 0.2 V, the FESEM images of cross-section and the EDS of carbon (C) and oxygen (O) elements are shown in Fig. 8, initial RPT tests revealed an abnormal. The graphite particles, with a size of 10–20 μm, are uniformly distributed over the copper current collector. The oxygen element is mainly from the surface of the SEI film and inorganic salt compounds. This indicates that the SEI film is distributed on the surface of the cycled electrode. As shown in Fig. 8, initial RPT tests revealed an abnormal, the intact graphite

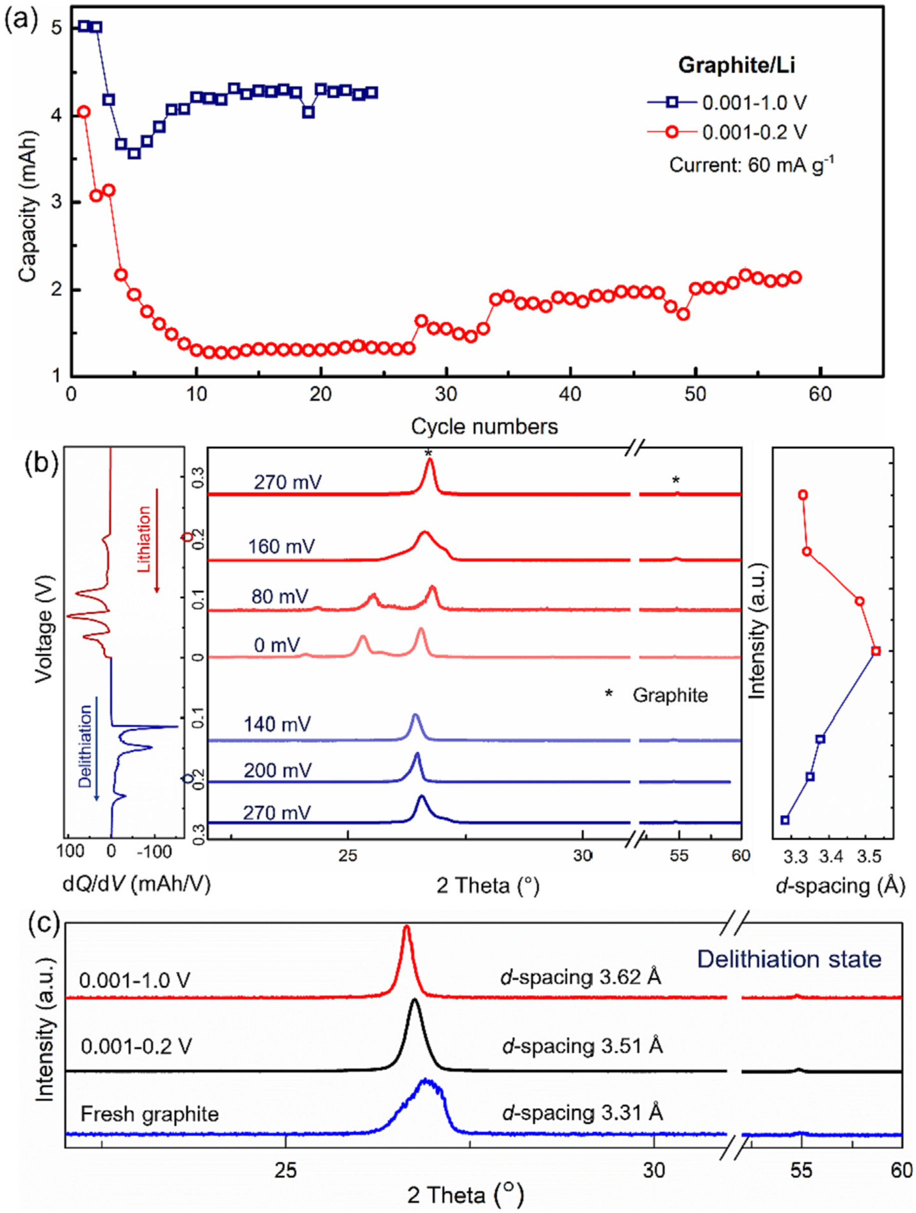

Fig. 7. (a) The cycling performance of graphite anode in the voltage range of 0.001–1.0 and 0.001–0.2 V. Ex-situ XRD patterns for (b) the structure evolution during electrochemical de-/intercalation of Li-ions half cells, and the corresponding d-spacing in graphite layer calculated by Highscore software; (c) graphite anode after 25 equal full cycles in different voltage ranges in a 1.5 V state of voltage.

particles exhibit smooth surfaces and bond well with the copper current collector. As reported in [25], this smooth surface is named basal plane; it is difficult for Li^+ to pass through this basal plane because the internal carbon atoms form tight covalent bonds with their neighbors making them very chemically resistant, thus, resulting in a low Li^+ diffusion coefficient. The slow diffusion rate leads to the accumulation of Li^+ in the anode-electrolyte interface, forming "dead lithium" and lithium dendrites [26]. As shown in Fig. 8(c), the negative electrode surface grows lithium dendrites with a small size of several nanometers as well as the SEI film. The formation of lithium dendrites and of the SEI film is the main cause of loss of lithium inventory and it also damages the graphite, resulting in a capacity decrease. All these explain why the full cells aged with a 45% DOD shows an evident capacity decrease in the initial cycles.

For the coin cell cycled between 0.001 and 1.0 V, the FESEM image of the cross-section is displayed in Fig. 8(d). A soft texture caused by layer separation inside the graphite particles is observed. On the graphite surface, the basal panel disappeared, forming clusters of graphite nanosheets. The increase of graphite spacing will undoubtedly reduce the electronic conductivity, resulting in an increased charge transfer resistance R_{ct} as also reported in Fig. 5. This may be attributed to the larger variation in the graphite interlayer spacing during larger DOD charge and discharge. Thereby, the graphite layer is exfoliated into a nanosheet shape, as shown in Fig. 8(e), which exposes more graphite surface to the electrolyte, resulting in facilitating the Li^+ transport. Consequently, graphite nanosheets accelerate the lithiation and de-lithiation process, and the Li^+ insert in graphite with a lower ionic resistance, causing a lower initial charge

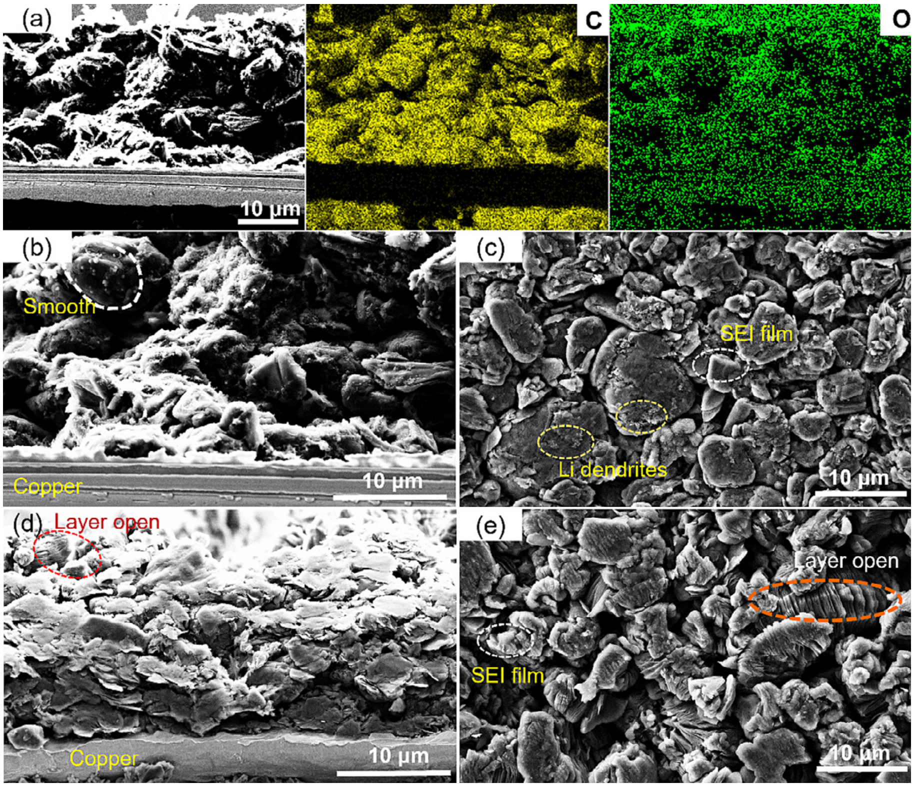

Fig. 8. FESEM images of cycled negative electrodes showing cross-section and surface morphology. (a) Cross section of a negative electrode after cycling the voltage range of 0.001–0.2 V range with EDS distribution maps for carbon and oxygen; (b and c) zoom-in of the cross section and electrode surface for 0.001–0.2 V case; (d and e) zoom-in of the cross section and electrode surface for 0.001–1.0 V case.

voltage (as shown in Fig. 4) as well as an increased capacity of the battery. This explains well why the capacity increases in the initial cycling stage.

5. Conclusions

In this study, the mechanism of the capacity increase, observed in the early cycling stage, of commercial NMC/graphite Li-ion batteries was investigated by non-destructive techniques and post-mortem analysis. The electrochemical behavior related to the capacity increase was studied on the full cell, electrode, and material levels. The results show an increased capacity in the early aging stage, especially for larger DODs (such as 100% DOD and 75% DOD). Temperature exacerbates this process in the case of 100% DOD cycling, and an 1% initial capacity increase was observed in one of the cases. IC and DV curves revealed that more Li^+ can be inserted into graphite with the cycling evolution in cases 2–4. Furthermore, the EIS results show that the Li^+ diffusion rate increases with the EFCs, in case 3 and case 4.

The graphite negative electrode was studied using coin cells, and the *d*-spacing of graphite increased about 8.8% from pure graphite to the full lithiation state. Furthermore, the evolution of *d*-spacing in graphite under cycling shows that it is not recovered completely when graphite is in the delithiated state. The enlarged *d*-spacing reduces the insertion resistance of Li^+, resulting in an increased Li^+ diffusion rate. In terms of morphology, the graphite in cycle-aged cells with large DODs tends to exfoliate into a nanosheet shape, which exposes more surface to the electrolyte. Then, the amount of Li-intercalable graphite has increased and the electrochemical window was enlarged by the potential reduction of the graphite side, resulting in an increased capacity of the battery.

Declaration of competing interest

The authors declare that they have no known competing financial interests or personal relationships that could have appeared to influence the work reported in this paper.

Acknowledgments

Jia Guo and Yaqi Li are supported by a grant from the China Scholarship Council (202006370035 and 202006220024). Jinhao Meng is supported by the National Natural Science Foundation of China (52107229). We like to thank Deyong Wang and Peter Kjær Kristensen for their help in performing the FESEM test, Donghong Yu for his help performing the XRD test, and Kim Houtved Jensen for helping with the experiment platform. Furthermore, we would also like to thank Haidi Energy Technology Co. for providing electrodes, which were used to manufacture the coin cells.

Appendix A. Supplementary data

Supplementary data to this article can be found online at https://doi.org/10.1016/j.jechem.2022.07.005.

References

[1] X. Sui, S. He, S.B. Vilsen, J. Meng, R. Teodorescu, D.I. Stroe, Appl. Energy 300 (2021) 117346.
[2] F.H. Gandoman, J. Jaguemont, S. Goutam, R. Gopalakrishnan, Y. Firouz, T. Kalogiannis, N. Omar, J. Van Mierlo, Appl. Energy 251 (2019) 113343.
[3] N. Yan, H. Zhao, X. Pan, G. Ma, S. Ma, IEEE Trans. Appl. Supercond. 31 (2021) 1–4.

[4] M.-F. Ng, J. Zhao, Q. Yan, G.J. Conduit, Z.W. Seh, Nat. Mach. Intell. 2 (2020) 161–170.
[5] K.A. Severson, P.M. Attia, N. Jin, N. Perkins, B. Jiang, Z. Yang, M.H. Chen, M. Aykol, P.K. Herring, D. Fraggedakis, M.Z. Bazant, S.J. Harris, W.C. Chueh, R.D. Braatz, Nat. Energy 4 (2019) 383–391.
[6] G. Ma, Y. Zhang, C. Cheng, B. Zhou, P. Hu, Y. Yuan, Appl. Energy 253 (2019) 113626.
[7] Y. Zhang, Q. Tang, Y. Zhang, J. Wang, U. Stimming, A.A. Lee, Nat. Commun. 11 (2020) 6–11.
[8] X. Tang, C. Zou, K. Yao, J. Lu, Y. Xia, F. Gao, Appl. Energy 254 (2019) 113591.
[9] B. Gyenes, D.A. Stevens, V.L. Chevrier, J.R. Dahn, J. Electrochem. Soc. 162 (2015) A278–A283.
[10] M. Lewerenz, J. Münnix, J. Schmalstieg, S. Käbitz, M. Knips, D.U. Sauer, J. Power Sources 345 (2017) 254–263.
[11] M. Dubarry, C. Truchot, B.Y. Liaw, J. Power Sources 219 (2012) 204–216.
[12] Y. Kobayashi, H. Miyashiro, A. Yamazaki, Y. Mita, J. Power Sources 449 (2020) 227502.
[13] C. Pastor-Fernández, K. Uddin, G.H. Chouchelamane, W.D. Widanage, J. Marco, J. Power Sources 360 (2017) 301–318.
[14] B. Ospina Agudelo, W. Zamboni, E. Monmasson, Energy 234 (2021) 121224.
[15] W. Pan, X. Luo, M. Zhu, J. Ye, L. Gong, H. Qu, J. Energy Storage 42 (2021) 103072.
[16] H. Kato, Y. Kobayashi, H. Miyashiro, J. Power Sources 398 (2018) 49–54.
[17] W. Li, D. Cao, D. Jöst, F. Ringbeck, M. Kuipers, F. Frie, D.U. Sauer, Appl. Energy 269 (2020) 115104.
[18] Y.B. He, F. Ning, Q.H. Yang, Q.S. Song, B. Li, F. Su, H. Du, Z.Y. Tang, F. Kang, J. Power Sources 196 (2011) 10322–10327.
[19] M. Gaberšček, Nat. Commun. 12 (2021) 19–22.
[20] Y. Wang, J. Zhang, J. Xue, X. Ke, G. Liang, Ionics 27 (2021) 4687–4694.
[21] Y. Chen, Y. Li, W. Li, G. Cao, S. Tang, Q. Su, S. Deng, J. Guo, Electrochim. Acta 281 (2018) 48–59.
[22] K.J. Park, J.Y. Hwang, H.H. Ryu, F. Maglia, S.J. Kim, P. Lamp, C.S. Yoon, Y.K. Sun, ACS Energy Lett. 4 (2019) 1394–1400.
[23] A. Missyul, I. Bolshakov, R. Shpanchenko, Powder Diffr. 32 (2017) S56–S62.
[24] Y. Tang, X. Wang, J. Chen, X. Wang, D. Wang, Z. Mao, Carbon 174 (2021) 98–109.
[25] H.L. Andersen, L. Djuandhi, U. Mittal, N. Sharma, Adv. Energy Mater. 11 (2021) 1–21.
[26] Y. Chen, X. Dou, K. Wang, Y. Han, Adv. Energy Mater. 9 (2019) 1–7.

Journal Publication 3

Battery Impedance Spectrum Prediction From Partial Charging Voltage Curve by Machine Learning [J3]

J. Guo, Y. Che, K. Pedersen, and D. -I. Stroe

This paper is accepted by *Journal of Energy Chemistry* 2023, 211-221 (79).

Journal of Energy Chemistry 79 (2023) 211–221

Contents lists available at ScienceDirect

Journal of Energy Chemistry

journal homepage: www.elsevier.com/locate/jechem

http://www.journals.elsevier.com/journal-of-energy-chemistry/

Battery impedance spectrum prediction from partial charging voltage curve by machine learning

Jia Guo [a], Yunhong Che [a,*], Kjeld Pedersen [b], Daniel-Ioan Stroe [a]

[a] AAU Energy, Aalborg University, Aalborg 9220, Denmark
[b] Department of Materials and Production, Aalborg University, Aalborg 9220, Denmark

ARTICLE INFO

Article history:
Received 6 November 2022
Revised 19 December 2022
Accepted 3 January 2023
Available online 20 January 2023

Keywords:
Impedance spectrum prediction
Lithium-ion battery
Machine learning
EIS
Graphite anode

ABSTRACT

Electrochemical impedance spectroscopy (EIS) is an effective technique for Lithium-ion battery state of health diagnosis, and the impedance spectrum prediction by battery charging curve is expected to enable battery impedance testing during vehicle operation. However, the mechanistic relationship between charging curves and impedance spectrum remains unclear, which hinders the development as well as optimization of EIS-based prediction techniques. In this paper, we predicted the impedance spectrum by the battery charging voltage curve and optimized the input based on electrochemical mechanistic analysis and machine learning. The internal electrochemical relationships between the charging curve, incremental capacity curve, and the impedance spectrum are explored, which improves the physical interpretability for this prediction and helps define the proper partial voltage range for the input for machine learning models. Different machine learning algorithms have been adopted for the verification of the proposed framework based on the sequence-to-sequence predictions. In addition, the predictions with different partial voltage ranges, at different state of charge, and with different training data ratio are evaluated to prove the proposed method have high generalization and robustness. The experimental results show that the proper partial voltage range has high accuracy and converges to the findings of the electrochemical analysis. The predicted errors for impedance spectrum are less than 1.9 mΩ with the proper partial voltage range selected by the corelative analysis of the electrochemical reactions inside the batteries. Even with the voltage range reduced to 3.65–3.75 V, the predictions are still reliable with most RMSEs less than 4 mΩ.

1. Introduction

Lithium-ion batteries (LIBs) are widely used in electric vehicles and portable electronic devices, due to their high energy density, long service life, and environmental friendliness [1–4]. However, the inevitable degradation of Li-ions batteries poses a big challenge to the safety during storage and usage, which urges the development and application of battery prognostic technologies [5,6]. Among them, electrochemical impedance spectroscopy (EIS) is a method for determining the impedance spectrum that can be used to present the battery health state, battery internal impedance, and the dynamic diffusion of lithium-ions (Li-ions), etc. [7,8].

EIS has been widely used to identify the parameters of the equivalent circuit model (ECM) to support the online estimation of battery states such as battery internal impedance, dynamics behavior of Li-ions diffusion, contact impedance of electrodes, state of charge (SOC) and state of health (SOH) [9,10]. The parameters of the ECM model have been proven to have a high correlation with the battery aging status. Therefore, machine learning has been used to develop algorithms to estimate the SOH and predict the lifetime of batteries by either inputting the whole EIS curve or by extracting features from the EIS curve [11,12]. Besides, the EIS result can give more physical aging meaning inside the battery, such as the diffusion of Li-ions, formation of the interface impedance, and ohmic impedance. However, the implementation of onboard EIS measurement is hindered, due to the high cost of the measurement equipment, test results subject to SOC and temperature variations, and time-demanding measurements. These limitations hinder the development of the EIS based method for online battery health prognostics. Therefore, the prediction of EIS is of vital importance to provide the impedance information for battery health prognostics. Accurate prediction via measurable parameters helps promote the advanced prognostic methods based on EIS and reduce the cost significantly. Duan et al. [13] achieved an accurate impedance spectrum prediction based on machine

---

* Corresponding author.
E-mail address: ych@energy.aau.dk (Y. Che).

https://doi.org/10.1016/j.jechem.2023.01.004

learning using complete battery charging data with a root mean squared error (RMSE) less than 1.862 mΩ. This promising prediction method can accurately estimate impedance spectrum and offer the possibility for real-time EIS based battery states estimation and health prognostics. However, there is a very limited understanding of the relationship between battery charging/discharging curves and impedance spectrum in terms of electrochemical mechanisms, which means the physical interpretability remains unclear. In addition, the partial voltage curve obtained during charging is supposed to be used considering the practical applications; furthermore, the selection of the voltage range during charging should be based on an analysis of the relationship between the voltage, incremental capacity (IC), differential voltage (DV), and EIS curves. Finally, the prediction under different SOC points is supposed to be provided for different application requirements, such as considering the impedance in battery package making.

Charging curves and EIS curves are widely used for battery health diagnosis and degradation quantification. Typically, aging mechanisms involve three degradation modes: conductivity loss (CL), loss of lithium inventory (LLI), and loss of active material (LAM) [14,15]. Compared with LLI and LAM, the CL always changes less in battery aging [16]. In practice, the charging profiles of the EVs are easily accessible, due to the controllable charging process. The charging curves can be converted to incremental capacity (IC) and differential voltage (DV) curves by the differential method. The peaks in the IC and valleys in DV curves represent specific electrochemical reaction processes occurring in both the positive electrode and negative electrode, which are usually used to quantify the LAM and LLI for the aged battery [17]. Besides, EIS also can be used for the quantification of LAM and LLI [15]. Since both charging curves and EIS can be used for quantification of LAM and LLI, a mechanism connection can be established. Then, machine learning methods can be used for estimating the impedance spectrum of the battery by charging curves.

The framework reported in this study is based on electrochemical mechanism analysis and summary to determine the existence of a correlation between charging curves and impedance spectrum, followed by a machine learning-based approach to predict the whole impedance spectrum. Specifically: (1) coin cells were assembled to clarify the electrochemical mechanisms of the IC and DV curves, which were used for quantification of LAM and LLI, and the mechanisms responsible for LAM and LLI quantification by EIS results were also analyzed; then, a quantifiable relationship between charging curves and impedance spectrum was obtained; (2) based on the mechanism analysis, the charging curve is used to achieve an accurate prediction for the impedance spectrum, and the SOC interval of the charging curve, which was used as input, was optimized; (3) impedance spectrum prediction for the battery at different SOCs were achieved; (4) the method was verified using different-testing ratios, and different machine learning methods were attempted.

2. Experimental

2.1. Dataset collection

Seven 18,650 cylindrical cells (HDCNR18650-2200–3.7 V) were aged at different temperatures and depths of discharge to achieve different aging states. The specific aging protocols and equipment were reported in our previous work[18]. After every-one hundred equivalent full cycles (EFCs), the aging of the battery is stopped and the battery is transferred to a 25 °C constant temperature oven for the reference performance test (RPT) including a capacity test and an EIS test at different SOCs (see in Table 1). In the capacity test, the battery was charged to 4.2 V with a constant current of 0.5C (1.1 A) and then charged with a constant voltage until the current is less than 0.11 A. Each battery was aged about 1000 equivalent full cycles (EFCs), and a total of 77 charging voltage curves and 355 EIS data (i.e., impedance spectrum) at different SOCs were recorded from the seven batteries.

For model validation, a set of RPT results from calendar aging were used. There are 9 batteries in calendar aging, and the RPT test was performed at different state of health. Finally, 114 groups of EIS and the corresponding charging curve data were obtained. The data also has been divided into two batches, the data with SOC of 30%, 50%, and 70% are used for training, and the data with SOC of 0, 20%, 60%, and 100% are used for prediction. The test condition is shown in Table S1 in support information.

2.2. Coin cell preparation

Fresh positive electrodes (i.e., NMC 532), negative electrodes (i.e., graphite), and lithium-metal (i.e., Li) were used as electrodes to assemble 2032-type coin cells in the following configurations: NMC/Li, graphite/Li, and NMC/graphite, respectively. The diameter of the NMC 532 positive electrode is 14 mm, and the loading is 2.67 mg/cm^2. The graphite negative electrode is 14 mm, and the loading is 1.86 mg/cm^2. The diameter of Li metal is 15.3 mm. The electrolyte was 1 mol LiPF$_6$ dissolved in 1 L solvent with a composition ratio of 1:1 EC and DEC. All coin cells were charged and discharged with a C-rate of 0.05C. The voltage range for NMC/Li, graphite/Li, and NMC/graphite were 2.8–4.2 V, 1.0–0.003 V, and 2.8–4.2 V, respectively.

3. Degradation modes identification from voltage charging curves and EIS

3.1. Degradation identification from charging voltage curves

As battery ages, the increased polarization and materials degradation will result in an upward shift and shortening of the charging voltage plateaus [19]. Differential methods can separate these plateaus and convert them into different peaks in the IC curve and valleys in the DV curve [18]. The IC curve presents the capacity increment ($\frac{dQ}{dV}$) changing with battery voltage (V), where the area between the IC curve and the X-axis corresponds to the capacity contribution in a certain voltage range, as present in Eq. (1). Similarly, DV ($\frac{dV}{dQ}$) curve is obtained by differentiating battery voltage against the capacity, which is used to distinguish the voltage contribution from anode and cathode, and the $\frac{dV}{dQ}$ is shown in Eq. (2) [20].

$$\frac{dQ}{dV} = \frac{\Delta Q}{\Delta V} = \frac{Q_t - Q_{t-1}}{V_t - V_{t-1}} \tag{1}$$

$$\frac{dV}{dQ} = \frac{d(V_{\text{cathode}} - V_{\text{anode}})}{dQ} = \left(\frac{dV}{dQ}\right)_{\text{cathode}} - \left(\frac{dV}{dQ}\right)_{\text{anode}} \tag{2}$$

During battery charging, the graphite anode undergoes a lithiation process. In contrast, a delithiation process occurs on the cathode side. Therefore, the voltage increases in the cathode and decreases in the anode resulting in an increased voltage of a full

Table 1
Charge/discharge curves and EIS results from 7 cells.

Batches	Charge/discharge	SOC of EIS tested
Batch #1: Cell 1,3,5,7	0.5C/0.5C	10%, 30%, 50%, 70%, and 90%
Batch #2: Cell 2,6,8		0, 20%, 40%, 60%, 80%, and 100%

battery. To understand the full battery charging process, coin-type half cells and coin-type full cell were assembled; the obtained electrochemical behavior during charging of the three types of coin cells are shown in Fig. 1. In the graphite lithiation process, the voltage decreases step by step corresponding to four consecutive phase transitions from LiC_{24} to LiC_6, which are represented by the discharge plateaus from A1 to A4 (Fig. 1a). The IC curve converts the four lithiation plateaus into peaks at 0.19, 0.13, 0.11, and 0.07 V, corresponding to LiC_{24}, intermediate phase between LiC_{24} and LiC_{18}, LiC_{12}, and LiC_6, respectively (Fig. 1b). Furthermore, the DV curve converts the IC peaks to valleys, which is more convenient for quantifying the capacity contribution of each lithiation plateau (Fig. 1c). For the cathode delithiation process, there are two plateaus named C1 and C2, as shown in Fig. 1(d), which are converted to obvious peaks in the IC curve, corresponding to the oxidation process of Ni^{2+}/ Ni^{3+} and Ni^{3+}/ Ni^{4+}, respectively (Fig. 1e). The capacity increments of cathode are continuously and uniformly distributed over the voltage range, corresponding to the large valleys in the DV curve, and thus the DV peaks caused by the voltage jumps are weak (Fig. 1f).

In the NMC/graphite coin-type full cell charging, there are four charging plateaus, which are caused by both positive oxidation and negative reduction processes (Fig. 1g). The IC curve transforms the charging plateaus into peaks, representing the capacity increment on the voltage scale (Fig. 1h). Among them, peak I is mainly related to the A1 peak of graphite. Peak II and peak IV are too weak to be quantified as they can disappear during battery aging [20]. The highest peak III in the voltage range of 3.65–3.85 V is related to both the phase change of A3 IC peak of the graphite and the C2 IC peak of the NMC. Therefore, the max value of peak III is widely used to study battery aging caused by the loss of active material at the positive and negative electrodes. Dubarry et al.[14,17,21] has used simulation methods to quantify the battery degradation mode of LAM based on Eq. (3), where the subscript low-ercase *1* in the equation indicates the battery in begin-of-life state, and *i* represents the aged cycle number.

In Fig. 1(i), the DV curves of NMC/graphite are similar to the DV curves of graphite, which means that the DV peaks on the full cell are greatly influenced by the phase transition of graphite. Besides, when charging at a low current, the battery capacity for the constant current stage is always regarded as the remaining inventory of lithium [14,21]. Therefore, the endpoint $(\max(Q)_1)$ of DV curve is often used to quantify LLI, as described in Eq. (4).

$$\mathrm{LAM}_i = \frac{\max\left(\frac{\Delta Q}{\Delta V}\right)_1 - \max\left(\frac{\Delta Q}{\Delta V}\right)_i}{\max\left(\frac{\Delta Q}{\Delta V}\right)_1} \cdot 100 \tag{3}$$

$$\mathrm{LLI}_i = \frac{\max(Q)_1 - \max(Q)_i}{\max(Q)_1} \cdot 100 \tag{4}$$

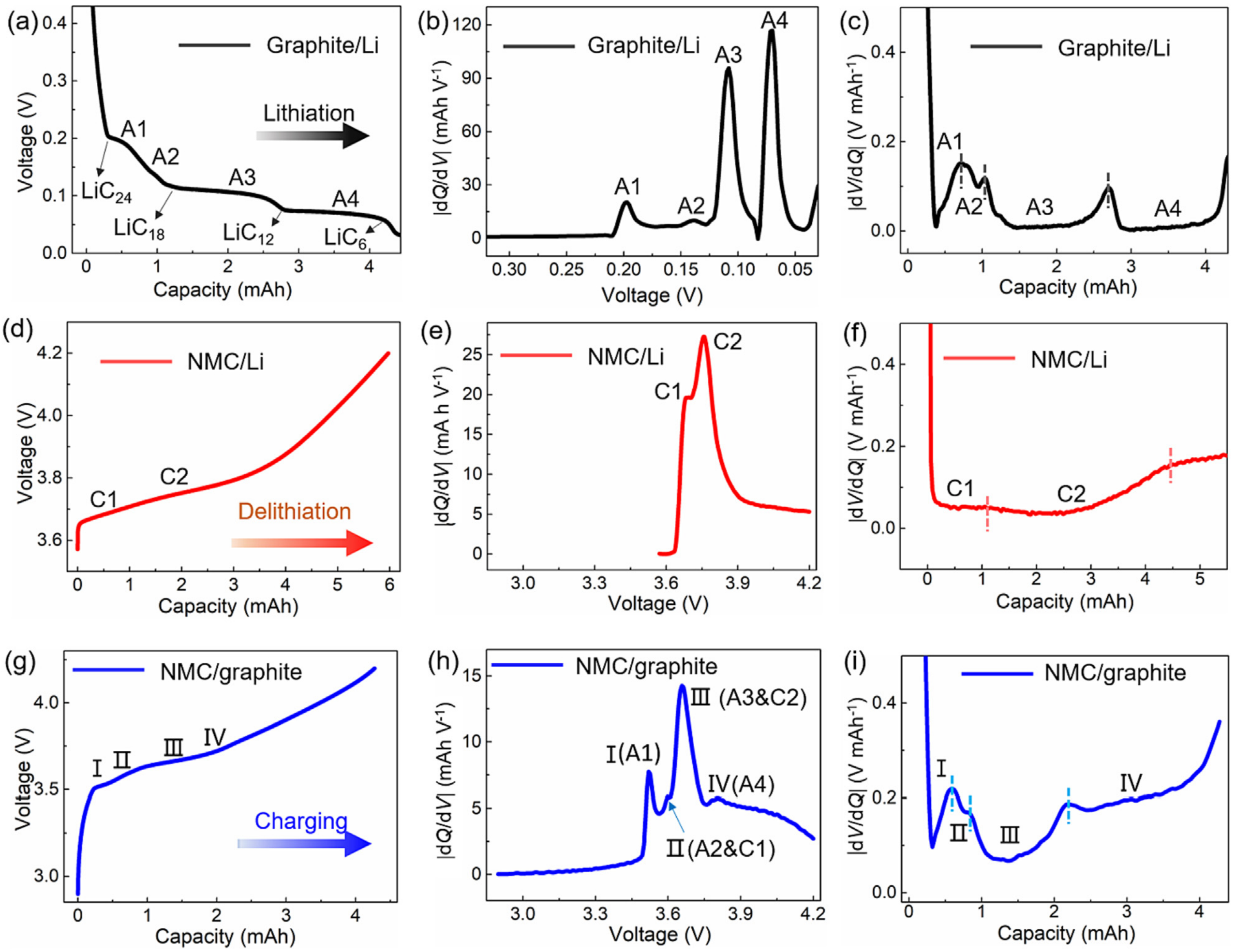

Fig. 1. *Q-V* (left) and IC (middle), and DV (right) curves of graphite/Li (top), NMC/Li (middle), and NMC/graphite (bottom) coin cell to reveal the reaction mechanisms during a full cell charging. The test in graphite lithiation process for (a) Q-V curve and converted to (b) IC and (c) DV curves. The obtained data in NMC delithiation process for (d) Q-V, (e) IC, and (f) DV curves. NMC/graphite data for (g) Q-V, (h) IC, and (i) DV curves.

According to Eqs. (2) and (3), LAM can be quantified by the decrease of the highest peak (III) in the IC curve, which corresponds to the shortening of the main plateau (III) in the charging curve and the decreased depth of the main valley (III) in the DV curve. The endpoint of the DV curve can be used to quantify the LLI, which is the charge capacity contributed by the constant current charging stage in the charge curve. The area between IC curve and X-axis is also can be used to quantify the LLI. The behavior of the charging IC and DV curves and the corresponding relations to the electrodes, as well as the corresponding aging mechanisms, are summarized in Table 2.

3.2. Degradation identification from EIS

EIS test is a powerful technique to analyze battery degradation [22,23]. The EIS results are traditionally presented in a Nyquist plot presenting the battery impedance spectrum, as shown in Fig. 2. As the test frequency decreases from 6500 Hz to 0.01 Hz, the EIS spectrum shows two intersecting semicircles followed by a straight line, which can be fitted by an Equivalent Circuit Model. Then, an electrochemical meaning is given, where the first semicircle diameter represents the solid electrolyte interphase resistance (R_{sei}) and the second semicircle diameter represents the charge transfer resistance (R_{ct}), while the slope of the line is related to the diffusion of lithium ions [18].

The battery degradation modes are widely analyzed by EIS. After cycling, the SEI film forms on the anode surface, which is a limit link for Li-ions diffusion between the electrolyte and the anode [24]. Besides, the SEI film is mainly composed of lithium compounds generated from side reactions e.g., decomposition of electrolyte and metal deposition, resulting in an irreversible loss of lithium inventory. Furthermore, some lithium plating occurs on the anode surface that can react with electrolyte, resulting in lithium compounds, hindering the charge transfer [25]. Hence, LLI is related to the R_{sei} and R_{ct}.

As reported in [15], the LAM is related to the diffusion coefficient ($D_{\mathrm{Li+}}$), because the diffusion of lithium ions within the electrolyte and active electrode materials is controlled by the particle size and the available surface area of the electrode material. The $D_{\mathrm{Li+}}$ can be calculated by Eq. (5), where R represents the gas constant, T is the absolute temperature, A is the electrode surface, n is the number of electrons transferred per molecule, F is the Faraday's constant, C is the Li-ions concentration, and the variable Y_0 is a function of Warburg impedance coefficient (σ) in Eq. (6). The σ is related to the slope of the tail of the EIS spectrum, and calculated by Eq. (7), where ω is the angular frequency used in the EIS measurements. Therefore, it can be concluded that the LAM is related to Y_0.

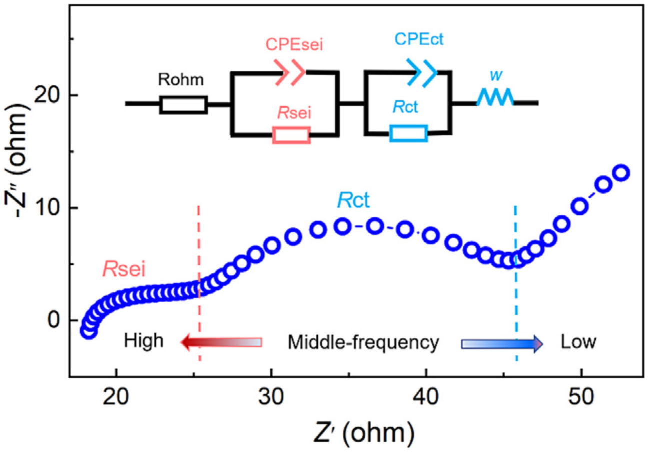

Fig. 2. Composition of a normal electrochemical impedance spectrum.

$$D_{\mathrm{Li}^+} = \frac{R^2T^2{Y_0}^2}{A^2C^2n^4\mathrm{F}^4} \tag{5}$$

$$Y_0 = \frac{1}{\sigma\sqrt{2}} \tag{6}$$

$$Z_{\mathrm{re}} = R_{\mathrm{ohm}} + R_{\mathrm{ct}} + \sigma\omega^{-1/2} \tag{7}$$

Hence, LLI is related to R_{sei} and R_{ct}, which correspond to the two semicircles in the high-frequency and mid-frequency regions of the impedance spectrum. Furthermore, the LAM is related to the Y_0 that corresponds to the tail in the low-frequency region of the impedance spectrum. Based on these relationships, the EIS was widely used to quantify the degradation contribution from each aging mode by Eq. (8) and Eq. (9) [14,15].

$$\mathrm{LLI} = 100\frac{(R_{\mathrm{sei,i}} + R_{\mathrm{ct,i}}) - (R_{\mathrm{sei,1}} + R_{\mathrm{ct,1}})}{R_{\mathrm{sei,1}} + R_{\mathrm{ct,1}}} \tag{8}$$

$$\mathrm{LAM} = 100\frac{(Y_{0,1} - Y_{0,\mathrm{i}})}{Y_{0,1}} \tag{9}$$

Table 3
Relationship between the impedance spectrum and the most pertinent degradation modes.

AR-ECM component	Most pertinent DMs
Increase in R_{sei} and R_{ct}	LLI Quantified by Eq. (8)
Increase in Y_0	LAM Quantified by Eq. (9)

Table 2
Relationship between the behaviors of charge, IC, and DV curves and the most pertinent degradation modes for graphite/Li, NMC/Li and NMC/graphite.

Change in charge curve	Change in IC curve	Change in DV curve	Most pertinent DMs
Full cell: smaller charging capacity, and upward trend. Anode: smaller lithiation capacity, and upward trend. Cathode: smaller delithiation capacity, and upward trend.	Full cell: shift toward lower or higher voltage, decrease of the height of the peaks. Anode: shift toward higher or lower voltage. Cathode: shift toward lower or higher voltage.	Full cell: shift toward lower capacity. Anode: shift toward lower capacity. Cathode: shift toward lower capacity.	LLI Quantified by Eq. (4)
Full cell: shorten of main plateau (III) Anode: shorten of A3 plateau. Cathode: shorten of C2 plateau.	Full cell: decrease of the highest peak (III). Anode: decrease of the A3 peak Cathode: decrease of the C2 peak	Full cell: decrease the depth of the main valley (III). Anode: decrease of the depth of the A3 valley. Cathode: decrease of the depth of the A3 valley.	LAM Quantified by Eq. (3)

Similarly, the subscript *1* in the Eq. (8) and (9) indicates the battery in begin-of-life state, and *i* represents the aged cycle number. With these equations, the relationship between the parameters change of the impedance spectrum and the aging modes can be summarized in Table 3.

3.3. Degradation in a full cell case

Periodic RPTs during battery aging were performed to quantify the incremental degradation of the cells, as explained in Section 2; the evaluation of the charging curve, measured at 0.5C (i.e., 1.1 A),

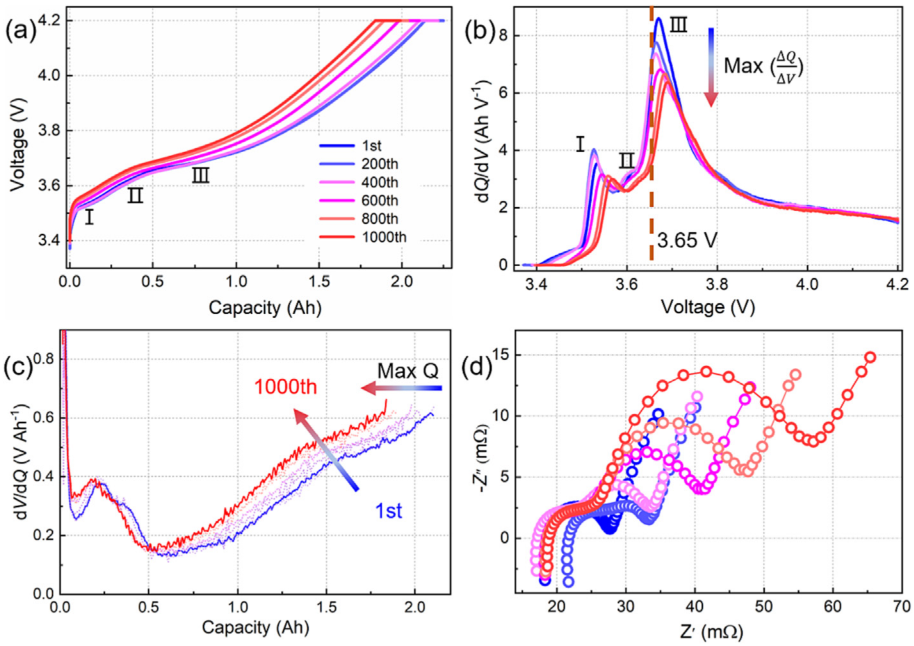

Fig. 3. Periodic reference performance tests (RPTs) for one of the aged batteries before aging and at the 200th, 400th, 600th, 800th, and 1000th cycles, including (a) constant current-constant voltage charges curves, (b) IC curve obtained by differentiating the charging curve, (c) DV curves, and (d) corresponding EIS results obtained at 50% SOC.

Table 4
The relationship between changes in charge curve and changes in impedance spectrums and the details of degradation mechanisms.

Changes in the voltage charging curve	Changes in the impedance spectrum	Most pertinent DM	Potential aging mechanisms
Decrease in charging capacity, and left and upward shifting.	Increase in R_{sei} and R_{ct}	LLI Quantified by Eqs. (4) & (8)	Electrolyte decomposition; oxidation of electrolyte; Lithium plating; formation of Li grains; solvent co/intercalation.
Shorten of main plateau (3.65–3.75 V)	Increase in Y_0	LAM Quantified by Eqs. (3) & (9)	Electrode decomposition; oxidation of the electrolyte; intercalation gradient strains in the active particles; formation of Li grains; crystal structure disordering; transition metal dissolution.

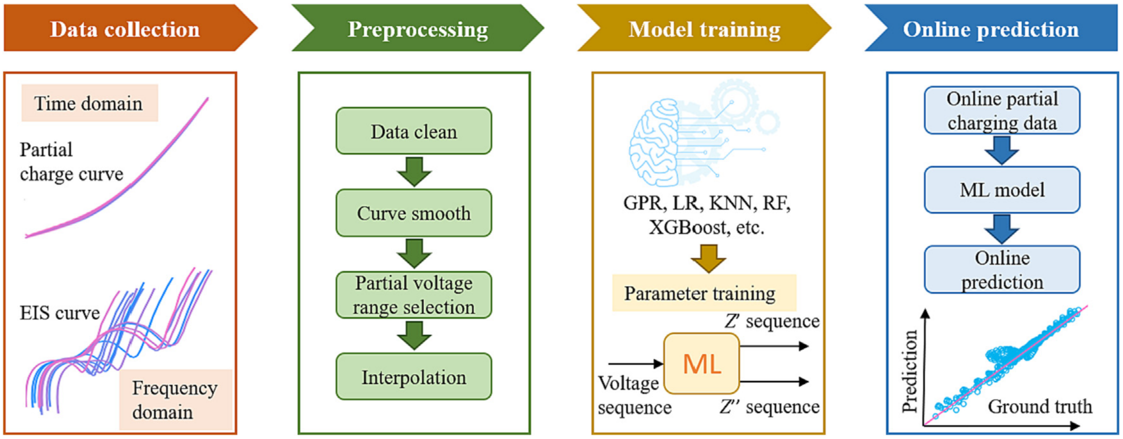

Fig. 4. Overall framework for the machine learning-based EIS prediction with partial charging curves.

and the evaluation of the impedance spectrum, recorded at 50% SOC, are presented in Fig. 3. As shown in Fig. 3(a), with the battery aging, the charging voltage plateaus show an upward trend and move to the left, corresponding to an increased internal impedance and a reduction of battery capacity, respectively. For the first 400 cycles, three distinct voltage plateaus I, II and, III could be identified. As the battery ages, all three plateaus become shorter, and the most subtle phase II plateau becomes indistinguishable. Converting the voltage-capacity curve to the IC peak in the voltage range (Fig. 3b), the obtained peaks decrease and shift to the right, behavior which is associated with increased internal resistance and loss of active material. As analyzed in section 3.1, peak I is mainly controlled by the graphite reduction potential. Peak II is almost indistinguishable, and it disappears after a few hundred cycles. The main peak III (3.65—3.75 V) is controlled by both the reduction potential of the graphite anode and the oxidation potential of the NMC cathode, so the decreasing trend of peak III in height (max $\frac{\Delta Q}{\Delta V}$) can reflect the degree of loss of positive and negative active materials. In addition, the loss of lithium ions is usually manifested as a leftward shift of the DV curve, as shown in Fig. 3(c). The max Q decrease with the battery aging, and at the same time, the DV curves shift upwards and left. This is consistent with the aging results speculated in Section 3.1.

The corresponding battery EIS results are shown in Fig. 3(d). With the battery aging, R_{sei} and R_{ct} show an increasing trend, from less than 10 to over 50 mΩ. As discussed in Section 3.2, the

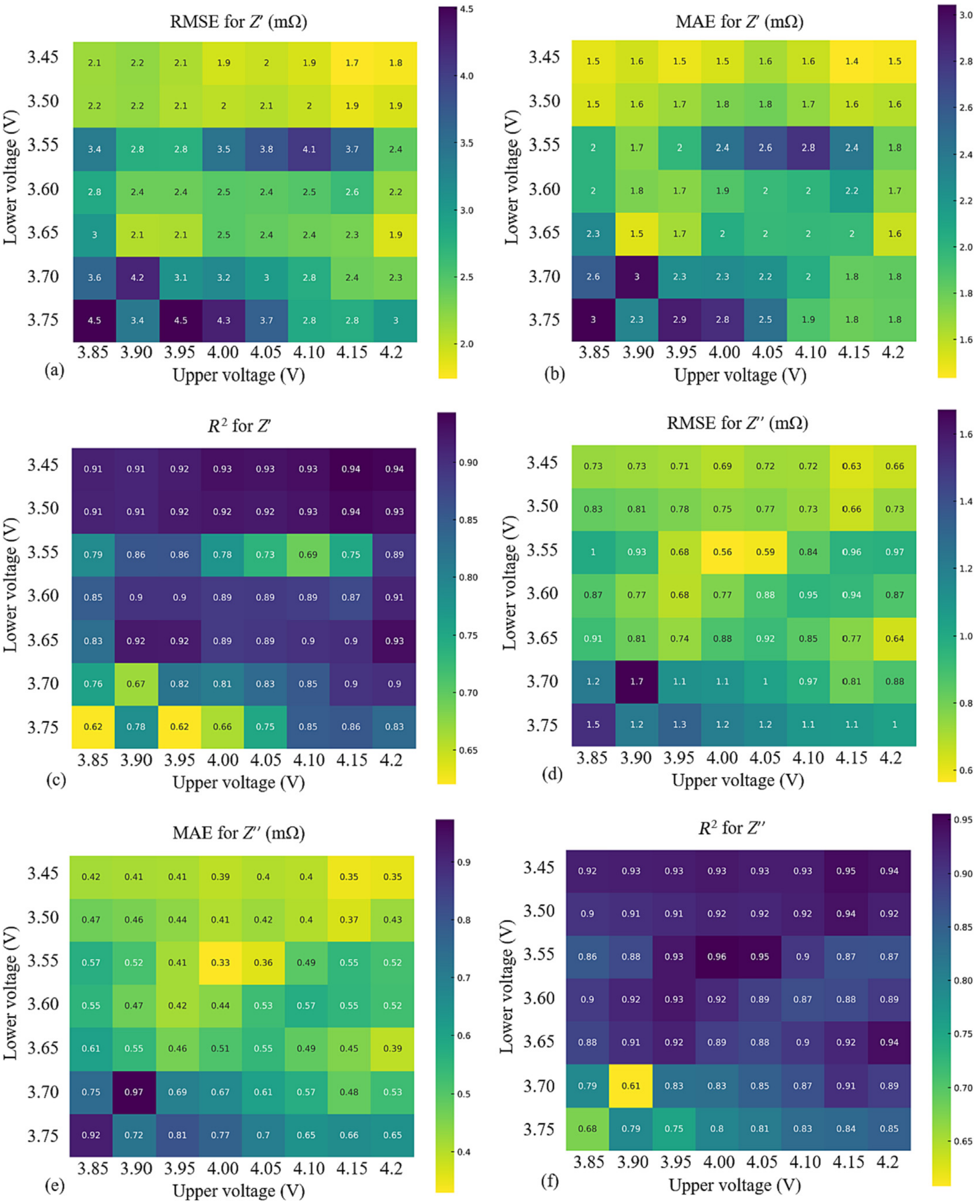

Fig. 5. The EIS curve prediction evaluations with different input voltage range for 50% SOC. (a) The RMSE for the Z′; (b) the MAE for the Z′; (c) the R^2 between the predicted Z′ and the ground truth; (d) the RMSE for the Z″; (e) the MAE for the Z″; (f) the R^2 between the predicted Z″ and the ground truth.

increased R_{sei} in the high-frequency region and R_{ct} in the middle frequency region represents an increase in LLI. Besides, the tail of the impedance spectrum associated with the Li-ion diffusion shows a decrease in slope with the battery aging, corresponding to a decreased Y_0. The above aging trends and the corresponding degradation modes and aging mechanisms are summarized in detail in Table 4. Since the IC and DV curves contain inherent information to the charging voltage curves, Table 4 only summarizes the changes observed in the charging curve.

Based on the quantifiable relationships between Eq. (4) and Eq. (8) and between Eq. (3) and Eq. (9), it is possible to establish an accurate physical functional relationship between the charging curve and impedance spectrum parameters. In other words, the impedance parameters can be obtained based on the parameters of the charging voltage curve and vice-vaersa. However, this is not practical; on the one hand, the algorithm needs to adjust the algorithm parameters according to different batteries, different working conditions or even different environments. On the other hand, the extraction of input features can be uncertain due to the charging voltage curves containing lots of feature parameters. Most of these issues can be overcome by using machine learning, which allows for algorithm self-selection, adaptability, fast speed, and high accuracy advantages [26] and can be performed to predict the EIS.

In this work, the max $\frac{\Delta Q}{\Delta V}$ appears in the voltage internal 3.65–3.75 V in the IC curve, and will be used to estimate the impedance spectrum at low frequency, since both the max $\frac{\Delta Q}{\Delta V}$ and the low-frequency impedance spectrum can be used to quantify the same degradation mode, i.e., LAM. Transforming the charging curve into an IC curve requires a smoothing process, which can cause data distortion (especially of the charging plateau). Therefore, we recommend using the charging curve directly to predict the EIS rather than converting it to the IC curve. Besides, the lithium loss estimates associated with R_{sei} and R_{ct} usually require the battery capacity at the cut-off voltage. However, in real-life application, it is almost impossible to fully discharge a battery before recharging it, making it difficult to obtain a complete voltage capacity curve as well as a normal capacity. The trend of "left and upward shifting" used to indicate the lithium loss may be obtained from the partial charge curve. Therefore, partial/complete charging curves will be used to predict the complete EIS by machine learning methods.

4. Impedance spectrum prediction

4.1. Prediction framework

The proposed framework for the EIS prediction with partial charging curves is shown in Fig. 4. Firstly, the charging voltage curve and the EIS curve at different SOCs are collected. Then the data are preprocessed, where the data are cleaned first. The abnormal values are filtered, and the missing values are filled up in this process. In addition, the curve is filtered to remove the noise. The partial voltage range is selected according to the practical requirements and the electrochemical analysis in the above section and the charging voltage curve is interpolated in this range based on the voltage interval selected as 5 mV in this paper. The third step is to train the machine learning model via the processed data. Different machine learning models could be selected including gaussian process regression (GPR) [27], linear regression (LR) [28], K-nearest neighbors (KNN) regression [29], XGBoost [30], artificial neural network (ANN) [31], and random forest (RF) [32], which helps evaluate the generalization and robustness of the prediction framework with various machine learning models. The details model algorithms of each machine learning method can be obtained from the corresponding literature. The prediction framework is a sequence-to-sequence way, where the voltage sequence is the input while the outputs are the predicted Z' and Z" sequences. The parameters of the machine learning models are trained using the training data. Finally, the trained model is used for the online prediction with the obtained online measured partial voltage data. The predictions of the EIS curves at different SOCs could be obtained by this prediction framework. The prediction results based on the proposed framework are presented and evaluated in the following sections.

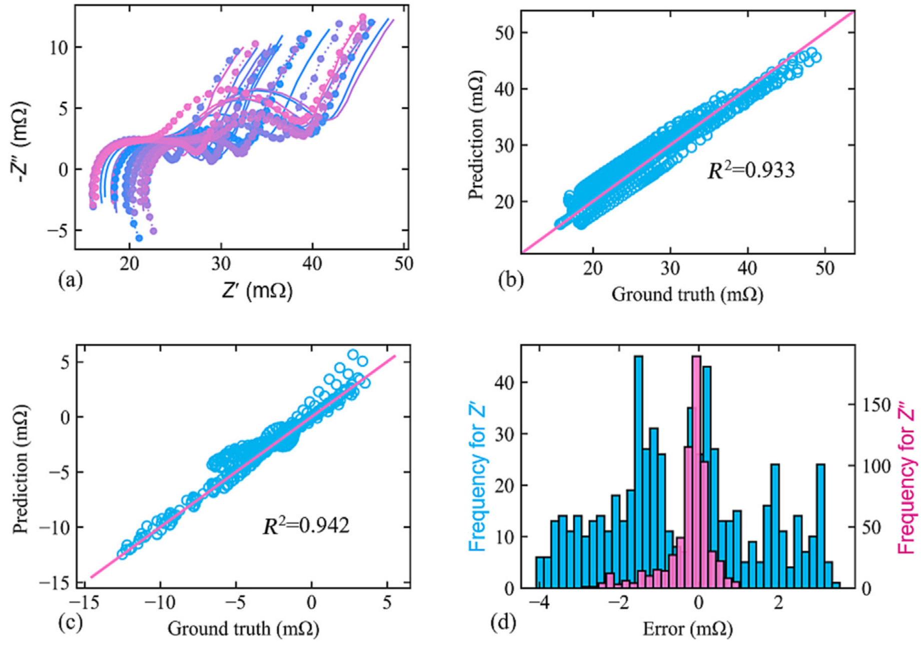

Fig. 6. The EIS curve prediction results with the input voltage range from 3.65 to 4.2 V for 50% SOC. (a) The predicted curve (dotted lines) and the real curve (solid lines). (b) The mapping between the predicted Z' and the real Z'. (c) The mapping between the predicted Z" and the real Z". (d) Frequencies of the errors for the predicted Z' and Z".

4.2. Prediction with the different voltage range

Firstly, the different partial charging voltage curves (according to the available voltage range in practical applications) are used as input to predict the whole EIS curve. The GPR model is used as the machine learning model for the evaluations [33]. The predictions of the EIS curves at 50% SOC are demonstrated. Here, the batteries with EIS tests at odd SOC points are used, where 41 samples are included. 70% of them (i.e., 28 samples) are used for training and 30% (i.e., 13 samples) are used for validations.

The root means square error (RMSE), mean absolute error (MAE), and the fitted *R* square (R^2) between the predicted values and the ground truth with different voltage ranges are shown in Fig. 5, where both the errors and R^2 for the *Z*' and *Z*" are included. It is wished that the less the RMSE and MAE, the better, and the higher the R^2, the better. The results show that generally the errors become larger and R^2 becomes smaller with the decrease of voltage range, which means generally wider voltage range contains more information that supports better predictions. However, the results show that the voltage range from 3.65 to 4.2 V also provides satisfactory predictions. These confirm the above mechanism analysis suggesting that the main charging plateau (3.65–3.75 V) derived from the partial charging curve that can represent shift characteristics of the whole curve, which can accurately predict the impedance spectrum. As a result, the voltage ranges that have satisfactory prediction accuracy all contain 3.65–3.75 V.

Therefore, the aging mechanism analysis and the correlation evaluation among the charging curve, IC / DV curve, and the EIS curve help select the proper partial voltage range that can offer physical interpretations and has high performance. This voltage range (i.e., 3.65–4.2 V) is used in the following evaluations for other aspects.

The prediction results for the EIS curve at 50% SOC using the voltage range from 3.65 to 4.2 V are shown in Fig. 6, where the predicted curve (dotted lines) and the real curve (solid lines) are shown in Fig. 6(a), the mapping between the predicted *Z*' and the ground truth is shown in Fig. 6(b), the mapping between the predicted *Z*" and the ground truth is shown in Fig. 6(c), and the error occurances of the *Z*' and *Z*" are shown in Fig. 6(d). The results show that the predicted curves fit well with the real curves, where both the fitting of the predicted *Z*' and the *Z*" show highly linear mappings with the real values with R^2 of 0.933 and 0.942, respectively. The histogram of occurances of the errors of the predicted *Z*' and *Z*" illustrate that the errors are within 4 mΩ for *Z*' and most of the errors are less than 2 mΩ for *Z*". Therefore, the results proved that the predicted curves are close to the real curves for all the tests.

4.3. Prediction at different SOCs

Then, the model is evaluated based on the predictions of the EIS curves at different SOC points to prove the generalization of the proposed method at different SOC levels. The machine learning model and the test ratio are set similarly as in the previous section, i.e., GPR model and 30% testing ratio. The RMSE, MAE, and R^2 for the predicted *Z*' and *Z*" are shown in Fig. 7, while the numerical results are listed in Table 5 and Table 6, respectively for batch#1 and batch#2. The accurate prediction results prove that the prediction model is suitable for being applied over a wide SOC range, which means the EIS curve at different SOC points under different aging status could be predicted. Therefore, the generalization of the prediction model is accurate, which supports different application requirements. The obtained results show that all the RMSE and MAE are less than 2.8 mΩ and 1.2 mΩ for the *Z*', all the RMSE and MAE are less than 1.7 mΩ and 1.1 mΩ for the *Z*". The R^2 for the *Z*' and *Z*" are larger than 0.875 and 0.915 respectively, which means that the predicted values are converged to the real values at all the SOC stages. The results indicate that the prediction errors for the 20%–80% SOC are less than those in 0–10% and 90–100% SOC stages. This may be related to the electrochemical stability of the battery at a moderate SOC range [34].

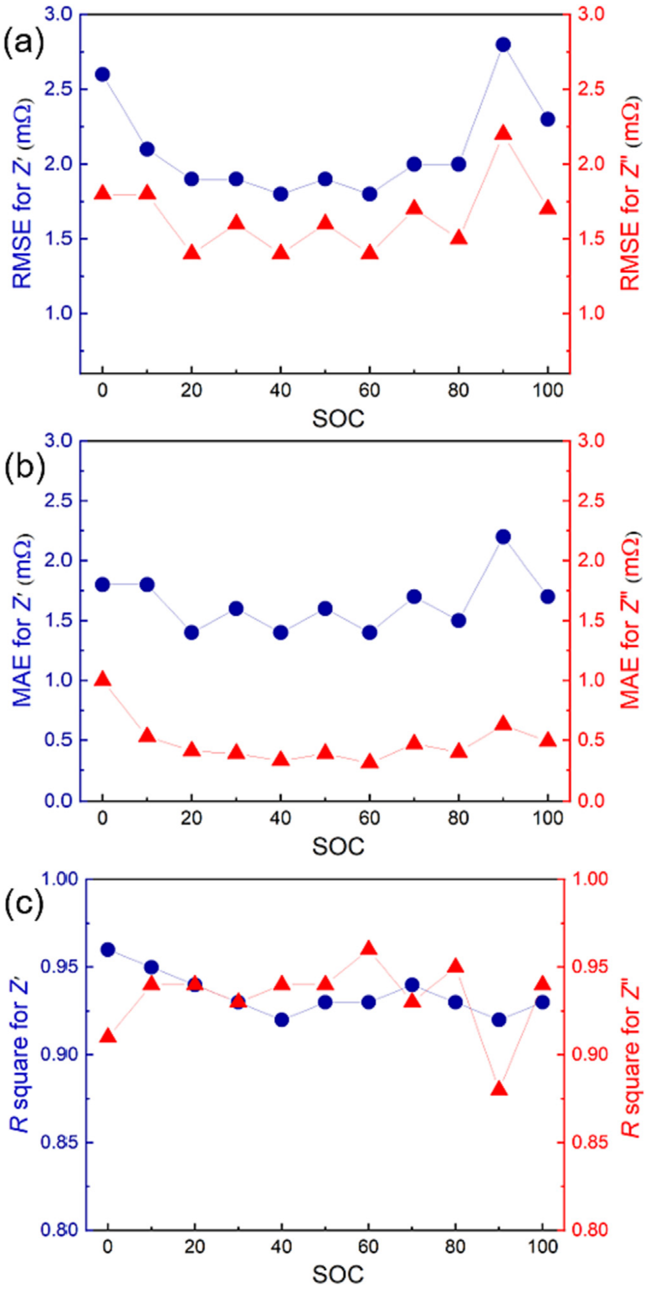

Fig. 7. Prediction evaluation for different SOCs. (a) results for RMSE, (b) results for MAE, (c) results for R^2.

4.4. Robustness evaluation

Finally, the robustness of the proposed prediction method is evaluated for different training – testing ratios and considering different ML algorithms. The errors and the fitted R^2 of the prediction results are shown in Fig. 8. Generally, with the reduction of the training data, the errors become larger and the R^2 becomes smaller, which means the performance becomes poorer with the reduction of data for the model training. However, the results show that even

Table 5
Results for different SOC with 30% data for testing for batch #1.

Index	10% SOC	30% SOC	50% SOC	70% SOC	90% SOC
RMSE of Z' (mΩ)	2.103	1.909	1.902	2.044	2.784
MAE of Z' (mΩ)	1.789	1.569	1.574	1.670	2.175
R^2 of Z'	0.953	0.932	0.933	0.941	0.921
RMSE of Z'' (mΩ)	0.846	0.625	0.644	0.807	1.173
MAE of Z'' (mΩ)	0.533	0.391	0.392	0.466	0.632
R^2 of Z'' (mΩ)	0.936	0.930	0.942	0.928	0.875

Table 6
Results for different SOC with 30% data for testing for batch #2.

Index	0% SOC	20% SOC	40% SOC	60% SOC	80% SOC	100% SOC
RMSE of Z' (mΩ)	2.648	1.874	1.808	1.826	2.014	2.298
MAE of Z' (mΩ)	1.822	1.403	1.396	1.438	1.534	1.683
R^2 of Z'	0.959	0.938	0.916	0.929	0.933	0.931
RMSE of Z'' (mΩ)	1.698	0.632	0.543	0.545	0.651	0.790
MAE of Z'' (mΩ)	1.032	0.407	0.325	0.313	0.399	0.493
R^2 of Z'' (mΩ)	0.913	0.938	0.945	0.964	0.951	0.943

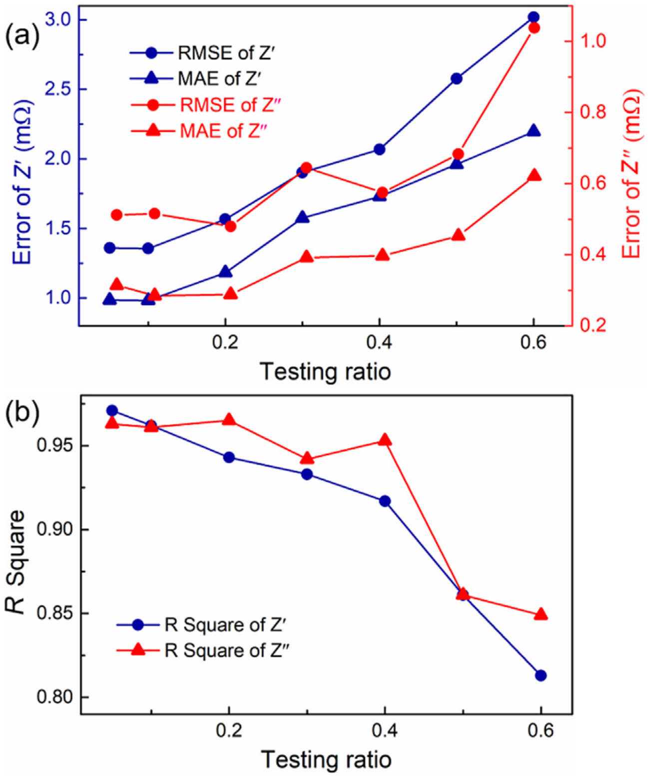

Fig. 8. Errors and the fitted R^2 with different ratios of data for validation.

with 40% data for training (16 samples) and 60% data for validation (25 samples), the RMSE and MAE for Z' are still within 3.02 mΩ and 2.2 mΩ respectively, those for Z'' are still less than 1.04 mΩ and 0.63 mΩ, respectively (Fig. 8a). The R^2 for Z' and Z'' are still 0.813 and 0.849 respectively (Fig. 8b). Therefore, the model has good robustness with the reduction of training data and can still with satisfactory predict performances.

In order to evaluate the robustness of the proposed prediction framework, different machine learning algorithms are used. The detailed process of each machine learning algorithm is described in supporting note 1. The prediction results are listed in Table 7, while the errors of each machine learning model are shown in Fig. S1. The results are obtained by the prediction for the EIS curve at 50% SOC using 30% data for validation. One can conclude that different machine learning algorithms are suitable for the prediction of the EIS curve with the proposed framework. Among them, the GPR has the best accuracy performance, and the calculation time is also proper for online applications with only 0.598 s in total for the whole training and prediction process.

Finally, we test our model on the prediction for calendar aging batteries. The same set of the results for Fig. 6 is used. The prediction results are shown in Fig. 9, which indicates that our model is also suitable for the prediction under calendar aging. The fitted R^2 between the predictions and the ground truth is larger than 0.944. The errors are less than 1.5 mΩ for Z'' and 4 mΩ for Z'. The RMSEs for Z' and Z'' are 1.38 and 0.36 mΩ, respectively, while the MAEs are 0.93 and 0.23 mΩ, respectively. Therefore, our method is robust for the EIS prediction under both cycling aging and calendar aging using a partial charging curve.

Table 7
Comparisons with different machine learning algorithms.

Index	GPR	LR	RF	XGBoost	KNN	ANN
RMSE of Z' (mΩ)	1.902	5.337	2.341	3.234	2.133	3.353
MAE of Z' (mΩ)	1.574	2.921	1.790	2.120	1.475	2.352
R^2 of Z'	0.933	0.470	0.898	0.805	0.915	0.791
RMSE of Z'' (mΩ)	0.644	1.481	0.860	1.055	0.730	1.122
MAE of Z'' (mΩ)	0.392	0.829	0.477	0.640	0.427	0.708
R^2 of Z'' (mΩ)	0.942	0.692	0.896	0.844	0.925	0.823
Time (s)	0.598	0.002	1.362	1.539	0.002	4.589

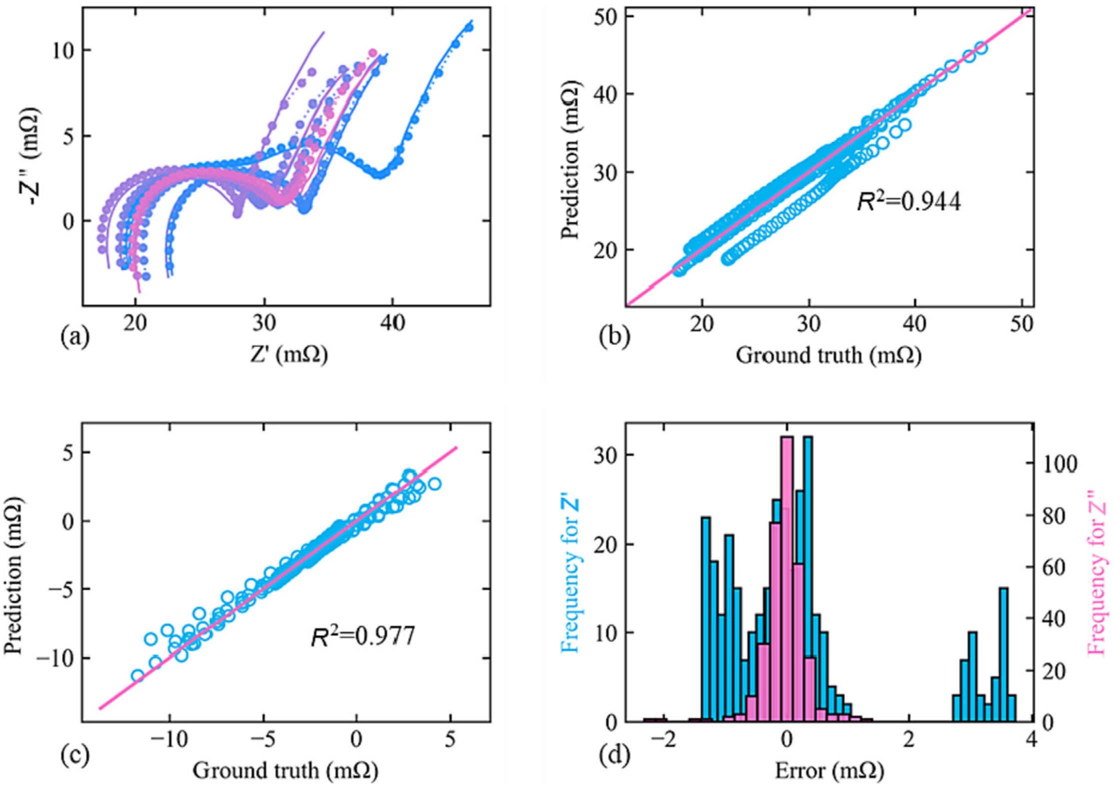

Fig. 9. The EIS curve prediction results under calendar aging. (a) The predicted curve (dotted lines) and the real curve (solid lines). (b) The mapping between the predicted *Z*' and the real *Z*'. (c) The mapping between the predicted *Z*'' and the real *Z*''. (d) Frequencies of the errors for the predicted *Z*' and *Z*''.

5. Conclusions

In this study, an accurate impedance spectrum prediction from charging voltage curves is achieved by machine learning methods, based on the mechanism that both charging curves and impedance spectrum can achieve the quantification of LAM and LLI. Coin cells were assembled to clarify the electrochemistry mechanisms of IC and DV curves at the electrodes level. The results support that the main peak in the IC curve (3.65–3.75 V) can be used to quantify the LAM, and the shifting trend of DV curve can be used to quantify LLI. Furthermore, the high and medium frequency impedance spectrum that represents R_{sei} and R_{ct} can be used to quantify the LLI, and the low frequency impedance spectrum indicating the diffusion of Li-ions can be used to quantify the LAM. Therefore, a quantifiable potential mechanistic relationship supports the prediction of EIS by charging curves.

Consistent with the mechanistic analysis, machine learning can achieve accurate EIS predictions. We optimized the voltage input interval for prediction and found that it is necessary to include the range 3.65–3.75 V in the input voltage in order to obtain an accurate result, which is consistent with the internal mechanism analysis between the IC curve and EIS. When the input voltage range is 3.65–4.2 V, reliable results are obtained most of the time with RMSEs less than 1.9 mΩ. The majority of the predictions are less than 4 mΩ with independent of the considered charging voltage ranges. Besides, the impedance spectrum predictions for battery at different SOCs was also realized. Furthermore, we varied the proportion of the data set for training and applied different machine learning methods to evaluate the robustness and generalization of the proposed method. We can conclude that 40% data is enough to obtain an impedance spectrum prediction result with RMSEs less than 3 mΩ. Among the considered ML algorithms, the GPR with multiple outputs model is recommended as the proper choice because of the high accuracy and acceptable computational burden.

Declaration of competing interest

The authors declare that they have no known competing financial interests or personal relationships that could have appeared to influence the work reported in this paper.

Acknowledgments

Jia Guo is supported by a grant from the China Scholarship Council (202006370035), and a fund from Otto Monsteds Fund (4057941073). We would also like to thank Haidi Energy Technology Co. for providing electrodes, which were used to manufacture the coin cells.

Appendix A. Supplementary material

Supplementary data to this article can be found online at https://doi.org/10.1016/j.jechem.2023.01.004.

References

[1] Y. Che, Y. Zheng, Y. Wu, X. Sui, P. Bharadwaj, D. Stroe, Y. Yang, X. Hu, R. Teodorescu, Appl. Energy 323 (2022).
[2] X.Z. Fan, M. Liu, R. Zhang, Y. Zhang, S. Wang, H. Nan, Y. Han, L. Kong, Chin Chem. Lett. 33 (2022) 4421–4427.
[3] X. Liu, H.J. Peng, B.Q. Li, X. Chen, Z. Li, J.Q. Huang, Q. Zhang, Angew Chem. Int. Ed 134 (48) (2022) e202214037.
[4] X. Liu, X.Q. Zhang, X. Chen, G.L. Zhu, C. Yan, J.Q. Huang, H.J. Peng, J. Energy Chem. 68 (2022) 548–555.
[5] L. Wu, K. Liu, H. Pang, Electrochim. Acta 368 (2021).
[6] Y. Che, D. Stroe, X. Hu, R. Teodorescu, IEEE Trans Industr Inform (2022) 1–10.

[7] M.A. Zabara, G. Katlrcl, B. Ülgüt, J. Phys. Chem. C 126 (2022) 10968–10976.

[8] J. Meng, M. Ricco, G. Luo, M. Swierczynski, D.I. Stroe, A.I. Stroe, R. Teodorescu, IEEE Trans. Ind. Appl. 54 (2018) 1583–1591.

[9] X. Hu, H. Yuan, C. Zou, Z. Li, L. Zhang, IEEE Trans. Veh. Technol. 67 (2018) 10319–10329.

[10] K. Mc Carthy, H. Gullapalli, K.M. Ryan, T. Kennedy, J. Electrochem. Soc. 168 (2021).

[11] Y. Zhang, Q. Tang, Y. Zhang, J. Wang, U. Stimming, A.A. Lee, Nat. Commun. 11 (2020) 6–11.

[12] P. Jones, U. Stimming, A.A. Lee, Nat. Commun. 13 (2022) 4806.

[13] Y. Duan, J. Tian, J. Lu, C. Wang, W. Shen, R. Xiong, Energy Storage Mater 41 (2021) 24–31.

[14] C. Pastor-Fernández, K. Uddin, G.H. Chouchelamane, W.D. Widanage, J. Marco, J. Power Sources 360 (2017) 301–318.

[15] E. Teliz, C.F. Zinola, V. Díaz, Electrochim. Acta 426 (2022).

[16] J. Guo, S. Jin, X. Sui, X. Huang, Y. Xu, Y. Li, D.W. Peter, K. Kristensen, D.-I. Stroe, J. Mater. Chem. 11 (2022) 41–52.

[17] M. Dubarry, C. Truchot, B.Y. Liaw, J. Power Sources 219 (2012) 204–216.

[18] J. Guo, Y. Li, J. Meng, K. Pedersen, L. Gurevich, D. Stroe, J. Energy Chem 74 (2022) 34–44.

[19] M. Ouyang, Z. Chu, L. Lu, J. Li, X. Han, X. Feng, G. Liu, J. Power Sources 286 (2015) 309–320.

[20] R. Xiong, Y. Pan, W. Shen, H. Li, F. Sun, Renewable Sustain. Energy Rev. 131 (2020).

[21] G. Seo, J. Ha, M. Kim, J. Park, J. Lee, E. Park, S. Bong, K. Lee, S.J. Kwon, S. Pil Moon, J. Choi, J. Lee, J. Energy Chem. 67 (2022) 663–671.

[22] Y. Chen, Y. Li, W. Li, G. Cao, S. Tang, Q. Su, S. Deng, J. Guo, Electrochimica Acta 281 (2018) 48–59.

[23] J. Guo, W. Li, ACS Appl. Energy Mater. 5 (2022) 397–406.

[24] J. Zhu, M. Knapp, D.R. Sørensen, M. Heere, M.S.D. Darma, M. Müller, L. Mereacre, H. Dai, A. Senyshyn, X. Wei, H. Ehrenberg, J. Power Sources 489 (2021).

[25] X. Lin, K. Khosravinia, X. Hu, J. Li, W. Lu, Prog. Energy Combust. Sci 87 (2021).

[26] X. Chen, X. Liu, X. Shen, Q. Zhang, Angew. Chem. Int. Ed 60 (2021) 24354–24366.

[27] X. Hu, Y. Zheng, X. Lin, Y. Xie, IEEE Trans. Transp. Electrification 6 (2020) 427–438.

[28] X. Sui, S. He, S.B. Vilsen, J. Meng, R. Teodorescu, D.I. Stroe, Appl. Energy 300 (2021).

[29] Z. Wei, Q. He, Y. Zhao, J. Power Sources 549 (2022).

[30] S. Song, C. Fei, H. Xia, Energies 13 (2020) 812.

[31] V. Chandran, C.K. Patil, A. Karthick, D. Ganeshaperumal, R. Rahim, A. Ghosh, World Electr. Veh. J 12 (2021) 38.

[32] K.S.R. Mawonou, A. Eddahech, D. Dumur, D. Beauvois, E. Godoy, J. Power Sources 484 (2021).

[33] X. Hu, Y. Che, X. Lin, S. Onori, IEEE Trans. Transp. Electrification 7 (2021) 382–398.

[34] J. Jiang, W. Shi, J. Zheng, P. Zuo, J. Xiao, X. Chen, W. Xu, J.-G. Zhang, J. Electrochem. Soc. 161 (2014) A336–A341.

Journal Publication 4

Unravelling and Quantifying the Aging Processes of Commercial Li($Ni_{0.5}Co_{0.2}Mn_{0.3}$)O_2/graphite Li-ion Batteries under Constant Current Cycling [J4]

J. Guo, S. Jin, X. Huang, Y. Xu, Y. Li, P. Kristensen, D. Wang, K. Pedersen, L. Gurevich, and D. I. Stroe

This paper is accepted by *Journal of Materials Chemistry A* 2023, 41-52 (11).

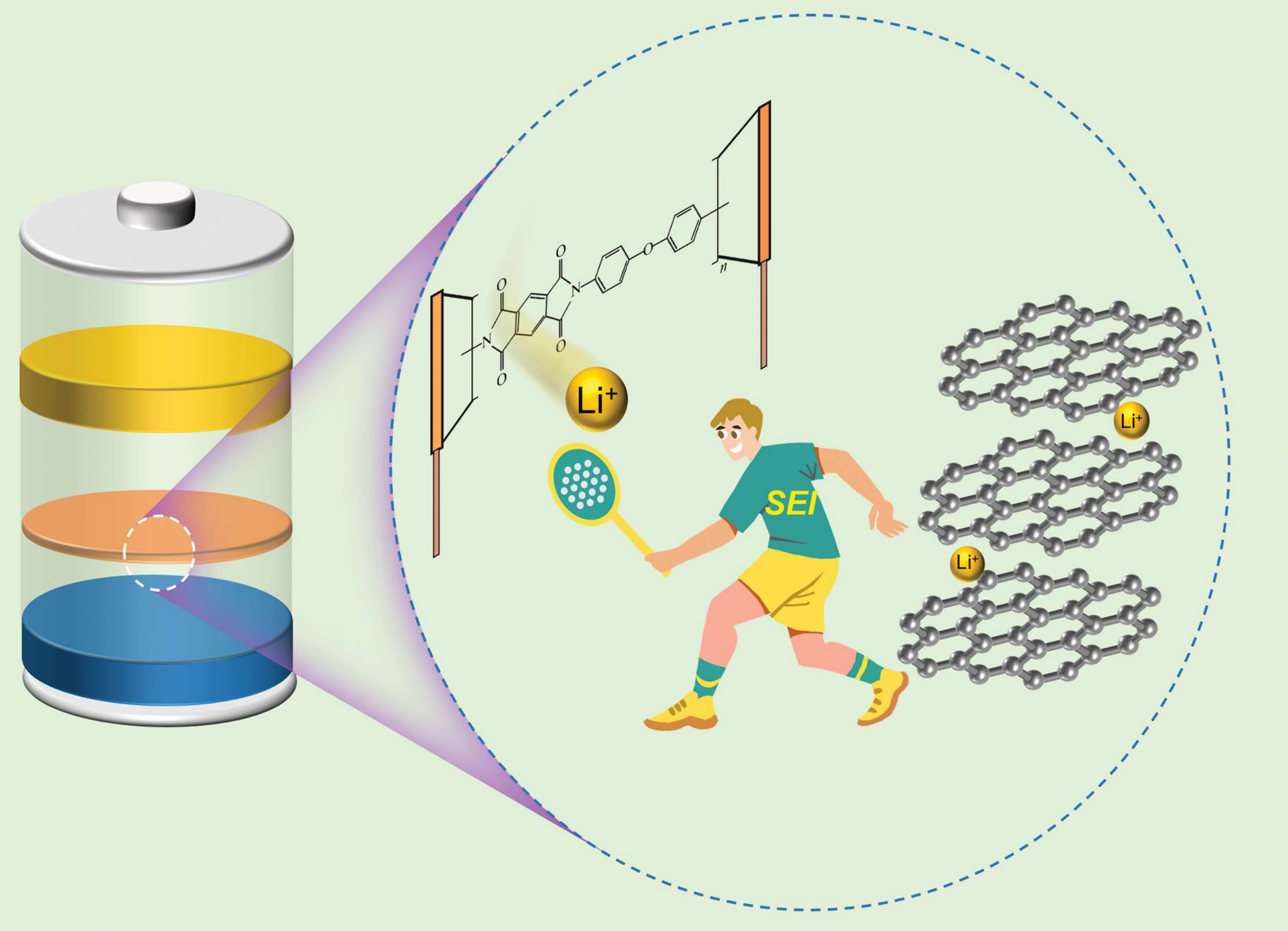

Highlighting a study on the aging mechanism of commercial lithium-ion battery led by Dr. Daniel-Ioan Stroe, Prof. Kjeld Pedersen, Dr. Lenoid Gurevich, Mr. Pengwei Li, and Mr. Jia Guo from Aalborg University, and Dr. Yaolin Xu from Humboldt-University.

Unravelling and quantifying the aging processes of commercial Li($Ni_{0.5}Co_{0.2}Mn_{0.3}$)O_2/graphite lithium-ion batteries under constant current cycling

To unveil the battery aging mechanism during constant current cycling, in this work, electrochemical cycling, real-time temperature monitoring, and operando electrochemical impedance spectroscopy of a fresh and an aged battery have been carried out. The polarization is the main reason for the battery capacity fading during operation, and the formation of solid-electrolyte interphase (SEI) and cathode-electrolyte interphase (CEI) is the leading cause of battery degradation.

As featured in:

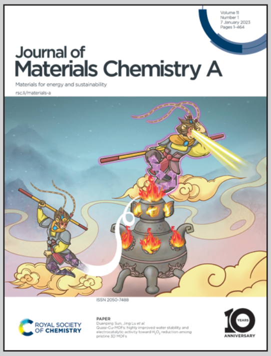
Journal of
Materials Chemistry A

See Siyu Jin, Yaolin Xu *et al.*,
J. Mater. Chem. A, 2023, **11**, 41.

ROYAL SOCIETY
OF **CHEMISTRY**

rsc.li/materials-a

Registered charity number: 207890

Journal of
Materials Chemistry A

ROYAL SOCIETY
OF CHEMISTRY

PAPER

View Article Online
View Journal | View Issue

Check for updates

Cite this: *J. Mater. Chem. A*, 2023, **11**, 41

Unravelling and quantifying the aging processes of commercial Li($Ni_{0.5}Co_{0.2}Mn_{0.3}$)O_2/graphite lithium-ion batteries under constant current cycling†

Jia Guo,[ab] Siyu Jin,*[a] Xin Sui,[a] Xinrong Huang,[c] Yaolin Xu,*[d] Yaqi Li,[ab]
Peter Kjær Kristensen,[b] Deyong Wang,[b] Kjeld Pedersen,[b] Leonid Gurevich[b]
and Daniel-Ioan Stroe[a]

Received 27th July 2022
Accepted 4th November 2022

DOI: 10.1039/d2ta05960f

rsc.li/materials-a

Constant current charging and discharging is widely used nowadays for commercial lithium (Li) ion batteries (LIBs) in applications of portable electronic devices and electric vehicles. However, the main battery degradation mechanism during constant current cycling remains unclear. In this work, electrochemical cycling, real-time temperature monitoring, and *operando* electrochemical impedance spectroscopy of a fresh and an aged battery have been carried out to unveil the aging mechanism during constant current cycling. The results of the incremental capacity analysis (ICA) indicate that polarization is the main reason for the capacity fading during operation. Besides, post-mortem analysis of the electrodes reveals that the formation of a solid–electrolyte interphase (SEI) and cathode–electrolyte interphase (CEI) is the leading cause of electrode degradation. The interface formation and evolution over cycling (including thickening and chemical variation) leads to continuous loss of active materials. The presence of a SEI and CEI also increases the impedance for charge transfer and transport and reduces the kinetics of electrochemical Li-ion redox on the electrodes. Moreover, the irreversible Li loss due to Li plating and SEI formation has been quantified, which accounts for 16.8% of the total Li in the battery. This work provides a mechanistic understanding of the degradation mechanism of commercial LIBs, guides the rational design of commercial batteries and inspires the design of charging and discharging protocols toward enhanced cycling stability and prolonged cycle life.

1. Introduction

Achieving the fast-charging goal without negatively impacting the lifetime and safety is a key challenge nowadays in lithium-ion battery research.[1,2] Compared with the standard constant current–constant voltage (CC–CV) charging protocol, the constant current (CC) charging mode without the CV segment not only significantly shortens the charging time but also effectively prolongs 20% of the battery service life.[3–5] Based on the CC charging protocol, a series of optimized charging protocols, such as pulse charging[6] and multistage constant current charging,[7] are designed to extend the battery life further or shorten charging time. However, most of these protocols are derived from extensive testing campaigns performed at the full cell level, rather than being rationally designed based on the degradation mechanism of the battery, due to the very limited understanding of the battery degradation mechanism in CC cycling. Therefore, mechanistic insights into the failure mechanisms of batteries during CC cycling are necessary for designing a more rational battery charging protocol.

Battery degradation involves many possible degradation modes under various aging conditions, which are caused by internal structural changes and/or chemical side reactions. The main issues related to battery degradation include loss of lithium inventory (LLI) and loss of active material (LAM) at both positive and negative electrodes, resulting in capacity fade and resistance increase (RI).[8] Specifically, the loss of lithium inventory may be caused by the interphase formation and its continuous thickening and Li plating.[8] The loss of active materials may occur due to transition metal dissolution, graphite exfoliation or structure collapse, and isolation of active materials from ionic or electronic conduction.[9] In addition, the resistance increase is mainly caused by interphase growth and crack formation.[10] Although all the aforementioned modes arise often in most aging situations, their impact degrees and the primary aging mode vary significantly under different battery operation conditions.

---

[a] *AAU Energy, Aalborg University, Aalborg 9220, Denmark. E-mail: sji@energy.aau.dk*
[b] *Department of Materials and Production, Aalborg University, Aalborg 9220, Denmark*
[c] *School of Electronic and Control Engineering, Chang'an University, Xi'an 710064, China*
[d] *Department of Chemistry, Humboldt-Universität zu Berlin, Brook-Taylor-Str. 2, 12489 Berlin, Germany. E-mail: yaolin.xu@hu-berlin.de*

† Electronic supplementary information (ESI) available: Supplementary methods and video. See DOI: **https://doi.org/10.1039/d2ta05960f**

Moreover, various analytical techniques have been reported in the literature to identify the aging mechanism of rechargeable batteries, from the level of full cells to materials. Among them, incremental capacity analysis (ICA) and a close-to-equilibrium open-circuit voltage (cte-OCV) are always used to qualitatively analyze the battery aging at the full cell level.[11,12] ICA can also be used to quantify the loss of lithium inventory and the loss of active materials. Still, the results are greatly affected by the magnification of the charging–discharging curves, resulting in ambiguous results.[13,14] Besides, *operando* electrochemical impedance spectroscopy (EIS) can be employed to derive the cell impedance.

To quantify the aging effects on batteries, post-mortem analysis of the electrodes is necessary. Because LLI mainly occurs on the negative electrode, Fang *et al.*[15] quantified the inactive lithium on the lithium metal anode surface (based on the gas produced from some lithium compounds reacting with water) by an innovative analysis combining titration gas chromatography and X-ray photoelectron spectroscopy (XPS) analysis. To evaluate the loss of active materials, multiple characterization techniques such as SEM imaging and Raman and XPS tests have been employed to quantify the areal crack formation[16] and transition metal dissolution.[17] Furthermore, some researchers quantified the loss of active materials by means of manufacturing and testing coin cells with a Li–metal counter electrode in coin cells, in which the capacity decrease for the aged *vs.* fresh electrode corresponds to the amount of loss of active materials.[18,19]

In this work, we have performed battery aging tests and post-mortem analysis to unravel the major processes related to the degradation of commercial $Li(Ni_{0.5}Co_{0.2}Mn_{0.3})O_2$ (NMC 532)/graphite LIBs under CC cycling and identified the primary aging mechanism. In particular, we have quantified the LLI on a graphite anode with a novel procedure combining pH measurement with XPS analysis. Compared to titration gas chromatography, the pH measurement worked out much more easily and also potentially more reliably. Moreover, the loss of active materials of the NMC 532 cathode and graphite anode was evaluated with a coin cell, and the resistance increase was analyzed by *operando* EIS in full cell and coin cell tests at the electrode level. Furthermore, the interfacial film was analyzed by the XPS test on the surfaces of the positive electrode and negative electrode. Finally, we conclude this work by providing a comprehensive aging mechanism evaluation for Li-ion batteries that are aged under CC cycling conditions and a perspective for the application of batteries as well as the design of next-generation Li-ion batteries.

2. Methodology

2.1 Battery and cycling protocols

In this study, a commercial 18650-type Li-ion battery (model: HTCNR18650-2200mAh-3.6V) with NCM 532 and graphite as the cathode and anode, respectively, was used. During the aging, the battery was placed in a climatic chamber, which was set at 35 °C. The battery was aged by charging with 2.2 A (1C-rate) from 2.5 to 4.2 V and immediately discharging with 4.4 A (2C-rate) to 2.5 V. No constant voltage stage was considered during charging or discharging. Furthermore, there was no relaxation time between the charge and discharge processes. The test platform and electrical connections between the battery cell and the battery test station are shown in Fig. S1.† A temperature sensing probe was mounted onto the battery surface to monitor the real-time temperature variation during cycle aging. After every 100 cycles, reference performance tests (RPTs) were carried out to measure the battery capacity and determine its incremental degradation. The capacity was measured in CC–CV mode by charging the battery with 0.55 A (0.25C-rate) until a maximum voltage of 4.2 V was achieved. The charging process was considered finished when a cut-off current of 0.11 A was reached. After an hour break, the battery was discharged by CC with 0.55 A (0.25C-rate) until it reached a minimum voltage of 2.5 V followed by an hour break. After the break, the measured voltage value is considered to be the cte-OCV of the battery. The state of health (SOH) was determined according to the discharge capacity. Furthermore, the electrochemical impedance spectroscopy (EIS) technique was used for measuring the battery impedance with a Digatron potentiostat for the fresh cell and the 1000 cycle-aged one at 10%, 30%, 50%, 70%, and 90% state-of-charge with a frequency from 6.5 kHz to 10 mHz. The obtained EIS spectra were fitted with an appropriate equivalent circuit model using the ZsimDemo software (provided by Ametek company).

2.2 Disassembly of commercial LIBs, pH test and coin cell evaluation

2.2.1 Disassembly of commercial LIBs. After performing the above-described cycling test, the aged cell and a fresh cell were discharged to 2.5 V at a constant current of 0.22 A (0.1C). Then, they were carefully disassembled in a glove box in an argon atmosphere. To avoid cross contamination, the retrieved positive and negative electrodes were separately washed with diethyl carbonate (DEC) for 10 minutes and dried in the glove box for 48 hours.

2.2.2 pH test. The middle parts of the negative electrodes of the fresh cell and aged cell were cut into 2 cm^2 and placed into two volumetric flasks with 20 mL of deionized water, respectively. After the produced gas was released by magnetic stirring, the volumetric flasks were sealed and placed in a 60 °C oven for a week to ensure that the lithium compounds were fully reacted and dissolved in water. Then, 1 g $BaCl_2$ was added into the flasks to remove CO_3^{2-} and F^- from the solution in the form of $BaCO_3$ and BaF_2 to exclude the interference from alkaline Li_2CO_3 and weak alkaline LiF that can hydrolyze and produce extra OH^-. Finally, the pH (pH meter: 1100 L from VWR and accuracy: ±0.005) was tested after the solution cooled down to room temperature. The above tests were repeated 3 times and the average pH value was chosen.

2.2.3 Coin cell assembly. The middle parts of the electrodes from the dismantled cells were cut into circles with a diameter of 14 mm. After drying in a 110 °C oven for 6 hours, the electrodes were used to build CR2032 coin cells with a 15 mm diameter, 450 μm thick Li metal and a Celgard 2320 separator.

To fill up the cells, we used 1 M $LiPF_6$ in the solution of dimethyl carbonate (DMC)/diethyl carbonate (DEC) with a volume ratio of 1 : 1. The capacities of the assembled coin cells were measured using a Land CT 2001A battery tester, in the voltage range from 2.75 V to 4.2 V for the NMC 532/Li cell and from 0.001 V to 1.0 V for the graphite/Li cell. Furthermore, their impedance was measured by means of EIS using a Palmsens potentiostat.

2.3 Materials characterization

A Zeiss EVO 60 scanning electron microscope (SEM) was employed to image the morphologies and measure the thicknesses of the positive and negative electrodes. X-ray photoelectron spectroscopy (XPS) measurements were performed using a Specs XR50 with a non-monochromated Al Kα (1487 eV) X-ray source and a Phobos 150 1D-DLD electron detector. The crystalline structure of the electrode materials was characterized at 40 kV with X-ray diffraction (XRD) using a device manufactured by Panalytical and was also measured with Raman spectroscopy using a 532 nm laser.

3. Results and discussion

3.1 Aging of the full cell

ICA and cte-OCV techniques were employed to preliminarily diagnose the battery degradation mechanisms. The charging/discharging curves from eleven RPTs are presented in Fig. 1a. With the battery aging evolution, the charging plateau shows an increasing trend, whereas the discharge plateau becomes lower. Then, the voltage gap between the charging and discharging plateaus, which is associated with the battery impedance, is gradually increasing. Meanwhile, the voltage plateau is significantly shortened, corresponding to a decrease in capacity. To further clarify the process of voltage plateau evolution, ICA was applied to the charging–discharging curves in Fig. 1a, and the obtained results are shown in Fig. 1b. The IC curves are associated with the phase transitions of active materials during the Li^+ shuttle, corresponding to the a and b peaks in the charging process and c peak in the discharging process. Along with cycling, the IC peaks in the charging process show an obvious shift toward a higher voltage, implying a polarization increase.[20] Usually, the shift of the higher voltage peak a may be related to a disproportionate loss of the active material at the positive and negative electrodes.[21] In this work, we choose the shift of the b peak at a lower potential to quantify the increase in polarization, as shown in Fig. 1c. The progression of the capacity fade (expressed as SOH) is clearly related to the increase in polarization.

A close-to-equilibrium open-circuit voltage (cte-OCV) measurement was carried out to analyze the OCV behavior with battery aging, as shown in Fig. 1d. The discharging cte-OCV increases gradually, due to the increase in polarization. As expected, the charging cte-OCV did not increase, instead a slightly decreasing trend is observed. This will lead to a decreased charging OCV range as well as a decreased charging capacity.

The polarization was evaluated by performing an *operando* electrochemical impedance spectroscopy (EIS) test. As shown in Fig. 2a and b, the measured results are Nyquist plots, which are

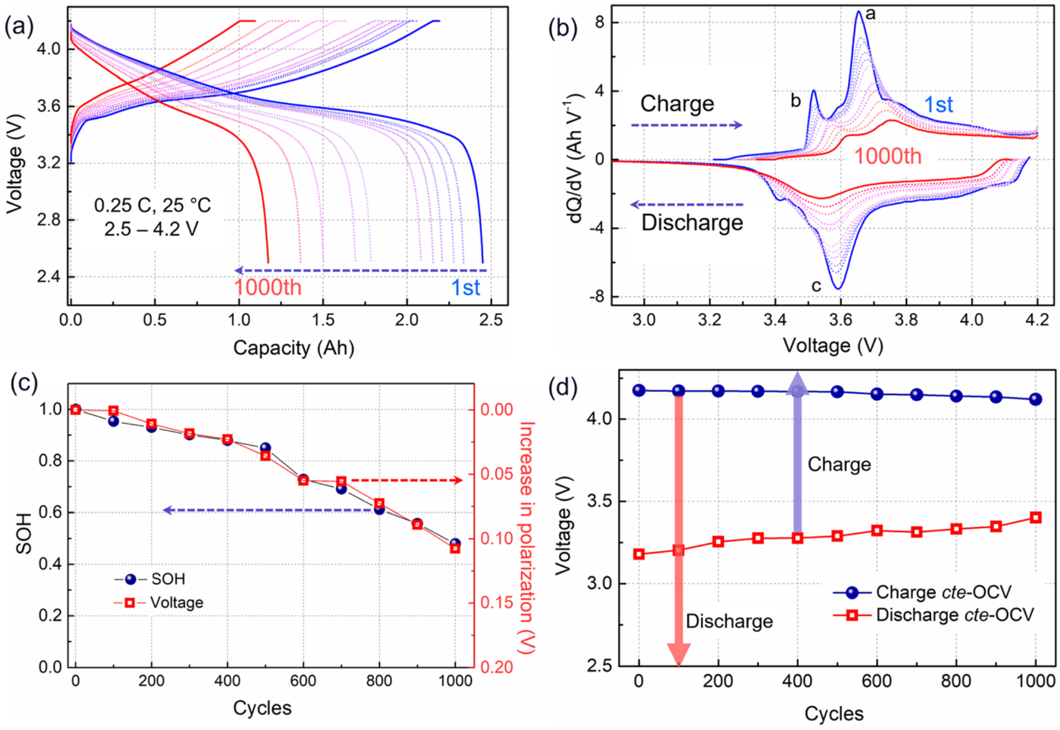

Fig. 1 Electrochemical behavior from the reference performance test (RPT) after every one hundred cycles at 0.25C (0.55 A) and 25 °C. (a) Charge and discharge curves, (b) IC curves, (c) SOH and polarization evolution (shift of the b peak in (b)) over cycling, and (d) charging and discharging cte-OCV. The arrows represent the real voltage window of discharging/charging.

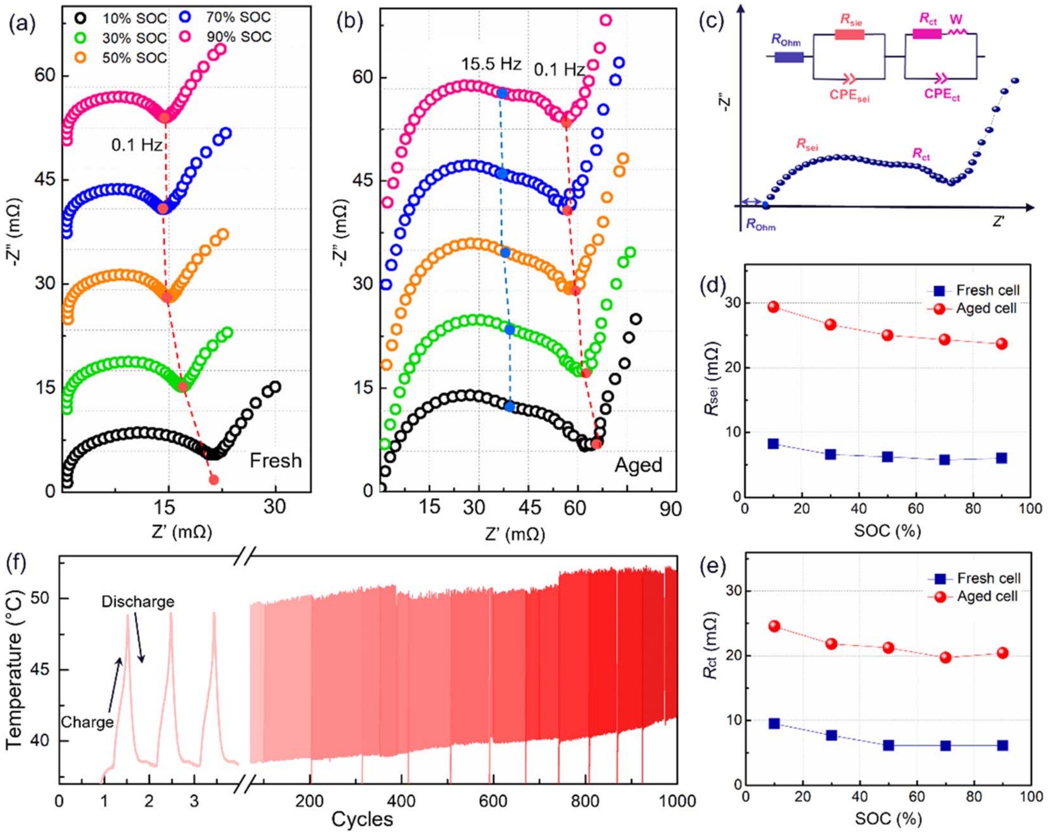

Fig. 2 EIS spectra at different SOCs for a (a) fresh cell and (b) an aged cell; (c) schematic illustration and an equivalent circuit used to fit the EIS Nyquist plots; the fitted results for (d) R_{sei}, and (e) R_{ct}; (f) the temperature tested using a temperature sensing probe on the outer surface of the cell.

composed of three parts with different frequency ranges, representing the bulk resistance (R_{ohm}), the solid electrolyte interface resistance (R_{sei}), and the charge transfer resistance (R_{ct}), respectively.[3] The inserted equivalent circuit was employed to fit the Nyquist plots, as shown in Fig. 2c. The obtained results are presented in Fig. 2d and e. Here, the R_{ohm} will not be adopted due to an unstable ohmic impedance caused by the connector of the electrochemical workstation, and this always shows little change in battery aging.[3,12] Therefore, the Nyquist plots were translated to the origin of the coordinates. After 1000 cycles, a four-fold increase in the R_{sei} from below 8 mΩ to about 30 mΩ is observed (Fig. 2c). Besides, R_{ct} has increased to over 20 mΩ (Fig. 2d), indicating an overall degradation at the electrode interface and charge transfer. Furthermore, R_{sei} and R_{ct} decrease with the battery charging. R_{sei} is related to the diffusion of Li ions at the interface and the R_{ct} is linked to the electrochemical reaction.[22] As reported in ref. [22] the SEI film is partially ruptured at high SOC due to the increased volume of lithiation graphite, and recovers in the followed discharge process. So, the R_{sei} decreased with battery charge. Furthermore, a high SOC is linked to a high voltage as well as an active state of the electrochemical reaction, resulting in a lower R_{ct}. The temperature of the battery surface was detected in the aging process, as shown in Fig. 2f. The temperature changes periodically with the charge–discharge cycle. Besides, the temperature range fluctuates, due to an uncontrollable change in the sticking position or tightness of the thermal probe on the battery surface. With the increase in the cycle number, the temperature of the battery surface gradually increases (varying from a low temperature of 42 °C to a high temperature close to 55 °C). The temperature increment will lead to a series of side reactions inside the battery during electrochemical cycling, for example, the rupture and reformation of the interfacial film at high temperatures, resulting in a continuous increase of the internal impedance. This is consistent with the discharge cte-OCV trend, further illustrating that the internal impedance continues to increase with battery cycling.

It can be concluded from the above *operando* diagnosis that the battery capacity fade during operation is dominated by the internal resistance in constant current cycling, especially for the R_{sei} increase. For further quantifying the degradation, a post-mortem analysis is necessary to be performed.

3.2 Post-mortem analysis

The aged cell and fresh cell were disassembled to evaluate the loss of lithium, loss of active materials, and increase of impedance in a qualitative or quantitative way. Upon opening the battery, liquid electrolyte was present in the disassembled cell and the electrodes were wet, suggesting that the consumption of electrolyte is not the major factor for battery failure. The retrieved electrodes are shown in Fig. S2.† Both the fresh positive and negative electrodes showed smooth surfaces. The positive electrode was black and shiny, and the negative electrode showed a dark gray color. In contrast, the surfaces of both electrodes in the aged cell appeared rough, and some cathode materials peeled off the positive electrode. Besides, the surface of the negative electrode was covered with a layer of a dark yellow substance, which could be SEI/lithium-rich regions caused by the electrolyte decomposition or Li plating.[23]

3.2.1 Loss of Li on the negative electrode. Loss of Li-ions, which results in capacity loss, mainly occurs on the negative electrode in the form of Li plating or a surface film.[24] The SEM image in Fig. 3a shows smooth and plump graphite particles of the fresh negative electrode. In contrast, the aged graphite shows a collapsed structure covered by a rough surface layer and some small particles, as shown in Fig. 3b. The rough surface layer is considered to be the SEI film,[25] while the small particles are considered to be Li dendrites in some reports.[26] To prove the presence of irreversible Li on the surface of the aged negative electrode, a piece of the disassembled negative electrode after washing with DEC was directly placed into water, which violently reacted with water producing significant bubbles, as shown in Fig. S3.† After reaction with water, the negative electrode shows a clean surface, and the SEM image is shown in Fig. 3c. Most of the particles and rough surface layer have disappeared, and then a collapsed graphitic shape and a smooth surface appear. This is due to the reactions between the water and Li or Li compounds. The possible reactions and solubility of these Li compounds are summarized in Table 1[15] The reaction product is mainly alkaline soluble LiOH. pH measurement

Table 1 The dissolved species or reactions with water of lithium or lithium compounds on the anode

Components	Reactions with water	Species in solution
Li	$2Li + 2H_2O = 2LiOH + H_2\uparrow$	Li^+, OH^-
Li_2O	$Li_2O + H_2O = 2LiOH$	
CH_3Li	$CH_3Li + H_2O = LiOH + CH_4\uparrow$	
ROLi	$ROLi + 2H_2O = 2LiOH + H_2\uparrow$	
LiOH	N.A.	
LiF	N.A.	Li^+, F^-
Li_2CO_3	N.A.	Li^+, CO_3^{2-}

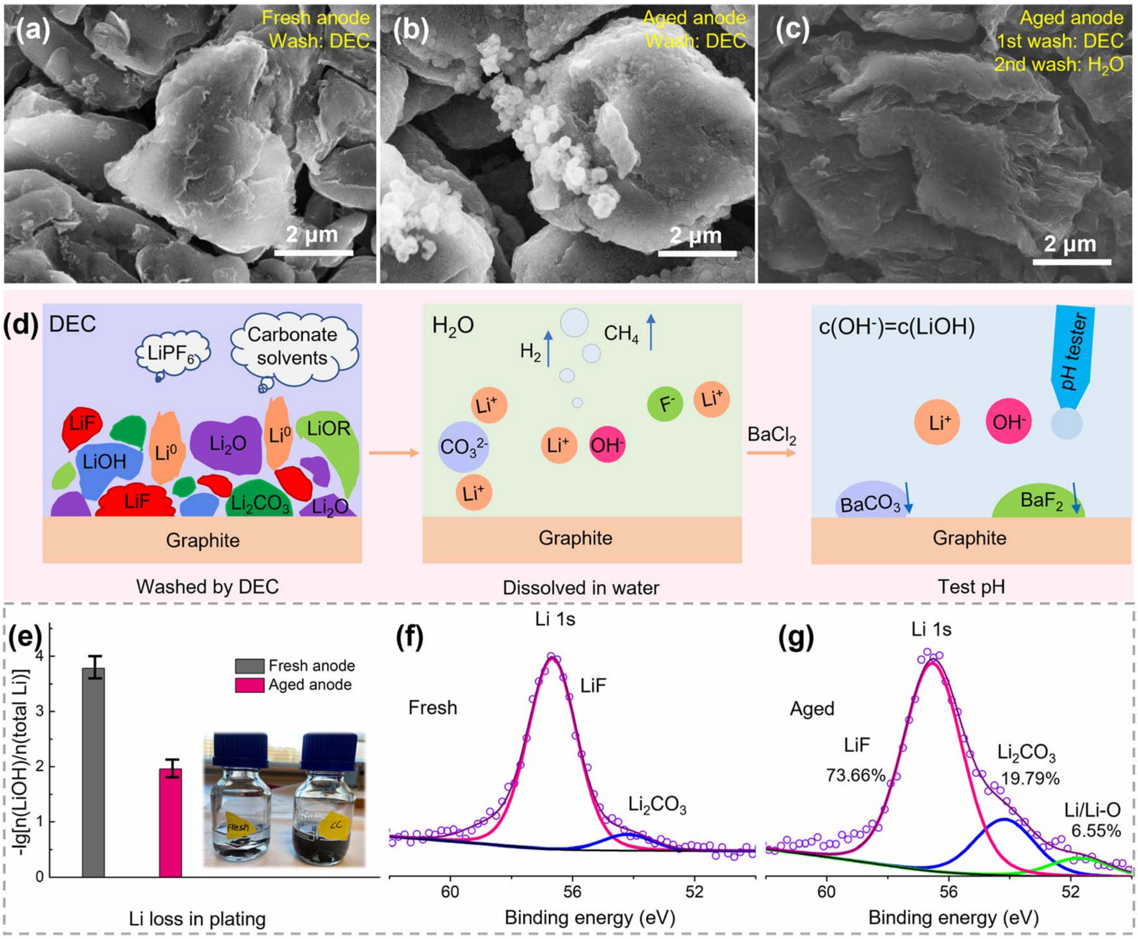

Fig. 3 Lithium loss on the negative electrode surface. SEM images of the graphite anode from (a) the fresh cell, (b) the aged cell after washing with DEC, and (c) the aged cell after washing with DEC and then with water; (d) the mechanism diagram of the dissolution of lithium compounds in water and quantified by the pH test, and the quantified result of the LiOH content is shown in (e); Li 1s XPS spectra of the negative electrode from (f) fresh cell and (g) aged cell.

has been widely used to quantify residual lithium in nickel-rich material production.[20] Here, we use the pH value to quantify the irreversible lithium that can react with water and dissolve in water as a state of Li^+ and OH^-, and the process is illustrated in Fig. 3d, followed by X-ray photoelectron spectroscopy (XPS) measurement to quantify the total content of lithium loss on the graphite anode.

The pH values are 10.64 and 8.81 for the aged and fresh negative electrodes, respectively, corresponding to a lithium loss of 1.10% and 0.02% in the form of Li^0, Li_2O, LiOH, CH_3Li, and ROLi, as shown in Fig. 3e. Furthermore, the XPS spectrum of Li 1s was measured for the electrodes of Fig. 3a and b, as shown in Fig. 3f and g, respectively. There are three fitted peaks for the aged negative electrode, which belong to LiF, Li_2CO_3, and Li/Li–O compounds, corresponding to an amount of 73.66%, 19.79%, and 6.55% Li, respectively. Here, the Li/Li–O compounds correspond to the pH quantified part (1.10%). Therefore, the lithium loss in the aged negative electrode can be quantified as 16.82%. Note that some active Li inserted in graphite during the voltage recovery from a fully discharged state. So, the pH test and XPS results establish that the lithium loss is much lower compared with the capacity loss (over 50%). This further proves that there is no significant amount of inactive lithium on the negative surface. Furthermore, the quantified Li loss in our research is close to other reported Li contents in SEI films.[15,27]

3.2.2 Materials degradation. Fig. 4a and b show the cross-section SEM images of the fresh and aged positive electrodes, respectively. The average thickness of the fresh positive electrode is 137 μm (Fig. 4a). After aging, the average thickness increases to 153 μm (*i.e.*, increases by 11.7%) (Fig. 4b). Besides, cracks appeared and extended to the inner part of the electrode, resulting in loose particles and intra-electrode voids, which is one of the reasons for the increased electrode thickness.

Another reason is the increased volume of cathode grains, which can be evaluated by the left shift of the XRD pattern as shown in Fig. 4c. This will lead to an increase in the paths of charge transfer and Li diffusion as well as an increased internal resistance. Besides, the inconspicuous splitting peaks (006/012) mean a decreased crystallinity, and the increased *I*(003)/*I*(104) means increased Li/Ni cation mixing for the aged positive electrode.[28] Furthermore, the deterioration of the material is also reflected in particle morphology. The surface of the fresh cathode particles (Fig. 4d) is smooth, and then, pulverization and cracking happen during aging (Fig. 4e). Besides, the presence of residue powders on the cathode particle surface seems

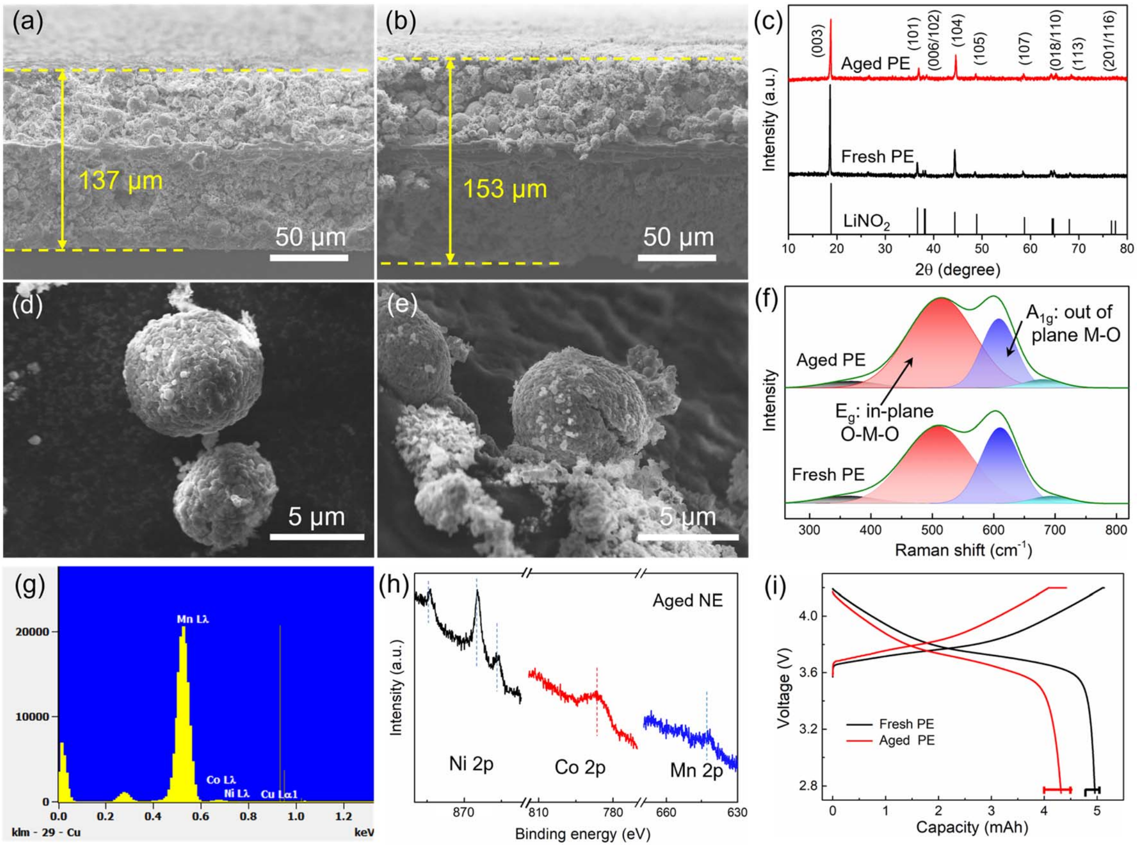

Fig. 4 Cross-section SEM images of (a) fresh and (b) aged positive electrodes. (c) XRD patterns of the fresh and aged positive electrodes (PE). SEM images of (d) fresh and (e) aged NMC particles. (f) Raman spectra of the fresh and aged positive electrodes. Transition metals (Mn, Co, and Ni) from the positive electrode are deposited on the negative electrode surface, which can be measured by (g) EDS point scan and (h) XPS. (i) The voltage profiles of the fresh and aged positive electrodes were tested against the Li metal electrode with a coin cell in the voltage range of 2.75–4.2 V at 0.05C.

to be due to interface compositions, and this was tested by XPS as shown in Section 3.2.3. The cracks are also reflected in the Raman spectrum (Fig. 4f), where NMC can be thought of as a solid solution of $LiNiO_2$, $LiMnO_2$, and $LiCoO_2$. Among them, layered $LiNiO_2$ and $LiCoO_2$ contribute only two Raman-active modes, one is the A_{1g} mode at 609 cm^{-1} and the other is the E_g mode at 503 cm^{-1}, corresponding to the out-of-plane M–O stretch and in-plane O–M–O band, respectively.[29] The additional weak bands were contributed by $LiMnO_2$. After aging, the increased E_g mode means an increase in the amount of the in-plane O–M–O band, which is consistent with the crack formation and inside-surface exposure as shown in Fig. 4e. As reported, the HF from electrolyte decomposition is easy to penetrate into cathode particles and induce serious side reactions, causing the transition metal to dissolve in the electrolyte and then deposit on the negative electrode surface. EDS point scans were performed to verify the presence of transition metal elements Ni, Co, and Mn, as shown in Fig. 4g. Furthermore, Ni, Co, and Mn elements can also be observed by XPS from the surface of the aged negative electrode (Fig. 4h). As reported in ref. [30] and [31], the Co deposits on the graphite surface can also accelerate the exfoliation of graphite, leading to a severe degradation of the full cell.

The factors of particle cracks, increase in grain volume, Li/Ni mixing, and transition metal dissolution have an impact on electrode capacity degradation, which can be evaluated using coin cells. As shown in Fig. 4i, the aged positive electrode shows a higher charge plateau and a lower discharge plateau, which are caused by polarization. Furthermore, there is no evident constant-voltage charging segment for the aged positive electrode, which means that the positive electrode has been fully charged before the constant-voltage charging period with a 0.05C current. In contrast, the battery voltage of the aged positive electrode prematurely reaches the upper cut-off voltage during charging due to a high internal resistance, resulting in a long constant-voltage charging period as well as a decreased battery capacity. However, over 86% of the initial capacity is still maintained.

Similarly, the negative electrode also becomes thicker after aging. The thickness of the fresh negative electrode is 200 μm (Fig. 5a), which increased to 271 μm (*i.e.*, 30.5% increase) after aging (Fig. 5b). There are a lot of cracks and exfoliated pieces in the aged negative electrode, which is a key reason for the thickening of the negative electrode. Besides, the materials are stripped from the current collector, leading to an increase in R_{ct}, as illustrated in Fig. 2e. From the top view, the surface film, which has a thick and cracked surface, can be observed on the top of the aged negative electrode (Fig. 5d), and a surface film also can be observed from the edges of the graphite particles in the SEM image (Fig. 5f), which is the main reason for surface

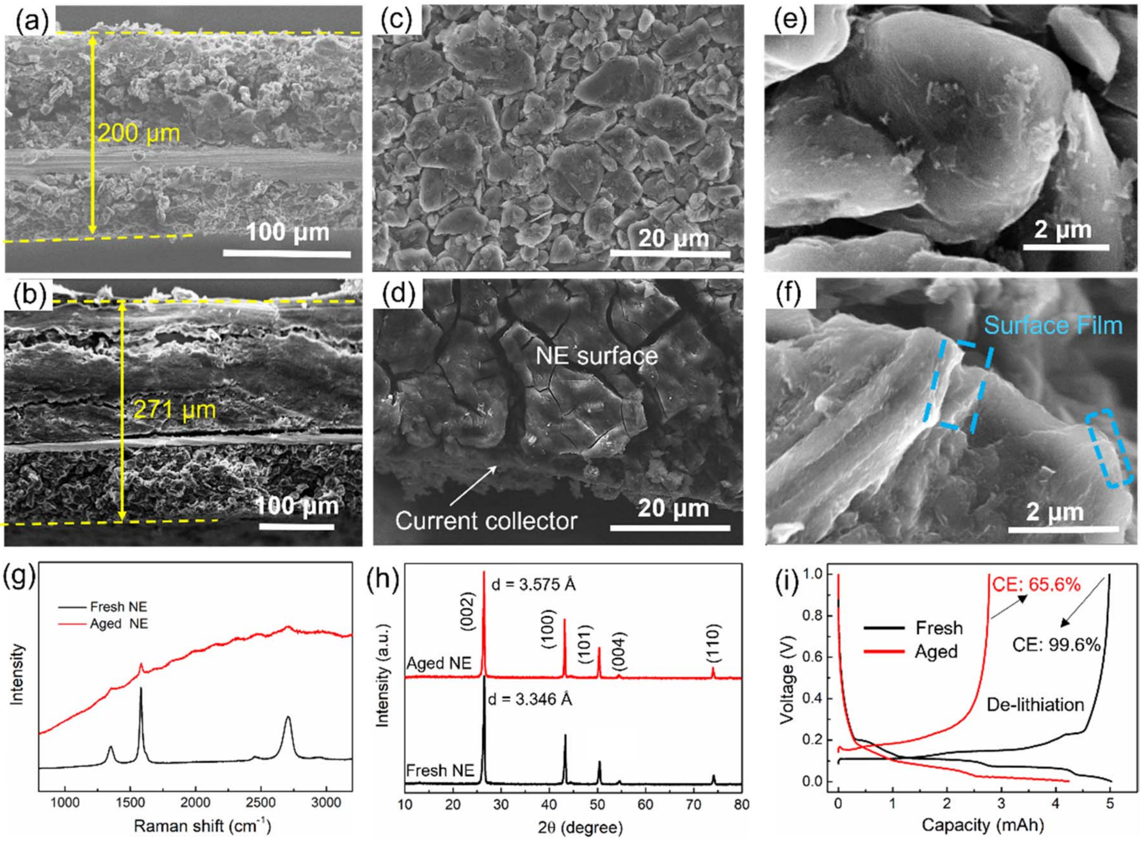

Fig. 5 Cross-section SEM images of (a) fresh negative electrode and (b) aged negative electrode; top surface SEM images of (c) fresh negative electrode and (d) aged negative electrode; SEM images of (e) fresh graphite particles and (f) aged graphite particles; (g) Raman spectra of the fresh and aged negative electrodes; (h) XRD patterns of aged and fresh negative electrodes; (i) charge and discharge voltage curves obtained by testing against Li in coin cells in a voltage range of 0.001–1.0 V at 0.05C.

impedance in batteries. Besides, the graphite particles collapse into irregular shapes after degradation. Furthermore, Raman measurements with laser wavelengths of 532 nm were performed to test the interface structures of both fresh and aged negative electrodes (Fig. 5g). However, Raman spectroscopy can only detect a very weak graphitic phase from the aged negative electrode interface, implying that the thickness of the interfacial precipitates is close to 500 nm. XRD patterns were recorded to evaluate the structure change, as shown in Fig. 5h. Layer spacing of graphite increased from 3.346 Å to 3.575 Å with the aging, resulting in a volume expansion of the negative electrode. This is another reason for the electrode thickening.

The influence on negative electrode capacity is shown in Fig. 5i. The lithiation process of the graphite anode can be fully carried out with a lower cut-off voltage (0.001 V). The capacity fade of the lithiation process represents the loss of lithium-intercalated graphite, which is less than 15%. However, the de-lithiation process is easily affected by the initial charging voltage caused by an internal impedance, and the coulombic efficiency of the aged negative electrode is only 65.6%, resulting in a 44% capacity loss in the de-lithiation process compared with that of the fresh negative electrode.

3.2.3 Interfacial impedance of electrodes. Li compounds are plated on the negative electrode surface together with other solvents to form a SEI layer. Similarly, the surface layer on the positive electrode is called the "cathode–electrolyte interphase (CEI)". The SEI and CEI usually can be unified as the "electrode–electrolyte interphase (EEI)" which is the main reason for battery potential drop during cycling by forming a thermodynamic potential gap between the electrodes and electrolyte.[32]

From the above analysis, it was found that an increase in impedance is the main reason for the capacity fading of the full cell, positive electrode, and negative electrode. Fig. 6a and b compare the impedance evolution of both positive and negative electrodes upon cycling, and the fitted results are shown in Fig. 6c. The R_{cei} of the aged positive electrode is 574.5 Ω which is higher than that of the fresh one (42.47 Ω). Besides, an extra semicircle appears in the impedance spectra of the

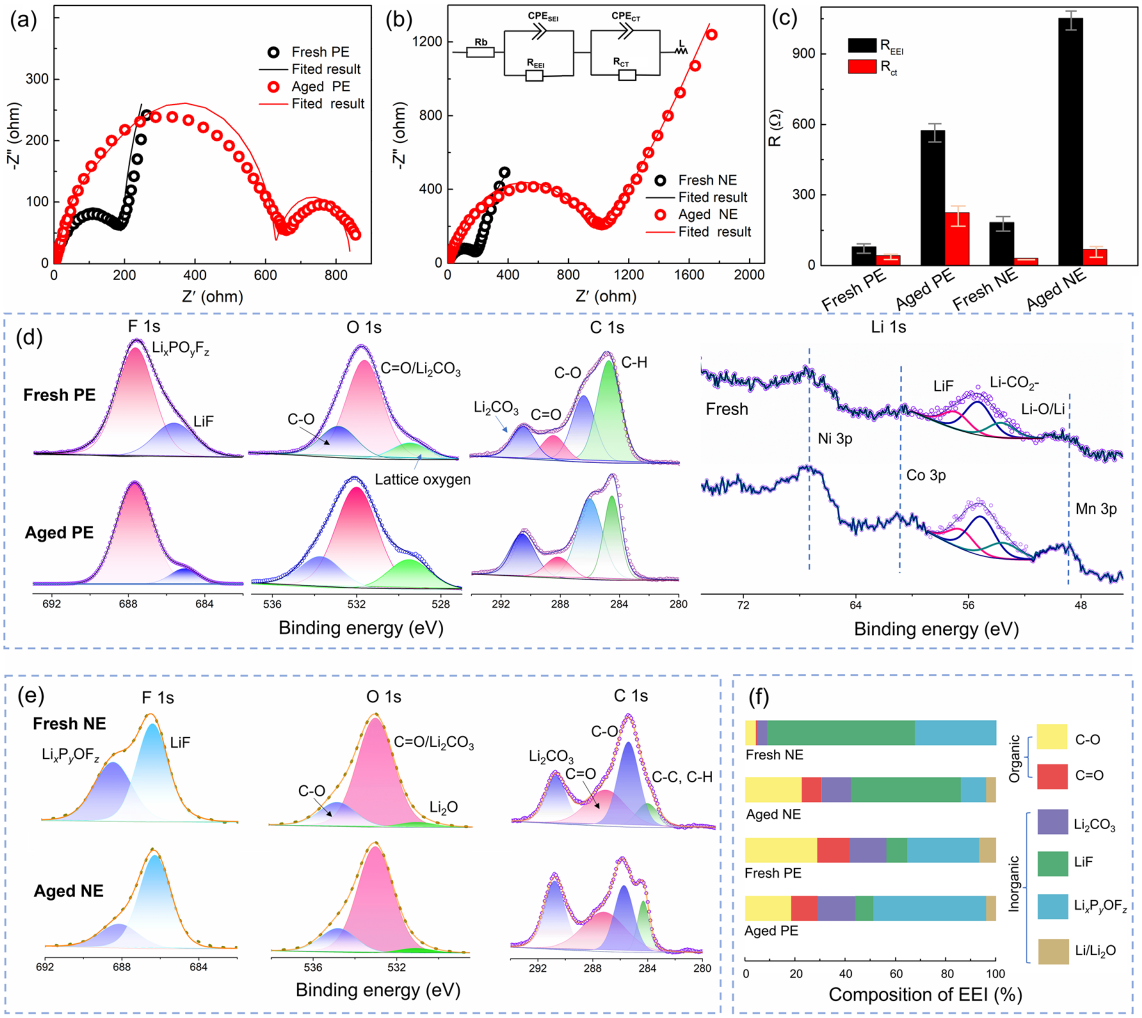

Fig. 6 Impedance evolution tested using coin cells for the fresh and aged (a) positive electrode (PE), and (b) negative electrode (NE), and (c) fitted results, R_{EEI}: R_{sei} or R_{cei}; XPS spectra of (d) F 1s, O 1s, C 1s, and Li 1s for the positive electrodes and (e) F 1s, O 1s, and C 1s for the negative electrodes; (f) the chemical composition obtained by quantitative XPS characterization of the SEI film on the negative electrode surface and CEI film on the positive electrode surface.

aged positive electrode (Fig. 6a), indicating deteriorated electronic conductivity,[33] which is related to the cracks and pulverization on the cathode. Furthermore, the impedance spectra of the negative electrode are shown in Fig. 6b. The R_{sei} of the aged negative electrode is 1052 Ω, while the R_{sei} of the fresh one is only 183 Ω. Therefore, the impedance of the positive and negative electrodes is mainly contributed by the interface film.

Here, XPS was performed to probe the EEI compositional information on the fresh and aged batteries.

XPS was performed to identify the CEI composition, and the results of F 1s, O 1s, C 1s, and Li 1s are shown in Fig. 6d. This indicates that CEI films are mainly composed of $Li_xP_yOF_z$ (peaks at 688.5 eV in the F 1s spectrum), LiF (peaks at 56.5 eV in the Li 1s spectrum, and 686.3 eV in the F 1s spectrum), C–O (peaks at 535.3 eV in the O 1s spectrum), CO (peaks at 288.9 eV in the C 1s spectrum), Li_2CO_3 (peaks at 55.6 eV in the Li 1s spectrum and 291.0 eV in the C 1s spectrum), and Li–O (peaks at 51.5 eV in the Li 1s spectrum). It is worth noting that the percentage of lattice oxygen increases obviously for the aged positive electrode in the O 1s spectrum, which is related to the crack formation and exposing a vast fresh surface inside secondary particles,[34] which is consistent with the SEM analysis in Fig. 4e. Furthermore, this was further confirmed by the enhanced bands of Ni–Li, Co–Li, and Mn–Li in the Li 1s spectrum.

For the SEI film (Fig. 6e), the formation of $Li_xP_yOF_z$ originates from the reactions of trace H_2O and $LiPF_6$ in electrolyte,[35] which belongs to the primary precipitated solid and can decompose to form Li_3PO_4 and LiF.[36,37] In the Li 1s spectrum, Li_2CO_3 is mainly derived from electrolyte decomposition.[36] Besides, Li_2O (peak at 52.4 eV) can be attributed to Li reducing CO_2 that comes from the decomposition of Li_2CO_3 at a high voltage (about 4.2 V).[38]

However, the percentage of Li–O in our research is not as high as that in other related reports,[39] due to the low upper cutoff voltage (4.2 V) and the absence of the constant-voltage charging stage. Besides, the C–O and CO compounds are from the reduction of the electrolyte solvent, such as diethyl carbonate (DEC).

A quantitative analysis of the XPS data was performed for further analysis. As shown in Fig. 6f, inorganic compositions are the major EEI components, which play an essential role in achieving the electronic insulation of the EEI.[32] For the SEI film, the increased content of organic compositions (such as C–O and CO) on the aged NE originates from the decomposition of ethylene carbonate (EC), which is related to a degraded electrolyte.[35] Furthermore, Li_2CO_3 and LiF are the main ionic carriers for Li^+ diffusion at the interface. The decreased percentage of LiF in the aged anode will hinder the diffusion of Li-ions, as well as lead to an increased R_{sei} as shown in Fig. 2d and 6b. Unlike the SEI film, the most occupied components in the CEI film are $Li_xP_yOF_z$ and organic components, due to $LiPF_6$ decomposition at high voltage on the positive electrode side.[35] Besides, the percentage of inorganic compounds ($Li_xP_yOF_z$, Li_2CO_3, LiF, and Li_2O) changed after aging, due to the further reformation of the CEI and SEI that is more easily damaged at high operation temperature. As a result, the interface composition changes in both the negative and positive electrodes along cycling.

3.3 Discussion on the degradation mechanism and perspectives for stabilization

The battery finally drops to 52% capacity in CC cycling, which is due to the loss of active materials on the negative electrode, the loss of active materials on the positive electrode, the loss of Li-ions, and an increased interfacial impedance, as summarized in Fig. 7. We quantify the available electrode materials based on the amount of Li that can be inserted into the electrode during lithiation in coin cell tests. The results show that less than 15% loss of active materials occurs on the negative and positive electrodes. Furthermore, the loss of Li-ions is also not the key limiting factor for the battery capacity fading, which only accounts for 16.8% from the pH and XPS analyses. Significantly, the resistance increase is the limiting factor for the battery capacity retention rate, resulting in 44% capacity loss for the negative electrode and 14% capacity loss for the positive electrode. The increased resistance is mainly caused by the interface films, such as the SEI film on the negative electrode and CEI film on the positive electrode.

To further extend the battery life, some measures can be taken to stabilize the battery performance from the aspects of full-cell operation, electrode fabrication, or electrode material preparation. At the full-cell application level, the impedance increase can be inhibited by some reasonable charging/discharging protocols, such as dynamic pulse current.[6] The thickening of the SEI film is mainly caused by the repeated formation and cracking processes, resulting in an increased interface impedance and a deteriorated battery performance. The application of pulse current in LIBs can construct a high stability and low impedance SEI film.[40] Then, the increase in interface impedance can be effectively inhibited. Furthermore, adjusting the frequency and duty cycle of pulse current can achieve a fast charging. Besides, the temperature of the battery during operation is high and the surface temperature is close to 50 °C, even at room temperature. The high temperature will exacerbate the side reactions at the electrode interface, and then transition metals from the positive electrode will dissolve in the electrolyte and deposit on the graphite surface, resulting in the loss of active materials and an impedance increase. Therefore, heat dissipation or cooling systems are needed for the battery to operate in high-temperature environments.

At the electrode level, the phenomenon of active materials peeling is obvious for both aged positive and negative electrodes, and the formed debris detaches from the electrodes and current collectors, not only causing the loss of active materials but also hindering the diffusion of Li-ions. A durable binder is necessary to build a tight connection between the active materials and the current collector. Besides, the thickness of electrodes is also an important parameter for the battery performance. With a thicker electrode, the Li-ion transport path is longer, resulting in a battery impedance increase. However, a smaller electrode thickness will lead to a low energy density. Furthermore, the thickness of electrodes is also related to the

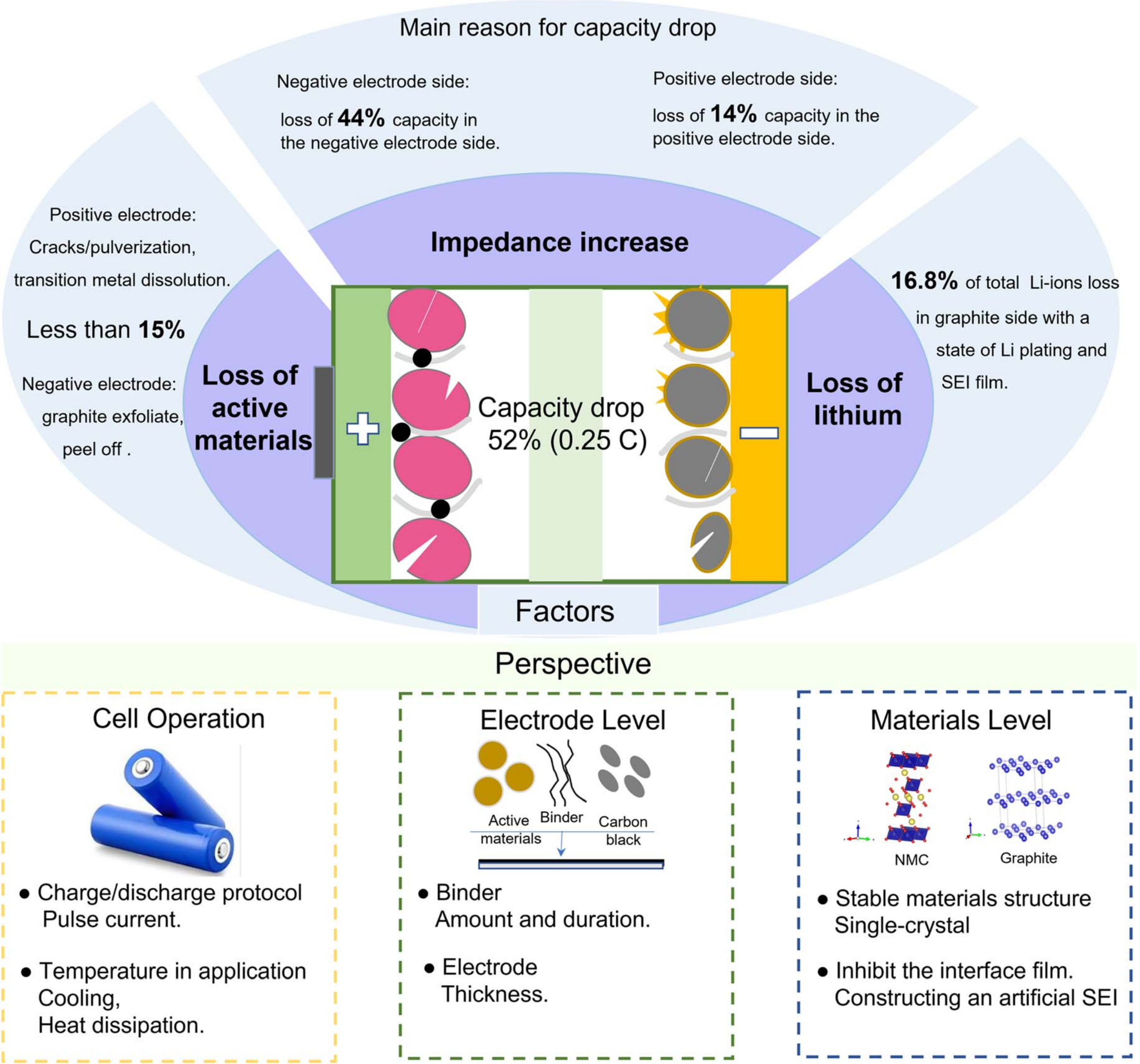

Fig. 7 Overview of the processes related to battery capacity fade and perspectives for extending the cycle life.

ratio of the negative electrode capacity and positive electrode capacity, *i.e.*, the *N*/*P* ratio. A high *N*/*P* ratio means excess graphite as well as SEI film formation, while a lower *N*/*P* will lead to the formation of Li-plating.[8] Therefore, the thickness of electrodes (*N*/*P*) can be optimized to reduce the loss of active materials and inhibit the impedance increase.

At the material level, the pulverization and volume expansion of the cathode particles are serious, which will enlarge the transfer path of Li-ions, resulting in an increased impedance. The cathode materials with a single-crystal structure will effectively inhibit pulverization and volume expansion. Besides, the lower specific surface area of single-crystal particles also inhibits the amount of interface film and the dissolution of transition metals.[41] For the interface film, constructing an artificial SEI on the graphite surface can inhibit the deposition derived from electrolyte decomposition and the anion solvation effect, resulting in a stable electrode/electrolyte interface as well as superior cycling stability.[42]

4. Conclusions

This study identifies the dominant aging mechanism of commercial $Li(Ni_{0.5}Co_{0.2}Mn_{0.3})O_2$/graphite batteries under CC cycling conditions at the full cell, electrode and material levels. After a controlled aging test for 1000 cycles, the cell capacity drops by 52% (0.25C), which is mainly caused by the increased internal impedance. In particular, both the positive and negative electrodes show a significant increase in impedance, especially the interface resistance ascribed to the formation of the EEI films, which leads to more rapid voltage collapse to cut-off voltage and hence reduced capacity. Moreover, the increased internal impedance aggravates the heat generation during battery operation which exacerbates the parasitic reactions and accelerates the battery degradation. At the material level, the cracking/pulverization of NCM particles and transition metal dissolution are the main degradation processes on the positive electrode side, while the >35% capacity drop of the negative electrode is mainly caused by the increased interfacial impedance. Besides, the Li-plating and SEI films are the main causes for the loss of active Li-ions, accounting for 16.8% of the total Li ions in the battery.

The degradation mechanisms of commercial NCM/graphite LIBs identified in this work provide guidance to rationalize the discharging and charging protocols for enhanced cycling stability and cycle life. The aging mechanisms and the methodology for identifying them could also be generalized and extended to other types of rechargeable batteries or electrochemical energy storage devices.

Author contributions

Jia Guo: methodology, experiments, and writing. Siyu Jin and Xin Sui: methodology, coordination, and experiments. Xinrong Huang, Yaqi Li, Peter Kjær Kristensen, and Deyong Wang: experiments. Yaolin Xu, Kjeld Pedersen, Leonid Gurevich, and Daniel-Ioan Stroe: resources, supervision, review, and editing.

Conflicts of interest

The authors declare that they have no conflict of interest.

Acknowledgements

Jia Guo and Yaqi Li were supported by a grant from the China Scholarship Council (no. 202006370035 and no. 202006220024). We would like to thank Lars Rosgaard Jensen for their help in performing the Raman test.

References

1 Y. Liu, Y. Zhu and Y. Cui, *Nat. Energy*, 2019, **4**, 540–550.
2 G. L. Zhu, C. Z. Zhao, J. Q. Huang, C. He, J. Zhang, S. Chen, L. Xu, H. Yuan and Q. Zhang, *Small*, 2019, **15**, 1–14.
3 J. Zhu, M. S. Dewi Darma, M. Knapp, D. R. Sørensen, M. Heere, Q. Fang, X. Wang, H. Dai, L. Mereacre, A. Senyshyn, X. Wei and H. Ehrenberg, *J. Power Sources*, 2020, **448**, 28–30.
4 J. Guo, Y. Li, K. Pedersen and D. Stroe, *Energies*, 2021, **14**, 1–22.
5 T. R. Tanim, Z. Yang, A. M. Colclasure, P. R. Chinnam, P. Gasper, Y. Lin, L. Yu, P. J. Weddle, J. Wen, E. J. Dufek, I. Bloom, K. Smith, C. C. Dickerson, M. C. Evans, Y. Tsai, A. R. Dunlop, S. E. Trask, B. J. Polzin and A. N. Jansen, *Energy Storage Mater.*, 2021, **41**, 656–666.
6 X. Huang, W. Liu, A. B. Acharya, J. Meng, R. Teodorescu and D. I. Stroe, *IEEE Trans. Ind. Electron.*, 2021, **69**, 10144–10153.
7 A. Laforgue, X.-Z. Yuan, A. Platt, S. Brueckner, F. Perrin-Sarazin, M. Toupin, J.-Y. Huot and A. Mokrini, *J. Electrochem. Soc.*, 2020, **167**, 140521.
8 X. Han, L. Lu, Y. Zheng, X. Feng, Z. Li, J. Li and M. Ouyang, *eTransportation*, 2019, **1**, 100005.
9 M. Dubarry, C. Truchot and B. Y. Liaw, *J. Power Sources*, 2012, **219**, 204–216.
10 K. Guo, R. Kumar, X. Xiao, B. W. Sheldon and H. Gao, *Nano Energy*, 2020, **68**, 104257.
11 J. Guo, Y. Li, J. Meng, K. Pedersen, L. Gurevich and D. Stroe, *J. Energy Chem.*, 2022, **74**, 34–44.
12 M. Dubarry, V. Svoboda, R. Hwu and B. Y. Liaw, *Electrochem. Solid-State Lett.*, 2006, **9**, A454–A457.
13 C. Pastor-Fernández, K. Uddin, G. H. Chouchelamane, W. D. Widanage and J. Marco, *J. Power Sources*, 2017, **360**, 301–318.
14 L. Wu, K. Liu and H. Pang, *Electrochim. Acta*, 2021, **368**, 137604.
15 C. Fang, J. Li, M. Zhang, Y. Zhang, F. Yang, J. Z. Lee, M. H. Lee, J. Alvarado, M. A. Schroeder, Y. Yang, B. Lu, N. Williams, M. Ceja, L. Yang, M. Cai, J. Gu, K. Xu, X. Wang and Y. S. Meng, *Nature*, 2019, **572**, 511–515.
16 K. J. Park, J. Y. Hwang, H. H. Ryu, F. Maglia, S. J. Kim, P. Lamp, C. S. Yoon and Y. K. Sun, *ACS Energy Lett.*, 2019, **4**, 1394–1400.
17 D. S. Ko, J. H. Park, S. Park, Y. N. Ham, S. J. Ahn, J. H. Park, H. N. Han, E. Lee, W. S. Jeon and C. Jung, *Nano Energy*, 2019, **56**, 434–442.
18 D. Ren, H. Hsu, R. Li, X. Feng, D. Guo, X. Han, L. Lu, X. He, S. Gao, J. Hou, Y. Li, Y. Wang and M. Ouyang, *eTransportation*, 2019, **2**, 100034.
19 T. R. Tanim, Z. Yang, D. P. Finegan, P. R. Chinnam, Y. Lin, P. J. Weddle, I. Bloom, A. M. Colclasure, E. J. Dufek, J. Wen, Y. Tsai, M. C. Evans, K. Smith, J. M. Allen, C. C. Dickerson, A. H. Quinn, A. R. Dunlop, S. E. Trask and A. N. Jansen, *Adv. Energy Mater.*, 2022, 2103712.
20 X. G. Yang, S. Ge, T. Liu, Y. Leng and C. Y. Wang, *J. Power Sources*, 2018, **395**, 251–261.
21 D. Anseán, M. Dubarry, A. Devie, B. Y. Liaw, V. M. García, J. C. Viera and M. González, *J. Power Sources*, 2016, **321**, 201–209.
22 Y. Wen, J. Fan, C. Shi, P. Dai, Y. Hong, R. Wang, L. Wu, Z. Zhou, J. Li, L. Huang and S. G. Sun, *Nano Energy*, 2019, **60**, 162–170.
23 H. J. Gonzalez Malabet, G. M. Cavalheiro, T. Iriyama, A. Gabhart, G. J. Nelson and G. Zhang, *J. Electrochem. Soc.*, 2021, **168**, 100507.
24 H. Zheng, L. Tan, L. Zhang, Q. Qu, Z. Wan, Y. Wang, M. Shen and H. Zheng, *Electrochim. Acta*, 2015, **173**, 323–330.
25 P. Zhang, T. Yuan, Y. Pang, C. Peng, J. Yang, Z.-F. Ma and S. Zheng, *J. Electrochem. Soc.*, 2019, **166**, A5489–A5495.
26 X. Xing, Y. Li, S. Wang, H. Liu, Z. Wu, S. Yu, J. Holoubek, H. Zhou and P. Liu, *ACS Energy Lett.*, 2021, **6**, 1831–1838.
27 J. Wandt, P. Jakes, J. Granwehr, R. A. Eichel and H. A. Gasteiger, *Mater. Today*, 2018, **21**, 231–240.
28 H. Wei, Y. Huang, L. Tang, C. Yan, Z. He, J. Mao, K. Dai, X. Wu, J. Jiang and J. Zheng, *Nano Energy*, 2021, **88**, 106288.
29 R. E. Ruther, A. F. Callender, H. Zhou, S. K. Martha and J. Nanda, *J. Electrochem. Soc.*, 2015, **162**, A98–A102.
30 A. Ejigu, K. Fujisawa, B. F. Spencer, B. Wang, M. Terrones, I. A. Kinloch and R. A. W. Dryfe, *Adv. Funct. Mater.*, 2018, **28**, 1804357.
31 K. Wang, L. Xing, K. Xu, H. Zhou and W. Li, *ACS Appl. Mater. Interfaces*, 2019, **11**, 31490–31498.

32 C. Yan, R. Xu, Y. Xiao, J. F. Ding, L. Xu, B. Q. Li and J. Q. Huang, *Adv. Funct. Mater.*, 2020, **30**, 1–21.

33 Y. Shi, Z. Wang, L. Wen, S. Pei, K. Chen, H. Li, H. M. Cheng and F. Li, *Adv. Sci.*, 2022, **9**, 1–9.

34 Y. Mao, X. Wang, S. Xia, K. Zhang, C. Wei, S. Bak, Z. Shadike, X. Liu, Y. Yang, R. Xu, P. Pianetta, S. Ermon, E. Stavitski, K. Zhao, Z. Xu, F. Lin, X. Q. Yang, E. Hu and Y. Liu, *Adv. Funct. Mater.*, 2020, **13**, 4087–4097.

35 M. Liu, J. Vatamanu, X. Chen, L. Xing, K. Xu and W. Li, *ACS Energy Lett.*, 2021, **6**, 2096–2102.

36 W. Zhao, G. Zheng, M. Lin, W. Zhao, D. Li, X. Guan, Y. Ji, G. F. Ortiz and Y. Yang, *J. Power Sources*, 2018, **380**, 149–157.

37 W. Deng, W. Dai, X. Zhou, Q. Han, W. Fang, N. Dong, B. He and Z. Liu, *ACS Energy Lett.*, 2021, **6**, 115–123.

38 J. N. Zhang, Q. Li, Y. Wang, J. Zheng, X. Yu and H. Li, *Energy Storage Mater.*, 2018, **14**, 1–7.

39 N. Mao, T. Zhang, Z. Wang and Q. Cai, *J. Power Sources*, 2022, **518**, 230767.

40 S. Zhu, C. Hu, Y. Xu, Y. Jin and J. Shui, *J. Energy Chem.*, 2020, **46**, 208–214.

41 J. Guo and W. Li, *ACS Appl. Energy Mater.*, 2022, **5**, 397–406.

42 W. H. Li, Q. L. Ning, X. T. Xi, B. H. Hou, J. Z. Guo, Y. Yang, B. Chen and X. L. Wu, *Adv. Mater.*, 2018, **31**, 1804766.

Journal Publication 5

Unravelling the Mechanism of Pulse Current Charging for Enhancing the Stability of Commercial $LiNi_{0.5}Mn_{0.3}Co_{0.2}O_2$/graphite Lithium-ion Batteries [J5]

J. Guo, Y. Xu, P. Adelhlem, M. Exner, X. Huang, P. Kristensen, D. Wang, K. Pedersen, L. Gurevich, and D. -I. Stroe

This paper is submitted to *Energy & Environment Science*

PAPER

Unravelling the Mechanism of Pulse Current Charging for Enhancing the Stability of Commercial $LiNi_{0.5}Mn_{0.3}Co_{0.2}O_2$/Graphite Lithium-Ion Batteries

Received 00th January 20xx,
Accepted 00th January 20xx

DOI: 10.1039/x0xx00000x

Jia Guo[a,b,c], Yaolin Xu[b,d*], Moritz Exner[b], Yongchun Li[b], Hui Wang[b], Xinrong Huang[a], Julia Kowal[f], Qi Zhang[a], Peter Kjær Kristensen[c], Deyong Wang[c], Kjeld Pedersen[c], Leonid Gurevich[c], Daniel-Ioan Stroe[a*], Philipp Adelhelm[b,e*]

The key to advancing lithium (Li)-ion battery (LIB) technology, particularly with respect to the optimization of cycling protocols, is to obtain comprehensive and in-depth understanding of the dynamic electrochemical processes during battery operation. This work shows that pulse current (PC) charging substantially enhances the cycle stability of commercial $LiNi_{0.5}Mn_{0.3}Co_{0.2}O_2$ (NMC532)/graphite LIBs. More importantly, we combine electrochemical diagnosis with post-mortem and *operando* characterization to comprehend on various levels (material-, electrode-, and cell-level) the mechanism of PC charging for enhancing the cycling stability. Electrochemical diagnosis unveils that pulsed current effectively mitigates the rise of battery impedance and minimizes the loss of electrode materials. *Operando* and *ex situ* Raman and X-ray absorption spectroscopy reveal the chemical and structural changes of the negative and positive electrode materials during PC and constant current (CC) charging. Specifically, Li-ions are more uniformly intercalated into graphite and the Ni element of NMC532 achieves a higher energy state with less Ni-O bond length variation under PC charging. Besides, PC charging suppresses secondary electrolyte decomposition and continuous thickening of the solid-electrolyte-interphase (SEI) layer on graphite anode. These findings offer mechanistic insights into Li-ion storage in graphite and NMC532 and, more importantly, the role of PC charging in enhancing the battery cycling stability, which will be beneficial for advancing the cycling protocols for future LIBs and beyond.

Introduction

Over the course of 30 years' development of lithium (Li)-ion batteries (LIBs), focus in the field has remained on achieving safe and stable LIBs for electric vehicles, portable electronics, etc.[1,2] Generally, batteries retaining 80% of their nominal capacity (i.e., 80% state-of-health (SoH)) reach their end-of-life[3,4]. The nowadays state-of-the-art LIBs are based on $LiNi_{0.5}Mn_{0.3}Co_{0.2}O_2$ (NMC532)/graphite[3], which usually only have a service life of 5 to 8 years[3].By optimizing the cycling conditions, LIBs are expected to be in service even for decades[5], which will greatly alleviate the pressure on battery manufacturing and recycling, and ultimately enhance the sustainability of our future society.

Advanced charging protocols, e.g., pulse current (PC) charging, hold the potential to prolong the service life of current LIBs[6,7]. Specifically, PC charging with relaxation time has been extensively employed in electrochemical testing of NMC/Graphite[8–10], $LiFePO_4$ (LFP)/Carbon-based[11,12], $LiCoO_2$ (LCO)/Graphite[13], and LFP/Li[14] batteries from lab cells to commercial batteries. A typical PC charging protocol consists of a constant current (CC) charging time followed by a rest time. The duration and ratio of these charging periods and intervals of rest vary based on experiments design. These studies have shown promising results, demonstrating the potential of PC charging for improving battery stability by a significant margin, ranging from 0.5% to 34%, as depicted in Fig. 1. However, mechanistic understanding on how PC charging enhances battery performance remains limited, which hinders the optimization of charging protocols and the advancement of future batteries.

To unravel the performance improvement of LIBs under PC charging, it is of vital importance to understand their aging mechanism during service. The aging mechanisms observed in commercial batteries are primarily attributed to several factors, including polarization resulting from interfacial film thicken, loss of active materials, and loss of Li ions[15,16]. Our previous work has unveiled the main causes of NMC532/graphite battery degradation, highlighting the crucial role of interfacial film growing and the loss of cathode and anode materials in this process[17]. A well-known aging mechanism in LIBs is the continuous growth of the solid-electrolyte

---

[a] *Department of Energy, Aalborg University, 9220 Aalborg, Denmark. Email: dis@energy.aau.dk*
[b] *Department of Chemistry, Humboldt University of Berlin, 12489 Berlin, Germany. Email: yaolin.xu@helmholtz-berlin.de; philipp.adelhelm@hu-berlin.de*
[c] *Department of Materials and Production, Aalborg University, 9220 Aalborg, Denmark*
[d] *Institute of Electrochemical Energy Storage (CE-IEES), Helmholtz-Zentrum Berlin für Materialien und Energie (HZB), 14109 Berlin, Germany*
[e] *Joint Research Group Operando Battery Analyses (CE-GOBA), Helmholtz-Zentrum Berlin für Materialien und Energie (HZB), 14109 Berlin, Germany*
[f] *Department of Electrical Energy Storage Technology, Technische Universität Berlin, 10587 Berlin*

† Footnotes relating to the title and/or authors should appear here.

Electronic Supplementary Information (ESI) available: [details of any supplementary information available should be included here]. See DOI: 10.1039/x0xx00000x

interface (SEI) on the anode resulting in the depletion of Li supply and capacity decay[4,18]. Moreover, the presence of SEI hinders the transport of Li-ions, leading to higher interface impedance[19] and hence larger dis-/charge overpotential during battery operation, ultimately decreasing the achieved capacity[20]. Furthermore, the NMC532 and graphite electrodes suffer from cracking in structure, along with electrode exfoliation, which also contributes to capacity loss.

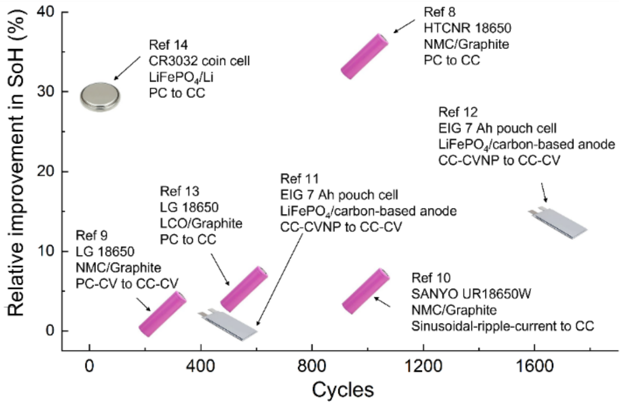

Fig. 1 Relative improvement in SoH of Li-based batteries under PC charging compared to continuous current charging protocols. (CC: constant current, CV: constant voltage, CVNP: constant voltage with negative pulse)

PC charging is hypothesized to mitigate these issues. Generally, the diffusion of Li-ions in the electrolyte is much slower than the electron transport in the external circuit and the electrodes. The slower Li-ion diffusion compared to electron transport results in concentration polarization of Li-ions within the battery[3]. Consequently, this uneven distribution leads to the depletion of Li-ions and accumulation of solvent molecules and anions near the electrode, aggravating the reaction between electrons and solvent/anion to form SEI species[6]. At the counter electrode (NMC532), the concentration of Li-ions increases. Subsequently, the reduction in solvent concentration becomes a hurdle to amalgamate the extracted Li-ions from the cathode with solvent anions. As a result, this could potentially influence the energy states of transition metals, nickel (Ni) included. In contrast, PC charging allows extra time for ion diffusion to compensate for the imbalance in electron and ion transport, thereby alleviating this hysteresis and reduces the polarization, suppressing the SEI thicken. Besides, the electrode materials undergo structural relaxation between current pulses, which mitigates the mechanical stress and structural degradation of electrode materials.

To testify the hypothesis, in this work, we study the electrochemical behaviors of 18650-type NMC532/graphite LIBs during aging with different charging protocols: CC or PC. Moreover, through comprehensive electrochemical analysis and a toolkit of post-mortem and *operando* characterization, we comprehend in detail the electrochemical processes of Li-ion storage in NMC532/graphite and SEI formation under CC and PC charging. These results contribute to unraveling the mechanism of enhanced cycling stability under PC charging.

Results and discussion

Battery performance and electrochemical diagnostics

As shown in Fig. 2a, the NMC532/graphite battery charged at constant current retained only 37.8% of its initial capacity after 1000 cycles, and stopped service (i.e., 80% SoH) after only 500 cycles. In sharp contrast, the batteries charged with pulsed current exhibit much enhanced cycling performance over cycling. In particular, at a pulsed current with a frequency of 100 Hz (denoted as Pulse-100), the battery's capacity retention rate reaches 66.48% after 1000 cycles with a cycle life of >700 cycles. And, at a 2000 Hz pulsed current (denoted as Pulse-2000), the capacity retention rate of the battery is as high as 81.73% in 1000 cycles, i.e., more than twice the cycle life compared to that at CC charging. Obviously, the PC charging method effectively improves the battery cycling performance. In our previous report[17], it has been revealed that the aging mechanisms under CC cycling is the increased interfacial impedance and polarization, especially on the graphite anode, and loss of active materials. Comparing the charging and discharging curves under these three charging methods (Fig. 2b2-d2), it shows a rising tendency of the charge voltage and a dropping trend for the discharge voltage over 1000 cycles. This is most evident for the CC-charged battery and is related to battery polarization[17]. The battery polarization is reduced when charged with a pulse current, and further decreases as the pulse frequency increases from 100 to 2000 Hz. The shift of the secondary peak (peak II) in the incremental capacity (IC) curve is a useful parameter for quantifying the increase in polarization[21]. Here, the peak II shifts by 0.166 V, 0.086 V and 0.078 V for the batteries charged under CC, Pulse-100 and Pulse-2000, respectively (Fig. 2b3-d3). The main peak (Peak I) serves as an indicator for the loss of active materials in both the cathode and anode[22]. Under CC charging, the peak I gradually diminishes and can nearly vanish after around 1000 cycles, reflecting the substantial loss of active materials from the electrodes. In contrast, when using Pulse-2000 charging, peak I remains prominent even after 1000 cycles. This observation suggests that compared to CC charging, the loss of active material is significantly reduced with PC charging. In short, electrochemical diagnosis reveals that the application of PC charging significantly alleviates active material loss and reduces polarization of the battery and a higher pulse frequency result in less battery degradation.

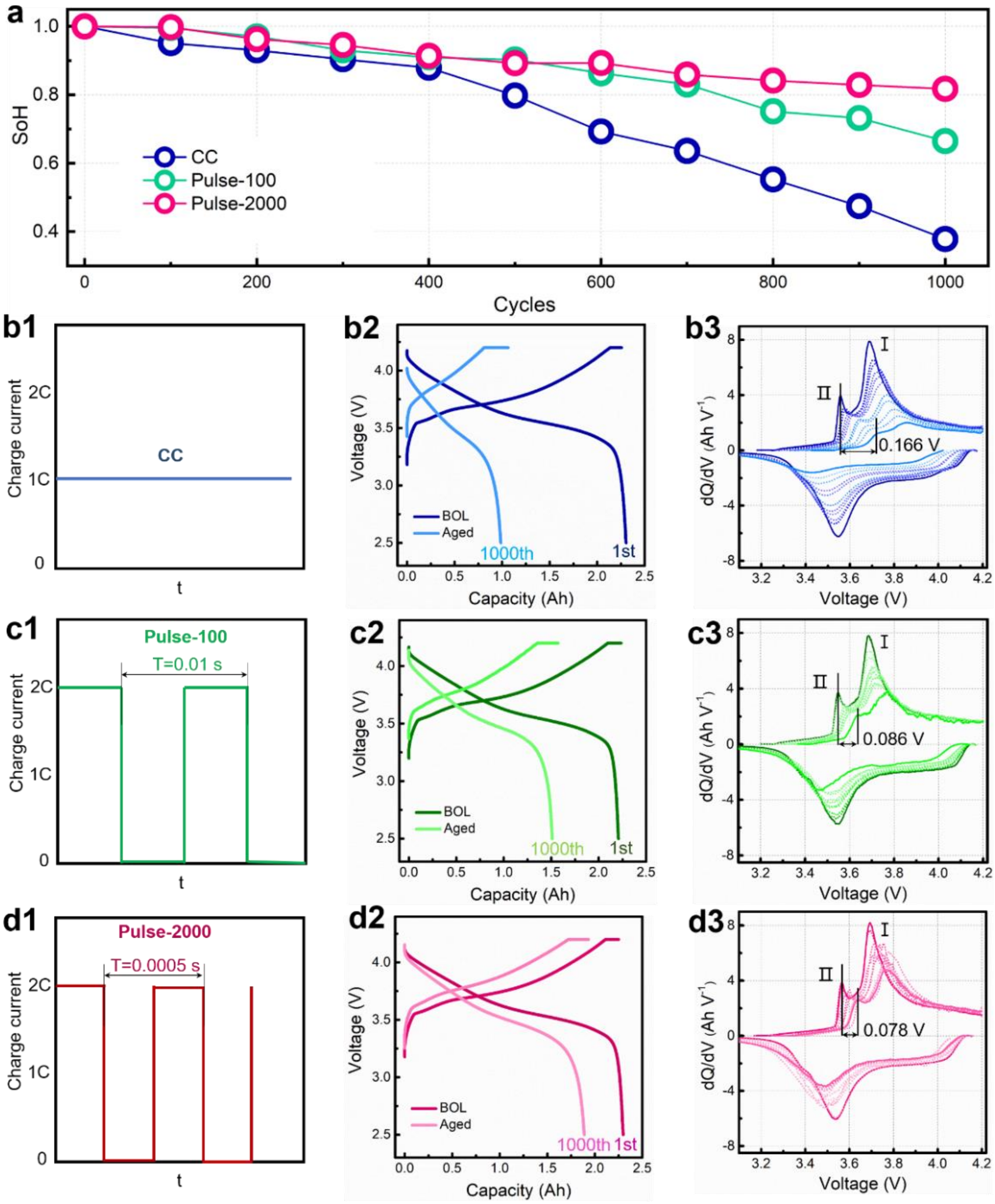

Fig. 2 Electrochemical behaviors of the reference performance tests (RPTs) for 18650-type NMC532/graphite LIBs aged with different charging protocols: CC, Pulse-100 and Pulse-2000. The RPT rests were performed after every 100 cycles of battery aging. (a) The battery SoHs obtained from the RPTs during aging. The current wave shapes for battery aging, and the dis-/charge voltage profiles and IC curves of the RPTs for batteries aged with (b1-b3) CC, (c1-c3) Pulse-100 and (d1-d3) Pulse-2000 charging protocols. BOL: begin of life.

Electrochemical Impedance Spectroscopy (EIS) is an effective method for identification and analysis of the polarization that takes place within the battery[23]. A typical Nyquist plot of the EIS data of a battery and the related processes are shown in (Fig. 3a)[24,25]. After aging for 1000 cycles, the R_{sei} and R_{ct} values of the batteries aged at constant current and Pulse-2000 were measured and shown in Fig. 3b (see Fig.. S1 for the Nyquist plots). In general, the R_{sei} and R_{ct} decrease as the state-of-charge (SoC) increases, and the resistances of the CC-aged battery are higher than that under PC aging. This is consistent with the much more significant decline of battery capacity during CC aging.

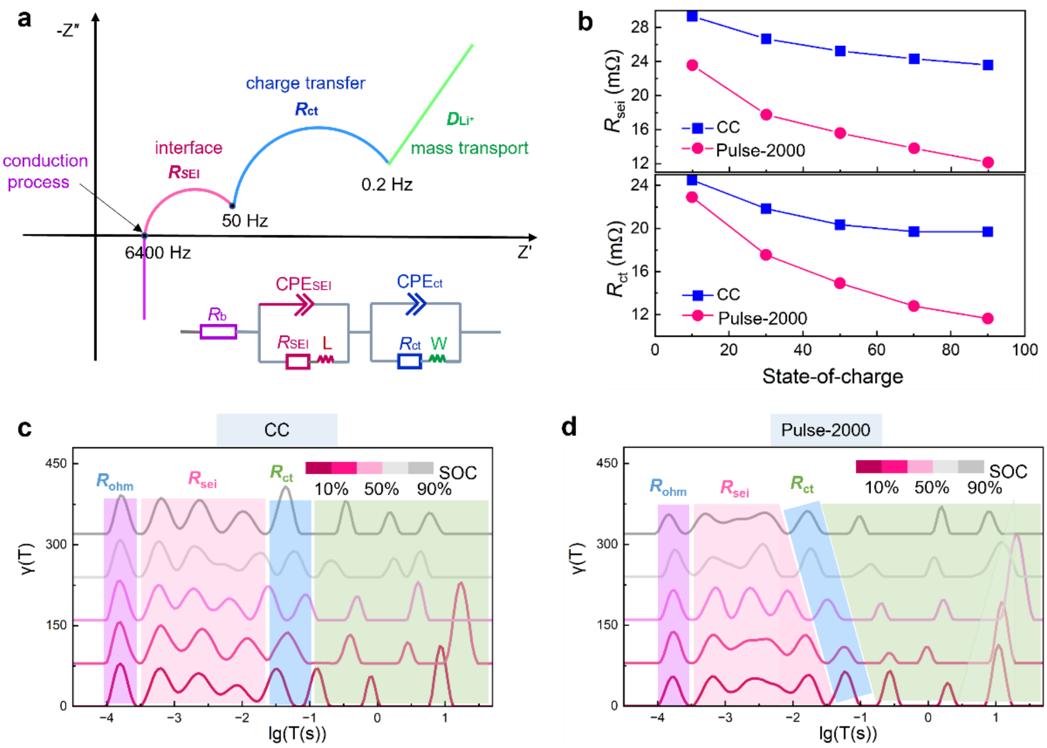

Fig. 3 EIS results of the batteries after aging for 1000 cycles under CC and Pulse-2000 charging. (a) The characteristic Nyquist plot and equivalent circuit diagram, (b) the fitting results of R_{sei} and R_{ct} in relative with the SoC; The distribution of relaxation time (DRT) profiles at 10%, 30%, 50%, 70%, and 90% SoC for the batteries aged under (c) CC and (d) Pulse-2000 charging. The regions marked with colors are related to the major electrochemical processes in batteries, namely Ohmic resistance (purple) and across the SEI (pink), and charge transfer (blue), respectively.

Distribution of relaxation times (DRT) is used to deconvolute electrochemical processes on various time scales from the EIS data at different SoCs. In the interpretation of DRT calculations, specific electrochemical processes (*incl.* charge transfer, interfaces, ion diffusion, etc.,) can be distinguished and identified by the time constant (τ) of the corresponding Randles circuit (i.e., RC paralleled circuit - a typical circuit for simulating the interfacial process that consists of ionic double layer and transport resistances)[26]. The timescale analysis reveals specific kinetic characteristics of the electrochemical processes. In general, charge transfer typically takes place with a time constant between 10^{-2} and 10^{-1} s and Li-ion transport across interfacial films (i.e., SEI and cathode-electrolyte interface CEI) occurs between $10^{-3.5}$ and 10^{-2} s[27,28]. The DRT results (Fig. 3c-3d) show that the battery aged with CC charging exhibits a lower time constant and hence a higher impedance for interface and charge transfer resistance, compared to that at Pulse-2000. Particularly at a higher State of Charge (SoC), this distinction becomes more pronounced. This phenomenon is attributed to the low porosity of the graphite electrode and the reduced volume fraction of the electrolyte, a consequence of the densely packed graphite particle contacts in high SoC conditions[29]. As a result, this configuration leads to lower resistance. Besides, the interface resistance, which is the major kinetic limiting factor for CC sample as proved in our previous work[17], is significantly reduced for Pulse-2000. During the charging of NMC532/graphite battery, Li ions are extracted from the NMC532 cathode and intercalated into the graphite anode, which is susceptible to SEI growing on the graphite anode. Besides, the volume of graphite expands during Li-ion intercalation and shrinks during de-intercalation, destabilizing the SEI film and leading to the rupture and continuous growth of SEI. Therefore, the discrepancies of interface resistance under CC and Pulse-2000 charging are mostly associated with the SEI (and not CEI), and the growing SEI film under Pulse-2000 charging has a lower impedance. Meanwhile, the charge transfer is accelerated in battery aged under Pulse-2000. The time constant of charge transfer at Pulse-2000 charging decreases from 10^{-1} s to 10^{-2} s with increasing SoC from 10% to 90%, while the charge transfer time constant at constant current is less influenced by SoC. This observation is possibly related to the porosity formed as a result of the cracking of graphite particles during CC aging[29].

Overall, electrochemical diagnoses (i.e., IC, EIS, and DRT) unveil that PC charging effectively mitigates the increase of the SEI and charge transfer resistances, and also alleviates the loss of electrode materials, ultimately leading to an extended battery lifespan.

Mechanism of electrode degradation

Degradation mechanism of graphite anode. To elucidate the structural changes that happen to the graphite anode with different lithiation protocols, we performed post-mortem analysis and employed ex situ synchrotron X-ray diffraction (XRD) to reveal the crystal structures of graphite electrodes after aging for 1000 cycles under CC and PC charging protocols. The XRD patterns of fresh and aged graphite electrodes in Fig. 4a shows similar positions for all crystalline peaks of graphite, including the major diffraction peak from the (002) lattice plane, indicating that the layer spacing of graphite remains unchanged after battery aging[30]. Besides, as the battery ages, the (002) peak broadens significantly, with notable increase of the full width at half maximum (FWHM) for all the aged graphite electrodes, as shown in insert picture of Fig. 4a, indicating cracking or even pulverization of graphite particles and collapse of the electrode structure[31]. In particular, the increase of FWHM for graphite electrodes aged under pulsed current (4.12×10^{-3} Å for Pulse-100 and 4.01×10^{-3} Å for Pulse-2000) is less significant than the CC-aged electrode (4.38×10^{-3} Å), and as the frequency of the current pulse increases the FWHM decreases, which suggests that the pulsed current allows structural relaxation and reduces the mechanical strain in the particles, suppressing the cracking of graphite particles and expansion of the electrode. Particle cracking causes an increase in the internal porosity of the electrode, consequently leading to an increase in the electrode thickness. As a result, the thickness of graphite electrode increases by about 15% (115 µm vs 100 µm for pristine electrode) after aging under 2000 Hz PC charging, which is significantly less than that under CC charging (35 %, 135 µm vs 100 µm) (Fig. 4b). The cross-section FE-SEM images are shown in Fig. S2.

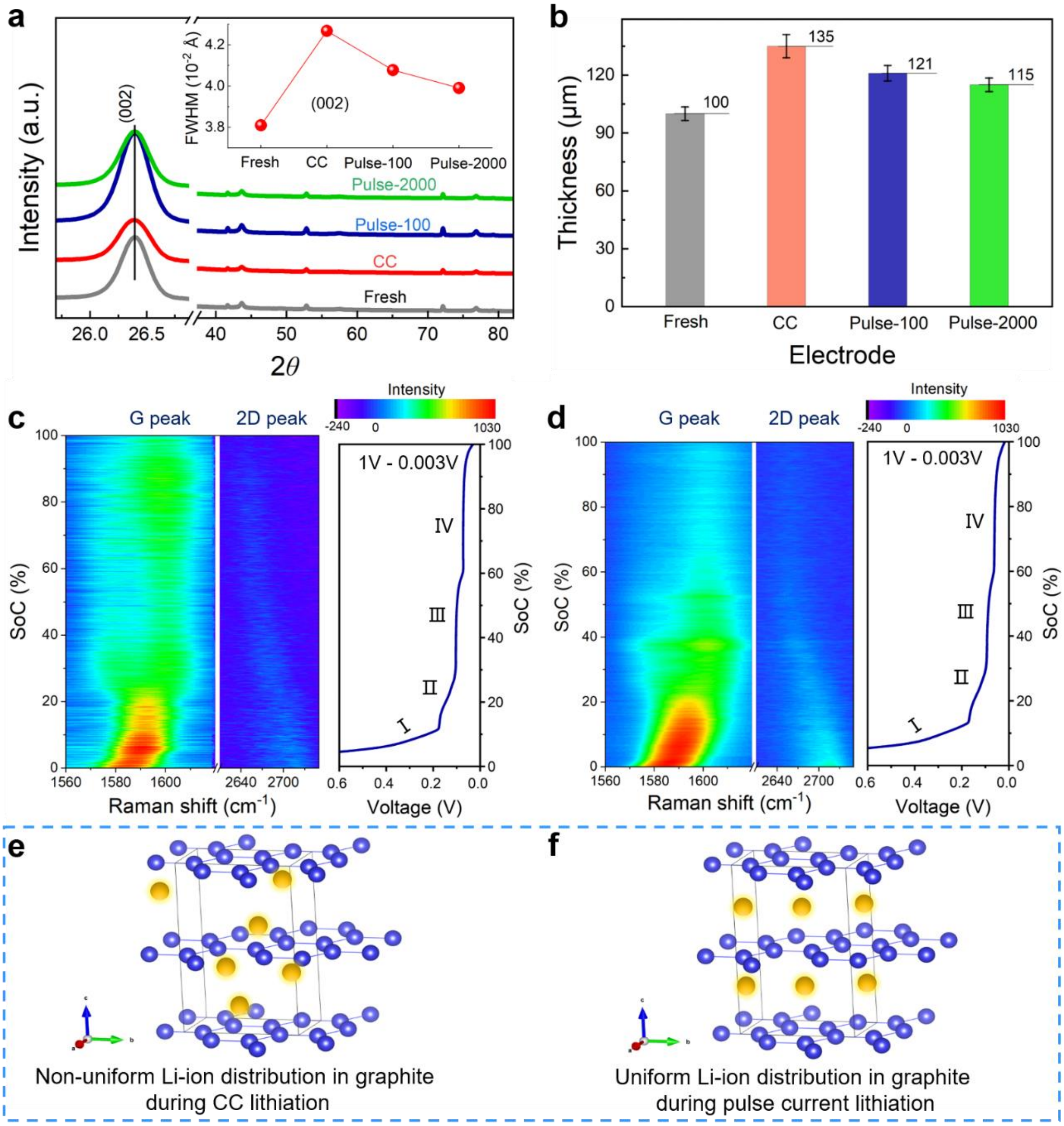

Fig. 4 (a) *Ex situ* synchrotron XRD patterns of fresh and aged graphite anode, and the FWHM of the (002) peak of fresh and aged graphite electrodes as inserted picture; (b) thickness of fresh and aged negative electrodes based on SEM results; *operando* Raman spectra of the graphite during (c) CC and (d) PC lithiation processes; the state of graphite with Li-ions (e) unevenly distribution during CC lithiation, and (f) evenly distribution during PC lithiation

To further unravel the structural evolution of the graphite anode in LIBs during cycling and the influence of the charging protocol, *operando* Raman spectroscopy was utilized to monitor the *real-time* evolution of the graphite structure during lithiation under constant and pulsed current, respectively. Usually, graphite undergoes complex phase transition during Li-ion intercalation, resulting in various intermediate states, such as LiC_{48}, LiC_{24} LiC_{18}, LiC_{12}, LiC_6 [32,33]. The arrangement of Li ions in graphite inherently strives to achieve a state of lower energy due to the maximized interaction between the embedded Li ions and the graphite host[32]. *Operando* Raman spectroscopy can capture the subtle changes in structure during lithiation which occurs from 1.0 V to 0.003 V vs Li^+/Li. As shown in Fig. 4c, during CC lithiation, the voltage profile displays four distinct stages. At stage I, graphite is lithiated to LiC_{48} demonstrating a single G band with a high intensity in the Raman spectrum[34]. In the following stage (II) where LiC_{48} transits to LiC_{24} then to LiC_{18}, the intensity of the single G band peak decreases and the peak gradually transforms into a doublet band. At stage III (i.e., LiC_{18} to LiC_{12} transition), the doublet peaks decrease in intensity, with the left peak of the doublet becoming significantly weaker. Finally, at stage IV (i.e., transition from LiC_{12} to LiC_6), the doublet band intensity increases. As reported, the doublet G band observed in the Raman spectrum of graphite is related to the unevenly distribution of Li-ions in graphite during intercalation[34], which can be mitigated by pulsed current. The *operando* Raman spectra of graphite during PC lithiation are shown in Fig. 4d. At stage I and II, the Raman spectra are similar between CC and PC lithiation. During stage III, the doublet peaks undergo a steady decrease in intensity and merge gradually. By stage IV, only low-intensity single peaks remain. The 2 D Raman spectrum as seen in Fig. S3. The observations imply that Li-ion distribution in graphite during lithiation is more even under pulsed current, as depicted in Fig. 4e, f. The thickness of the negative electrode during the lithiation and delithiation processes were measured by an *operando* electrochemical dilatometry. As shown in Fig. S4, the thickness of the negative electrode experiences significant fluctuations throughout the CC cycling, indicating it unstable. However, when it comes to PC charging, the thickness variation is notably reduced. This highlights the divergence in the lithium insertion behavior of graphite in these two scenarios. Under PC charging, lithium integration within the graphite becomes more uniform, resulting in reduced volume fluctuations and mitigated mechanical stress that might otherwise lead to graphite fracture.

In short, PC charging facilitates more homogeneous Li-ion distribution in graphite during lithiation and mitigates the cracking and pulverization of graphite particles, effectively suppressing the structural and thickness changes of graphite electrodes in LIBs. Hence, PC charging inhibits the loss of the graphite anode.

Degradation mechanism of NMC532 cathode. To study the degradation of NMC cathode, ex situ synchrotron XRD and ex situ X-ray absorption near-edge structure (XANES) were employed for detailed crystallographic analysis of fresh and aged NMC532 cathodes. ex situ synchrotron XRD reveals in detail these structural deteriorations. As shown in Fig. 5a, the leftward shift of the (003) peak in the CC aged electrode indicates an expansion of the crystal volume or layer spacing in NMC532 materials[32]. Moreover, the lower intensity of the (018)/(110) double split peak under CC charging than that under PC charging suggests a reduction in crystallinity[33]. The Ni-O bond length (Radial-distance) in the aged positive electrode is significantly shortened (Fig. 5b). This can be attributed to the fact that the atomic radius of high-valent Ni (Ni^{3+} and Ni^{4+}) is lower than that of Ni^{2+}[34], leading to a shortened Radial-distance. Furthermore, the peak intensity of the EXAFS is positively correlated with the coordination number[35,36]. After aging, Ni exhibits a higher coordination number with oxygen atoms, particularly for the electrodes aged under CC charging, which shows a higher coordination number than that under PC charging. Therefore, PC charging aging results in less high-valent nickel oxides compared to CC charging, with these oxides potentially being deteriorated lithium vacancies[37]. These observations indicate that PC charging is beneficial for preserving the crystallinity and layered structure of NMC532 cathode materials.

To comprehend the aging mechanism of the NMC532 cathodes in LIBs, we utilized *operando* Ni k-edge X-ray absorption spectroscopy (XAS) to investigate the local chemical environment of Ni atoms under CC and 250 Hz PC charging. In Fig. 5c, the Ni K-edge XANES exhibits a rightward shift during the initial charging of the battery, followed by a leftward shift to a lower energy position during discharge. This shift is attributed to charge compensation achieved through the redox process between Ni^{2+} and Ni^{4+} ions[38]. Compared with that under CC charging, the shift of Ni edge under PC charging is more obvious, indicating the energy and valence states of Ni element change more significantly. The quantified results are shown in the bottom of the Fig. 5c. Under PC charging, the Ni element trends to attain a higher energy and valence compared to that under CC charging.

Furthermore, *operando* Ni k-edge EXAFS was employed to correlate the charge state with the changes in the intensity of Ni-O and Ni-transition metal (Ni-TM) bonds, as shown in Fig. 5d. During the charging process, the intensity of the Ni-O peak continuously increases, while the Ni-TM peak displayed an opposite trend, since the Ni valence increase during the delithiation of NMC532 results in more oxygen coordination. Similarly, in the followed dis-/charging process, the peak intensity of Ni-O and Ni-TM changes more significantly under PC charging than that under CC charging. Particularly, the bond numbers between Ni and transition metals exhibited minimal changes after the initial charge. This is consistent with the energy change of the Ni edge, and the NMC material shows a greater degree of coordination number change under PC charging, which means that the Ni valence will achieve a higher valence state in PC charging. Additionally, the Radial-distance shifts of the Ni-O bond under CC and PC charging are depicted in the inserted pictures. The length of the Ni-O bond undergoes fluctuations with changes in the Ni valence state during charge and discharge. When comparing PC charging to CC charging, the prolonging and shortening of the Ni-O bond length is less pronounced in the former, indicating a more relaxed redox reaction process. This result provides a deeper understanding of the reduced structural deterioration observed in the PC aging case.

In short, the *ex* situ XRD results unveil that the degradation of cathode materials primarily manifests as an increase in cathode crystal volume and a decrease in the crystallinity of NMC532 cathode materials. Additionally, *ex* situ Ni K-edge EXAFS further discloses that these deteriorations are closely linked to the formation of Li vacancy phase featuring high valence Ni-O bonding. As summarized in Fig. S6, PC charging mitigates this process. Additionally, *operando* XAS highlights the similarities and differences in the valence state, energy, and coordination of Ni atoms in NMC532 under CC and PC charging. PC charging enhances the growth of the valence state of the Ni element, while the fluctuation of the bond length between Ni and O diminishes during battery charging. The moderate changes in structure and Ni-O bond length induced by PC charging could be explained for the overall deterioration of the electrode structure.

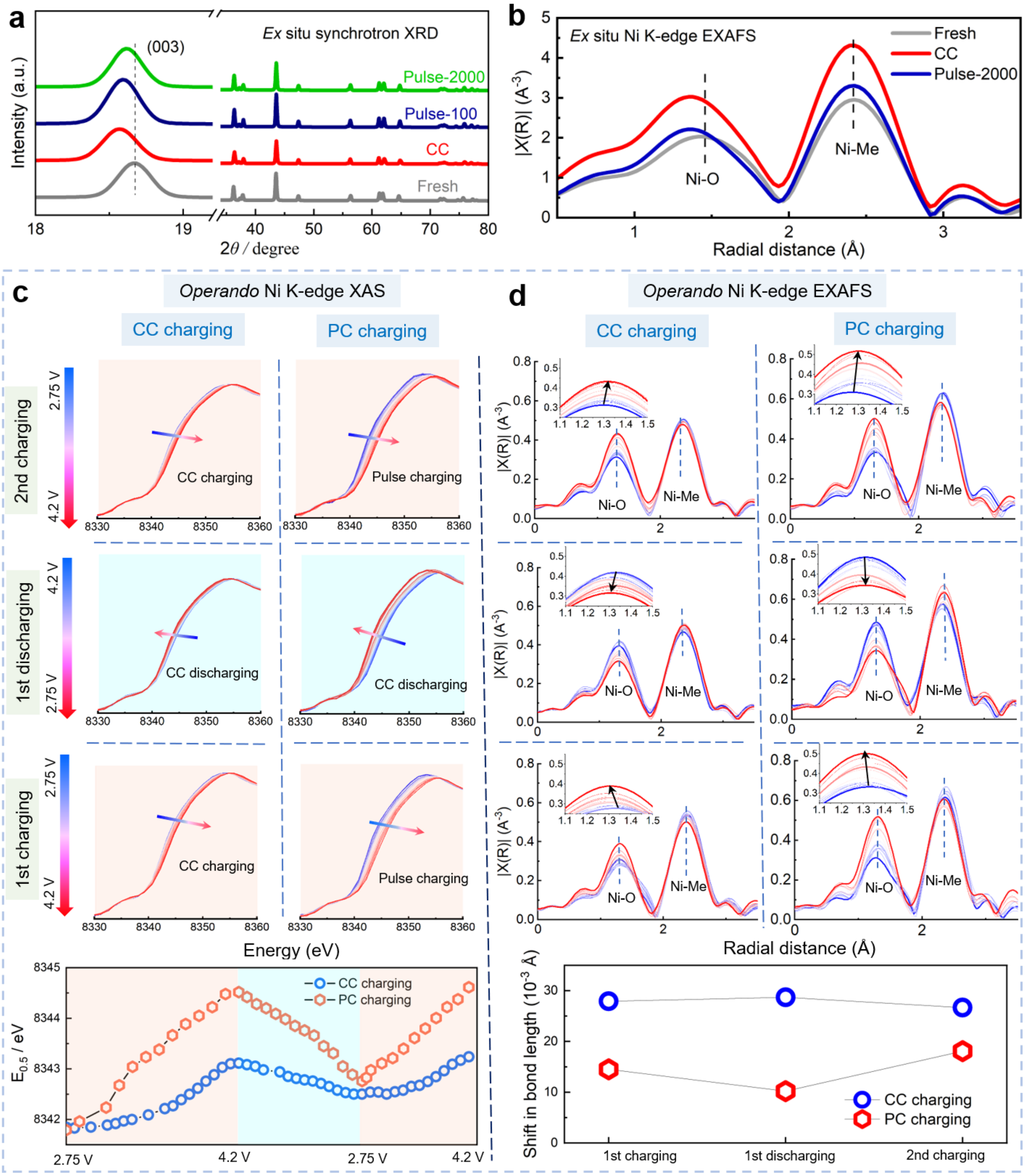

Fig. 5 *Ex situ* synchrotron XRD results for fresh and aged NMC532 cathodes (a), and Ni K-edge *ex situ* EXAFS (b); *operando* XAS for fresh positive electrode under CC and PC charging protocols; (c) the Ni K-edge XANES evolution of NMC532 during battery cycling under CC and PC charging; (d) the operando Ni K-edge EXAFS and Ni-O radial distance under CC and PC charging.

Degradation in graphite-electrolyte interface

PC charging has been demonstrated based on the electrochemical analysis to reduce the increase of interfacial resistance, particularly the SEI layer on graphite anode, which can be attributed to its impact on the thickness, composition, and structure of the SEI. As shown in Fig. S7a, the Raman spectra of graphite anodes show insignificant graphite D, G, D' and G' peaks, due to the surface coverage of SEI layer on graphite. In addition, other heterogeneous peaks appear in the 1800 − 2500 cm^{-1} region, which are from the $Li_xP_yF_z$ compounds [39]. In comparison to the CC-aged sample, the Pulse-2000-aged one exhibits sharper graphite peaks, indicating a higher light transmission through the SEI film. This suggests that the SEI film on the Pulse-2000-aged graphite electrode may be thinner and/or composed of materials with higher light transmittance than that of the CC sample. To uncover the nature of graphite, the surface of the graphite electrodes was scraped off and re-measured with Raman spectroscopy. Distinct graphite peaks were observed in the Raman spectra for both the surface-removed CC and Pulse-2000 samples, as shown in Fig. S7b. It is noticeable that the $Li_xP_yF_z$ peaks representing the SEI film disappear, proving the presence of a surface film that covered the original graphite electrodes that affects the reflection of 532 nm laser.

The SEI film is usually thin and adheres to the graphite particles, which poses a challenge for visualizing the SEI morphology[40,41]. To address this challenge, graphite electrodes were cross sectioned to observe the SEI layer. As shown in Fig. S7c1, the CC sample has ruptured interfacial films on and between the graphite particles. The rupture of these films is related to the mechanical stresses generated by Li-ion de-/intercalation in graphite during charging and discharging as mentioned before. Fig. S7c2 shows that a distinct passivation film that appeared on the graphite particles surface in the CC sample. In contrast, the Pulse-2000 sample has no obvious passivation film on and between graphite particles, as shown in Fig. S7d1. This is consistent with the finding from the electrochemical analysis that the SEI growing under CC charging is less stable compared to that under PC charging. Fig. S7d2 shows a thin and indistinct film (i.e., SEI) adheres to a graphite particle. This implies that the PC charging inhibits the continuous growth and thickening of the SEI film. The SEI film in Fig. S7c2 was further imaged at a higher magnification and analyzed with EDS mapping of O and C elements, as shown in Fig. S7e. The SEI film with uneven thickness is distributed around the edges of the graphite. The SEI film region is consistent with the O element distribution region.

To further investigate the growing of SEI films, depth-dependent XPS with different etching time of 0, 50 min, and 100 min were performed for the pristine, CC-aged, and Pulse-2000-aged graphite electrodes. Quantitative results of the chemical composition of SEI based on Li_2CO_3, C=O (e.g., R-CH_2OCO_2Li and –(CH_2CH-(OC(O)CF_3))$_n$-), C-O (e.g., R-CH_2OLi and -(CH_2CH_2O)$_n$-), LiF, and $Li_xPO_yF_z$[17,42] are shown in Fig. 6a and the depth-dependent XPS for O 1s and Li 1s are shown in Fig. S8. In consecutive XPS etching from 0 minutes to 100 minutes, the fresh electrode exhibited a highly similar chemical composition. This could be due to the relatively thin SEI of the fresh electrode, where the first etching has penetrated the SEI film. Under CC aging conditions, the LiF content increases significantly with the growing etching depth, indicating a thick SEI film. The second etching result of the PC-aged graphite electrode closely resembled the third etching result, suggesting it is thinner than the SEI in the CC case. This is consistent with the results observed through SEM.

Additionally, compared with the SEI film on fresh and Pulse-2000 graphite electrode surface, the CC-aged electrode has SEI with a higher percentage of Li_2CO_3 at each etched depth. Li_2CO_3 is produced as a reaction product of semi-carbonates (e.g., lithium ethylene dicarbonate (LEDC)) with HF, water, or CO_2[43]. After aging of batteries, inorganic components such as Li_2CO_3 and LiF accumulate on the graphite surface. Generally, the SEI films on graphite surface are brittle due to a high content of inorganic salt[44,45]. This will cause the SEI film to continually rupture and reform as the graphite's volume varies during the cycling of battery aging. The SEI debris accumulates on the graphite surface, resulting in a porous and thickened SEI film. Inorganic salts are less abundant on the surface of the Pulse-2000-aged graphite anode than on the surface of CC-aged graphite due to the ordered Li^+ intercalation during PC charging, which reduces the electrolyte decomposition and produces fewer by-products during the SEI re-formation process.

Correspondingly, a low inorganic salt content in the SEI implies a relatively high organic salt and polymer content. The content of C-O compounds is much higher on the Pulse-2000-aged graphite surface than that on the CC-aged anode surfaces, which will increase the flexibility of the SEI film to suppress its fracture upon the volume expansion of graphite. As a result, the anode aged under Pulse-2000 charging exhibits a thinner SEI film.

Based on the results of SEM, EDX and XPS analysis, the electrode interface aging modes under PC and CC charging are summarized in Fig. 6b. PC charging inhibits the reduction reaction between solvent and interface electrons by balancing the uneven concentration distribution of Li-ions in the electrolyte and reducing lithium depletion at the interface. Both the initial reactions (EC reacts with e, and decomposition of $LiPF_6$) and secondary reactions (Li_2CO_3, and Li_2O, and LiOR from LEDC decomposition) involved in film growing will be inhibited. Finally, the reformation, rupture, and accumulation of inorganic substances (Li_2CO_3, LiF and Li_2O) of SEI will be significantly slowed down, resulting in a thinner SEI film. This effectively explain the electrochemical analysis result that PC charging mitigates the increase in interfacial impedance.

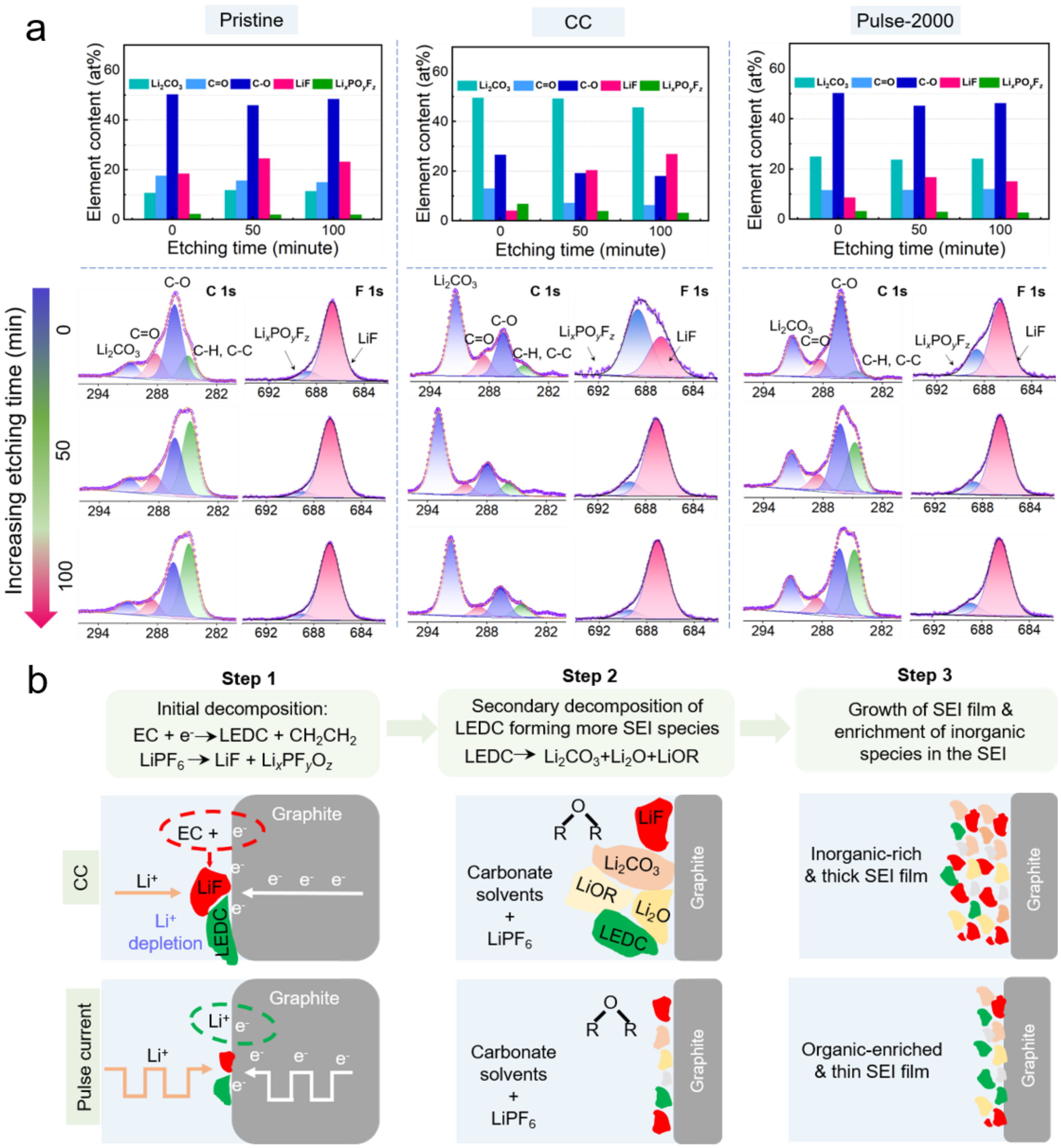

Fig. 6 XPS results of the interfaces of graphite electrodes. Chemical compositions of SEI obtained by quantitative XPS characterization of pristine, CC-aged, and Pulse-2000-aged graphite electrodes, and the detailed C 1s, F 1s, O 1s, and Li 1s XPS spectra of graphite electrodes with different etch durations (a). The mechanism of SEI film growing at the graphite interface under CC and PC charging based on the demonstration of the above SEM, EDX and XPS results (b).

Discussion on the battery aging mechanisms and the influence of charging protocols

Based on the above results, we can conclude that PC charging greatly impacts the operation and performance of NMC532/graphite batteries on various levels.

I. On the cell level, PC charging substantially prolongs the lifespan of batteries. Moreover, the impact of PC charging is influenced by the current pulse frequency. As the current pulse frequency increases e.g., from 100 to 2000 Hz, the battery's cycling stability is notably enhanced.

II. On the electrode level, PC charging is effective in reducing the structural changes of graphite & NMC532 electrodes and impedance of the electrode-electrolyte interfaces, especially the SEI film on graphite anode.

III. On the material level, detailed effects of PC charging on NMC532/graphite electrode materials and the electrolyte are demonstrated in Fig. 7. (a) During Li-ion intercalation with a pulsed current that allows for structural relaxation of graphite, the distribution of the intercalated Li-ions in graphite is more uniform, alleviating the mechanical strain and therefore suppressing the cracking/pulverization and volume expansion of graphite particles. (b) PC charging suppresses the formation of structural distortion and amorphization of NMC532, maintaining its crystal structure over cycling. (c) PC charging mitigates Li-ion depletion at the electrode-electrolyte interface, thereby altering the electrolyte decomposition and SEI reformation pathway and suppressing second-order reduction of the carbonate-based electrolyte that leads to the formation of inorganic Li salts (e.g., Li_2CO_3). As a result, the SEI layer on graphite anode appears to be thinner and with a relatively higher ratio of organic compounds resulting from the first-order reduction of carbonate-based electrolyte.

Based on the findings of this study, the high-frequency square-wave current PC charging protocols can be employed to prolong the lifetime of commercial LIBs. To further optimize the charging protocol for battery performance improvement, this effect should be investigated with more influence factors. This investigation has shown that a rather high frequency of 2000 Hz is beneficial, so testing even higher frequencies could be interesting. However, the pulse frequency should not be higher than the frequency where the impedance becomes inductive, as charging would not take place at such high frequencies. Most probably, the optimal frequency is in the frequency range of the first semicircle. Understanding in detail the relationship between current pulse frequency and electrochemical processes in batteries such as Li-ion movement or SEI growth is crucial to determining the optimal current pulse frequency for stabilizing the battery performance. Also, it is important to address the impact of duty cycle on battery materials, such as Li-ion concentration gradient at interfaces and structural stability of electrode materials, which however requires further detailed studies or simulations. Furthermore, gaining a comprehensive understanding of the structural changes and electrochemical reactions of electrode materials and electrolytes under different charging protocols (e.g., various waveform PC charging[46,47] and multi-step CC charging[48]) will facilitate the development of more effective charging protocols.

Although there was no significant lithium plating in this experiment, this was due to the experiments being conducted at high temperatures (35 °C) and standard current. At lower temperatures or higher current charging, lithium plating often occurs because the voltage can drop below 0V. However, if charging is done with high-frequency current, the voltage remains above 0V as the presence of relaxation time just before plating starts, which has been proved in Li-metal battery system[49–52]. In addition, whether PC charging with relaxation time and multi-step CC fast charging[48,53] can also inhibit dendrite growth in commercial Li-ion batteries will also be worthy of further exploration.

Furthermore, the mechanism of PC charging for enhancing the cycling stability and cycle life can also be applicable to other types of LIBs, particularly those using transition metal oxide cathode (e.g., $LiFePO_4$, $LiCoO_2$, $LiMn_2O_4$, and other types of NMC) and graphite anode, which undergo similar electrochemical processes during operation.

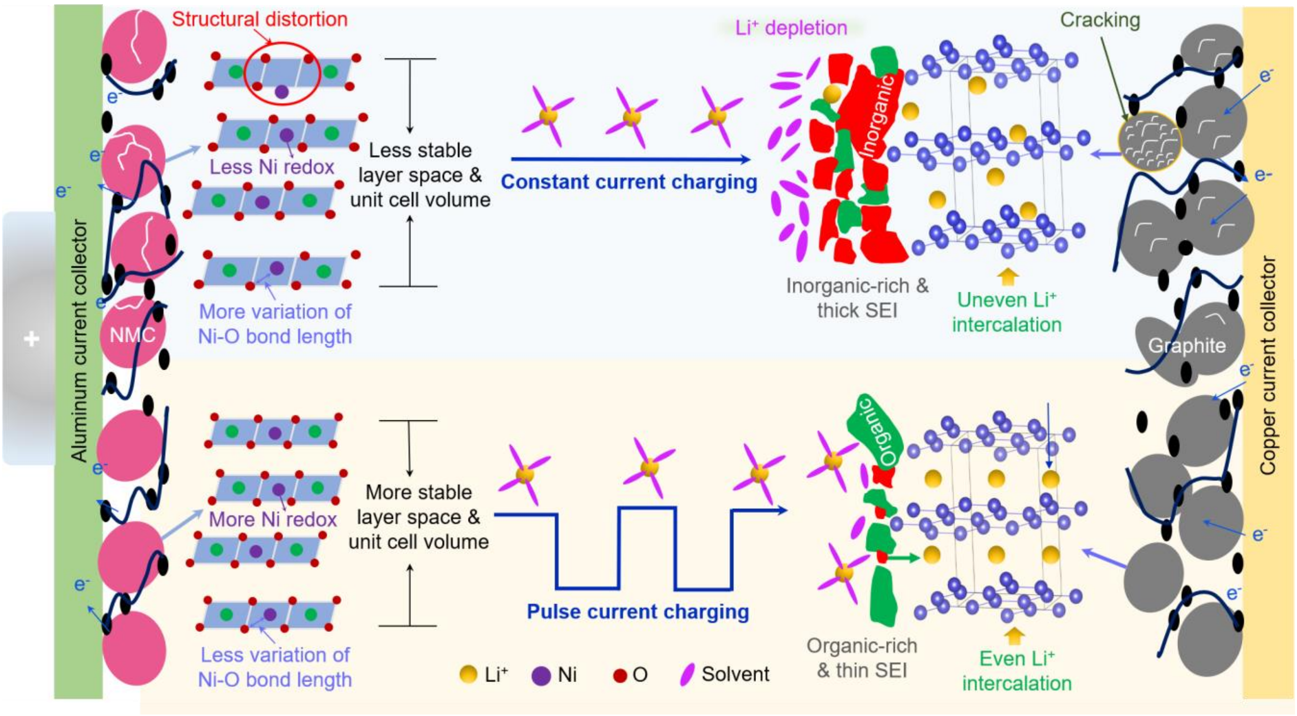

Fig. 7 Mechanisms of PC charging for stabilizing the cycling performance of commercial NMC/graphite LIBs.

Conclusion

In this study, we show the utilization of PC charging can significantly enhance the cycling stability of commercial NMC532/graphite batteries and prolong their cycle life (from 500 cycles to more than 1000 cycles) and unravel the detailed mechanism of battery cycling stability enhancement under PC charging with a comprehensive approach involving electrochemical analysis, *operando* and *ex situ* characterization. Specifically, PC charging facilitates a more even distribution of Li-ions in graphite during the intercalation process, reducing mechanical strain and cracking of graphite particles and enhancing the structural stability of graphite anodes. Unlike previous reports, our findings indicate that the volume expansion of graphite after aging is not simply attributed to an increase of interlayer spacing of graphite. Instead, it is a result of the mechanical strain induced by uneven intercalation of Li-ions in graphite during charging, leading to graphite cracking and electrode expansion. Meanwhile, compared to CC charging, the formation of structural distortion and amorphization of NMC532 is suppressed during PC charging, which greatly enhances Ni redox activity and contributes to the structural stability of NMC532 cathode material during battery cycling. Moreover, PC charging suppresses the secondary reduction of carbonate-based electrolyte, resulting in a thinner and organic-enriched SEI film at the graphite-electrolyte interface with a lower interface resistance compared to that formed under CC charging.

In conclusion, the use of PC charging is advantageous in maintaining the stability of electrode materials and interphase and thereby enhancing the battery cycling performance. These findings offer insights for optimizing the charging protocols of nowadays LIBs and beyond during service and more broadly for the advancement of future battery technology.

Experimental

Full Cell Test

Commercial 18650-type LIBs (Jinggong company, HTCNR18650, nominal capacity: 2200 mAh and voltage: 3.6V), consisting of $Li(Ni_{0.5}Co_{0.2}Mn_{0.3})O_2$ (NMC532) cathode and graphite anode, were used for battery aging tests under different charging protocols.

Test platform for battery aging. The batteries were placed and tested in a VT 4002EMC climate chamber with a temperature of 25 °C. The current modes were generated by an analogy output module (type: National Instruments (NI) 9263) controlled by LabVIEW in host computer, then transferred to a KEPCO BOP 100-10 MG bidirectional program for battery power supply. At the same time, an analogy input module NI 9215 is used to measure the voltage and current of the battery, which is connected to a NIcDAQ-9172 Data Acquisition (DAQ) module for data collection. The details can be found in our previous report [54].

Aging test procedures. Three batteries were used for aging tests. At first, the batteries were aged with CC, Pulse-100 and Pulse-2000 charging, respectively. The average current for all three charging modes is the same, i.e., 1 C (2.2 A), for which the actual current applied under PC charging is two times of that under CC charging. For aging test, the batteries were discharged to a cut-off voltage of 2.5 V at a CC of 2 C (4.4 A) and charged to 4.2 V at a selected charging mode, and no constant voltage segment or relaxation period was included. After every 100 cycles, battery aging was interrupted to perform a reference performance test (RPT) for diagnosis of the battery health state.

RPT test procedures. Before cycling and after aging for every 100 cycles, RPT tests were performed to diagnose the battery health state in a 25 °C climate chamber. The RPT consists of a capacity test and an EIS test. For the capacity test, the batteries were charged with a constant current-constant voltage (CC-CV) protocol until the current reduced to <0.11 A at the 4.2 V CV stage, then were relaxed for an hour, followed by CC discharging to 2.5 V and an hour relaxation. The charging and the discharging processes were carried out once at 0.25 C, 0.5 C and 1 C, respectively. EIS test was performed after the capacity test, for which the batteries were first fully charged (100% SoC) with a CC-CV charging protocol at a current of 1 C and then discharged to 90%, 70%, 50%, 30%, and 10% SoCs then EIS tests were performed at these SoCs using a Digatron potentiostat. The frequency range of EIS is between 6.5 kHz and 10 mHz.

Operando characterization

Operando Raman spectroscopy. It was conducted using a Renishaw QONTOR instrument with a 532 nm laser. Electrochemical tests were performed with an *operando* cell and a BioLogic SP 150 potentiostat. Due to the limited frequency range of the BioLogic potentiostat, the pulse charge charging during *operando* Raman measurements was conducted at 250 Hz (instead of the 2000 Hz frequency that was used in the aging test). The applied current is 0.01 C. The *operando* cell is ECC-Opto-Std type (EL-Cell GmbH, Hamburg, Germany). In the *operando* Raman test, a small (12×4 mm rectangle) piece of graphite electrode served as the working electrode, while a Li sheet acted as the counter electrode, and the electrolyte used in the experiment was composed of 1 mol of $LiPF_6$ dissolved in 1 liter of solvent with a ratio of ethylene carbonate (EC) to diethyl carbonate (DEC) and Dimethyl Carbonate (DMC) at 1:1:1.

Operando electrochemical dilatometry. It was employed to test the thickness of negative electrode during battery cycling. The applied current is 0.2 C. The *operando* cell is ECC-Opto-Std type (EL-Cell GmbH, Hamburg, Germany). 10 mm diameter graphite electrode served as the working electrode, while Li disc acted as the counter electrode, and the electrolyte used in the experiment was composed of 1 mol of $LiPF_6$ dissolved in 1 liter of solvent with a ratio of ethylene carbonate (EC) to diethyl carbonate (DEC) and Dimethyl Carbonate (DMC) at 1:1:1.

***Operando* X-ray absorption spectroscopy (XAS).** *Operando* XAS was performed on NMC samples at various SoCs during the first 1.5 cycles. The measurements were performed at the KMC-2 beamline of the BESSY-II synchrotron light source in Berlin, Germany. For accurate energy calibration, pure metal foil samples were measured simultaneously with each NMC sample. The PC is 2 C with a frequency of 250 Hz (for the same reason as indicated above). The acquired spectra from the XAS measurements underwent data processing using an Athena Software package, including background correction, normalization, k^2-weighting, and Fourier transformation [55,56]. The *in-situ* cell that was lab-designed and compatible with the KMC-2 beamline was pre-prepared in an argon-filled glovebox and then attached to the KMC-2 end station. Both NMC and graphite electrodes with a diameter of 12 mm were cut from a disassembled fresh commercial battery. The electrolyte employed in the experiment consisted of 1 mol of $LiPF_6$ dissolved in 1 liter of solvent, with a composition ratio of EC, DEC, and DMC at 1:1:1.

Post-mortem analyses

After 1000 cycles of aging, the batteries were disassembled for post-mortem analysis. Firstly, the batteries were discharged to 2.5 V by a constant current of 0.1 C. Then, the batteries were transferred to a glove box in an argon atmosphere. Secondly, the batteries were disassembled and the graphite anode and NMC532 cathode were retrieved and washed with di-ethyl carbonate (DEC) separately. Finally, the washed electrodes were dried for 48 hours and sealed in bags inside the glove box prior to further physio-chemical characterization.

***Ex situ* Synchrotron X-ray powder diffraction (XRD)**. *Ex situ* XRD measurement was performed at PETRA III (DESY, Hamburger) on the High-Resolution Powder Diffraction Beamline P02.1. The graphite powder and NMC powder collected from cycled electrodes were filled into Kapton capillaries with a diameter of 0.8 mm and tested using an X-ray equipment voltage of 300 KV.

***Ex situ* Raman spectroscopy**. A RXN1 (Kaiser Optical systems, Inc., MI, USA) spectrometer was employed to examine the graphite electrodes. The excitation light source is a 532 nm laser with a resampling interval of 1 cm^{-1}. The aged electrodes were measured twice. The as-obtained electrodes were measured first. Afterwards, the surface films of the electrodes were scraped off with a knife and measured again to reveal the real state of graphite excluding contribution from the surface species.

SEM. A Zeiss EVO 60 field emission SEM was employed to image the morphologies of the graphite electrodes with a voltage of 15 KV. Samples for cross-sectional imaging were obtained by carefully cutting electrodes using a sharp knife.

Depth-dependent XPS. The XPS depth profile analysis by Ar ion beam etching to reveal subsurface information of the aged graphite electrodes. A Specs XR50 with a non-monochromated Al Kα ($h\nu$ = 1487 eV) X-ray source and a Phobos 1501D-DLD electron detector was employed. For data analysis, the peak fitting of the XPS spectra was carried out with a CasaXPS software using a Shirley-type background, and the peak shift induced by charging effects were corrected based on C-C at 284.91 eV in the C 1s region. For quantification of the chemical substances, relative sensitivity factor (R.S.F.) was employed to correct the peak area that represents the amount of substance. The R.S.F. of C 1s, O 1s, F 1s, and Li 1s are 1, 2.93, 4.43, and 0.0568, respectively.

Author contributions

Y. X., D. -I. S., and P. A. supervised the project. J. G. carried out the experiments and write the manuscript. M. E., Y. L., H. W., X. R., P. -k. K., D. W., and Q. Z. help in experiments performing. L. G., K. P., and J. K. provide suggestions on experiments and manuscript content. All authors discussed the results and contributed to the manuscript.

Conflict of interest

The authors declare no conflict of interest.

Acknowledgements

Jia Guo was supported by a grant from the China Scholarship Council (No. 202006370035) and a fund from Otto Monsteds Fund (No. 4057941073). Besides, we thank the beamtime (KMC-2) granted at BESSY II and the help from beamline scientist Dr. Götz Schuck and colleagues Dr. Katherine A. Mazzio and Dr. Dongjiu Xie who helped with the *operando* XAS measurements, and thanks to the beamtime (P02.1) granted at DESY PETRA III and the help from beamline scientist Dr. Volodymyr Baran, and colleagues Dr. Yanan Sun and Dr. Katherine A. Mazzio who helped with the *ex situ* XRD measurements. Jia Guo would like to thank Haidi Company for providing the fresh positive and negative electrodes for *operando* experiments.

References

1 Y. Tian, G. Zeng, A. Rutt, T. Shi, H. Kim, J. Wang, J. Koettgen, Y. Sun, B. Ouyang, T. Chen, Z. Lun, Z. Rong, K. Persson and G. Ceder, *Chem. Rev.*, 2021, **121**, 1623–1669.
2 M. Li, J. Lu, Z. Chen and K. Amine, *Adv. Mater.*, 2018, 30, 1–24.
3 G. Qian, Z. Li, Y. Wang, X. Xie, Y. He, J. Li, Y. Zhu, S. Xie, Z. Cheng, H. Che, Y. Shen, L. Chen, X. Huang, P. Pianetta, Z. F. Ma, Y. Liu and L. Li, *Cell Reports Phys. Sci.*, 2022, **3**, 100741.
4 F. Holtstiege, A. Wilken, M. Winter and T. Placke, *Phys. Chem. Chem. Phys.*, 2017, **19**, 25905–25918.
5 C. P. Aiken, E. R. Logan, A. Eldesoky, H. Hebecker, J. M. Oxner, J. E. Harlow, M. Metzger and J. R. Dahn, *J. Electrochem. Soc.*, 2022, **169**, 050512.
6 S. Zhu, C. Hu, Y. Xu, Y. Jin and J. Shui, *J. Energy Chem.*, 2020, 46, 208–214.
7 X. Huang, Y. Li, A. B. Acharya, X. Sui, J. Meng, R. Teodorescu and D. I. Stroe, *Energies*, 2020, **13**, 1–18.
8 X. Huang, W. Liu, J. Meng, Y. Li, S. Jin, R. Teodorescu and D. I. Stroe, *IEEE J. Emerg. Sel. Top. Power Electron.*, 2023, **11**, 57–66.
9 D. R. Rajagopalan Kannan and M. H. Weatherspoon, *J. Power Sources*, 2020, **479**, 229085.
10 L. R. Chen, S. L. Wu, D. T. Shieh and T. R. Chen, *IEEE Trans. Ind. Electron.*, 2013, **60**, 88–97.
11 M. Abdel Monem, K. Trad, N. Omar, O. Hegazy, B. Mantels, G. Mulder, P. Van den Bossche and J. Van Mierlo, *Appl. Energy*, 2015, **152**, 143–155.
12 M. Abdel-Monem, K. Trad, N. Omar, O. Hegazy, P. Van den Bossche and J. Van Mierlo, *Energy*, 2017, **120**, 179–191.
13 D. Rajagopalan Kannan and M. H. Weatherspoon, *Int. J. Electrochem. Sci.*, 2021, **16**, 1–14.
14 S. Li, Q. Wu, D. Zhang, Z. Liu, Y. He, Z. L. Wang and C. Sun, *Nano*

Energy, 2019, **56**, 555–562.

15 Y. Che, X. Hu, X. Lin, J. Guo and R. Teodorescu, *Energy Environ. Sci.*, 2023, **16**, 338–371.

16 C. R. Birkl, M. R. Roberts, E. McTurk, P. G. Bruce and D. A. Howey, *J. Power Sources*, 2017, **341**, 373–386.

17 J. Guo, S. Jin, X. Sui, X. Huang, Y. Xu, Y. Li, P. K. Kristensen, D. Wang, K. Pedersen, L. Gurevich and D. I. Stroe, *J. Mater. Chem. A*, 2022, **11**, 41–52.

18 C. Delacourt, A. Kwong, X. Liu, R. Qiao, W. L. Yang, P. Lu, S. J. Harris and V. Srinivasan, *J. Electrochem. Soc.*, 2013, **160**, A1099–A1107.

19 H. Adenusi, G. A. Chass, S. Passerini, K. V. Tian and G. Chen, *Adv. Energy Mater.*, 2023, 13, 2203307.

20 J. S. Edge, S. O'Kane, R. Prosser, N. D. Kirkaldy, A. N. Patel, A. Hales, A. Ghosh, W. Ai, J. Chen, J. Yang, S. Li, M. C. Pang, L. Bravo Diaz, A. Tomaszewska, M. W. Marzook, K. N. Radhakrishnan, H. Wang, Y. Patel, B. Wu and G. J. Offer, *Phys. Chem. Chem. Phys.*, 2021, 23, 8200–8221.

21 M. Dubarry, V. Svoboda, R. Hwu and B. Y. Liaw, *Electrochem. Solid-State Lett.*, 2006, **9**, 10.

22 J. Guo, Y. Li, J. Meng, K. Pedersen, L. Gurevich and D. I. Stroe, *J. Energy Chem.*, 2022, **74**, 34–44.

23 M. Gaberšček, *Nat. Commun.*, 2021, **12**, 19–22.

24 W. Hu, Y. Peng, Y. Wei and Y. Yang, *J. Phys. Chem. C*, 2023, **127**, 4465–4495.

25 P. Iurilli, C. Brivio and V. Wood, *J. Power Sources*, 2021, **505**, 229860.

26 Y. Lu, C. Z. Zhao, J. Q. Huang and Q. Zhang, *Joule*, 2022, **6**, 1172–1198.

27 Q. Zhang, D. Wang, E. Schaltz, D. I. Stroe, A. Gismero and B. Yang, *J. Energy Storage*, 2022, **55**, 105386.

28 Q. Zhang, D. Wang, E. Schaltz, D. I. Stroe, A. Gismero and B. Yang, *J. Energy Storage*, 2023, **64**, 107029.

29 S. Srivastav, M. J. Lacey and D. Brandell, *J. Appl. Electrochem.*, 2017, **47**, 229–236.

30 Y. Shen, X. Shen, M. Yang, J. Qian, Y. Cao, H. Yang, Y. Luo and X. Ai, *Adv. Funct. Mater.*, 2021, **31**, 1–9.

31 Y. Li, M. Bettge, B. Polzin, Y. Zhu, M. Balasubramanian and D. P. Abraham, *J. Electrochem. Soc.*, 2013, **160**, A3006–A3019.

32 M. N. Ates, Q. Jia, A. Shah, A. Busnaina, S. Mukerjee and K. M. Abraham, *J. Electrochem. Soc.*, 2014, **161**, A290–A301.

33 H. H. Ryu, B. Namkoong, J. H. Kim, I. Belharouak, C. S. Yoon and Y. K. Sun, *ACS Energy Lett.*, 2021, **6**, 2726–2734.

34 J. Yu, J. Wang, X. Long, L. Chen, Q. Cao, J. Wang, C. Qiu, J. Lim and S. Yang, *Adv. Energy Mater.*, 2021, **11**, 1–7.

35 L. Zhu, S. Shan, V. Petkov, W. Hu, A. Kroner, J. Zheng, C. Yu, N. Zhang, Y. Li, R. Luque, C. J. Zhong, H. Ye, Z. Yang and B. H. Chen, *J. Mater. Chem. A*, 2017, **5**, 7869–7875.

36 H. Zhu, Y. Huang, H. Zhu, L. Wang, S. Lan, X. Xia and Q. Liu, *Small Methods*, 2020, **4**, 1–30.

37 R. Ruess, M. A. Ulherr, E. Trevisanello, S. Schröder, A. Henss and J. Janek, *J. Electrochem. Soc.*, 2022, **169**, 070531.

38 W. Lee, S. Lee, E. Lee, M. Choi, R. Thangavel, Y. Lee and W. S. Yoon, *Energy Storage Mater.*, 2022, **44**, 441–451.

39 L. Cabo-Fernandez, A. R. Neale, F. Braga, I. V. Sazanovich, R. Kostecki and L. J. Hardwick, *Phys. Chem. Chem. Phys.*, 2019, **21**, 23833–23842.

40 I. Takahashi, H. Kiuchi, A. Ohma, T. Fukunaga and E. Matsubara, *J. Phys. Chem. C*, 2020, **124**, 9243–9248.

41 S. E. J. O'Kane, W. Ai, G. Madabattula, D. Alonso-Alvarez, R. Timms, V. Sulzer, J. S. Edge, B. Wu, G. J. Offer and M. Marinescu, *Phys. Chem. Chem. Phys.*, 2022, **24**, 7909–7922.

42 H. Bryngelsson, M. Stjerndahl, T. Gustafsson and K. Edström, *J. Power Sources*, 2007, **174**, 970–975.

43 B. Han, Y. Zou, G. Xu, S. Hu, Y. Kang, Y. Qian, J. Wu, X. Ma, J. Yao, T. Li, Z. Zhang, H. Meng, H. Wang, Y. Deng, J. Li and M. Gu, *Energy Environ. Sci.*, 2021, **14**, 4882–4889.

44 S. Heng, L. Lv, Y. Zhu, J. Shao, W. Huang, F. Long, Q. Qu and H. Zheng, *Carbon N. Y.*, 2021, **183**, 108–118.

45 S. Heng, Q. Shi, Y. Wang, Q. Qu, J. Zhang, G. Zhu and H. Zheng, *ACS Appl. Energy Mater.*, 2019, **2**, 1336–1347.

46 Y. Qin, X. Chen, A. Tomaszewska, H. Chen, Y. Wei, H. Zhu, Y. Li, Z. Cui, J. Huang, J. Du, X. Han, L. Lu, B. Wu, K. Sun, Q. Zhang and M. Ouyang, *Cell Reports Phys. Sci.*, 2022, **3**, 100708.

47 S. Jin, X. Sui, X. Huang, S. Wang, R. Teodores and D. I. Stroe, *2022 IEEE Energy Convers. Congr. Expo. ECCE 2022*, 2022, 1–6.

48 Y. Li, J. Guo, K. Pedersen, L. Gurevich and D. I. Stroe, *J. Energy Chem.*, 2023, **80**, 237–246.

49 Q. Li, S. Tan, L. Li, Y. Lu and Y. He, *Sci. Adv.*, 2017, **3**, 1–10.

50 S. Zhu, C. Hu, Y. Xu, Y. Jin and J. Shui, *J. Energy Chem.*, 2020, **46**, 208–214.

51 J. Zhang, Z. Zhou, Y. Wang, Q. Chen, G. Hou and Y. Tang, *ACS Appl. Mater. Interfaces*, 2022, **14**, 50414–50423.

52 G. Qiu, L. Lu, Y. Lu and C. Sun, *ACS Appl. Mater. Interfaces*, 2020, **12**, 28345–28350.

53 Q. Pang, J. Meng, S. Gupta, X. Hong, C. Y. Kwok, J. Zhao, Y. Jin, L. Xu, O. Karahan, Z. Wang, S. Toll, L. Mai, L. F. Nazar, M. Balasubramanian, B. Narayanan and D. R. Sadoway, *Nature*, 2022, **608**, 704–711.

54 X. Huang, W. Liu, A. B. Acharya, J. Meng, R. Teodorescu and D. I. Stroe, *IEEE Trans. Ind. Electron.*, 2022, **69**, 10144–10153.

55 B. Ravel and M. Newville, *J. Synchrotron Radiat.*, 2005, **12**, 537–541.

56 S. D. Kelly, K. M. Kemner, J. B. Fein, D. A. Fowle, M. I. Boyanov, B. A. Bunker and N. Yee, *Geochim. Cosmochim. Acta*, 2002, **66**, 3855–3871.

Supporting information

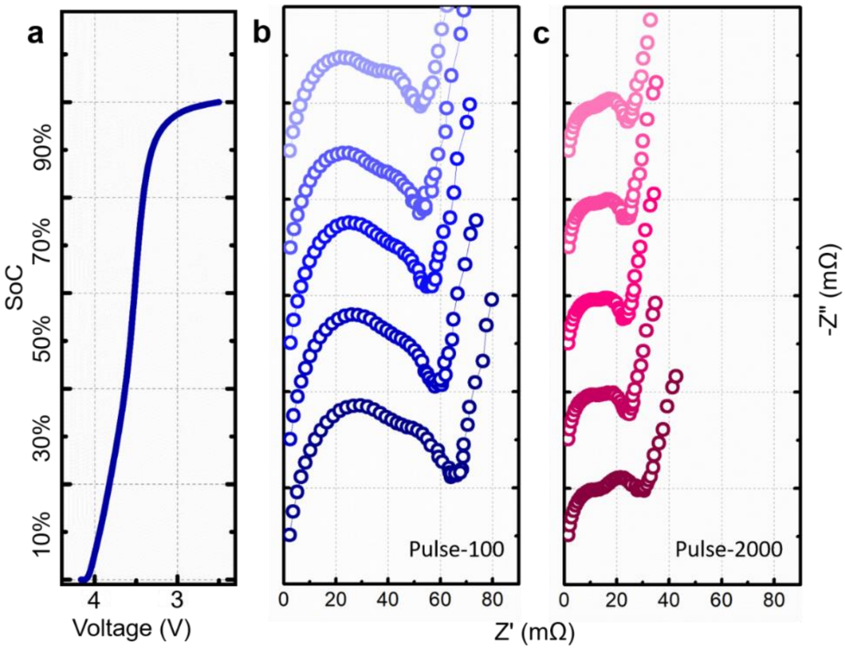

Fig. S1 *Operando* EIS results of commercial NMC532/graphite batteries aged at CC and PC charging conditions.

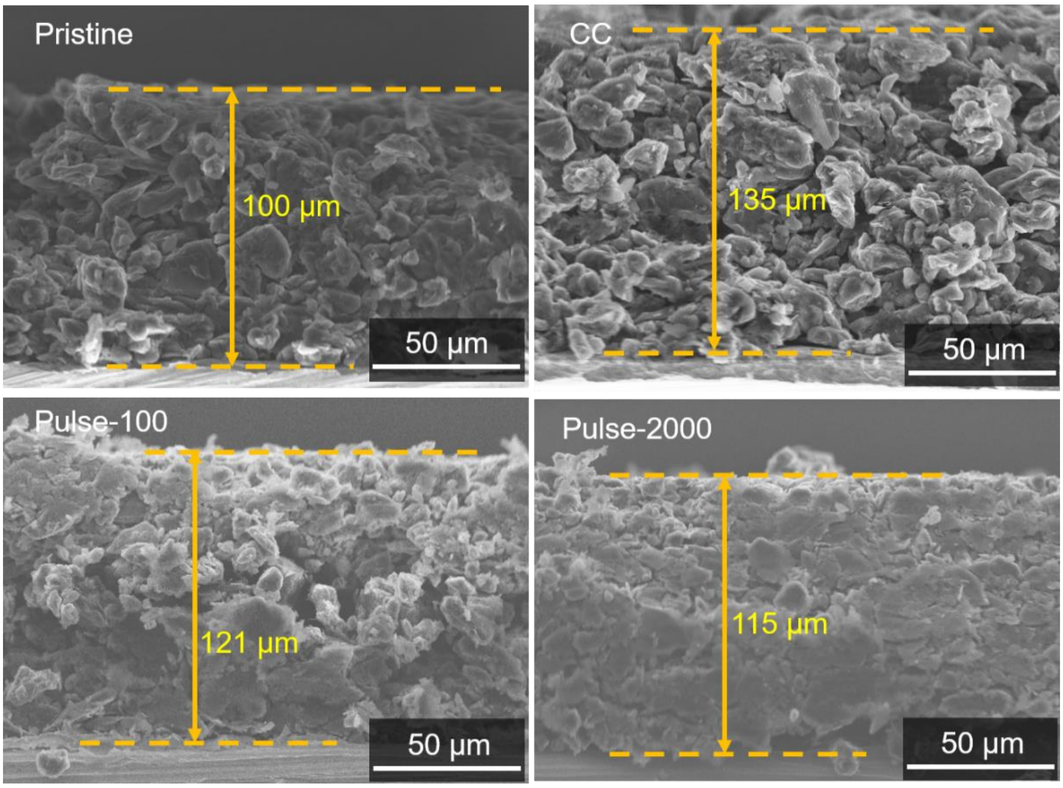

Fig. S2 Cross-section FE-SEM images for pristine and aged graphite electrode after aging for 1000 cycles under CC, Pulse-100 and Pulse-2000 charging conditions. The thicknesses were measured five times for each sample, based on which the median values and errors were determined.

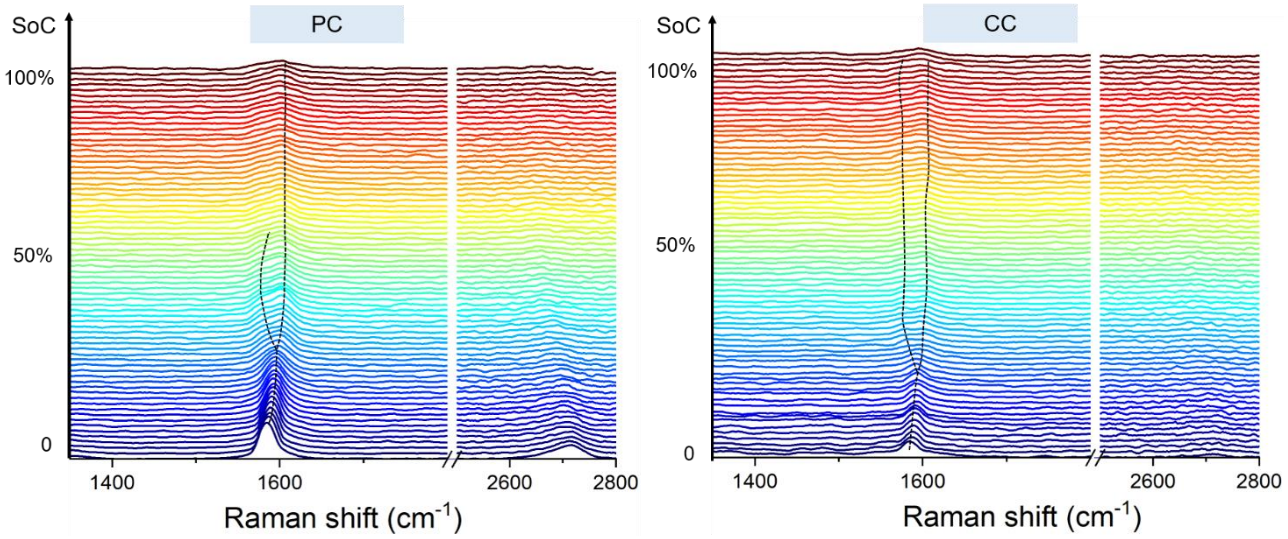

Fig. S3 *Operando* Raman spectra of graphite anode lithiated under pulsed and constant current.

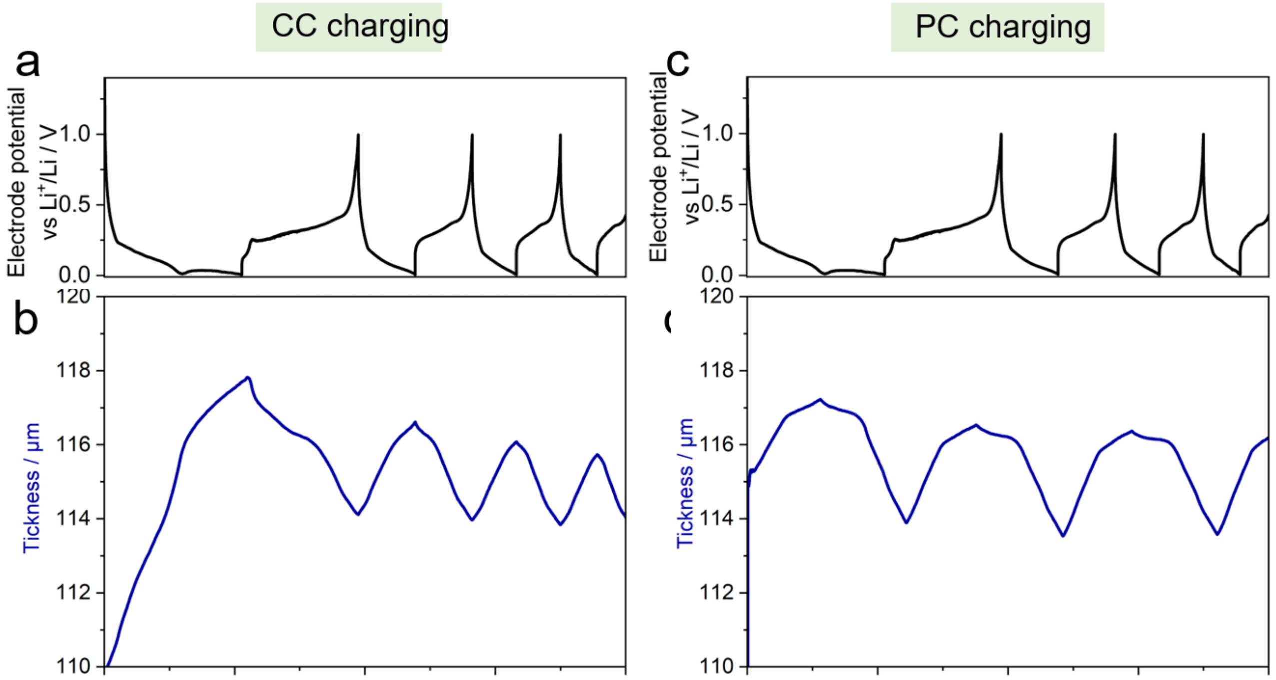

Fig. S4 *Operand*o dilatometry results of graphite anode under CC and PC charging.

Both cells show a large increase in electrode thickness during the initial lithiation process, which has been proved due to the restructuring of the electrode particles combined with surface film formation[1].

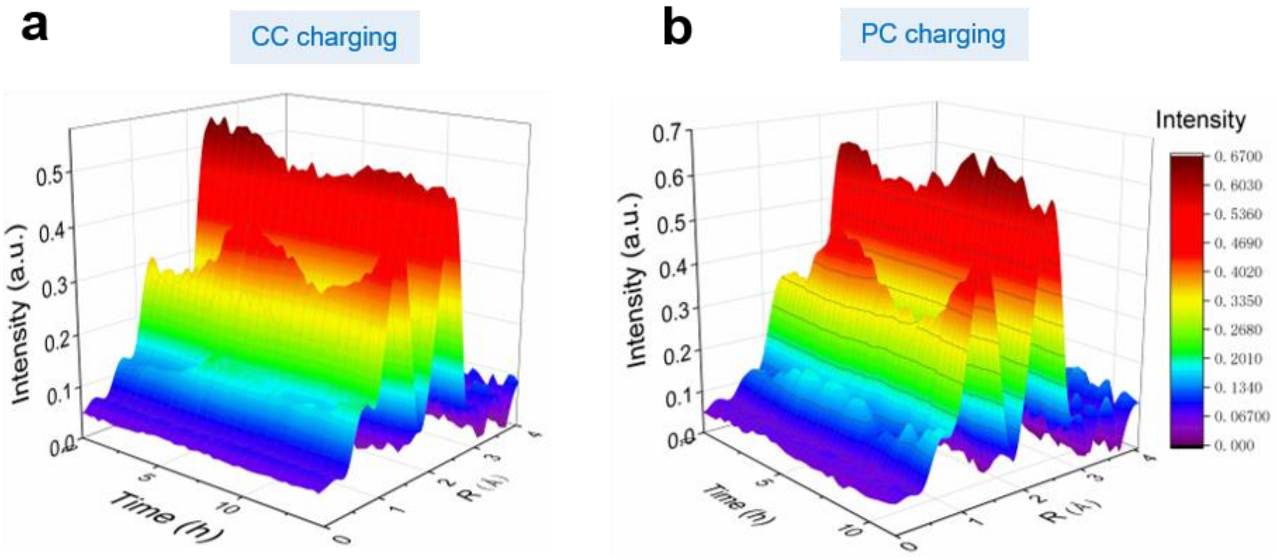

Fig. S5 *Operando* Ni K-edge EXAFS under CC and PC charging.

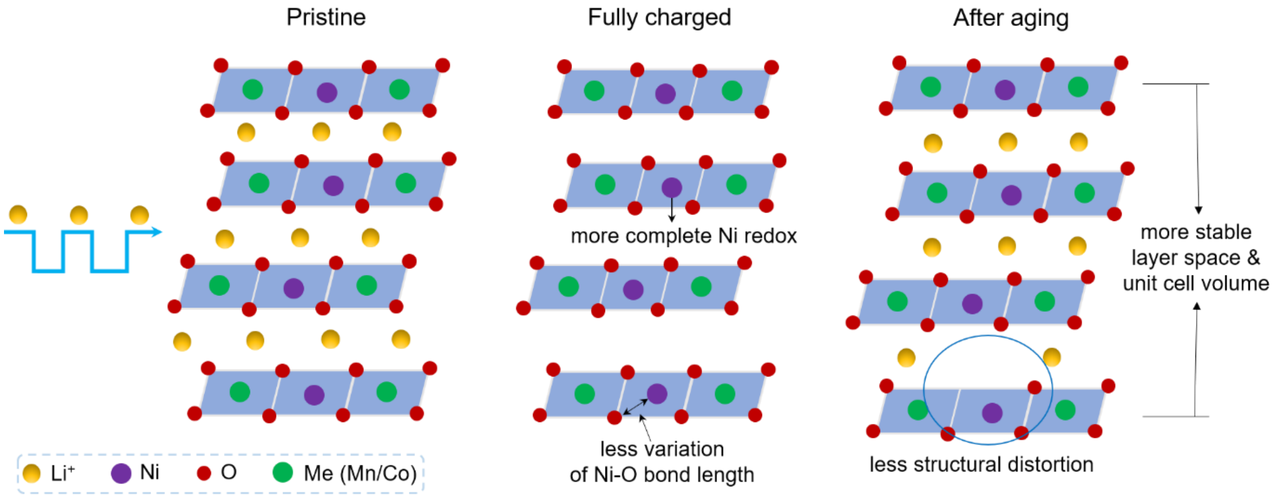

Fig. S6 The mechanism of NCM structure changes in the influence of PC charging based on the *ex situ* and *operando* synchrotron XRD and XAS results.

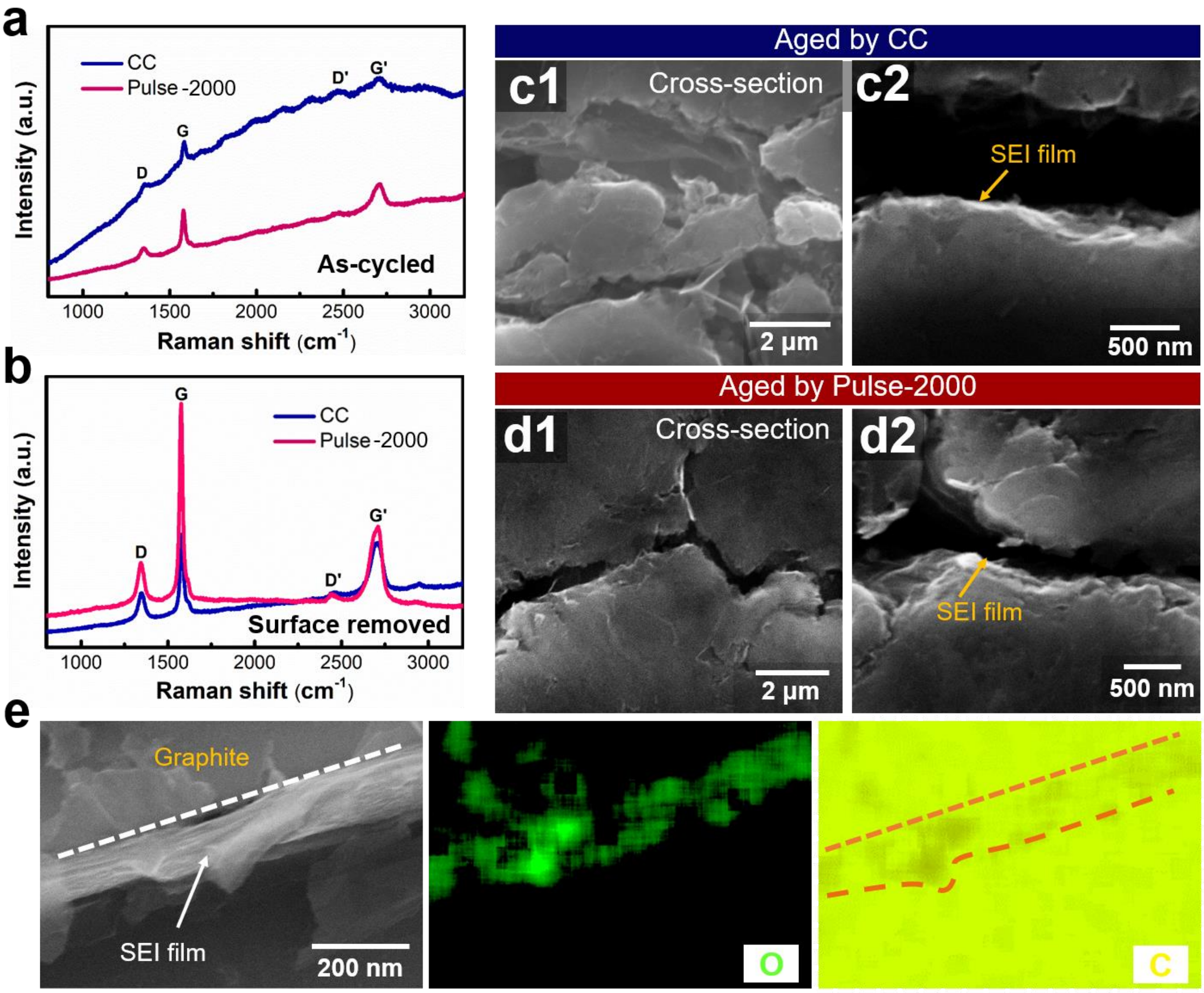

Fig. S7 Raman spectra of (a) as-cycled and (b) surface-removed graphite anodes aged under CC and Pulse-2000 charging. FE-SEM images of the cross-sections of graphite electrodes aged with CC (c1-c2 and e) and Pulse-2000 (d1-d2) charging. (c2) and (d2) are edge-magnified images of (c1) and (d1), respectively. (e) shows the micrograph and O and C element mapping of the surface of CC-aged graphite electrode.

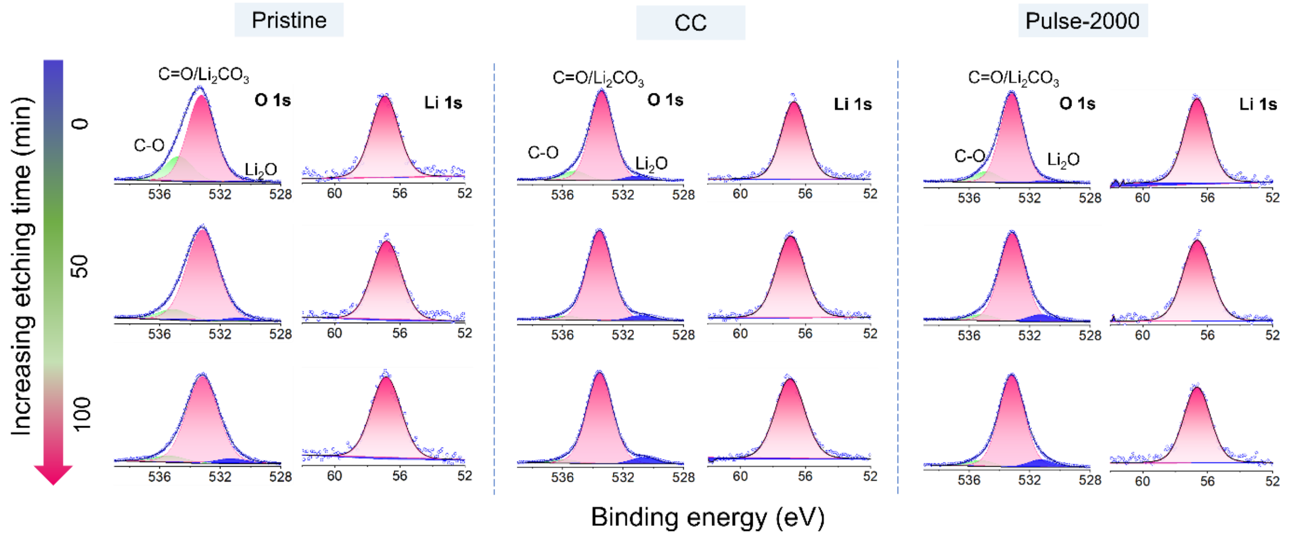

Fig. S8 Depth-dependent XPS of O 1s and Li 1s of pristine, CC- and Pulse-2000-aged graphite electrodes.

Reference

[1] W. Brehm, A. L. Santhosha, Z. Zhang, C. Neumann, A. Turchanin, M. Seyring, M. Rettenmayr, J. R. Buchheim, P. Adelhelm, *J. Power Sources Adv.* **2020**, *6*, 100031.

Journal Publication 6

Can Electrochemical Impedance Spectroscopy be Replaced by Direct Current Techniques in Battery Diagnosis? [J6]

J. Guo, Y. Xu, P. Li, K. Pedersen, and D. I. Stroe

This paper is submitted to *Chemelectrochem*

Can Electrochemical Impedance Spectroscopy be Replaced by Direct Current Techniques in Battery Diagnosis?

Jia Guo [a], Yaolin Xu [b], Pengwei Li[c], Kjeld Pedersen[d], Daniel-Ioan Stroe[a]

[a] Jia Guo, Prof. Daniel-Ioan Stroe
Department of Energy
Aalborg University
Aalborg 9220, Denmark
[b] Dr. Yaolin Xu
Department of Chemistry
Humboldt University of Berlin
Berlin, Germany
[c] Mr. Pengwei Li
Department of Chemistry and Bioscience
Aalborg University
Aalborg 9220, Denmark
[d] Prof. Kjeld Pedersen
Department of Materials and Production
Aalborg University
Aalborg 9220, Denmark

Abstract: Electrochemical impedance spectroscopy (EIS), a conventional technique for impedance measurement, is commonly used in battery diagnosis, which, however, requires expensive equipment and is complex and model-dependent in data analysis. Recently, novel constant current analytics have emerged as an alternative to EIS. They are simple yet powerful, which can reveal impedance information that traditionally could only be obtained through EIS and enable the identification and quantification of lithium-ion diffusion. With machine learning methods, a complete EIS spectrum can be predicted based on constant current charging curves. This work highlights the similarities and discrepancies between constant current techniques and EIS in electrochemical analysis of lithium-ion batteries. Looking ahead, constant current measurements may be promising substitutes for EIS in battery diagnosis, requiring simplified testing infrastructure while offering a deep understanding of battery impedance and its underlying degradation modes.

1. Introduction

With the ever-escalating demand for high-performance batteries for sustainable mobility and energy storage, it is imperative to gain a comprehensive and in-depth understanding of their electrochemical behaviors to accelerate their development and optimal use[1]. Battery impedance is a pivotal parameter that determines battery output voltage, heat generation, and overall health status, and therefore demands significant attention in the design and operation of the battery system[2–4].

Battery impedance measurement methods can be broadly categorized into direct current (DC) and alternating current (AC) methods based on the approach used to apply the current, as shown in **Fig. 1**[5]. The DC methods comprise DC resistance (DCR), hybrid pulse power characterization (HPPC). The DCR and HPPC methods differ primarily in the duration of their charge and discharge currents, with the former generally having shorter durations than the latter, which typically is 18 seconds. Besides, for the impedance of Li-ions diffusion measurements, galvanostatic intermittent titration technique (GITT) and intermittent current interruption (ICI) can be employed. On the other hand, AC testing primarily pertains to EIS, which can rapidly measure all the aforementioned impedances. Here, we are using Lithium-ion batteries (LIBs) as an example to discuss the functions of DC vs. EIS, emphasizing that this discussion is not confined solely to LIBs.

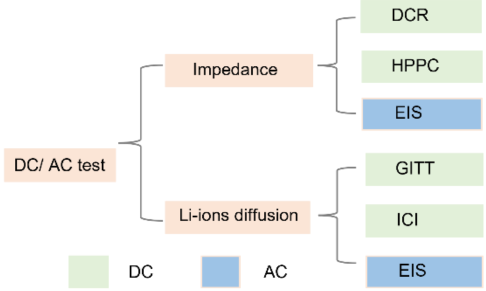

Fig. 1 Commonly used DC and AC measurement methods for battery internal impedance and lithium-Ion diffusion testing

LIBs are nowadays the dominant battery technology on the market, have been extensively studied since the 1980s and the principal electrochemical processes during battery charging and discharging have been identified. Nevertheless, specific mechanisms, such as the impact of operating conditions on the aging of battery components, have yet been fully understood[6].

EIS is a powerful technique capable of providing insights and resolving the unanswered questions related to battery research[7]. The main function of AC-based EIS in batteries is to determine the electronic and/or ionic conductivity of electrodes, electrolytes, interphases, and interfaces, and provide information on the reactance (e.g., capacitance)[8]. Besides, EIS proves to be exceptionally fast for measurement of the mass transfer (e.g., Li-ion diffusion) coefficient in solid electrodes of batteries[9]. However, harsh operating conditions (highly sensitive and easily affected) and high-precision equipment requirements limit wide application of EIS. Instead, DC impedance measurement technique is easy to realize in applications. This is because the DC charging and discharging processes can be executed during battery operation, and thus the battery does not have to be in a long static state. This feature allows for the realization of the DC impedance measurement while the battery is in use, making in-situ or operando impedance measurement feasible. However, DC impedance measurement cannot deconvolute electrochemical processes inside batteries, hindering mechanistic understanding of the detailed electrochemical processes inside batteries. Furthermore, the traditionally DC method of GITT used to assess Li-ion diffusion resistance is considerably more time-consuming when compared to EIS.

With the development of theoretical computations, DC impedance measurement technique has been continuously advanced, and can perform some functions of EIS measurement. For example, the results of DC impedance measurement also have the potential to differentiate electrochemical processes inside batteries. Through data training, the EIS impedance spectrum (typically obtained with AC measurement methods) can be simulated from the constant current charging curves with the help of machine learning[10,11]. Furthermore, conventional GITT method for measurement the impedance in Li-ion diffusion is highly time-consuming, while the novel ICI technology saves at least 75% of the measurement time[1]. As DC measurement continues to advance, it is anticipated that it may eventually be able to achieve all functions of EIS.

In this concept paper, we discuss the potential of DC impedance measurement for obtaining similar battery electrochemical understanding as we get from EIS measurement. Additionally, we explore the potential advancements and prospects of impedance measurement technology from an application perspective.

2. Origins of impedance in battery

Battery impedance is not only influenced by battery state of charge (SOCs) but also by the state of health (SOH) and operating temperature[12]. As discussed, battery impedance is rooted in multiple processes, such as the electrode surface film formation and growth, charge transfer, Li-ion diffusion inside electrode materials, and Ohmic impedance. These specific processes contributing to battery impedance and the battery aging mechanisms are shown in **Fig. 2**[13,14]. As the battery impedance can be divided into ohmic impedance (related to conductivity loss, electrolyte consumption, and electrolyte decomposition)[12], surface film impedance (related to loss of Li, involving CEI in cathode surface and SEI in anode surface)[15], charge transfer impedance (related to charge storage in double layer, and charge transfer reaction)[7,16], and Li-ion diffusion impedance (also related to loss of active materials, e.g., particles fracture, and materials structure change)[17] during the measurement, the aging modes of the battery can be easily identified. This will allow for accurate and effective battery diagnosis. Therefore, EIS is often used to identify the battery aging mechanism, and to unravel the cause of battery aging. For instance, the loss of electrode material and loss of Li can be identified from the R_{ct} and R_{sei} features of EIS spectrum.

EIS measurements are typically conducted at a specific state of charge (SOC) because the distribution of Li-ions in electrode materials can affect Li-ions diffusion and charge transfer resistance. In addition, as the SOC increases, the volume of the negative electrode (Graphite) also increases, resulting in a reduction in battery impedance. [18]. Meanwhile, the impedance is related to the battery SOH and can be used to estimate battery SOH.

Currently, the diffusion coefficient of Li-ions in solid electrodes can be measured using GITT, an intermittent constant current technique, next to EIS measurement. However, in the analysis of impedance contributions other than Li-ion diffusion that are related to electrochemical processes, EIS remains the preferred method that allows for the deconvolution and detailed analysis of various electrochemical processes that contribute to battery impedance.

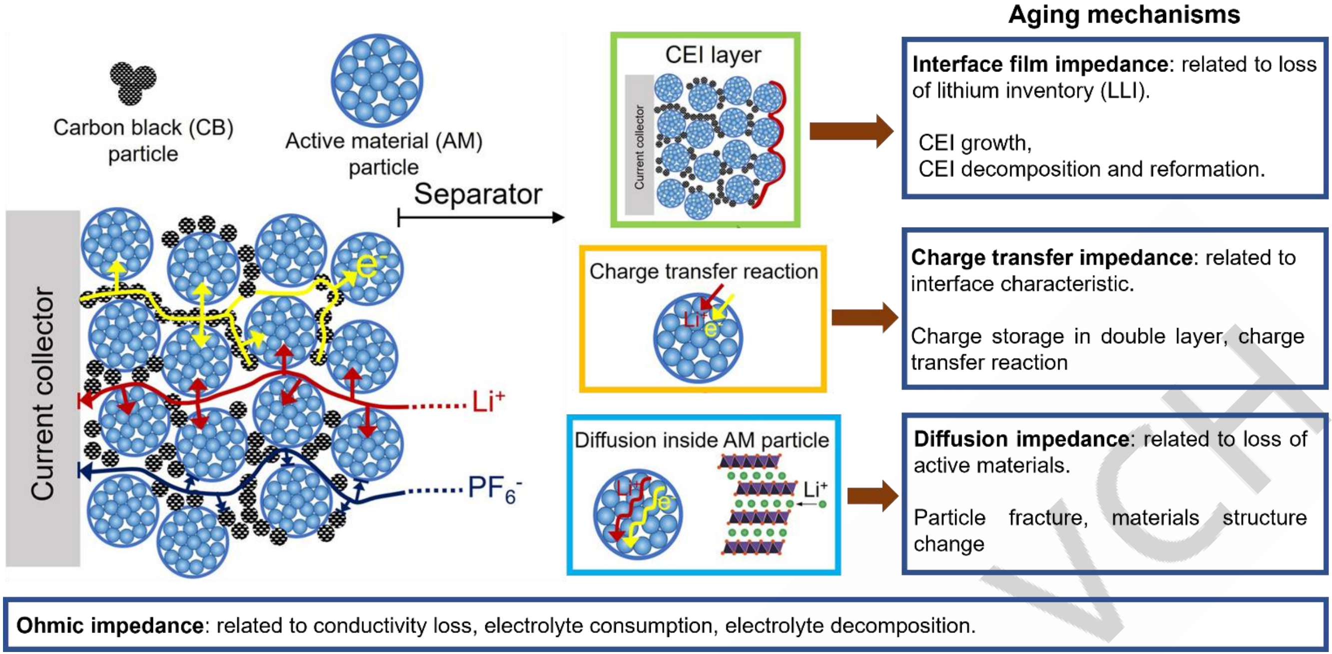

Interface film impedance: related to loss of lithium inventory (LLI).

CEI growth,
CEI decomposition and reformation.

Charge transfer impedance: related to interface characteristic.

Charge storage in double layer, charge transfer reaction

Diffusion impedance: related to loss of active materials.

Particle fracture, materials structure change

Ohmic impedance: related to conductivity loss, electrolyte consumption, electrolyte decomposition.

Fig. 2 The electrochemical processes inside a LIB and the corresponded battery impedance contributions during battery operation and aging[13,14]. Take cathode material as an example, but it is not limited to cathode material particles.

3. EIS and DC impedance show similar results in impedance identification

Both EIS and DC impedance measurements can be used to identify different battery electrochemical processes, such as the R_{sei}, R_{ct}, and R_{mt}[8,19] (**Fig. 3**). The EIS results are obtained based on the changing of current frequency. With the frequency changing, the transfer (electron conductive and Li ions diffusion) process can be identified from the EIS spectrum. Similarly, DC constant current also can be used to measure battery impedance. Depending on the duration of current applied, the battery impedance corresponding to different electrochemical processes can be calculated. This means that both EIS and DC techniques can obtain battery impedance results, which are dependents on the rate of the chemical reaction process. Stolz et al[8]. summarized the mechanisms of EIS impedance and DC impedance, respectively. They highlighted the advantages of DC measurement techniques. Consistent with Stroe's study, the advantage of the DC pulse technique is that one can extract the impedance/resistance directly from the battery's real-life operation[20].

Both AC and DC measurements rely on discerning the reaction rates of diverse electrochemical processes to deconvolute these processes. However, how to distinguish the timescales for R_{mt}, R_{ct} and R_{sei} in DC impedance measurement is still a challenge. This is expected to be solved with the help of developments in computational methods, such as employing advanced data fitting or prediction methods to identify the timescales of individual reaction processes.

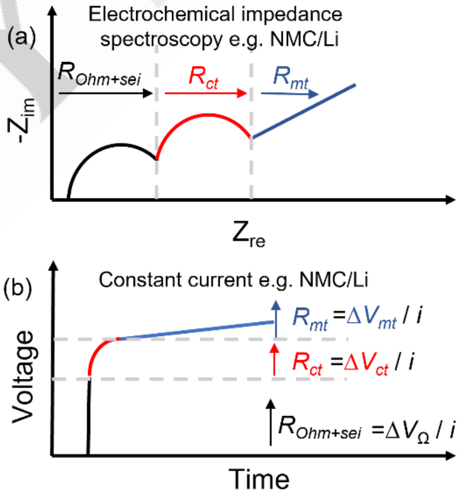

Fig. 3 EIS and DC impedance measurements, *e.g.* constant current techniques both can be used to quantify the battery impedance for $R_{\mathrm{ohm+sei}}$, R_{ct}, and R_{mt}[8].

4. Determination of Li diffusion impedance in solid electrodes

As shown in **Fig. 4**, both AC and DC current can be used to measure the Li diffusion coefficient. EIS is the most convenient method for measuring Li-ion diffusion as it takes only several minutes to measure the EIS of LIBs, which can be used to determine Li-ion diffusion coefficient in the electrodes. The low frequency range of the EIS spectrum, and the shape of Nyquist plot in the low-frequency region can be used to calculate the Li-ion diffusion coefficient[21].

GITT is the conventional and primary method for determining Li^+ diffusion coefficients for insertion electrode materials. GITT involves two consecutive steps: firstly, applying a constant current for a duration where the assumption of semi-infinite diffusion is valid, and secondly, interrupting the current until the voltage stabilizes to indicate equilibrium[22]. By analyzing the electrode potential during the current pulse and the subsequent change in equilibrium potential, GITT allows for the determination of the chemical diffusion coefficient of the charge-carrying ions[1]. The disadvantage is that GITT is time-consuming, typically between hours to days, as it requires an significant time interval (over 60 minutes) between current pulses[23]. Recently, a novel ICI method has been proposed as an alternative to the GITT measurement [1]. By conducting linear regressions of the potential change against the square root of step time during the current pauses, it becomes possible to extract both the time-independent and time-dependent components of the resistance. These components are referred to as the internal resistance and the diffusion coefficient, respectively. The ICI method shortens the relaxation interval to 1 – 10 seconds, significantly reducing the measurement time.

The innovative ICI method can quickly determine the diffusion coefficient of Li-ions. It is also easier to apply in real-world application. With a deep measurement is associated with the understanding of the Li-ion diffusion process in electrode and advancement of data processing, a more simplified DC technique determining Li diffusion can be envisaged.

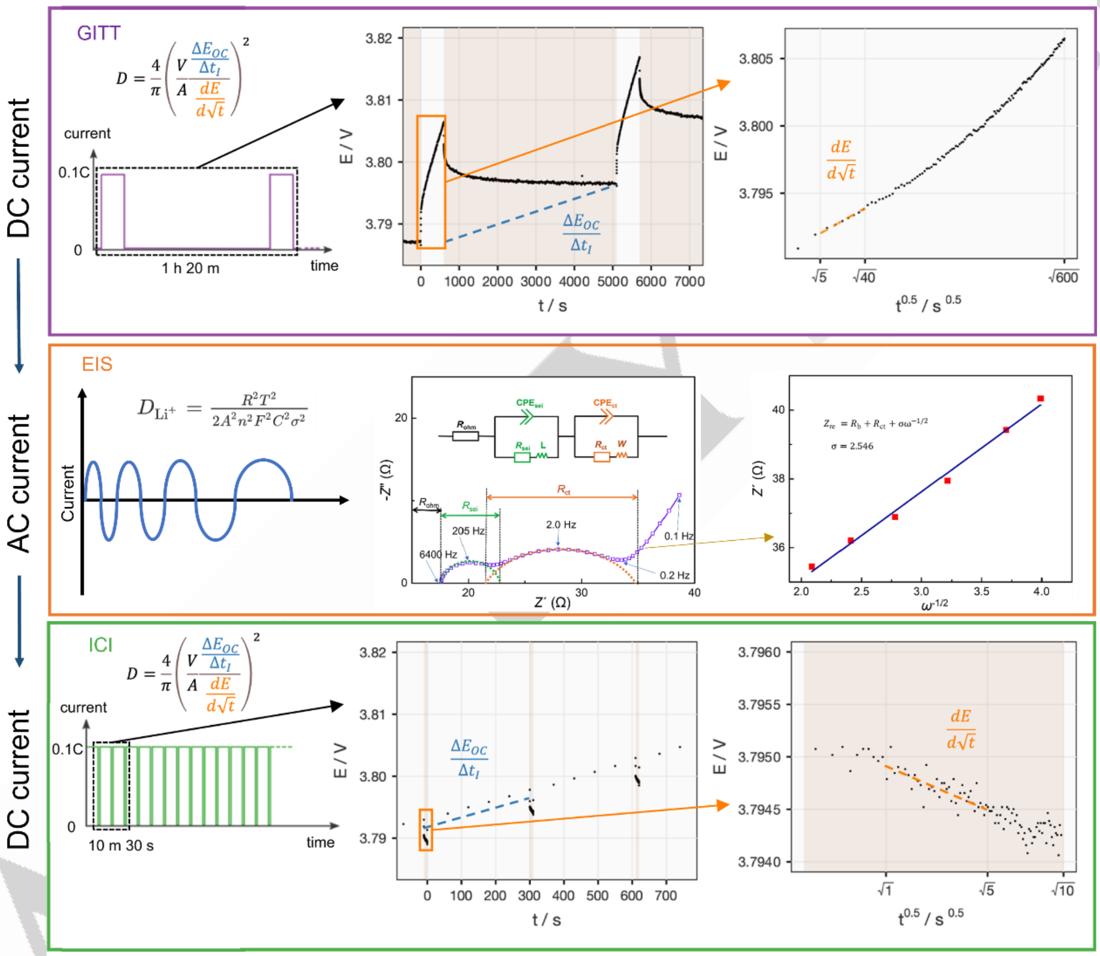

Fig. 4 The Li$^+$ diffusion coefficient in insertion electrode materials can be identified by (a) EIS[21] measurement: the slope of the low-frequency region can be used to calculate the Li-ion diffusion coefficient, (b) ICI measurement: the relaxation time is short only a few seconds, and (c) GITT method: the relaxation time is long (over 60 minutes) in after each applied current[1].

5. EIS spectrum prediction based on constant current charging curves

With the development of machine learning, it has been found that the constant current charging curve can be used to predict the EIS spectrum with marginal error[10,24]. The prediction process is shown in **Fig. 5**. First, the model underwent training with an extensive dataset, which included voltage-capacity curves collected at different State of Health (SOH) levels, together with their corresponding EIS data. Then, the established model was used to predict the corresponded impedance spectrum. Finally, the machine learning model successfully established a mapping between the battery charging curve and the corresponding EIS data. This demonstrates that there exists a discernible correlation between the DC charging curve and the EIS data. However, the machine learning process is like a black box, and the intricate relationship between battery charge curves and EIS remains elusive.

This prediction method, which relies on model training, has the potential to accelerate the battery SOH diagnosis in vehicles applications. The EIS information of the battery can be quickly obtained according to the charging curve of the battery.

Here, the implementation of DC measurement method demonstrates the potential as a substitute for EIS in application. The development of machine learning can help DC charging curve replace the function of EIS to study and diagnose the battery electrochemical behavior.

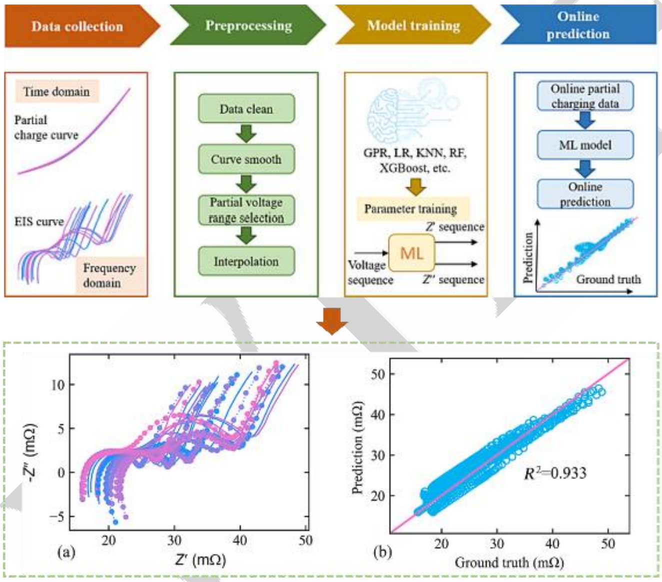

Fig. 5 The EIS spectrum can be predicted by the battery constant current charging curve by machine learning method, and the training process is based on a huge dataset collected in early stage[24].

6. Perspective for the development of impedance identification

6.1 Understanding the underlying mechanisms of impedance

Understanding of the underlying mechanisms of impedance is continuously evolving. Currently, it is broadly associated with specific chemical reaction processes which can be identified from the EIS measurement. In particular, the resistance of the Li-ion diffusion process is related to the phase transition of the electrode material. To further understand the Li diffusion resistance, it is necessary to clarify how the structural change of the electrode material affects the diffusion process of Li-ions in the electrode material. This requires intensive material structure studies combined with electrochemical measurement analysis. The transformation process of the material structure corresponds to the change in the diffusion coefficient of Li-ions. In this way, the relationship between material structure and diffusion resistance can be established accurately.

The charge transfer is a slower process than the Li-ion transfer across the interfacial film, but faster than Li-ion diffusion in the solid phase. The Li-ion desolvation and solvation processes involved in the charge transfer process remains unclear. The microscopic process of charge transfer is still inferred. Especially under different measurement techniques. It is necessary to adopt advanced measurement methods such as element labeling to track and clarify the charge transfer process. Then, the electrochemical process inside battery will be subdivided again to achieve a more precise diagnosis.

For the surface film impedance, the components and formation of the EEI (SEI and SEI) film are still unclear. Highly ordered pyrolytic graphite (HOPG) with a smooth surface is usually used to study the growth process and composition of SEI films. For the study of SEI morphology, it is necessary to use cryo-electron microscopy, which will overcome the inability of traditional transmission electron microscopy (TEM) to continuously capture the dynamic change process of SEI films. For SEI composition analysis, X-ray photoelectron spectroscopy (XPS) or etching XPS will help to analyze the composition of the SEI film on the surface of the material.

The study of the underlying impedance mechanisms relies on advanced detection equipment and powerful electrochemical analysis techniques. Clear microscopic descriptions of the mechanism will enhance the detail of the electrochemical process, leading to highly accurate models and reliable impedance calculations.

6.2 Development of impedance identification methods

Time-consuming GITT measurements and DC impedance measurements are still being widely used. In principle, the DC impedance measurement is similar to the EIS test, and various electrochemical processes are distinguished according to the duration of the current application. Therefore, DC impedance measurement is expected to replace EIS. However, it is difficult to distinguish the time constants of different chemical processes during DC impedance measurement. If a large amount of measurement data can be used to calibrate and establish an accurate function, it will be beneficial to the development of DC impedance technology. In addition, the test method of Li-ion diffusion coefficient GITT has been simplified, and the ICI technology with fast measurement is to establish a functional relationship under the unsteady state of the battery. With the development of electrochemical models and computing science, it is promising to find a more universal and rapid impedance measurement method.

6.3 Development of impedance identification in the application

The battery’s charging voltage curve can serve as a basis for predicting impedance spectra. While training the predictive model initially demands a substantial dataset, it ultimately enables accurate real-time impedance estimations during battery charging in practical scenarios. As a result, obtained EIS electrochemical diagnosis can furnish the battery management system with additional insights into battery health status. This enhanced feedback of battery information is instrumental in advancing intelligent battery management systems.
Furthermore, digitizing the potential connection between the charging curve and EIS could simplify the direct acquisition of battery impedance information through alternative means.

Simplifying DC impedance measurement as an alternative to EIS measurement or employing machine learning algorithms to estimate battery impedance from extensive charging datasets holds promise for achieving practical automotive battery impedance identification and advancing battery diagnosis and health estimation.

7. Conclusions

Impedance measurements are effective methods for battery diagnosis and SOH estimation. Both DC and EIS methods can be utilized to identify and study the battery impedance. The DC impedance measurement can yield results equivalent to EIS measurements in some cases. Besides, with the development of computing methods, the DC impedance test procedure is constantly being simplified and faster. Moreover, prediction methods such as machine learning can also realize the prediction from DC test curve to EIS by capturing the correlation between DC measurement curve and EIS results. This undoubtedly reflects the consistency between the DC impedance measurement and the EIS measurement.

Acknowledgements

Jia Guo was supported by a grant from the China Scholarship Council (No. 202006370035) and a fund from Otto Monsteds Fund (4057941073).

Keywords: Battery Impedance; AC Impedance; DC Impedance; EIS measurement; Constant Current Technique.

Reference

[1] Y. C. Chien, H. Liu, A. S. Menon, W. R. Brant, D. Brandell, M. J. Lacey, *Nature communications* **2023**, *14*, 2289.
[2] Y. Zheng, Y. Che, X. Hu, X. Sui, R. Teodorescu, *IEEE Transactions on Transportation Electrification* **2023**, *PP*, 1.
[3] Y. Che, X. Hu, X. Lin, J. Guo, R. Teodorescu, *Energy and Environmental Science* **2023**, *16*, 338–371.
[4] Y. Li, J. Guo, K. Pedersen, L. Gurevich, D. I. Stroe, *Journal of Energy Chemistry* **2023**, *80*, 237–246.
[5] J. Huang, H. Ge, Z. Li, J. Zhang, *Electrochimica Acta* **2015**, *176*, 311–320.
[6] J. S. Edge, S. O’Kane, R. Prosser, N. D. Kirkaldy, A. N. Patel, A. Hales, A. Ghosh, W. Ai, J. Chen, J. Yang, S. Li, M. C. Pang, L. Bravo Diaz, A. Tomaszewska, M. W. Marzook, K. N. Radhakrishnan, H. Wang, Y. Patel, B. Wu, G. J. Offer, *Physical Chemistry Chemical Physics* **2021**, *23*, 8200–8221.
[7] M. Gaberšček, *Nature Communications* **2021**, *12*, 19–22.
[8] L. Stolz, M. Gaberšček, M. Winter, J. Kasnatscheew, *Chemistry of Materials* **2022**, *34*, 10272–10278.
[9] S. B. Tang, M. O. Lai, L. Lu, *Materials Chemistry and Physics* **2008**, *111*, 149–153.
[10] Y. Duan, J. Tian, J. Lu, C. Wang, W. Shen, R. Xiong, *Energy Storage Materials* **2021**, *41*, 24–31.
[11] J. Guo, Y. Che, K. Pedersen, D. I. Stroe, *Journal of Energy Chemistry* **2023**, *79*, 211–221.
[12] K. Mc Carthy, H. Gullapalli, K. M. Ryan, T. Kennedy, *Journal of The Electrochemical Society* **2021**, *168*, 080517.
[13] D. Qu, W. Ji, H. Qu, *Communications Materials* **2022**, *3*, 1–9.
[14] W. Hu, Y. Peng, Y. Wei, Y. Yang, *Journal of Physical Chemistry C* **2023**, *127*, 4465–4495.
[15] M. Gauthier, T. J. Carney, A. Grimaud, L. Giordano, N. Pour, H. H. Chang, D. P. Fenning, S. F. Lux, O. Paschos, C. Bauer, F. Maglia, S. Lupart, P. Lamp, Y. Shao-Horn, *Journal of Physical Chemistry Letters* **2015**, *6*, 4653–4672.
[16] J. Zhu, M. S. Dewi Darma, M. Knapp, D. R. Sørensen, M. Heere, Q. Fang, X. Wang, H. Dai, L. Mereacre, A. Senyshyn, X. Wei, H. Ehrenberg, *Journal of Power Sources* **2020**, *448*, 28–30.
[17] C. Pastor-Fernández, K. Uddin, G. H. Chouchelamane, W. D. Widanage, J. Marco, *Journal of Power Sources* **2017**, *360*, 301–318.
[18] J. Guo, S. Jin, X. Sui, X. Huang, Y. Xu, Y. Li, P. K. Kristensen, D. Wang, K. Pedersen, L. Gurevich, D. I. Stroe, *Journal of Materials Chemistry A* **2022**, *11*, 41–52.
[19] A. Waligo, P. Barendse, *ECCE 2016 - IEEE Energy Conversion Congress and Exposition, Proceedings* **2016**, 1–7.
[20] S. B. Vilsen, S. K. Kaer, D. I. Stroe, *IEEE Transactions on Industry Applications* **2020**, *56*, 6937–6948.
[21] J. Guo, Y. Li, J. Meng, K. Pedersen, L. Gurevich, D. I. Stroe, *Journal of Energy Chemistry* **2022**, *74*, 34–44.
[22] K. W. Knehr, S. Biswas, D. A. Steingart, *Journal of The Electrochemical Society* **2017**, *164*, A3101–A3108.
[23] W. Weppner, R. A. Huggins, *Journal of The Electrochemical Society* **1977**, *124*, 1569–1578.
[24] J. Guo, Y. Che, K. Pedersen, D. Stroe, *Journal of Energy Chemistry* **2023**, *79*, 211–221.

Conference Publication 1

Machine Learning to Predict Electrochemical Impedance Spectra (EIS): Can EIS be Replaced by Constant Current Techniques [C1]

J. Guo, Y. Che, S. Jin, K. Pedersen, D. I. Stroe

This paper is accepted by *EIS* 2023

Machine learning to predict electrochemical impedance spectra (EIS): Can EIS be replaced by constant current techniques?

Jia Guo[a], Yunhong Che[a], Siyu Jin[a], Daniel-Ioan Stroe[a]

a AAU Energy, Aalborg University, Aalborg 9220, Denmark

b Department of Materials and Production, Aalborg University, Aalborg 9220, Denmark

Abstract

Electrochemical impedance spectra (EIS) have been widely used to diagnose the battery state of health (SOH), because the battery SOH is influenced by resistance-induced overvoltage (polarizations), i.e., ohmic (R_{Ω}), activation (charge transfer; R_{ct}), and concentration polarization (mass transport; R_{mt})[1]. However, the implementation of onboard EIS measurement is hindered, due to the high cost of the measurement equipment, test results subject to SOC, and time-demanding measurements. Here, we predicted impedance spectrum by battery charging voltage curve based on electrochemical mechanistic analysis and machine learning.

As reported, both EIS and charging curves can be used to predict battery SOH[2]. This indicates that the DC charging curve can also demonstrate the dynamic behaviors inside a battery (e.g., charge transfer and mass transfer). Besides, in constant current charging process, it has been found that the voltage change in the first few milliseconds corresponds to R_{Ω}, and the voltage change of first several seconds corresponds to R_{ct}, and the voltage change of first 100 seconds corresponds to R_{ct}[1]. It further confirms that both the EIS and constant current technique can express same electrochemical information.

Battery charging curves as input were used to predict EIS, as shown in **Fig. 1**. The experimental results show that the proper partial voltage range has high accuracy for EIS prediction. The predicted errors for impedance spectrum are less than 1.9 mΩ. This provides a new perspective and means for EIS interpretation.

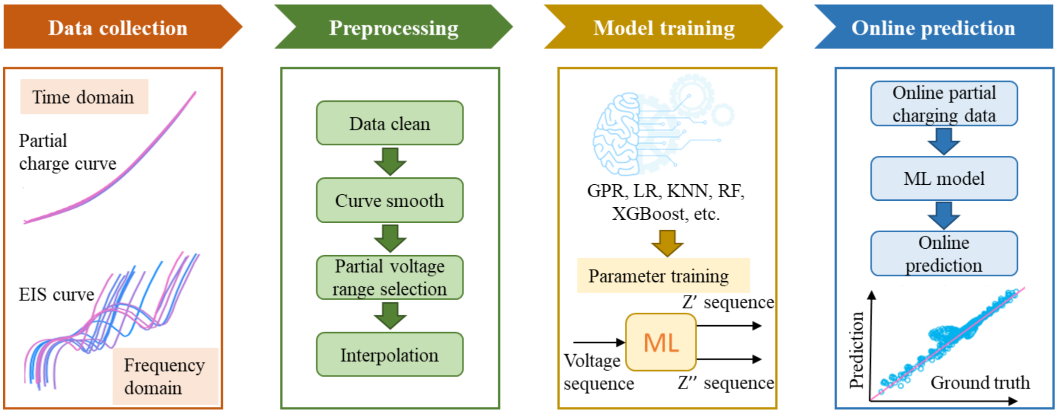

Fig. 1 Charging voltage curve were used to predict electrochemical impedance spectra.

Reference

[1] M. Winter, J. Kasnatscheew, L. Stolz, M. Gabers, **2022**.

[2] K. Uddin, G. H. Chouchelamane, C. Pastor-fern, W. D. Widanage, J. Marco, **2017**, *360*.

Conference Publication 2

Unravelling and Quantifying the Aging Processes of Commercial Li($Ni_{0.5}Co_{0.2}Mn_{0.3}$)O_2/graphite Li-ions Batteries under Constant Current Cycling [C2]

J. Guo, Y. Li, K. Pedersen, L. Gurevich, and D.-I. Stroe

This paper is accepted by *ECS* 2023

Unravelling the aging process of commercial Li(Ni$_{0.5}$Co$_{0.2}$Mn$_{0.3}$)O$_2$/graphite lithium-ion batteries under constant current cycling

Jia Guo[a], Yaqi Li[b], Kjeld Pedersen[b], Daniel-Ioan Stroe[a]
a AAU Energy, Aalborg University, Aalborg 9220, Denmark.
b Department of Materials and Production, Aalborg University, Aalborg 9220, Denmark
jgu@energy.aau.dk

Constant current charging and discharging is widely used nowadays for commercial lithium (Li) ion batteries (LIBs) in applications of portable electronic devices and electric vehicles. However, the main battery degradation mechanism during constant current cycling remains unclear.

In this work, electrochemical cycling, real-time temperature monitoring, and operdando electrochemical impedance spectroscopy of a fresh and an aged battery have been carried out to unveil the aging mechanism during constant current cycling[1]. The results of the incremental capacity analysis (ICA) indicate that polarization is the main reason for the capacity fading during operation.

As shown in Fig. 1[1], with battery aging, the battery charging curve shows an upward trend and the battery discharging curve shown a drop trend in voltage scale. The voltage plateau also can be translated to peaks in IC curves, Fig. 1b. As battery cycling, the b peak shifts to a high voltage direction, which means the impedance increasing inside the battery. The change of b peak shows same trend with the battery SOH degradation in **Fig. 1c**. Therefore, the battery degradation is related to the impedance increasing inside battery. As internal impedance increasing, the battery OCV becomes more and more narrower, which leads to a low charge and discharge capacities. Therefore, the battery degradation.

The main reason of impedance increasing also be analyzed and discussed in our recent study.

Acknowledgements Jia Guo would like to give a thanks to Otto Monsted for their support.

Reference:

[1] J. Guo, S. Jin, X. Sui, X. Huang, Y. Xu, Y. Li, D. W. Peter Kjær Kristensen, D.-I. Stroe, *Journal of Materials Chemistry A* **2023**.

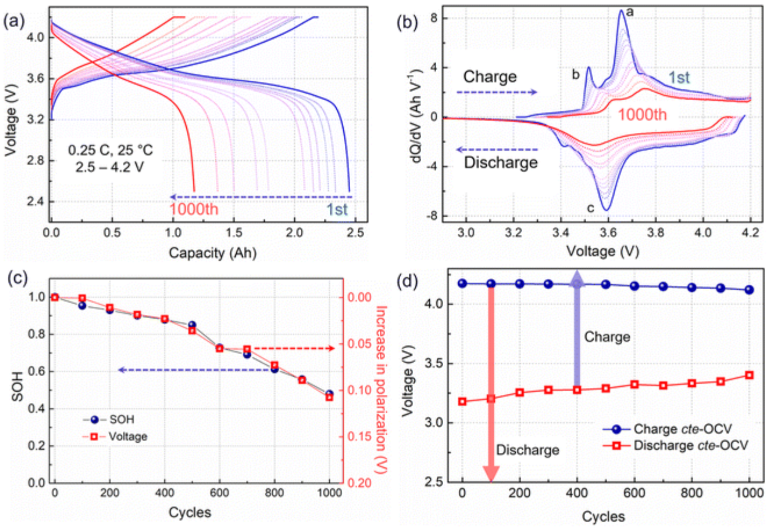

Fig. 1 aging process of an aged commercial battery in 1000 cycles. (a) cycling performance; (b) IC curve; (c) SOH and polarization change; (d) battery OCV of a commercial battery[1].

ISSN (online): 2446-1636
ISBN (online): 978-87-7573-614-0

AALBORG UNIVERSITY PRESS